EFFECT OF NEW SAMPLES IN THE T2K OFF-AXIS NEAR DETECTOR FOR THE T2K OSCILLATION ANALYSIS

By

Jacob Alexander Morrison

A DISSERTATION

Submitted to
Michigan State University
in partial fulfillment of the requirements
for the degree of

Physics – Doctor of Philosophy

2019

ABSTRACT

EFFECT OF NEW SAMPLES IN THE T2K OFF-AXIS NEAR DETECTOR FOR THE T2K OSCILLATION ANALYSIS

By

Jacob Alexander Morrison

The Tokai-to-Kamioka (T2K) experiment is a long baseline neutrino oscillation experiment. T2K uses a beam of muon neutrinos (neutrino beam mode) or antineutrinos (antineutrino beam mode) produced at the Japan Proton Accelerator Research Complex and directed towards the Super-Kamiokande detector to study neutrino oscillations in two ways. One is the disappearance of muon neutrinos as they oscillate to other flavors of neutrinos, while the other is the appearance of electron neutrinos that have oscillated from muon neutrinos. In addition to the far detector, Super-Kamiokande, a suite of detectors is set close to the neutrino source to probe the beam composition prior to the neutrinos oscillating.

Within the neutrino oscillation analysis, uncertainties due to the neutrino beam flux and the cross section of neutrinos serve as the largest sources of error on the oscillation parameters. By including data from the Near Detector at 280 m (ND280), the uncertainties on the flux and cross section can be constrained beyond what the data at the far detector can do on its own. This work describes the near detector maximum likelihood fit and how it is used to constrain uncertainties for the oscillation analysis.

For this thesis, new data samples were included in the near detector fit so that the antineutrino beam mode samples would be treated in the same way as the neutrino beam mode samples. The results are consistent with those seen before; however, they also indicate that certain checks should be updated when the new neutrino interaction model is available before fully transitioning to the new samples. Additionally, tests were performed to study the effect of alternative cross section models on the near detector fit. These studies showed that there is not enough freedom in the current cross section model to fully describe any effects on the data if the underlying cross section differed from the current model.

For,
Kaleigh
I love you!

ACKNOWLEDGMENTS

As anyone who has written a dissertation would tell you, researching and writing such an extensive document is no easy task. Over the past four years, a great number of people have helped and supported me while I have been working on mine.

To those at Michigan State, thank you for all the fun we have had over the years. Kendall, thank you for being an awesome thesis advisor. Your insights into physics have introduced me to a new way of looking at things. Matt and Luke, thank you for your help with programming and for the time spent discussing the various projects I have worked on. Andrew, thank you for your invaluable discussions on coding, frustrations with ROOT, traveling, and, most importantly, sports. Our time spent traveling around Japan together, from Fukuoka and Hiroshima to Toyama and SK to all over Tokyo, those times will stay with me for the years to come. Jake, thank you for the time spent working on homework and studying for finals as we went through classes. Dan, thank you for being willing to go over presentations and application essays and for your thoughtful insights into neutrino physics.

To the support staff at Michigan State, thank you for all the hard work that you do every day to make this department run smoothly. Kim, thank you for always having a smile ready and for keeping everything (and everyone) in line. Brenda, thank you for making the process of setting up travel and getting refunds a breeze and for always knowing where Kendall is in the world on any given week (especially in the summer).

To all those I have had a chance to work with on T2K, thank you for all that you do in advancing our knowledge of neutrinos. While there a many people I have worked with directly over the last few years, I want to highlight a few. Hayato-san, thank you for hosting me at IPMU in the summer of 2016. The opportunity to live and work in Japan over that summer was one of the highlights of my time in graduate school. Christophe, thank you for your help, both during that summer while I was working on NEUT and while I was preparing my thesis by getting me set up with the P-Theta code to produce SK event distributions. Ciro, thank you for your help in getting HighLAND running and

for your quick replies to all my questions. Mark, thank you for your keen insights into the BANFF and for the useful discussions covering everything from working on the BANFF code to analyzing fit results. John, thank you for your support in the trenches of working on the BANFF. Being able to work alongside someone on the BANFF code made it much easier to handle, especially during the pressure of preparing inputs for the oscillation analysis.

I also want to thank my family for their support and prayers over the years, especially the last eight at the University of Alabama and Michigan State. It has been hard being so far away, but I know you are always a phone call or text message away. Thank you, Dad, for always being a good sounding board and for editing anything from undergraduate papers to my resumé to my dissertation. Mom, thank you for your love and support and always being available to talk whenever I need you. Abbey and Claire, thank you for being the best sisters that a brother could have.

To the new family that I gained while I was working on my doctorate, thank you for opening your home to me and letting me join your family.

And, most especially, thank you to my beautiful wife, Kaleigh, for your love and encouragement over the last two years. I would not have made it to this point without you there beside me. I love you, Kaleigh.

TABLE OF CONTENTS

LIST OF TABLES

LIST OF FIGURES

CHAPTER 1

EXECUTIVE SUMMARY

Neutrinos have been astounding physicists for almost a century. Over the last twenty years, they have provided one of the best views of physics beyond the Standard Model due to their non-zero mass, which was confirmed through the ability for neutrinos to oscillate. Since the discovery of neutrino oscillations, each of the fundamental parameters governing the probability for a neutrino to oscillate has been measured, with the exception of one. This parameter is related to charge-parity violation and its measurement remains one of the highest priorities for current and future experiments studying neutrino oscillations. Similarly, while neutrino oscillations demonstrate that neutrinos have mass, the values and ordering of these masses have yet to be determined. One experiment making measurements of neutrino oscillations is the Tokai-to-Kamioka (T2K) experiment.

Since 2010, T2K has been studying neutrino oscillations using a beam of muon neutrinos (or antineutrinos) generated on the east coast of Japan which are directed towards the west coast of Japan and are detected in the Super-Kamiokande (SK) detector. The distance between the production point and SK is 295 km, which is chosen to maximize the probability that the muon (anti)neutrinos oscillate to the other flavors of neutrinos. At a basic level, the T2K oscillation analysis counts the number of muon (anti)neutrino interactions close to the production point, and then compares that with the number of muon (anti)neutrino interactions at SK. This type of analysis is called a muon (anti)neutrino "disappearance" analysis. Additionally, the number of electron (anti)neutrino interactions can be counted at SK, which is called the electron neutrino "appearance" analysis.

The largest uncertainties in the T2K neutrino oscillation analysis are related to the neutrino beam flux and the neutrino cross section. In order to reduce these uncertainties, data from the Near Detector at 280 m (ND280) is included in the analysis, which allows the uncertainties on the neutrino flux and the cross section to be constrained simultaneously. By simultaneously constraining these uncertainties, correlations between them can be used to reduce the uncertainties more than they

could be individually. The process for constraining these uncertainties with the near detector data uses a binned maximum likelihood fit, which bins the observed interactions, or events, based on their topological sample, which separates the events based on what outgoing particles are observed, and the outgoing lepton's momentum and angle with respect to the neutrino beam.

Currently, the neutrino data samples used at the "near" detector are categorized in a similar way to those at the "far" detector. However, the antineutrino samples are categorized in a simpler way for the near detector compared to those at the far detector. For this thesis, the antineutrino samples were updated to more closely match both the neutrino samples at the near detector and the far detector samples. Studies to compare results using the new samples to those using the old samples were performed and are described here. These include looking at changes to the near detector portion of the oscillation analysis and how this might affect the overall results for the T2K oscillation analysis.

Chapter 2 will provide an overview of the history of neutrino physics, including the discovery and theory of neutrino oscillations and an introduction to the types of neutrino interactions. The chapter will conclude with a summary of the current understanding of neutrino oscillations and some of the open questions that remain, including the order of the neutrino masses, the existence of charge-parity violation in neutrino interactions, and the existence of sterile neutrinos. In Chapter 3, the T2K experiment will be described in detail, including the production of neutrinos at the Japan Proton Accelerator Research Complex and the detectors used to detect these neutrinos. Chapter 4 will describe the procedure used in the oscillation analysis, as well as how the work presented in this thesis fits into the overall analysis. Chapter 5 will discuss the data used and the process of selecting data into samples for the oscillation analysis, while Chapter 6 will cover the systematic uncertainties related to the near detector, ND280. Chapter 7 will present the results from the studies performed. Finally, Chapter 8 will give a summary of the work presented here, as well as providing insight into further studies that can be performed to improve the neutrino oscillation analysis at T2K.

CHAPTER 2

NEUTRINO PHYSICS

2.1 A History of Neutrinos

2.1.1 Initial Postulation

In the early 1930s, a problem had arisen in nuclear beta decay, in which a radioactive nucleus, X, decays into a slightly lighter nucleus, Y, emitting an electron in the process:

$$X \rightarrow Y + e^{-}. \tag{2.1}$$

In these types of two-body decays, the energies of the outgoing particles are kinematically determined in the center-of-mass frame, where the parent particle, X, is stationary and the decay products, Y and e^{-}, come out with equal and opposite momenta. In this case, the energy of the electron is determined by

$$E_e = \left(\frac{m_X^2 - m_Y^2 + m_e^2}{2m_X} \right) c^2. \tag{2.2}$$

Once the masses have been determined, the energy of the electron should be fixed. However, in experiments studying nuclear beta decay, the energy of the electron varied considerably, as seen in Figure 2.1.

In order to rectify this problem, Wolfgang Pauli proposed that a third particle was emitted, along with the daughter nucleus and electron, during beta decay. In order to conserve charge, the particle had to be neutral. Furthermore, because the energy of the electron could range up to a limit of Equation 2.2, the particle had to be very light. Pauli called his theoretical particle the "neutron." However, Chadwick's discovery of the particle known today as the neutron preempted the name, though this particle was too massive to be Pauli's proposed particle.

In 1933, Enrico Fermi proposed a new theory for beta decay [26] which successfully included Pauli's particle, which he called the "neutrino." Fermi's theory that included the neutrino, denoted

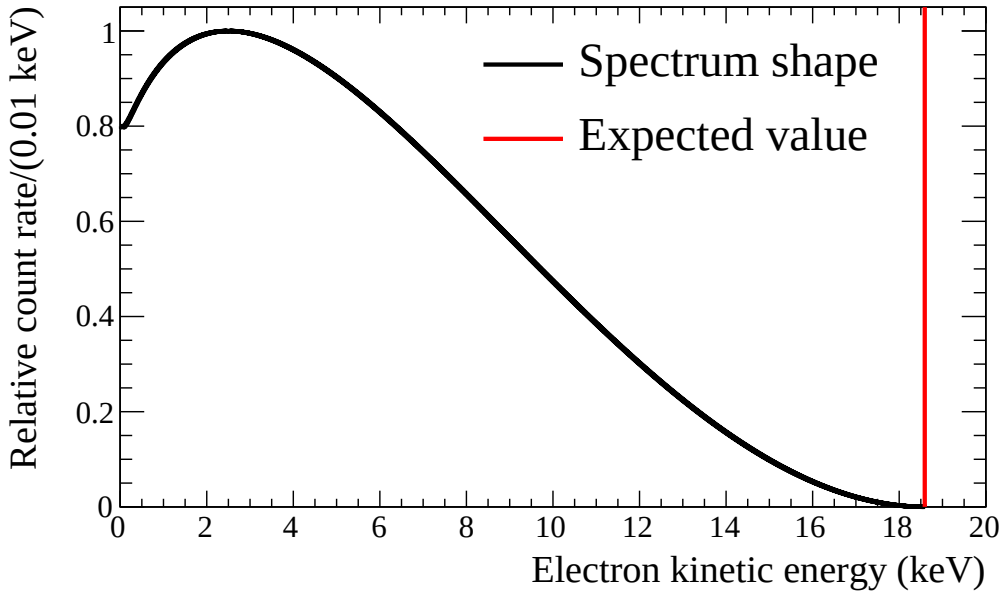

Figure 2.1: The shape of the energy spectrum of the outgoing electron from the beta decay of tritium compared with the expected value from a two-body beta decay given by Equation 2.2. Figure from [1].

by the Greek letter, ν, gave the beta decay process:

$$n \rightarrow p + e^{-} + \nu, \tag{2.3}$$

where the neutron, n, is confined in nucleus X and the proton, p, is confined in nucleus Y. This process is very close to the current understanding of the beta decay process, with one slight difference that will be seen shortly.

2.1.2 Further Evidence

In the early 1930s, cosmic rays provided one of the significant sources of particle measurements. Cosmic rays are high energy charged particles which originate in astrophysical processes. Primarily, cosmic rays are protons, but they can also be heavier ions. When these particles approach the Earth, they can interact with molecules found in the upper atmosphere. These interactions produce secondary particles, most of which decay prior to reaching the surface of the Earth. However, due

to time dilation, some of these secondary particles are able to reach the surface. In either case, scientists are able to study cosmic rays through the particles detected on the ground.

One secondary particle which often reaches the Earth's surface is the muon. Because of this, cosmic ray muons have been well-studied. Similar to beta decay, the decay of the muon produces an electron with a range of energies, which means there must be at least one additional neutral particle originating in the decay process. The accepted explanation [27] for this is that there must be two neutrinos produced with the electron:

$$\mu \rightarrow e + 2\nu. \tag{2.4}$$

In the late 1940s, C. F. Powell performed an experiment that observed tracks from charged particles involved in cosmic ray interactions through the use of photographic emulsions [28]. Using the tracks produced by particles traveling through the emulsion, their interactions in the medium, and their decay, the nature of cosmic rays could be studied. The results of his experiment showed clear evidence that another secondary particle, now known to be the pion, existed. The pion decays into a muon and, due to conservation of momentum, another particle. This other particle had to be neutral, as there was no track left in the emulsion as it traveled. Therefore, it was postulated that the pion must decay via:

$$\pi \rightarrow \mu + \nu. \tag{2.5}$$

2.1.3 The First Observation

By the 1950s, increasing theoretical evidence for the neutrino existed, be it from muon, pion, or unstable nuclei decay, but there was no experimental verification. In 1953, Konopinski and Mahmoud [29] introduced a concept which would help in the determination of whether a given reaction was possible or not. This concept became known as the lepton number, where a lepton number of +1 was assigned to the electron, negatively charged muon, and neutrino, while the positron, positively charged muon, and antineutrino were given a lepton number of −1. Any other particles would receive a lepton number of 0. They proposed that the total lepton number must

be conserved within particle interactions. Due to this, it was determined that the neutrino in beta decay must, in reality, be an antineutrino, and the beta decay process given by Equation 2.3, must actually be

$$n \rightarrow p + e^{-} + \bar{\nu}. \tag{2.6}$$

By this time, neutrinos were understood to have a small cross section, or probability to interact, with matter. Because of this, an intense source of either neutrinos or antineutrinos is needed to achieve a statistically significant result in a reasonable amount of time. In order to study antineutrinos, nuclear reactors provided the best option, as they were thought to be the most intense source of antineutrinos available.

Under this assumption, Reines and Cowan conducted an experiment at the Savannah River nuclear reactor in South Carolina, which had an antineutrino flux of of 1.2×10^{13} particles per square centimeter per second [30]. They used a detector containing water doped with $CdCl_2$ and instrumented with scintillator coupled to photomultiplier tubes, allowing them to detect light produced inside the detector. Through inverse beta decay ($\bar{\nu} + p \rightarrow e^{+} + n$), the presence of antineutrinos could be detected in one of two ways:

1. The positron would annihilate with an electron in the water, producing light via $e^{+} + e^{-} \rightarrow 2\gamma$.

2. The neutron would be captured on a cadmium nucleus, which would produce an excited state that would decay by emitting a photon. An example of this would be, $n + {}^{113}\mathrm{Cd} \rightarrow {}^{114}\mathrm{Cd} \rightarrow {}^{114}\mathrm{Cd} + \gamma$.

Because neutron capture takes more time than electron-positron annihilation, a characteristic delayed coincidence signal could be looked for in the experiment. In 1956, Cowan and Reines confirmed the existence of the neutrino by observing two or three interactions per hour while the reactor was running [31, 32].

2.1.4 Proposal of Different Neutrino Types

Around this time, an issue with the concept of conservation of lepton number arose. A rule of thumb in particle physics, is that "[a]nything that is not compulsory is forbidden" [33]; specifically, if an interaction is not observed, then it is expressly forbidden by a conservation law. Based on the conservation of lepton number, the muon can decay via $\mu \rightarrow e + \gamma$. However, this decay is never observed, which is contradictory to the law of the conservation of lepton number.

One answer to this problem posited that the lepton number is actually divided among the lepton flavors, or types [34, 35]. Under this new assumption, there would be an electron and an electron neutrino (each having an electron number of +1), while the muon would have a corresponding muon neutrino (both with a muon number of +1). Correspondingly, there would be matching antiparticles, but with lepton numbers of −1. In this case, the muon decay, $\mu \rightarrow e + \gamma$, would be forbidden, as the muon and electron numbers are not conserved across the interaction. Using this modified conservation of lepton number, the muon decay shown in Equation 2.4 would now become

$$\mu^- \rightarrow e^- + \nu_\mu + \bar{\nu}_e \tag{2.7}$$

$$\mu^+ \rightarrow e^+ + \bar{\nu}_\mu + \nu_e \tag{2.8}$$

for muons and antimuons, respectively. Furthermore, the pion decay in Equation 2.5 now becomes

$$\pi^+ \rightarrow \mu^+ + \nu_\mu \tag{2.9}$$

$$\pi^- \rightarrow \mu^- + \bar{\nu}_\mu. \tag{2.10}$$

The equation for beta decay (Equation 2.3) becomes

$$n \rightarrow p + e^- + \bar{\nu}_e, \tag{2.11}$$

which matches the current understanding of beta decay.

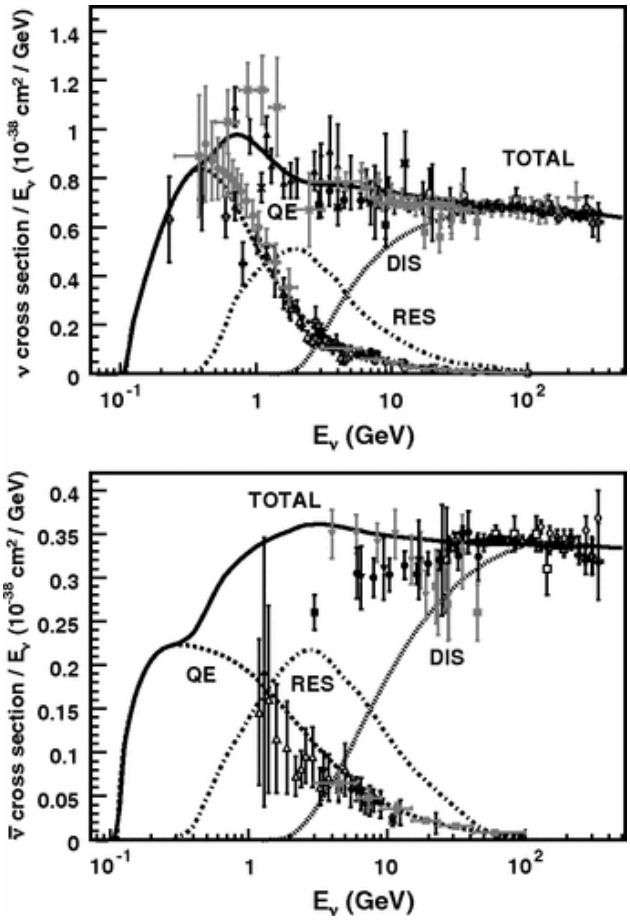

Figure 2.2: Total neutrino (top) and antineutrino (bottom) charged current cross section per nucleon (for an isoscalar target) divided by neutrino energy and plotted as a function of energy. Additionally, the total cross section is separated into CCQE (labeled as QE), CC resonant (RES), and deep inelastic scattering (DIS) cross sections. Figure from [13].

2.1.5 Detecting the Muon and Tau Neutrinos

In order to verify this solution, experiments began looking for evidence of a distinct muon type neutrino. Because the neutrino cross section is small (Figure 2.2 shows the size of the cross section), either an intense source of neutrinos or a large detector and lots of time is needed to search for muon neutrinos. Thankfully, nature provides a large source of muon neutrinos and antineutrinos through the decay of cosmic ray muons. However, these also provide a large source of electron neutrinos and antineutrinos, making it hard to distinguish between the two flavors of neutrinos. Rather than relying on naturally produced muon neutrinos, experimentalists can artificially produce

them in a laboratory by accelerating protons in a particle accelerator and colliding them with a target. This would create a similar situation to that of cosmic rays colliding with particles in the upper atmosphere, producing pions which decay into muons and muon neutrinos or antineutrinos.

Using this technique, Lederman, Schwartz, and Steinberger [36] designed an experiment that accelerated protons to 15 GeV before colliding them with a beryllium target at Brookhaven National Laboratory. These collisions produced copious amounts of pions traveling approximately in the same direction as the protons. The pions would then decay into muons and muon neutrinos and antineutrinos. A thick iron wall was stationed downstream from the target to stop the muons and prevent them from traveling through the detector. Neutrinos produced from the muons decaying in the iron wall would be focused in the direction the muons were traveling, rather than the beam direction, giving a much lower background of electron neutrinos and antineutrinos compared to neutrinos coming from cosmic rays.

On the downstream side of the iron wall, a spark chamber detector was situated. The detector consisted of ten 1 ton modules, each of which contained a series of parallel aluminum plates. The volume between the plates was filled with a gas, which, when a charged particle passed through it, would ionize along the particle's track, producing a visible spark. Muons traveling through the detector could be distinguished from electrons by the fact that they could travel through several aluminum plates before interacting, whereas electrons could not. The neutrino interactions observed in this experiment were consistent with neutrinos produced from the decay of pions into muons and muon neutrinos, the latter of which would interact in the detector to produce muons and not electrons. Due to this fact, these neutrinos are a distinct flavor from those seen by Reines and Cowan, establishing the existence of the muon neutrino.

In 1975, a new lepton, the tau, τ, was discovered by Martin Lewis Perl and the SLAC–LBL group [37]. As it had already been determined that there was a neutrino partner for the electron and muon, this discovery created the need for a third neutrino flavor, ν_τ.

In order to directly observe tau neutrinos, the DONUT (Direct Observation of the NU Tau) experiment was created [38]. This experiment used protons accelerated to 800 GeV at the Tevatron

at Fermi National Accelerator Laboratory which were directed towards a 1 m long tungsten target. Through the decay of D_S mesons ($D_S^+ \rightarrow \tau^+ + \nu_\tau$), tau neutrinos could be produced. Using a detector which could differentiate between electrons, muons, and taus, the experiment analyzed 203 neutrino interactions and found four ν_τ interactions, thus confirming the existence of the tau neutrino [38].

2.1.6 Current Understanding

Today, the neutrino has been incorporated into the Standard Model, which describes the elementary particles and how they interact with one another. The Standard Model has been in development since the middle of the twentieth century and provides the theoretical description of the electroweak and strong forces. Two types of particles are included in the Standard Model, the spin-$\frac{1}{2}$ fermions and the integer spin bosons, which mediate the electroweak and strong forces [27].

The fermions are divided into two groups, the leptons and the quarks. The leptons include the electron, muon, and tau particles, as well as the corresponding neutrinos described in Section 2.1. There are six different types of quarks, the up (u), charm (c), and top (t), which have a charge of $+2/3$, while the down (d), strange (s), and bottom (b) quarks have a charge of $-1/3$. The quarks are able to interact with the charged leptons through both the weak and electromagnetic forces, while they can interact with neutrinos via the weak force.

The bosons include the photon, γ, which mediates the electromagnetic force, and the gluon, g, which is the mediator of the strong force. For the weak force, there are two mediators, the $W^\pm$ and the Z^0, which are described in more detail in Section 2.2. The Higgs boson, H, is the most basic manifestation of the Brout-Englert-Higgs mechanism, which gives the $W^\pm$ and Z bosons their mass through their interaction with the Higgs field. A summary of the particles can be found in Table 2.1.

Fermions			Bosons
u	c	t	γ
d	s	b	g
e	μ	τ	$W^{\pm}, Z$
ν_e	ν_μ	ν_τ	H

Table 2.1: Standard Model of Particle Physics. The top portion under the "Fermions" heading shows the quarks, while the bottom shows the leptons.

2.2 Neutrino Interactions

According to the Standard Model, neutrinos are only able to interact with matter via the weak force. Weak interactions are mediated by either the Z^0 or the $W^{\pm}$. The Z^0 is a neutral particle with a mass of 91.1876 ± 0.0021 GeV/c^2 [3], while the $W^{\pm}$ is a charged particle with a mass of 80.385 ± 0.015 GeV/c^2 [3]. Interactions mediated by the Z^0 are called neutral current (NC) interactions, while those mediated by the $W^{\pm}$ are called charged current (CC) interactions. In a neutral current interaction, a neutrino or antineutrino (of any flavor) interacts with a quark or lepton (of any flavor), transferring energy and momentum via a Z^0. Aside from transferring energy and momentum, the particles are unchanged after the interaction. Charged current interactions occur when a neutrino or antineutrino interacts via the $W^{\pm}$ to produce a lepton of the same flavor. Because these interactions produce a charged lepton in the final state, they are easier to detect than neutral current interactions.

While interactions on individual quarks are allowed by the Standard Model, quarks do not appear as free particles, but are bound in nucleons[1], such as the proton (uud) and neutron (udd). Interactions between neutrinos or antineutrinos and nucleons are classified into multiple categories.

[1]Generically, quarks are bound in hadrons, which includes mesons, such as the pion, and baryons, such as the proton and neutron.

Name	Abbreviation	Neutrinos	Antineutrinos
CC Quasi-Elastic	CCQE	$\nu_l + n \rightarrow l^- + p$	$\bar{\nu}_l + p \rightarrow l^+ + n$
CC 2 particle 2 hole	2p2h	$\nu_l + np \rightarrow l^- + p + p$	$\bar{\nu}_l + np \rightarrow l^+ + n + n$
CC resonant Pion Production	CCRES	$\nu_l + p \rightarrow l^- + \Delta^{++} \rightarrow l^- + p + \pi^+$ $\nu_l + n \rightarrow l^- + \Delta^+ \rightarrow l^- + p + \pi^0$ $\nu_l + n \rightarrow l^- + \Delta^+ \rightarrow l^- + n + \pi^+$	$\bar{\nu}_l + n \rightarrow l^+ + \Delta^- \rightarrow l^+ + n + \pi^-$ $\bar{\nu}_l + p \rightarrow l^+ + \Delta^0 \rightarrow l^+ + n + \pi^0$ $\bar{\nu}_l + p \rightarrow l^+ + \Delta^0 \rightarrow l^+ + p + \pi^-$
CC Coherent Pion Production	CCCoh	$\nu_l + A \rightarrow l^- + A + \pi^+$ (where A is a nucleus)	$\bar{\nu}_l + A \rightarrow l^+ + A + \pi^-$ (where A is a nucleus)
CC Other	CCOther	$\nu_l + (n \text{ or } p) \rightarrow l^- + (p \text{ or } n)+$ pions	$\bar{\nu}_l + (p \text{ or } n) \rightarrow l^+ + (n \text{ or } p)+$ pions
NC Resonant Pion Production	NCRES	$\nu_l + n \rightarrow \nu_l + \Delta^0 \rightarrow \nu_l + n + \pi^0$ $\nu_l + p \rightarrow \nu_l + \Delta^+ \rightarrow \nu_l + p + \pi^0$ $\nu_l + n \rightarrow \nu_l + \Delta^0 \rightarrow \nu_l + p + \pi^-$ $\nu_l + p \rightarrow \nu_l + \Delta^+ \rightarrow \nu_l + n + \pi^+$	$\bar{\nu}_l + n \rightarrow \bar{\nu}_l + \Delta^0 \rightarrow \bar{\nu}_l + n + \pi^0$ $\bar{\nu}_l + p \rightarrow \bar{\nu}_l + \Delta^+ \rightarrow \bar{\nu}_l + p + \pi^0$ $\bar{\nu}_l + n \rightarrow \bar{\nu}_l + \Delta^0 \rightarrow \bar{\nu}_l + p + \pi^-$ $\bar{\nu}_l + p \rightarrow \bar{\nu}_l + \Delta^+ \rightarrow \bar{\nu}_l + n + \pi^+$
NC Other	NC Other	$\nu_l + (n \text{ or } p) \rightarrow \nu_l + (p \text{ or } n)+$ pions	$\bar{\nu}_l + (n \text{ or } p) \rightarrow \bar{\nu}_l + (p \text{ or } n)+$ pions

Table 2.2: Types of neutrino and antineutrino interactions. l can be either e, μ, or τ. The "Other" category covers any high energy interactions that produce more than one pion. The pions in these interactions can be charged or neutral or both. Note, this does not cover all interactions that may fall within a given interaction type. Table from [1]

Furthermore, experiments tend to use nuclei which contain more than one nucleon, opening up additional processes in which the neutrino can interact with multiple nucleons or the entire nucleus. Some of these interactions can be seen in Table 2.2.

The charged current quasi-elastic (CCQE) process is of particular interest. As a CC process, the outgoing charged lepton can be detected and identified to determine the flavor of the incoming neutrino. The energy from the neutrino can be calculated using the momentum of the outgoing lepton (p_μ) and the angle between the neutrino path and the lepton path (θ_l), which is fairly well known for a neutrino beam:

$$E_\nu = \frac{m_p^2 - (m_n - E_b)^2 - m_l^2 + 2(m_n - E_b)E_l}{2(m_n - E_b - E_l + p_l \cos\theta_l)}, \tag{2.12}$$

where m_p is the proton mass, m_n is the neutron mass, and m_l and E_l are the mass and energy of the lepton, respectively. The E_b term is related to the energy it takes to remove the neutron from the nucleus.

Interactions between neutrinos and nuclei pose a number of experimental problems. In the case of interactions occurring on multiple nucleons, like 2p2h, described in more detail in Section

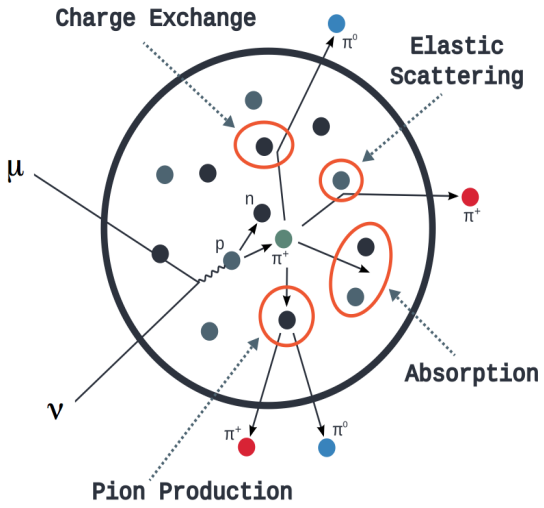

Figure 2.3: Various types of final state interactions occurring within a nucleus. Figure from [14].

4.3.2.1, or on the entire nucleus, like CC coherent, the outgoing particles mimic other types of interactions (CCQE and CC resonant, respectively) in terms of what is measured in a detector. These processes can be misidentified for a number of reasons, including outgoing protons and pions having energies below the threshold for detection or the detector being insensitive to outgoing particles, like neutrons. Furthermore, while leptons can easily escape the nucleus, other particles such as protons and pions, may interact inside the nucleus. This process is called a final state interaction (FSI), and a diagram of some of the types of final state interactions can be seen in Figure 2.3. When these interactions occur, the particles which the detector could detect may be different from the particles produced in the initial interaction. These processes create added levels of difficulty when it comes to measuring neutrino interactions by altering the reconstructed energy spectrum. For example, if the outgoing pion from a CC resonant interacts within the nucleus and is absorbed, the interaction could be misidentified as a CCQE interaction. In this instance, the neutrino energy would be calculated via Equation 2.12, which does not account for the pion, resulting in an incorrect reconstructed energy.

2.3 Neutrino Oscillations

The concept of neutrino oscillations arose to describe the solar neutrino problem and the atmospheric neutrino anomaly (both of which are described in more detail in Section 2.3.1). In neutrino oscillations, a neutrino of one flavor changes into a different flavor as it travels through space and time. Through these oscillations, some neutrinos may change to a flavor which an experiment is not sensitive to, causing fewer neutrinos of the original flavor to be measured than expected, referred to as "neutrino disappearance." Conversely, "neutrino appearance" is when neutrinos of one flavor are detected from a neutrino source of a different flavor.

2.3.1 Motivation

As the study of neutrinos from various sources progressed, differences between the theoretical predictions and the observed number of neutrinos arose. The two main discrepancies were the solar neutrino problem and the atmospheric neutrino anomaly.

The Solar Neutrino Problem

As the 1960s progressed, models of the sun were developed based on the results of experiments looking for interactions thought to occur inside the sun. As many of these interactions produce neutrinos across different energy ranges, the study of solar neutrinos would provide critical information on how the sun works.

The Homestake solar neutrino experiment was built in the mid-1960s [39] and was placed nearly 1500 m below the surface in the Homestake Gold Mine in Lead, South Dakota. By placing the experiment at such a depth, the cosmic ray muon background could be greatly reduced. The detector was made of a tank holding 615 tons of tetrachloroethylene (C_2Cl_4), which was used to detect neutrinos through the interactions of electron neutrinos with chlorine atoms,

$$\nu_e \; + \; {}^{37}\mathrm{Cl} \; \rightarrow \; {}^{37}\mathrm{Ar} \; + \; e^{-}. \tag{2.13}$$

To see if this interaction occurred, helium gas was bubbled through the tetrachloroethylene, extracting the gaseous argon, which was then passed over an absorber that absorbed the argon. ^{37}Ar

is a radioactive isotope of argon; therefore, the number of decays could be counted in the absorber to determine the number of neutrino interactions that occurred in the detector.

One of the early results of the Homestake experiment [40] set an upper limit of 0.5 interactions per day where they had expected to see between two and seven interactions per day in the detector. At the time, it was assumed that there was a problem with the solar model and a theoretical paper [41] was published that argued the models could be sufficiently modified to make them agree better with the Homestake results.

In the years following the first Homestake result, the solar model continued to be developed. Alongside the model development, Homestake continued to operate, measuring the solar neutrino flux down to energies of 0.814 MeV, which is the minimum energy required of a neutrino to interact via Equation 2.13. However, by the late 1970s, attempts to reconcile the Homestake result with the theoretical solar models were thwarted to the point that the issue was declared the "Solar Neutrino Problem."

Additional experiments probing different neutrino energy regions only deepened the problem. One such experiment was Kamiokande-II, a water Cherenkov detector and precursor to the Super-Kamiokande experiment (described in Section 3.3). Water Cherenkov detectors work by instrumenting a volume of water with sensitive light detectors, which detect light produced by particles traveling faster than the speed of light in water, called Cherenkov radiation [42]. The Kamiokande-II experiment worked by looking for the elastic scattering of electron neutrinos with electrons via:

$$\nu_e + e^- \rightarrow \nu_e + e^-, \tag{2.14}$$

which can occur either through the exchange of a $W^{\pm}$ or a Z boson. The kinematics of this interaction, in addition to the ability to reconstruct the direction of the electron, provided enough information to determine the direction of the incoming neutrino, which confirmed these neutrinos were coming from the sun. In order to distinguish signal interactions from background, Kamiokande-II required that the outgoing electrons met a certain energy threshold. By enforcing this minimum energy, Kamiokande-II was only sensitive to the highest energy solar neutrino

production channels, primarily $^8\mathrm{B} \rightarrow {}^8\mathrm{Be}^* + e^+ + \nu_e$ decays. In 1990, the experiment observed a neutrino flux of 0.46 ± 0.05 (stat.) ± 0.06 (syst.) relative to the solar neutrino prediction [43]. While this result confirmed the deficit seen by Homestake, the two deficits were in disagreement when considering the neutrino production channels to which Homestake was sensitive.

During its tenure, Kamiokande-II was restricted to looking for elastic scattering of neutrinos, which was due to the use of "normal" water (H_2O). In order for an electron neutrino to interact via a charged current process, a neutron is required and, while oxygen contains a number of neutrons, the energy threshold for the interaction $^{16}\mathrm{O} + \nu_e \rightarrow {}^{16}\mathrm{F} + e^-$ is 15.4 MeV. This is above the energy of most solar neutrinos, and is nearing the expected maximum energy of solar neutrinos, 18.8 MeV [44]. Because of the high threshold and the relatively low number of solar neutrinos above this energy, these interactions are suppressed. Therefore, even the most energetic of electrons would not be able to reach the threshold for signal-background discrimination.

The Solar Neutrino Problem was resolved by the Sudbury Neutrino Observatory (SNO) [45]. SNO is a one kton water Cherenkov detector located at the 6800 foot level of the Creighton Mine in Sudbury, Ontario, Canada. Rather than using "normal" water, SNO employed the use of heavy water (D_2O), where the hydrogen atoms have been exchanged for deuterium (d) atoms, which is an isotope of hydrogen with one neutron. This allows SNO to be sensitive to both a charged current interaction channel:

$$\nu_e + d \rightarrow p + p + e^- \tag{2.15}$$

and a neutral current interaction channel:

$$\nu_e + d \rightarrow p + n + \nu_e. \tag{2.16}$$

In 2001, a potential solution to the Solar Neutrino Problem was proposed in a joint measurement by SNO and Super-Kamiokande (the successor to Kamiokande-II) [46]. By this time, SNO had observed enough ν_e charged current interactions to make a precise measurement of the solar neutrino flux. When combined with the Super-Kamiokande elastic scattering results, which were sensitive to all three flavors, this indicated there was also a flux from ν_μ and ν_τ. The combined result fell within the solar model prediction for the total neutrino flux.

Using neutral current interactions, SNO was able to improve its measurements. In order to measure these interactions, the experiment relied on detecting the outgoing neutron from Equation 2.16, which is beyond the traditional abilities of a water Cherenkov detector. To detect the neutron, SNO used a variety of neutron capture methods over the course of its three operational phases.

Based on data from its first phase, which ended in May 2001, SNO independently confirmed the presence of muon neutrinos and tau neutrinos, in addition to the expected electron neutrinos, in the solar neutrino flux [47]. This result showed a total neutrino flux consistent with the solar model prediction. Therefore, the solution to the Solar Neutrino Problem required that solar neutrinos be able to oscillate between flavors.

The Atmospheric Neutrino Anomaly

One of the areas of physics that grew in interest during the 1980s was the search for proton decay. While this process is forbidden in the Standard Model, many theories beyond the Standard Model include proton decay. Due to its theoretically long half life, searches for proton decay require a large detector that is heavily shielded from external backgrounds, like cosmic ray muons, and holds a multitude of protons. While placing this detector deep underground would greatly reduce the cosmic ray muon background, atmospheric neutrinos would continue to stream through the detector. Therefore, it was necessary for the atmospheric neutrino flux to be well understood when searching for proton decay.

At the time, there were many theoretical models of the atmospheric neutrino flux. These models were based on the cosmic ray muon flux, which, in combination with the understanding of the production of atmospheric neutrinos from these muons, provided a good prediction of the neutrino flux. Additionally, the processes to produce atmospheric neutrinos formed a prediction of the ratio between muon neutrinos and electron neutrinos, as a function of energy. For lower energies, both pion decay and muon decay would occur, giving a ratio of approximately $2:1$ for $(\nu_\mu + \bar{\nu}_\mu) : (\nu_e + \bar{\nu}_e)$. However, as the energies increased, more and more muons would reach the surface before decaying, reducing the number of electron neutrinos or antineutrinos, thereby increasing this ratio.

The Irvine-Michigan-Brookhaven (IMB) and Kamioka Nucleon Decay (KamiokaNDE) experiments were two proton decay experiments studying the atmospheric neutrino background in more detail. Both detectors were able to distinguish between muon and electron neutrinos[2], allowing them to make measurements of the atmospheric neutrino flavor ratio. Each experiment compared the observed flavor ratio (R_{obs}) to the prediction from theory (R_{theory}), which differed significantly from one another. The result from IMB showed a ratio of R_{obs}/R_{theory} that was $0.54 \pm 0.05 \pm 0.11$ [48], while KamiokaNDE had a result of $0.60^{+0.07}_{-0.06} \pm 0.05$ [49]. Both results showed a deficit of observed results compared to the theoretical prediction, which was designated the "Atmospheric Neutrino Anomaly."

This anomaly was solved by Super-Kamiokande in 1998 [15]. In addition to being able to distinguish between flavors of neutrinos, the direction of the outgoing lepton allowed the experiment to determine the direction of the incoming neutrino. When this direction was compared with the cosine of the angle made with respect the vertical, a clear angular dependence was seen in the difference between the model predicted interaction rate and the measured rate.

This angular dependence can be shown to tie in to how far the neutrino traveled. When $\cos\theta = 1$, the neutrino is coming from directly overhead and only traverses a few tens of kilometers of atmosphere. Conversely, if $\cos\theta = -1$, then the neutrino is coming up from below and had to travel through thousands of kilometers of Earth. In neutrino oscillation theory (discussed in Section 2.1.6), the probability for a neutrino to oscillate has a sinusoidal dependence on L/E, where L is the distance traveled by the neutrino and E is the neutrino energy. Figure 2.4 shows an L/E dependence consistent with the oscillation of ν_μ to ν_τ. Therefore, the Atmospheric Neutrino Anomaly was solved by taking into account neutrino oscillations.

[2]These experiments were unable to determine the charge of the outgoing lepton, so they could not distinguish between neutrinos and antineutrinos.

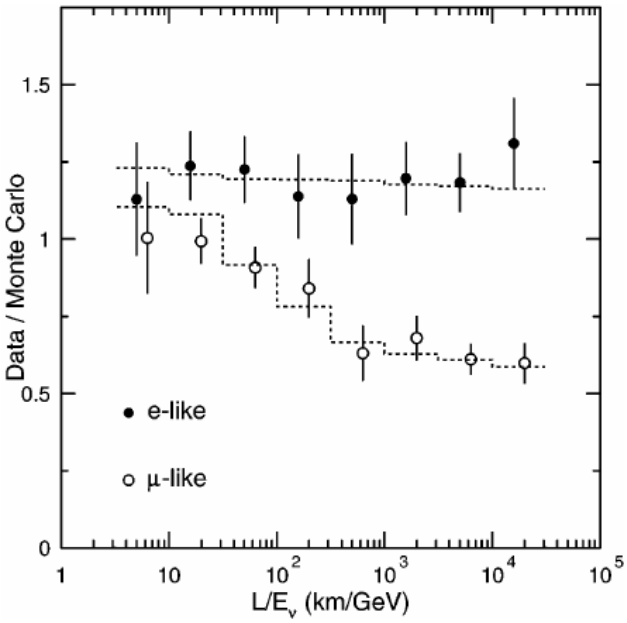

Figure 2.4: The ratio of the number of data interactions to the number of predicted interactions assuming no neutrino oscillations (from Monte Carlo) as a function of L/E in Super-Kamiokande. The points show the ratio, while the dashed lines show the expected shape when including oscillations of ν_μ to ν_τ. Figure from [15].

2.3.2 Theory

The ability for neutrinos to oscillate provided a solution to both the Solar Neutrino Problem and the Atmospheric Neutrino Anomaly. This section will describe the theory behind how neutrinos oscillate[3].

Neutrino Oscillations in Vacuum

In the Standard Model, neutrinos are assumed to be massless. However, for neutrino oscillations to occur, it is required that neutrinos have a nonzero mass[4]. Therefore, neutrino oscillations provide a unique window into studying physics beyond the Standard Model.

To see the relation between the neutrinos having mass and neutrino oscillations, consider the quantum mechanical states of the the neutrino flavors (called the flavor eigenstates), $|\nu_e\rangle$, $|\nu_\mu\rangle$, and

[3]Throughout this section, natural units ($\hbar = c = 1$) will be used.

[4]Technically, at least two of the three mass states must be non-zero. The lightest mass state is allowed to be massless.

$|\nu_\tau\rangle$. Using the Hamiltonian operator, H, the total energy of a state, $|\psi\rangle$, and its time evolution can be determined using the Schrödinger Equation

$$i\frac{\partial}{\partial t}|\psi(t)\rangle = H|\psi(t)\rangle\,. \tag{2.17}$$

If H is time independent, the solution takes the form

$$|\psi(t)\rangle = e^{-iHt}|\psi(0)\rangle\,, \tag{2.18}$$

where $|\psi(0)\rangle$ can be written as a superposition of orthonormal eigenstates of the Hamiltonian, $|\psi_j\rangle$. Applying these superpositions, Equation 2.18 becomes

$$|\psi(t)\rangle = \sum_j a_j e^{-iE_j t}|\psi_j\rangle\,. \tag{2.19}$$

Equation 2.19 shows that the time dependent phase in each eigenstate is a function of the eigenstate's energy (the eigenvalue of the Hamiltonian). Any changes in phase between the various eigenstates of the system produce changes that can be observed experimentally. This is because the probability to observe state $|\psi(0)\rangle$ after time, t, is $|\langle\psi(0)|\psi(t)\rangle|^2$.

The total energy, E, of a massive neutrino that does not sit in a potential field is

$$E = \sqrt{|\vec{p}|^2 + m^2}, \tag{2.20}$$

where $\vec{p}$ is the momentum and m is the mass of the neutrino. Therefore, the Hamiltonian of the neutrino propagating through time is mass dependent. The eigenstates of the free particle Hamiltonian are called the mass eigenstates and, currently, there is believed to be three states, $|\nu_1\rangle$, $|\nu_2\rangle$, and $|\nu_3\rangle$. The Pontecorvo-Maki-Nakagawa-Sakata (PMNS) matrix, named for the theorists who first developed the theory of neutrino oscillations [50, 51], shows the relationship between the flavor eigenstates and mass eigenstates. Using the PMNS matrix, neutrino oscillations can be parameterized using three mixing angles, θ_{12}, θ_{23}, and θ_{13}, and a CP (charge-parity) violating phase, δ_{CP}. The matrix[5] can be written as a product of three rotation matrices with a complex

[5]In addition to the three matrices shown, a fourth matrix containing the so-called "Majorana"

phase

$$U = \begin{pmatrix} U_{e1} & U_{e2} & U_{e3} \\ U_{\mu 1} & U_{\mu 2} & U_{\mu 3} \\ U_{\tau 1} & U_{\tau 2} & U_{\tau 3} \end{pmatrix} = \begin{pmatrix} 1 & 0 & 0 \\ 0 & c_{23} & s_{23} \\ 0 & -s_{23} & c_{23} \end{pmatrix} \begin{pmatrix} c_{13} & 0 & s_{13}e^{-i\delta_{CP}} \\ 0 & 1 & 0 \\ -s_{13}e^{i\delta_{CP}} & 0 & c_{13} \end{pmatrix} \begin{pmatrix} c_{12} & s_{12} & 0 \\ -s_{12} & c_{12} & 0 \\ 0 & 0 & 1 \end{pmatrix}, \quad (2.21)$$

where $c_{ij} = \cos\theta_{ij}$ and $s_{ij} = \sin\theta_{ij}$.

From the PMNS matrix, the correspondence between the flavor (subscript f) and mass (subscript m) eigenstates is

$$|\nu_f\rangle = \sum_{m=1}^{3} U^*_{fm} |\nu_m\rangle \quad (2.22)$$

$$|\bar{\nu}_f\rangle = \sum_{m=1}^{3} U_{fm} |\bar{\nu}_m\rangle \quad (2.23)$$

for neutrinos and antineutrinos, respectively.

Now that a relationship between the flavor and mass eigenstates has been determined, the time evolution of the flavor eigenstates can be determined. A simplified derivation, like the one found in [55], provides a sufficient result, but a more detailed derivation can be found in the article, *Neutrino Masses, Mixing, and Oscillations* of [3]. In this simpler derivation, start by taking the ultrarelativistic limit of Equation 2.20, which is a valid approximation as neutrinos have very small masses and travel nearly at the speed of light. Assuming all mass eigenstates travel at the same momentum ($p \approx E$, in this limit), the energy eigenstates can be Taylor expanded as

$$E_j \approx E + \frac{m_j^2}{2E}. \quad (2.24)$$

Because neutrinos are traveling close to the speed of light, then the travel time, t, is approximately the distance traveled, L, divided by the speed of light and can be used in the oscillation probabilities

CP-violating phases can be included. These phases only have physical effects if neutrinos are Majorana particles, where the neutrino is its own antiparticle. However, even if neutrinos are Majorana particles, these phases do not affect the probability for oscillation, as the phases cancel when calculating the probability. Therefore, it is not possible to determine if neutrinos are Majorana particles or not from oscillation experiments, which means other experiments are needed to study this. Such experiments include EXO [52], MAJORANA [53], and XMASS [54].

seen in Equation 2.25 (neutrinos) and Equation 2.26 (antineutrinos):

$$P(\nu_\alpha \to \nu_\beta) = \delta_{\alpha\beta} - 4\sum_{k>j} \mathcal{R}^{kj}_{\alpha\beta} \sin^2\left(\frac{1.267\Delta m^2_{kj} L}{E}\right) + 2\sum_{k>j} \mathcal{I}^{kj}_{\alpha\beta} \sin\left(\frac{2.534\Delta m^2_{kj} L}{E}\right) \tag{2.25}$$

$$P(\bar{\nu}_\alpha \to \bar{\nu}_\beta) = \delta_{\alpha\beta} - 4\sum_{k>j} \mathcal{R}^{kj}_{\alpha\beta} \sin^2\left(\frac{1.267\Delta m^2_{kj} L}{E}\right) - 2\sum_{k>j} \mathcal{I}^{kj}_{\alpha\beta} \sin\left(\frac{2.534\Delta m^2_{kj} L}{E}\right), \tag{2.26}$$

where $\mathcal{R}^{kj}_{\alpha\beta} = \mathrm{Re}[U^*_{\alpha k} U_{\beta k} U_{\alpha j} U^*_{\beta j}]$, $\mathcal{I}^{kj}_{\alpha\beta} = \mathrm{Im}[U^*_{\alpha k} U_{\beta k} U_{\alpha j} U^*_{\beta j}]$, and $\Delta m^2_{kj} = m^2_k - m^2_j$. In Equations 2.25 and 2.26, the constants within the sine functions arise by requiring Δm^2_{kj}, L, and E have units of eV, kilometers, and GeV, respectively.

Specifically, on T2K, Equation 2.25 (Equation 2.26) can be be used to calculate the muon (anti)neutrino disappearance probability and the electron (anti)neutrino appearance probability. To first order, the disappearance probability is

$$P(\nu_\mu(\bar{\nu}_\mu) \to \nu_\mu(\bar{\nu}_\mu)) \approx 1 - 4\cos^2\theta_{13}\sin^2\theta_{23}(1 - \cos^2\theta_{13}\sin^2\theta_{23})\sin^2\left(\frac{\Delta m^2_{32} L}{4E}\right) + [\text{solar and matter effect terms}], \tag{2.27}$$

while the appearance probability is

$$\begin{aligned} P(\nu_\mu(\bar{\nu}_\mu) \to \nu_e(\bar{\nu}_e)) \approx{}& \sin^2\theta_{23}\sin^2 2\theta_{13}\sin^2\left(\frac{\Delta m^2_{31} L}{4E}\right) \\ &+ \sin^2 2\theta_{23}\sin 2\theta_{13}\cos\theta_{13}\sin\left(\frac{\Delta m^2_{21} L}{4E}\right)\sin\left(\frac{\Delta m^2_{31} L}{4E}\right) \\ &\times \left[\cos\left(\frac{\Delta m^2_{32} L}{4E}\right)\cos\delta_{CP} - (+)\sin\left(\frac{\Delta m^2_{32} L}{4E}\right)\sin\delta_{CP}\right] \\ &+ [\text{solar and matter effect terms}], \end{aligned} \tag{2.28}$$

where the solar terms have been left out, as T2K is not sensitive to these oscillations. The probabilities for neutrino and antineutrino disappearance in Equation 2.27 are the same if matter effects, which are described below, are neglected. However, even with the inclusion of matter effects, at the T2K peak neutrino energy and baseline, the probability only differs by about 0.1% from the probability seen in Equation 2.27 [25][6]. Through Equation 2.27, T2K is able to measure $|\Delta m^2_{32}|$ and $\sin^2 2\theta_{23}$, but the octant[7] in which θ_{23} lives cannot be determined through the disappearance channel.

However, through the appearance channel, T2K is sensitive to the octant of θ_{23} as the leading term is proportional to $\sin^2 \theta_{23}$. The discovery of the octant of θ_{23} has important theoretical ramifications for the understanding of neutrino mixing and masses [56]. If θ_{23} were to have "maximal" mixing ($\theta_{23} = 45°$), there could be a potential symmetry in the mixing of muon neutrinos with tau neutrinos [57]. On the other hand, the order of the neutrino masses may be tied to which octant θ_{23} lives in [58].

In addition to being sensitive to the octant of θ_{23}, the neutrino and antineutrino appearance probability in Equation 2.28 differs by an opposite sign in the third term. If CP violation exists in neutrino oscillations (implying δ_{CP} is not 0 or $\pm\pi$), then a difference between $P(\nu_\mu \rightarrow \nu_e)$ and $P(\bar{\nu}_\mu \rightarrow \bar{\nu}_e)$ would be present and potentially measurable through neutrino appearance measurements at T2K.

Neutrino Oscillations in Matter

While the theory described previously is sufficient for neutrino oscillations in vacuum, experiments studying oscillations do not exist strictly in a vacuum. Whether the neutrinos are coming from the atmosphere, traveling through the matter that comprises the Earth, or starting somewhere in the ultradense core of the Sun, it is important to consider the effect matter has on neutrino oscillations. This effect is called the Mikheyev-Smirnov-Wolfenstein (MSW) effect, and is named after the theorists who developed the theory [59, 60]. Colloquially, the MSW effect is known by

[6]It should be noted that T2K includes all terms in the probability for their oscillation analysis.

[7]The octant describes whether $\theta_{23} > 45°$ or $\theta_{23} < 45°$.

the name matter effects.

As neutrinos travel through matter, there is a non-zero probability they interact. When considering the time evolution of neutrinos traveling to the detector, processes which do not have any neutrinos in the final state, such as many charged current processes, are not relevant, as they serve to only slightly reduce the neutrino flux. Furthermore, neutral current interactions occur independently of the flavor of neutrino, affecting each mass eigenstate equally. Neglecting these various types of interactions only leaves one type of interaction, elastic scattering off of electrons via the W boson. As the electron neutrino is the only flavor that can occur in the W mediated interaction, this effect is flavor dependent and will have an effect on neutrino oscillation.

In order to determine the size of the matter effects, start by considering the Hamiltonian of the neutrino traveling in a vacuum. Here, the energy of the neutrino is the sum of the mass energy of the neutrino and its kinetic energy. However, in matter, an effective potential energy term must be included in the Hamiltonian due to the ability for electron neutrinos and antineutrinos to elastically scatter. The potential energy term is dependent on how far the neutrino travels through matter and the electron density of that matter. Because of the additional term, the new Hamiltonian will have different mass eigenstates than the Hamiltonian for neutrinos in vacuum, which implies the effective mass for each mass eigenstate will be different in matter. Therefore, the probability for neutrino oscillations to occur is dependent on these different mass eigenstates and the PMNS matrix modified to give the relationship between the flavor eigenstates and the matter mass eigenstates. The resultant probability is a complicated combination of the various mixing parameters and the mass squared differences. While the probability is not shown here, a full treatment of the effect can be found in many sources, such as [61] and [62]. For this thesis, it is sufficient to know that matter effects have important effects on the measurement of neutrino oscillations and, therefore, must be taken into account.

Parameter	Best Fit Value	3σ Band
Δm^2_{21} [10^{-5} eV^2]	7.37	6.93 – 7.96
$\Delta m^2_{31(32)}$ [10^{-5} eV^2]	2.56 (2.54)	2.45 – 2.69 (2.42 – 2.66)
$\sin^2\theta_{12}$	0.297	0.250 – 0.354
$\sin^2\theta_{23}$, $\Delta^2_{31(32)} > 0$	0.425	0.381 – 0.615
$\sin^2\theta_{23}$, $\Delta^2_{32(31)} < 0$	0.589	0.384 – 0.636
$\sin^2\theta_{13}$, $\Delta^2_{31(32)} > 0$	0.0215	0.0190 – 0.0240
$\sin^2\theta_{13}$, $\Delta^2_{31(31)} < 0$	0.0216	0.0190 – 0.0242
δ_{CP}/π	1.38 (1.31)	2σ: 1.0 – 1.9 (2σ: 0.92 – 1.88)

Table 2.3: Current understanding of the neutrino oscillation parameters and their 3σ allowed ranges. Parameter values are derived from a global fit to current neutrino oscillation data [2]. In the case of δ_{CP}, the 2σ allowed range is shown. The values (values in parentheses) are for $m_1 < m_2 < m_3$ ($m_3 < m_1 < m_2$). Δm^2, as defined in [2], is $\Delta m^2 = m_3^2 - (m_2^2 + m_1^2)/2$. Under this definition, $\Delta m^2 > 0$ for $m_1 < m_2 < m_3$ and $\Delta m^2 < 0$ for $m_3 < m_1 < m_2$. Values are given of $\Delta m^2_{31} > 0$ for $m_1 < m_2 < m_3$ and $\Delta m^2_{32} < 0$ for $m_3 < m_1 < m_2$. Table from [3].

2.4 The Current Knowledge of Neutrinos

Over the last few decades, many experiments have measured the parameters involved in neutrino oscillations, including the the PMNS mixing angles, the CP violating phase, and the mass squared differences. As it stands, the current understanding of each of these parameters can be found in the 2018 edition of the Particle Data Group's Review of Particle Physics [3] and is summarized in Table 2.3.

The data shown in Table 2.3 comes from a variety of experiments:

1. Solar neutrino experiments are sensitive to $\sin^2\theta_{12}$ and Δm^2_{21} through the disappearance of electron neutrinos.

2. Reactor neutrino experiments are sensitive to $\sin^2\theta_{12}$, $\sin^2\theta_{13}$, and Δm^2_{21} through the disappearance of electron antineutrinos.

3. Atmospheric neutrino experiments are sensitive to $\sin^2\theta_{23}$ and $|\Delta m^2_{32}|$ or $|\Delta m^2_{31}|$ through the

disappearance of muon neutrinos.

4. Accelerator-based neutrino experiments are sensitive to $\sin^2\theta_{23}$ and $|\Delta m^2_{32}|$ or $|\Delta m^2_{31}|$ through the disappearance of muon neutrinos, as well as $\sin^2\theta_{13}$ and δ_{CP} through the appearance of electron neutrinos.

While many questions regarding neutrino oscillations have been answered, three particular questions have yet to be answered. First, do neutrino oscillations exhibit CP violation? Until recently, with the measurement of a non-zero $\sin^2\theta_{13}$, the potential for CP violation in the lepton sector was not well known. With the results from Daya Bay and T2K, $\sin^2\theta_{13}$ was found to be not only non-zero, but large enough that a measurement of δ_{CP} was experimentally possible. Results from T2K [63] have hinted at a value of δ_{CP}, but this remains an area of particular interest, both now and into the future.

Another open question in neutrino oscillation physics concerns the order of the mass eigenstates, which pertains to the sign of $\Delta m^2_{kj} \equiv m^2_k - m^2_j$. Typically, neutrino oscillation experiments study oscillations through a disappearance channel, which depends on calculating $P(\nu_\alpha \rightarrow \nu_\alpha)$. In the case of neutrino disappearance, $\mathcal{I}^{kj}_{\alpha\beta} = 0$ in Equations 2.25 and 2.26 for $P(\nu_\alpha \rightarrow \nu_\alpha)$, and the oscillation probability is not dependent on the sign of Δm^2_{kj}. However, when taking matter effects into consideration, the probability can be sufficiently modified such that the sign of Δm^2_{kj} can be measured. With solar neutrinos, the extreme electron density in the core of the sun causes significant effects due to the MSW effect [64]. Due to this, measurements have been able to establish that $m_1 < m_2$. Furthermore, it has been determined that $|\Delta m^2_{32}| \approx |\Delta m^2_{31}| >> \Delta m^2_{21}$, but it has yet to be established whether the order of masses is $m_1 < m_2 < m_3$ (called the normal hierarchy) or $m_3 < m_1 < m_2$ (called the inverted hierarchy). The determination of the mass hierarchy is considered one of the primary goals for current and future neutrino experiments.

A third question that remains open to consideration is the existence of the so-called "sterile" neutrino. In the Standard Model, the three neutrinos are all left-handed, where the spin is antiparallel to its momentum, and the antineutrinos are all right-handed. Because there are no right-handed

neutrinos, or left-handed antineutrinos, neutrinos are not able to gain their mass through the Higgs mechanism and, therefore, should be massless. However, because neutrino oscillations imply that neutrinos do, in fact, have mass, this means that the Standard Model must be extended. One of the simplest answers to rectify this issue would be to introduce right-handed neutrinos. These neutrinos would only interact via gravity and would be considered "sterile." As these neutrinos do not interact via the weak force, they could not be detected in a typical neutrino oscillation experiment. However, due to their being more than three neutrinos, sterile neutrinos could be detected indirectly through their modification to the oscillation probabilities. While a number of experiments have seen anomalies in their data [65, 66, 67] consistent with sterile neutrinos, there remains heavy tension as to their existence. This is due to several results from searches for sterile neutrinos that show no evidence for sterile neutrinos existing [68, 69]. In particular, T2K has studied the impact of the existence of a sterile neutrino in the oscillation analysis and there was no evidence for the existence of a sterile neutrino seen in their results [70, 71]. As the work presented in this thesis is based on the data seen by T2K, the analysis presented here presumes that sterile neutrinos do not exist.

CHAPTER 3

THE T2K LONG BASELINE NEUTRINO EXPERIMENT

The Tokai-to-Kamioka (T2K) experiment [16] is a long baseline neutrino oscillation experiment. It was designed to observe and measure the mixing of muon neutrinos with electron neutrinos using an intense beam of muon neutrinos created via a 30 GeV proton beam at the Japan Proton Accelerator Research Complex (J-PARC) facility in Tokai, Japan. The proton beam is guided into a graphite target, producing hadrons through proton interactions in the target. The resulting hadrons are focused by a set of magnetic horns, which can select either π^+, for a beam primarily composed of ν_μ, or π^-, for a beam primarily consisting of $\bar{\nu}_\mu$. The focused hadrons are pointed towards a 96 m long tunnel, where neutrinos are produced through the hadrons decaying. The neutrino beam is then observed by two near detectors, which are 280 m from the target, and a far detector, Super-Kamiokande (SK), which is 295 km from the target (see Figure 3.1).

The distance between the target and the far detector, called the baseline, is chosen such that the peak of the neutrino energy spectrum, 0.6 GeV, sits in the first oscillation maximum. This corresponds to the first minimum of the ν_μ survival probability, which can be seen in Figure 3.2. By choosing this location, T2K is able to measure neutrino oscillations through the disappearance of muon neutrinos and through the appearance of electron neutrinos. Oscillation into tau neutrinos also occurs in the neutrino beam; however, charged current ν_τ interactions are not measured because of the unlikely chance for producing a τ lepton at the neutrino energies of the T2K beam, as the

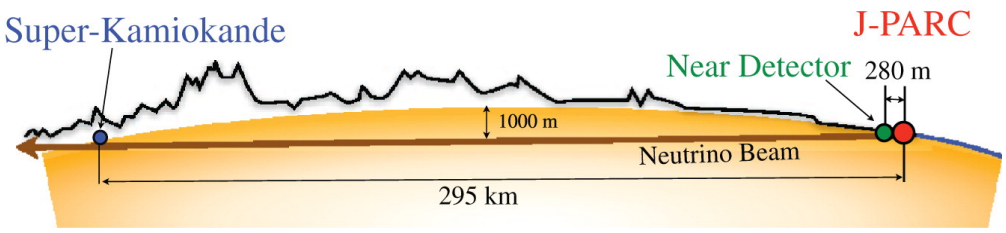

Figure 3.1: Schematic of the T2K experiment. Figure from [16].

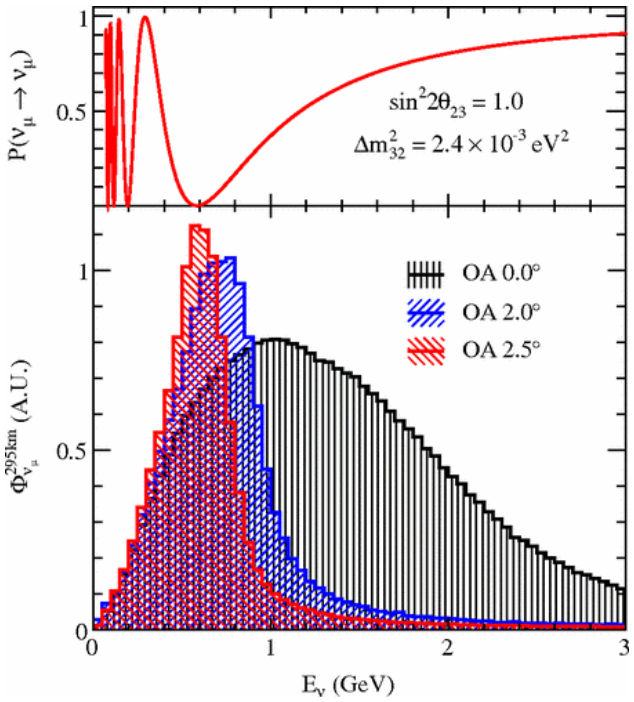

Figure 3.2: The muon neutrino survival probability at 295 km (top) and neutrino fluxes for different off-axis (listed as OA in the figure) angles (bottom). It should be noted that the flux predictions are normalized so that the units on the y-axis are arbitrary. Realistically, the total flux decreases for higher off-axis angles. Figure from [17].

neutrino needs to have more than 1.75 GeV of energy to create a τ at rest.

3.1 Japan Proton Accelerator Research Complex

The J-PARC beamline was constructed for T2K and consists of three accelerators, a linear accelerator (LINAC), a rapid-cycling synchrotron (RCS), and a main ring (MR). Initially, a beam of H^- is accelerated to 400 MeV in the LINAC before being converted to a beam of H^+ by charge-stripping foils at the injection point to the RCS. The particles are then accelerated up to 3 GeV in the RCS, which has a cycle of 25 Hz and holds two bunches, or groups, of particles per cycle. Approximately 5% of the bunches are supplied to the MR [16], while the rest are sent to the muon and neutron beamlines used by other experiments at J-PARC. The particles which are supplied to the MR are accelerated up to 30 GeV before being used to produce the T2K beam.

In order to generate the T2K neutrino beam, the proton beam is extracted from the MR using

a set of 5 kicker magnets, which are used to redirect the beam through a single turn. A single extraction of the proton beam is called a "spill" and contains 8 bunches of protons separated by about 560 nanoseconds between bunches, for a total duration of approximately 5 microseconds. By having a solid understanding of the time structure for the extracted proton beam, the T2K beam trigger is able to discriminate between various backgrounds, such as cosmic rays, and the beam signal in the T2K detectors.

T2K has been collecting data since 2010. The amount of data collected is calculated by counting the number of protons impinging on the target (protons on target, or POT). Using the POT collected to determine the amount of data acquired is done because the amount of POT directly correlates to the beam power and the number of spills collected. The amount of POT collected and the corresponding T2K run periods can be seen in Figure 3.3.

3.1.1 The T2K Neutrino Beamline

The spills extracted from the MR are directed towards the T2K neutrino beamline, which has two parts, the primary and secondary beamline, as seen in Figure 3.4. The purpose of the primary beamline is to bend the extracted proton bunches to point in the direction of the secondary beamline, which is in line with the T2K detectors, as well as focusing the beam to have the desired profile at the target. Furthermore, the intensity, position, profile, and proton beam loss are measured in the primary beamline. The characteristics of the proton beam are measured because a well-tuned beam is essential for producing a stable neutrino beam.

As the proton beam enters the secondary beamline, the protons impinge upon a target to produce secondary mesons, which consist mostly of pions and kaons. The target is a graphite rod with a diameter of 2.6 cm and a length of 91.4 cm, which is equivalent to 1.9 interaction lengths for the proton beam. The target is cooled by helium gas to offset the heat load from the pulsed beam.

The secondary mesons are focused with three magnetic horns [72]. The target sits inside the first horn, whose objective is to collect the mesons produced via the proton interactions, while the second and third horns focus the mesons into a beam. Each horn is made up of two coaxial

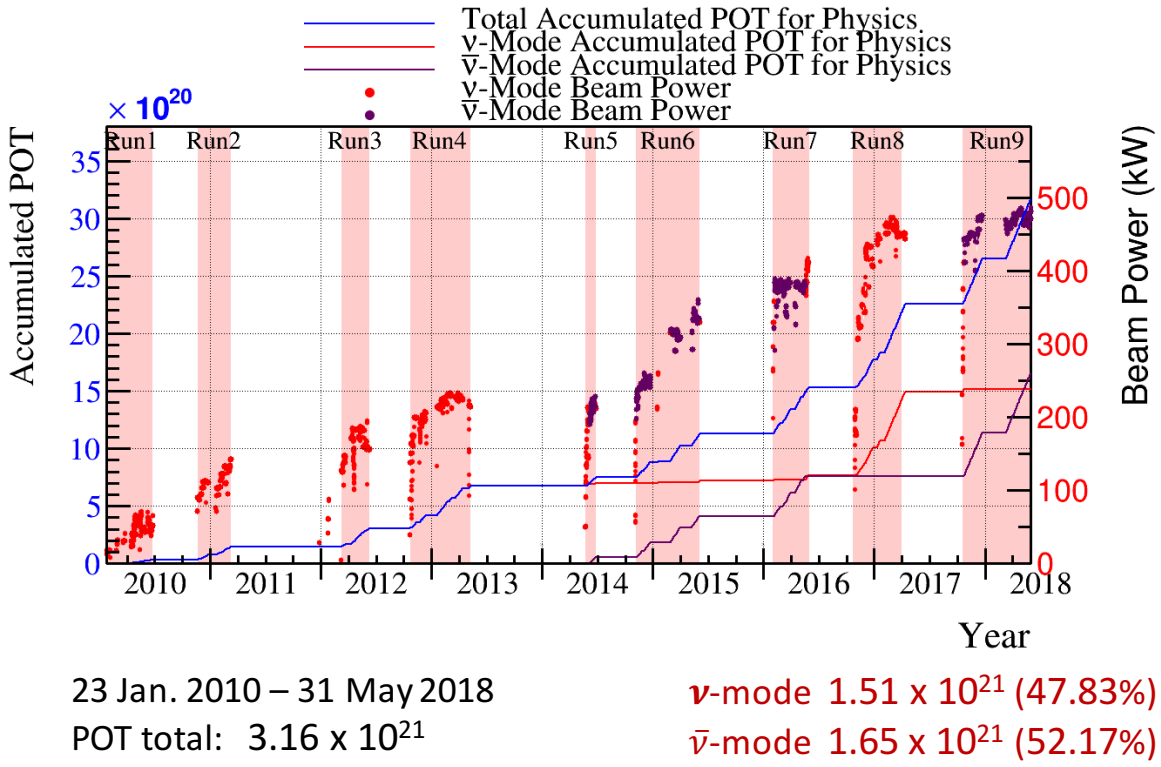

Figure 3.3: The POT collected at T2K between January 2010 and May 2018. The red shaded regions show when the T2K beam was being produced. Figure from [18].

conductors which form a closed volume. A toroidal magnetic field is generated within the volume between the conductors, which varies as 1/(distance from the beam axis). The magnetic horns are operated with a 250 kA pulsed current and produce a maximum magnetic field of 1.7 Tesla. By using the magnetic horns, the neutrino flux is increased by approximately a factor of 16 for the peak energy at the far detector [16].

The current which powers the magnetic horns can run in two modes to focus either positively or negatively charged mesons, producing a primarily neutrino or antineutrino beam. The current used to focus positively charged mesons and creates a beam primarily made of neutrinos, is called neutrino mode or Forward Horn Current (FHC). On the other hand, the current which focuses

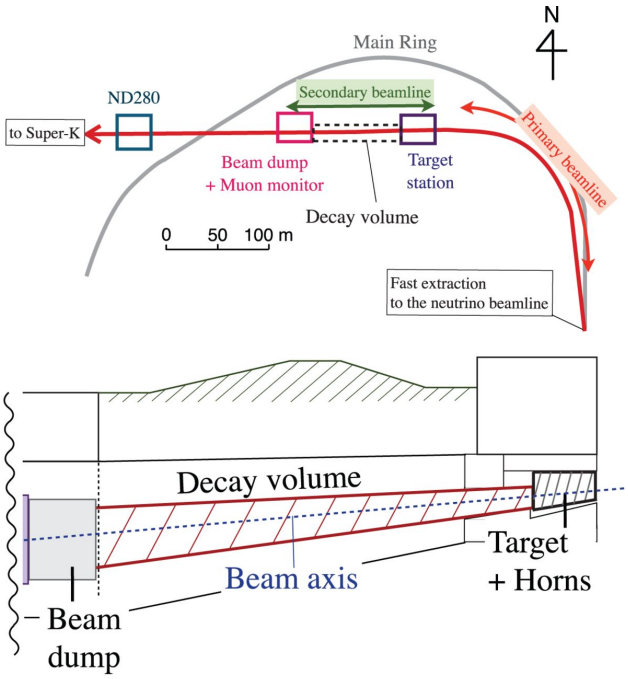

Figure 3.4: **Top:** Overview of the T2K beamline. **Bottom:** Side view of the secondary beamline. Figure from [19].

negatively charged mesons, to produce a beam mostly composed of antineutrinos, is referred to as antineutrino mode or Reverse Horn Current (RHC).

The focused mesons enter a 96 m long tunnel, which provides a volume for the mesons to decay to produce muon neutrinos and antineutrinos:

$$\pi^+ \rightarrow \mu^+ + \nu_\mu \qquad K^+ \rightarrow \mu^+ + \nu_\mu \qquad \text{(FHC primarily)}$$
$$\pi^- \rightarrow \mu^- + \bar{\nu}_\mu \qquad K^- \rightarrow \mu^- + \bar{\nu}_\mu. \qquad \text{(RHC primarily)}$$

The resulting beam is dominated by muon neutrinos (or antineutrinos), but a small contribution of electron neutrinos and antineutrinos come from decays including

$$K^+ \rightarrow \pi^0 + e^+ + \nu_e$$

and

$$\mu^+ \rightarrow e^+ + \nu_e + \bar{\nu}_\mu$$

in FHC.

A beam dump is situated at the end of the decay volume, where all hadrons from the beam and any muons with energies below approximately 5 GeV are stopped. Muons above that energy pass through the beam dump and are measured by muon monitors [73], which are directly behind the beam dump. These measurements are used to validate the stability of the neutrino beam bunch-by-bunch, because muons are produced along with neutrinos primarily through two-body pion decay. The neutrinos produced from meson decay pass through the beam dump and become the T2K neutrino beam.

3.1.2 The Off-Axis Neutrino Beam

One of the T2K near detectors and the far detector are set 2.5° off-axis with respect to the primary proton beam. This is done to make use of the fact that the energy of neutrinos emitted at large angles to the parent meson in a two-body pion or kaon decay depends weakly on the momentum of the parent meson.

To show this weak dependence, consider neutrinos produced via the two-body decay of a pion into a muon and a muon neutrino[1]. Using energy and momentum conservation, an expression can be written which relates the neutrino energy, E_ν, to the pion energy, E_π, the pion mass, m_π, and the muon mass, m_μ:

$$E_\nu = \frac{m_\pi^2 - m_\mu^2}{2(E_\pi - p_\pi \cos\theta)}, \tag{3.1}$$

where θ is the angle between the direction the pion is traveling and the direction of the emitted neutrino. Differentiating the previous equation with respect to E_π and holding θ constant, a maximum for E_ν is found for $E_\pi = E_\pi^{max} = p_\pi/\cos\theta$. By substituting E_π^{max} into Equation 3.1, the maximum neutrino energy E_ν^{max}, for a given angle θ, is:

$$E_\nu^{max}|_\theta = \frac{m_\pi^2 - m_\mu^2}{2E_\pi^{max}\sin^2\theta}. \tag{3.2}$$

[1]The treatment described here is based on the off-axis neutrino beam description in [74].

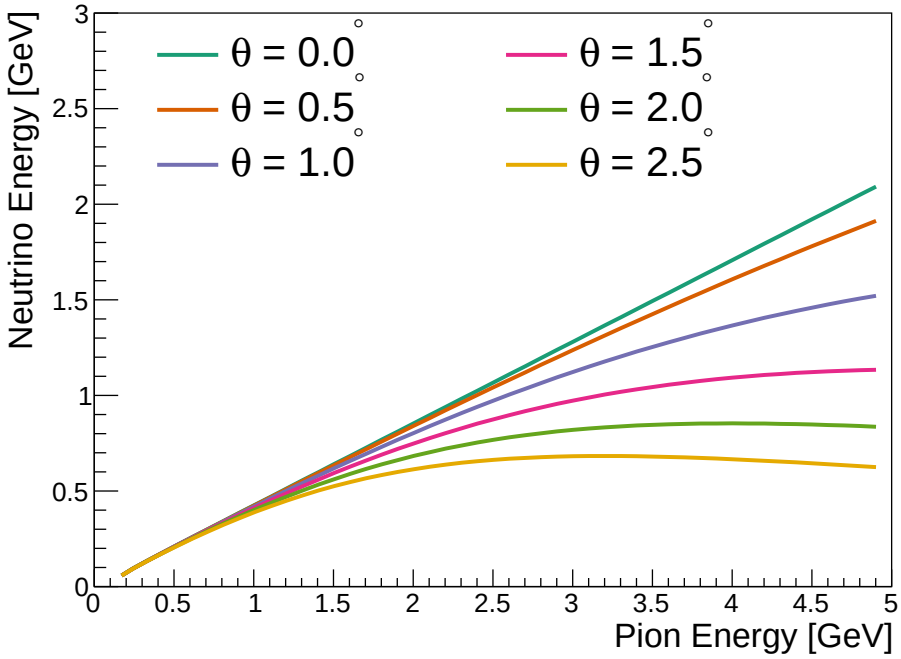

Figure 3.5: Neutrino energy as a function of the pion energy for neutrinos produced from the two-body decay of pions into a muon and a neutrino. Predictions are shown for various angles between the neutrino and pion directions.

When pion energies are either greater than or less than E_{π}^{max}, the energy of the neutrino is less than E_{ν}^{max}. Because of this, when the emission angle, θ, is large, the range of possible neutrino energies is decreased. This means that pions with a wide range of energies will produce neutrinos with similar laboratory energies when they decay. Figure 3.5 shows the neutrino energy at various pion energies and angles.

By setting the detectors at an angle to the beam, T2K takes advantage of this property to generate a neutrino beam with a narrow spread in energies. Figure 3.2 shows that, for an angle of 2.5°, the flux is more sharply peaked than the on-axis flux as a function of neutrino energy. The energy of the proton beam and the off-axis angle were chosen in such a way that the peak neutrino energy is approximately 0.6 GeV, which corresponds to the first oscillation maximum and maximizes the effect of neutrino oscillation at the far detector.

3.2 The T2K Near Detectors

T2K uses a pair of near detector situated 280 m from the target to measure the neutrino beam prior to the neutrinos oscillating. This allows the properties of the beam, including its position and the number of muon neutrino interactions, to be measured prior to neutrino oscillations occurring. The two near detectors are the Interactive Neutrino GRID (INGRID) detector and the Near Detector at 280 m (ND280).

3.2.1 The Interactive Neutrino GRID Detector

The primary task of the INGRID detector [16, 75], which is positioned in line with the proton beam, is to monitor the direction and profile of the beam. Because the energy spectrum of the beam is dependent on the off-axis angle (as shown in Figures 3.2 and 3.5), it is essential to measure the direction of the neutrino beam very precisely.

The INGRID detector, seen in Figure 3.6, consists of 16 identical modules, 14 of which are arranged in a cross formation, while the other 2 are set at off-axis positions from the cross. It was designed so the cross formation covers a 10 m $\times$ 10 m range in the transverse direction to the neutrino beam. The modules of the vertical and horizontal arms of the cross overlap at the center of the cross and are directly aligned with the direction of the proton beam. Each module in INGRID is made of alternating layers of iron plates and planes of scintillator bars. These layers are surrounded by veto scintillator planes to reject any interactions which take place outside the module. Each scintillator bar contains a wavelength-shifting (WLS) fiber, which is set in a 3 mm-diameter hole in the center of the bar and is connected to a multi-pixel photon counter (MPPC) [76] at one end. The MPPC converts the light from the WLS fiber into an electronic signal, which allows the data to be read out from the detector. INGRID detects enough neutrino interactions to measure the neutrino interaction rate with 4% precision daily, while also providing monthly measurements of the center of the neutrino beam to an accuracy better than 0.4 milliradians.

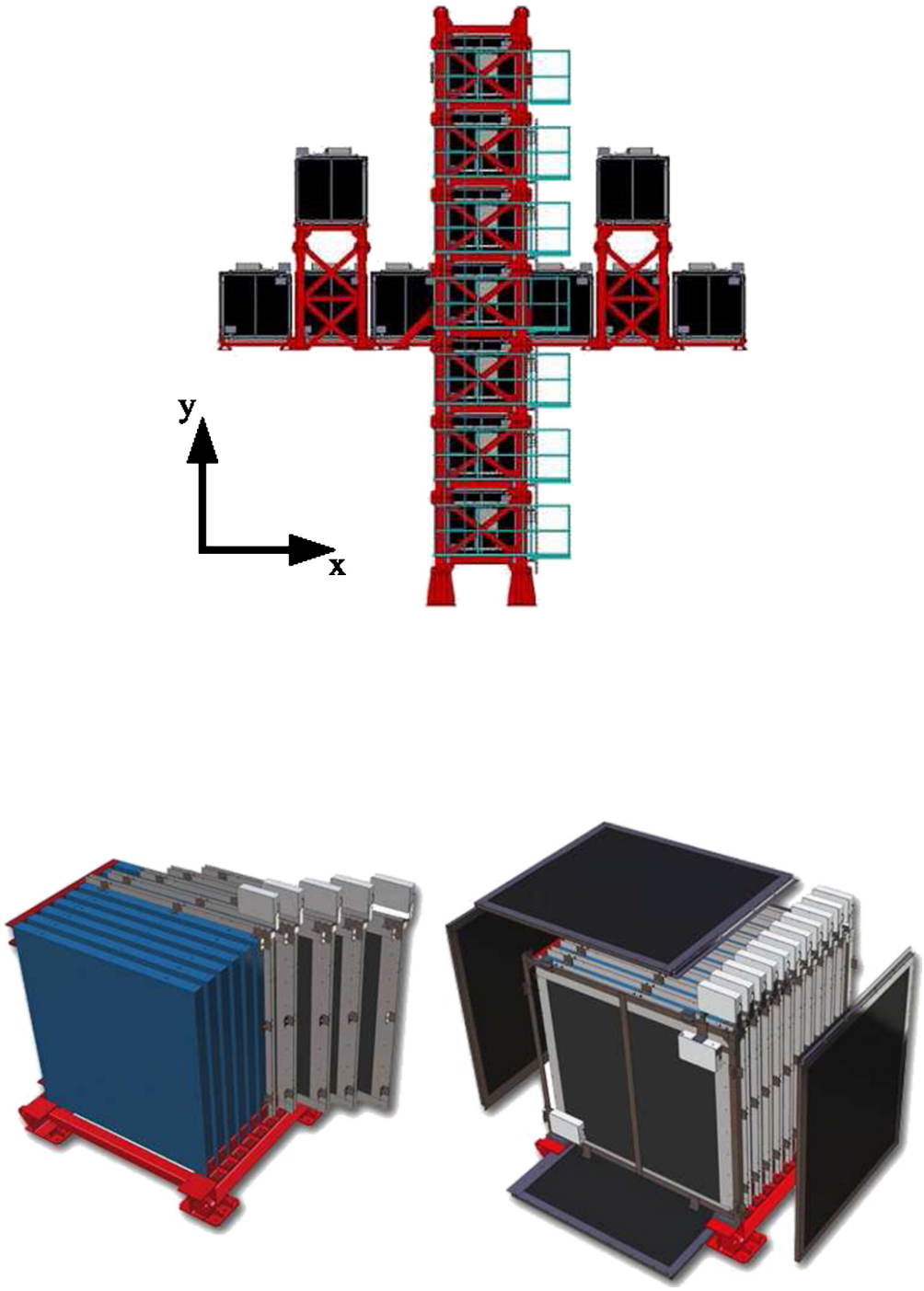

Figure 3.6: **Top:** The INGRID detector. **Bottom Left:** An INGRID module showing the scintillator planes (blue) and the iron plates (gray). **Bottom Right:** An INGRID module with the veto planes (black) shown. Figure from [16].

3.2.2 The Near Detector at 280 Meters

ND280 [16] sits 280 m from the proton target. However, unlike INGRID, ND280 sits 2.5° off-axis. It consists of five different detectors, of which the main portion is called the tracker. The tracker is made of three time projection chambers (TPCs) and two fine-grained detectors (FGDs). The Pi-Zero Detector (PØD) sits upstream of the tracker and is used for measuring the π^0 background from neutral current interactions. The PØD and the tracker sit in a 6.5 m × 2.6 m × 2.5 m metal frame, which is surrounded by an electromagnetic calorimeter (ECal). The recycled UA1 magnet encapsulates the ECal and is instrumented with the side muon range detector, which detects muons that escape out the sides of ND280. The layout of ND280 can be seen in Figure 3.7. This thesis focuses on interactions in the tracker, while the other detectors provide supplemental information when performing the analysis.

UA1 Magnet

Prior to being used by T2K, the magnet was used by the UA1/NOMAD experiment. It provides a near constant dipole magnetic field within ND280, which allows for accurate momentum measurements and particle charge identification. The magnetic field is generated by passing a 2900 A current through a set of water-cooled aluminum coils within the magnet [16]. The inner dimension of the coils measures 7.0 m × 3.5 m × 3.6 m, while the outer dimension is 7.6 m × 5.6 m × 6.1 m. In between the inner and outer dimensions, there are sixteen flux return yokes. The aluminum coils and return yokes are separated into two mirror-symmetric halves. This allows the magnet to be opened for access to the other detectors. Additionally, the magnet is instrumented with scintillator to function as a side muon range detector (SMRD).

The Side Muon Range Detector

The SMRD is incorporated into the magnet yoke that surrounds the inner detectors of ND280. Its objectives are to detect muons that escape the detector with large angles relative to the

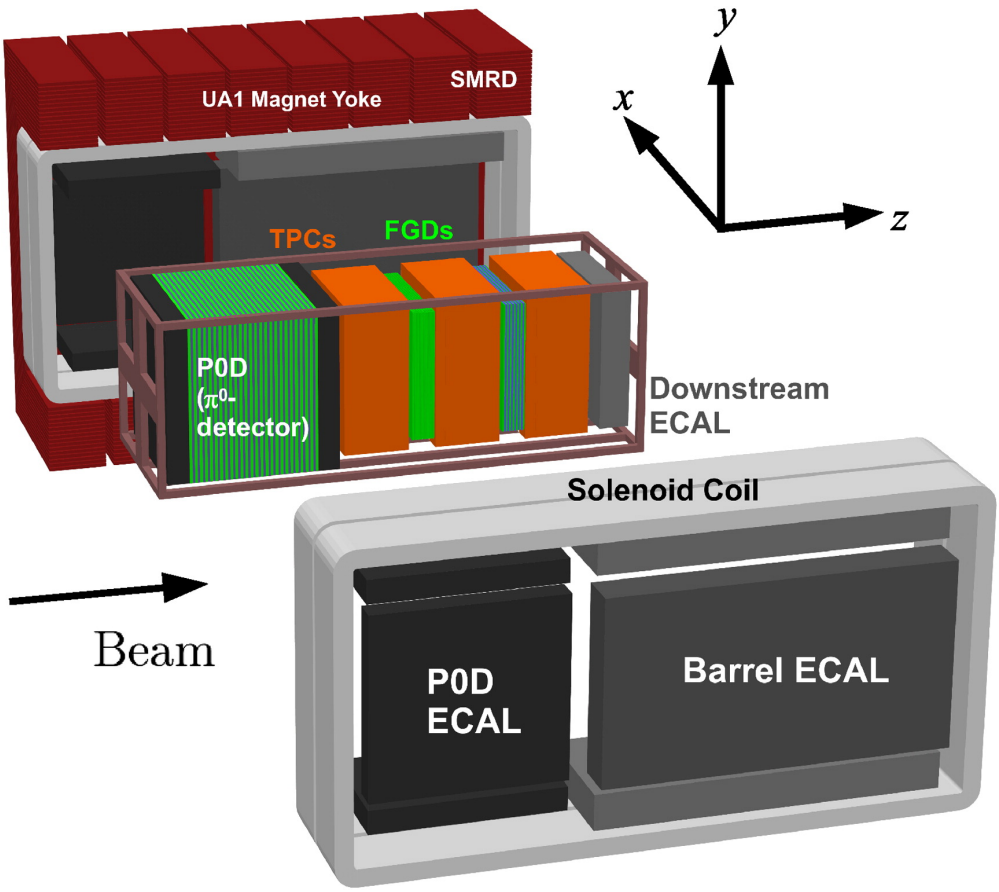

Figure 3.7: The layout of ND280. Figure from [16].

beam direction and to serve as a veto for particles entering the ND280 volume. Furthermore, it identifies beam interactions which occur in the magnet and the surrounding detector pit. The SMRD is installed in the air gaps between the steel plates that serve as the magnet return yoke. In total, there are 440 scintillator modules, which consist of either four or five scintillation counters, depending on whether the module sits in a horizontal or vertical air gap. The scintillation counters are optimized in such a way as to maximize the active area in each gap.

The Electromagnetic Calorimeter

The ECal is a sampling electromagnetic calorimeter that provides almost complete coverage for particles exiting the tracker or the PØD. Because the tracker is unable to detect neutral

pions, the ECal is used to reconstruct any π^0's produced within the tracker volume. It consists of layered scintillator bars and layers of lead, which provides an interaction target for neutrinos and functions as a radiator for producing electromagnetic showers.

Within the ECal, there are three types of modules [77]. The six Barrel ECal modules are placed parallel to the beam axis along the sides of the tracker. Each module in the Barrel ECal consists of 31 layers of 50 scintillator bars each, interwoven with 1.75 mm thick lead sheets. The Downstream ECal sits at the end of the tracker and is similar in composition to the Barrel ECals, but with 34 scintillator layers, instead of 50. Finally, the six PØD ECal modules surround the PØD parallel to the beam axis. Because the PØD was designed to detect π^0's, the ECal is used to provide additional energy information. Therefore, it only has six layers of scintillator, but is alternated with 4 mm thick lead sheets, rather than the 1.75 mm thick sheets used in the Barrel and Downstream ECals.

The Pi-Zero Detector

The PØD was designed to measure neutral current interactions on water, which is the same target used at SK, and consists of scintillator modules alternated with lead and bronze sheets and fillable water target bags. While the beam is running, these bags can either be filled with water, or left empty. By using data collected in both configurations, a subtraction analysis can be performed to determine the neutrino-water cross section. The PØD contains 40 scintillator modules, which consist of two perpendicular layers of triangular scintillator bars with a WLS fiber running through the middle of each bar. The total active volume is 2103 mm $\times$ 2239 mm $\times$ 2400 mm, and has a total mass of 13.3 tons when the water bags are empty, or 16.1 tons when the bags are filled [78].

Fine-Grained Detectors

The two FGDs [79] are used to provide a large target mass for neutrino interactions in ND280 as well as to track short-ranged, charged particles close to the point of interaction. These short-ranged particles are important to accurately measure, as they aid in identifying the type

of neutrino interaction that occurred. Therefore, the FGDs must be able to measure charged particles with fine granularity, such that the individual particle tracks and directions can be resolved.

Each FGD is instrumented with scintillator bars that are 1864.3 mm long with a square cross section of 9.6 mm. Each bar contains a WLS fiber running down its center and is mirrored on one end. The opposite end contains a MPPC to register hits occurring in the bar. Because they must be operated in the magnetic field of ND280, MPPCs are used, rather than photomultiplier tubes. The scintillator bars are arranged into "XY" modules, where each module contains 192 bars in both the horizontal and vertical directions. FGD1 contains only scintillator bars, which are arranged in 15 XY modules. On the other hand, FGD2 contains seven XY scintillator modules, which are alternated with six 2.5 cm thick layers of water.

Time Projection Chambers

The TPCs provide 3D tracking and particle identification for charged particles, which is crucial for identifying neutrino interactions occurring in the FGDs. Furthermore, the magnetic field in ND280 allows the particle charge and momentum to be measured. Because the TPCs are able to distinguish between particles with opposite charges, ND280 is able to differentiate between neutrino and antineutrino interactions, as the outgoing leptons have different charges. There are three identical TPCs, which sandwich the FGDs, such that TPC1 sits upstream of FGD1, TPC2 sits between FGD1 and FGD2, and TPC3 sits downstream of FGD2.

Each TPC has two chambers (see Figure 3.8), where the inner chamber is filled with an argon-based drift gas and the outer chamber is filled with carbon dioxide for insulation [80]. The walls of the inner box are made of composite panels with copper clad skins. The panels, in conjunction with a central cathode panel in the middle of the inner box, create a uniform electric drift field in the volume of the TPC [80]. As a charged particle traverses the TPC, it produces ionization electrons in the gas, which drift away from the central cathode towards

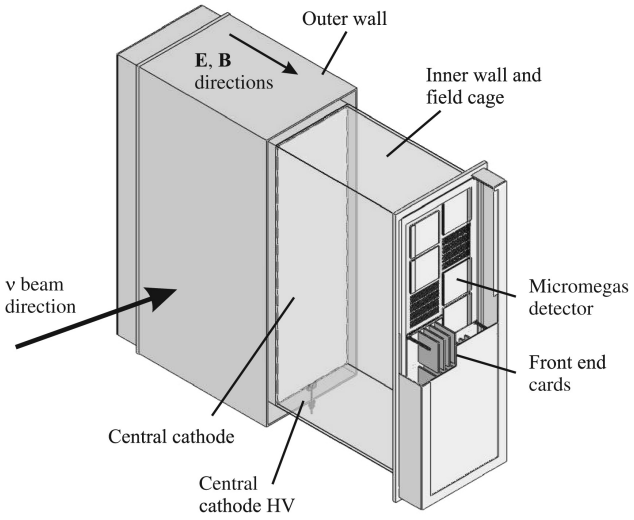

Figure 3.8: Simplified diagram of a single time projection chamber. Figure from [16].

readout planes at the ends of the detector. The readout planes consist of twelve modules that sample and multiply the electrons [80, 81].

3.3 The T2K Far Detector – Super Kamiokande

The T2K far detector, Super-Kamiokande [82], is a 50 kton water Cherenkov detector. It is located 295 km west of the interaction target and buried 1 km deep in Mt. Ikenoyama.

SK, as seen in 3.9, is a cylindrical tank, 42 m tall with a 39 m diameter, and is filled with pure water. The tank is divided into two volumes, the inner and outer detectors, and are separated by a cylindrical stainless-steel framework. The outer detector is primarily used as an active veto for backgrounds, such as cosmic ray muons and interactions occurring in the surrounding rock, and has an efficiency of almost 100% in rejecting cosmic ray backgrounds. The inner detector is instrumented with 11,129 inward-facing 50 cm-diameter photomultiplier tubes (PMTs). This provides about 40% coverage on the surrounding walls and gives enough spatial resolution to reconstruct the position of the products from neutrino interactions.

Neutrino interactions in SK tend to produce charged particles above the energy threshold to

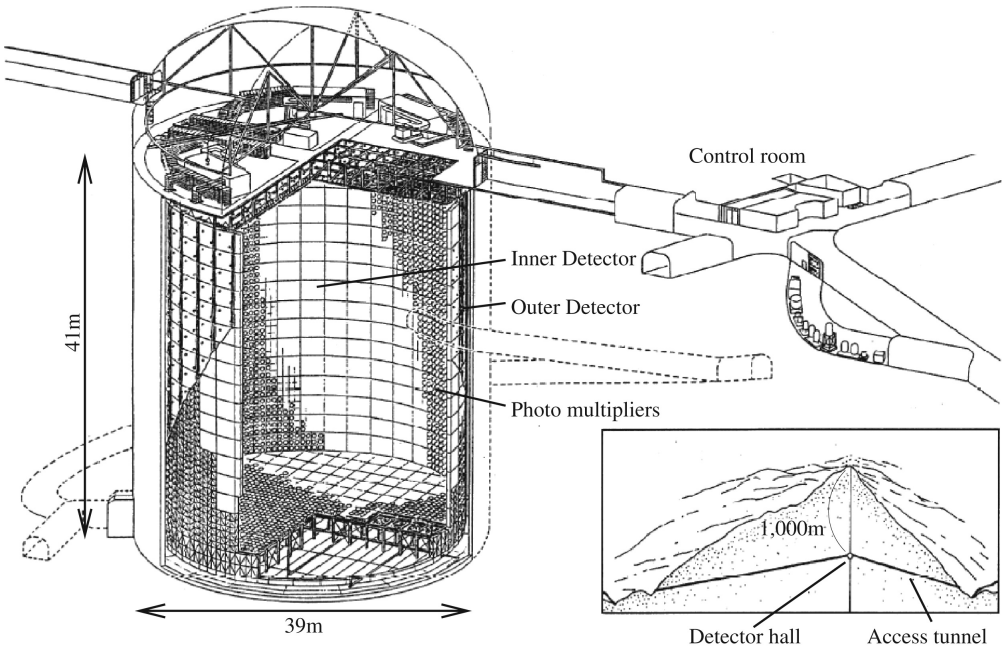

Figure 3.9: The Super-Kamiokande detector. Figure from [16].

produce Cherenkov radiation as they travel through the water. The photons from the Cherenkov radiation are emitted in a cone and are detected by the PMTs in a hit pattern shaped like a ring[2]. The pattern of hits, plus timing information, allows information to be extracted from the interaction, such as the its location, the momenta of outgoing particles, and the flavor of the charged lepton.

The oscillation analysis at T2K relies on identifying neutrino interactions and determining the energy and flavor of the incoming neutrino. If the interaction is a CCQE interaction, then the energy of the neutrino can be reconstructed from momentum and direction of the outgoing lepton. However, if the interaction is a CC resonant pion production interaction, not only is the momentum and direction of the outgoing lepton needed, but the kinematics of the outgoing pion are needed to properly reconstruct the energy of the neutrino. In both cases, the flavor can be inferred from the flavor of the detected lepton.

It is important to keep in mind that the SK detector does not have a magnetic field. Without a magnetic field, SK is unable to distinguish between positive leptons from antineutrino interactions

[2]See Figures 4.1 and 4.2 for examples on what these rings look like.

and negative leptons from neutrino interactions. Therefore, it is important that the antineutrino and neutrino components of the beam be measured at ND280 to accurately predict the components at SK.

SK has been running since 1996, and because of the long time in which is has been running, the behavior of the detector is well understood. Data collected from cosmic ray muons and atmospheric neutrino interactions give a number of control samples unrelated to the T2K beam. These samples are used to assess the detector response and systematic uncertainties. By way of example, atmospheric neutrino data can be used to quantify the uncertainty for correctly counting the number of rings seen in an interaction [83].

CHAPTER 4

THE OSCILLATION ANALYSIS AT T2K

4.1 The T2K Oscillation Analysis

4.1.1 Overview and Motivation

The main goal of the T2K experiment is to measure neutrino oscillations at Super-Kamiokande (SK). At a basic level, this is done by comparing the number of candidate neutrino interactions, or events, at ND280 with the number observed at SK. Because ND280 sits only 280 m from the target, the neutrinos have not had a chance to oscillate, so the measurement is of the unoscillated neutrino beam. On the other hand, with SK being nearly 300 km from the source, the neutrinos have had time to oscillate into other neutrino flavors, allowing the oscillated beam of neutrinos to be measured.

The number of predicted events can be naively calculated as [84]

$$N_{ND280}^{\alpha\to\alpha}(p_{reco}) = \sum_i \Phi_\alpha(E_{true}) \times \sigma_\alpha^i(p_{true}) \times \epsilon_\alpha(p_{true}) \times R_i(p_{true}; p_{reco}) \tag{4.1}$$

for ND280, and

$$N_{SK}^{\alpha\to\beta}(p_{reco}) = \sum_i \Phi_\alpha(E_{true}) \times P_{\alpha\beta}(E_{true}) \times \sigma_\beta^i(p_{true}) \times \epsilon_\beta(p_{true}) \times R_i(p_{true}; p_{reco}) \tag{4.2}$$

for SK. Here, $N_{ND280(SK)}(p_{reco})$ is the predicted event rate as a function of the reconstructed muon kinematics, where p_{reco} is the reconstructed muon four-momentum. The primary difference between N_{ND280} and N_{SK} is the oscillation probability, $P_{\alpha\beta}$, included in the far detector event rate. Other than $P_{\alpha\beta}$, the other four components are similar between ND280 and SK. The neutrino flux as a function of true neutrino energy, $\Phi_\alpha(E_{true})$, combined with the neutrino cross section, $\sigma_{\alpha(\beta)}^i(p_{true})$, provides a prediction on the number of events expected in the detector. The detector efficiency, $\epsilon_{\alpha(\beta)}(p_{true})$, represents how well the detector can detect interactions occurring in the detector. Finally, the event rate is dependent on the reconstructed kinematic variables, as this is

	μ-like Events		e^--like Events		
Error Source	ν-mode	$\bar{\nu}$-mode	ν-mode	$\bar{\nu}$-mode	ν-mode CC1π
Beam (without ND280 data)	8.0%	7.3%	8.0%	8.1%	8.9%
Beam (with ND280 data)	4.3%	4.1%	4.4%	4.2%	4.4%
Cross section (without ND280 data)	12.3%	10.3%	12.3%	10.1%	8.7%
Cross section (with ND280 data)	5.6%	4.4%	8.4%	6.2%	5.6%
Beam + Cross section (without ND280 data)	14.5%	12.6%	14.5%	13.0%	12.6%
Beam + Cross section (with ND280 data)	4.4%	2.9%	7.7%	5.7%	5.6%
SK+FSI+SI	3.3%	2.9%	4.1%	4.3%	16.6%
Total (without ND280 data)	15.0%	13.0%	15.0%	13.7%	20.1%
Total (with ND280 data)	5.5%	4.4%	8.8%	7.3%	17.8%

Table 4.1: Uncertainty on the number of events in each SK sample separated by error source with and without the constraint provided by the ND280 data. The SK+FSI+SI uncertainties are not constrained by the ND280 data. Table from [4].

what is measured in the detector. However, the other components in Equations 4.1 and 4.2 are dependent on the true kinematic variables. Therefore, a function, $R_i(p_{true}; p_{reco})$, is included to represent the probability an event with a true four-momentum, p_{true}, is reconstructed with a four-momentum, p_{reco}. This function is dependent on the type of interaction, i, as well as detector and nuclear effects.

$P_{\alpha\beta}$ includes the information regarding the fundamental neutrino oscillation parameters, which are the signal parameters in an oscillation analysis. Systematic uncertainties on these parameters come from the other components found in Equations 4.1 and 4.2. For T2K, the largest sources of uncertainty come from the neutrino flux and cross sections. These uncertainties can be reduced, or constrained, by using data from other experiments, such as the NA-61/SHINE experiment [85] for the flux or MINERνA [86] for the cross sections. Additionally, data from ND280 can be used to constrain these uncertainties. By including data from the near detector, the T2K neutrino flux and cross section can be simultaneously constrained. This reduces the uncertainty beyond what data from external experiments could do on their own. Table 4.1 shows the effect of including the near detector data on a recent T2K oscillation analysis.

The T2K oscillation analysis framework is a three step process.

1. External data is used to produce prior constraints on the flux and cross section, as well as for the detector systematic uncertainties. The flux and cross section constraints are discussed in more detail in Section 4.3, while the ND280 systematic uncertainties are covered in Chapter 6.

2. The ND280 data is included by performing a binned maximum likelihood fit, where the data is divided in bins based on their topological sample (described in Chapter 5) and their reconstructed momentum, p, and angle with respect to the neutrino beam, $\cos\theta$. These kinematic variables were chosen as ND280 was designed to measure the kinematics of the outgoing lepton from a neutrino interaction. They can then be used to calculate the neutrino energy, which is needed to determine the oscillation parameters. Finally, as SK primarily uses lepton kinematics, it is beneficial to use the same variables in each detector.

   The prior constraints determined in the previous step are treated as nuisance parameters in the fit. The output from this fit is a tuned set of flux and cross section parameters and their corresponding covariance, and is passed on to the final step of oscillation analysis. The likelihood fit is described in Section 4.2.

3. The final step in the process is the determination of the neutrino oscillation parameters themselves. This is done through a binned likelihood fit to the SK data (described in Section 4.1.3), using the results of the fit to the ND280 data as a prior constraint term. The data selection process for SK is described in Section 4.1.2.

This three step process is called a sequential likelihood maximization. Rather than fitting a global likelihood to all three data sets, which is computationally expensive, each data set receives its own treatment. This greatly decreases the complexity of each step, making the overall process computationally tractable.

4.1.2 Data Selection at Super-Kamiokande

As described in Section 3.3, events at SK are observed by characteristic rings seen in the detector. These rings come from the Cherenkov radiation emitted by particles as they travel through the detector. SK, in particular, looks for rings that could be the result of a muon or electron produced in a charged current neutrino interaction. This section will provide an overview for the event selection at SK.

At the far detector, the data (and simulation) is split into five selections: single-ring muon-like ($1R_\mu$) and single-ring electron-like ($1R_e$) for both neutrino and antineutrino beam modes, plus an electron-like CC$1\pi^+$ selection in neutrino mode. There is no difference in the $1R_\mu$ and $1R_e$ selections between beam modes, as SK cannot distinguish between the charge of the lepton. For more details on the selection process at SK, see [87].

The $1R_\mu$ selection must pass the following criteria:

- **Fiducial Volume:** The event must be fully contained within the fiducial volume of Super-Kamiokande. Furthermore, the event must be reconstructed within the fiducial volume.
- **Cherenkov Rings:** Only events which have one ring found by the ring counting algorithm are used.
- **Ring PID:** The ring must be identified as muon-like by the PID algorithm.
- **Reconstructed Momentum:** The muon reconstructed momentum must be greater than 200 MeV/c.
- **Decay Electrons:** The number of decay electrons must be less than or equal to one.
- π^+ **Rejection Cut:** The event must pass the π^+ rejection cut: $\ln(\mathcal{L}_{\pi^+}/\mathcal{L}_\mu) < 0.15 p_\mu$, where $\ln(\mathcal{L}_{\pi^+}/\mathcal{L}_\mu)$ is the log-likelihood ratio of the π^+ and μ hypotheses and p_μ is the momentum of the muon.

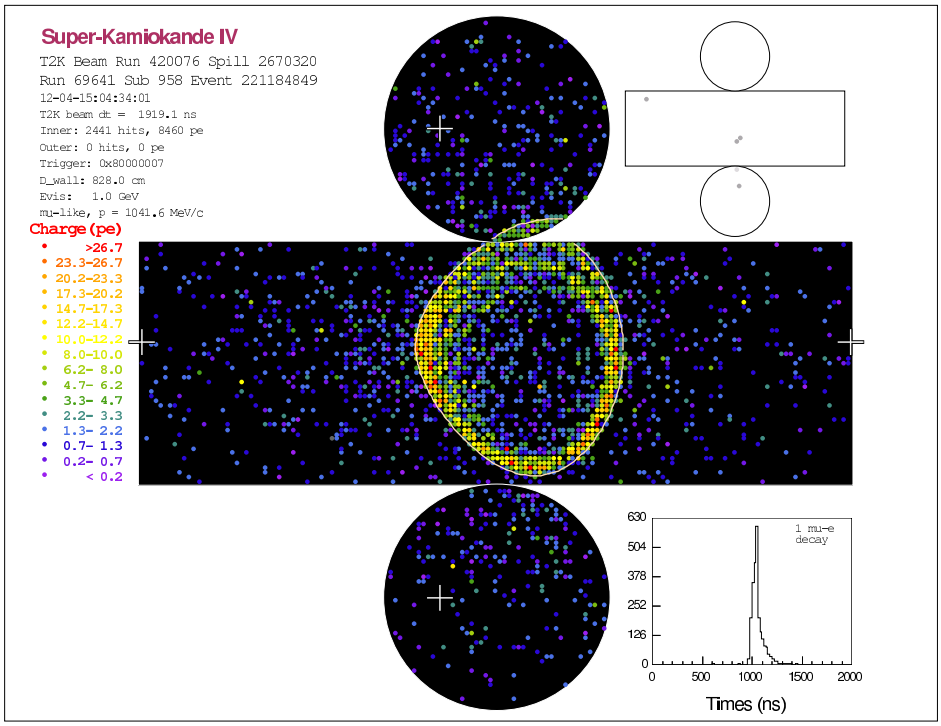

Figure 4.1: Example event display of a muon-like event at Super-Kamiokande. Photomultiplier tubes that have charge deposited in them during the event are shown as colored circles, where the color represents how much charge was deposited. The time distribution of hits can be seen in the bottom right corner. Figure from [20].

Based on a Monte Carlo data set, the purity for the $1R_\mu$ sample is 82.86% in neutrino beam mode and 79.72% in antineutrino beam mode [88]. An example of a muon-like event can be found in Figure 4.1.

The $1R_e$ selection is as follows:

- **Fiducial Volume:** The event must be fully contained and reconstructed within the fiducial volume of Super-Kamiokande.
- **Cherenkov Rings:** Only events which have one ring found by the ring counting algorithm are used.
- **Ring PID:** The ring must be identified as electron-like by the PID algorithm.
- **Visible Energy:** There must be at least 100 MeV of visible Cherenkov light in the detector.

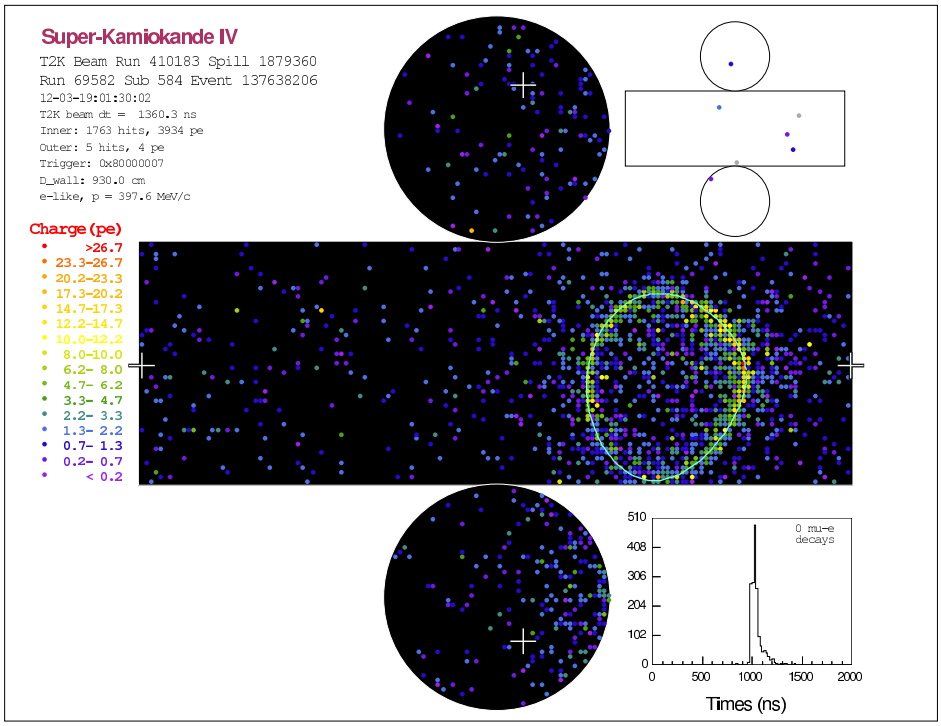

Figure 4.2: Example event display of an electron-like event at Super-Kamiokande. Photomultiplier tubes that have charge deposited in them during the event are shown as colored circles, where the color represents how much charge was deposited. The time distribution of hits can be seen in the bottom right corner. Figure from [20].

- **Decay Electrons:** There can be no decay electrons within the event.
- **Reconstructed Neutrino Energy:** The reconstructed energy of the neutrino must be less than 1250 MeV.
- π^0 **Rejection Cut:** The event must pass a cut for neutral pions: $\ln(\mathcal{L}_{\pi^0}/\mathcal{L}_e) < 175 - 0.875 m_{\pi^0}$, where $\ln(\mathcal{L}_{\pi^0}/\mathcal{L}_e)$ is the log-likelihood ratio of the π^0 and e hypotheses and m_{π^0} is the mass of the π^0.

The purity for the $1R_e$ sample is 81.18% in neutrino beam mode and 61.99% in antineutrino beam mode [88]. An example of an electron-like event can be found in Figure 4.2.

The electron-like CC$1\pi^+$ selection is similar to the $1R_e$ selection, with one key modification. Whereas, the $1R_e$ sample requires there to be no decay electrons in the event, the CC$1\pi^+$ selection

requires there to be one decay electron. This electron is considered to be the result of a decaying π^+; therefore, these events are selected into the electron-like CC1π^+ sample. The purity in this sample is 78.75% [88].

4.1.3 The Oscillation Fit at Super-Kamiokande

The T2K oscillation analysis employs two main methods, a hybrid frequentist-Bayesian method to deal with nuisance parameters and a fully Bayesian analysis, which uses a Markov chain Monte Carlo method [89]. It should be noted, the fully Bayesian method fits the near and far detector data simultaneously, combining the second and third steps of the sequential likelihood.

The oscillation fit uses a binned likelihood, given by:

$$\mathcal{L}(N_e^{obs}, N_\mu^{obs}, \vec{o}, \vec{f}) = \mathcal{L}_{main}(N_e^{obs}, N_\mu^{obs}, \vec{o}, \vec{f}) \times \mathcal{L}_{sys}(\vec{f}), \tag{4.3}$$

where N_e^{obs} is the observed number of electron-like events, N_μ^{obs} is the number of observed muon-like events, $\vec{o}$ are the oscillation parameters ($\sin^2\theta_{23}$, $|\Delta m^2_{32}|$, $\sin^2 2\theta_{13}$, and δ_{CP}) and $\vec{f}$ are the nuisance parameters. These nuisance parameters include the cross section model parameters, the flux parameters, the SK detector systematics, and the final state interaction and secondary interaction model uncertainties. The likelihood is divided into two parts, $\mathcal{L}_{main}$ and $\mathcal{L}_{sys}$. $\mathcal{L}_{main}$ is the term which compares the data with the predicted event rates using the oscillation and nuisance parameters, while $\mathcal{L}_{sys}$ is a Gaussian penalty term which only depends on the nuisance parameters.

For the hybrid fit approach, the nuisance parameters are marginalized by integrating the likelihood over the values of the nuisance parameters. This is done by generating 10,000 throws of the nuisance parameters based on their priors and then fitting these distributions. This produces a grid of likelihoods for the various parameter sets, whereby the fit is marginalized by choosing the set of parameters with the lowest χ^2. Furthermore, the oscillation parameters can be marginalized over to produce 2D intervals. Here, the parameters are marginalized by throwing the parameter values according the parameter type and range given in Table 4.2. One exception to the marginalization process is the mass hierarchy, where it is fixed to be either normal or inverted hierarchy. After

Parameter	Prior Type	Bounds
$\sin^2\theta_{23}$	Uniform	[0.3, 0.7]
$\sin^2 2\theta_{13}$ w/ reactor constraint	Gaussian	0.0830 ± 0.0031
$\sin^2 2\theta_{13}$ w/o reactor constraint	Uniform	[0.03, 0.2]
$\sin^2 2\theta_{12}$	Gaussian	0.851 ± 0.020
$\lvert\Delta m^2_{32}\rvert$ (NH) or $\lvert\Delta m^2_{13}\rvert$ (IH)	Uniform	$[2.3, 2.7] \times 10^{-3}$ eV^2/c^4
Δm^2_{21}	Gaussian	$(7.53 \pm 0.18) \times 10^{-5}$ eV^2/c^4
δ_{CP}	Uniform	$[-\pi, +\pi]$
Mass Hierarchy	Fixed	NH or IH

Table 4.2: Priors used for the oscillation parameters during the marginalization process. "NH" denotes normal hierarchy, while "IH" denotes inverted hierarchy. Table from [5].

the nuisance parameters have been marginalized over, the $\Delta\chi^2$ for the marginalized likelihood is minimized to determine the best fit oscillation parameters.

Because the nuisance parameters are marginalized, the result is not an exact set of best fit parameters corresponding to the best fit spectrum. Rather, the best fit spectrum is produced by using the thrown nuisance parameters:

$$N_j^{marg} = \frac{\sum_{i=1}^{n} \mathcal{L}(N_i^{obs}, \vec{o}, \vec{f_i}) \times N_j^{pred}(\vec{o}_{bf}, \vec{f_i})}{\sum_{i=1}^{n} \mathcal{L}(N_i^{obs}, \vec{o}_{bf}, \vec{f_i})}, \tag{4.4}$$

where n is the number of nuisance parameter throws, $\vec{o}_{bf}$ is the best fit oscillation parameters, and $\vec{f_i}$ is the i-th set of thrown nuisance parameters.

4.2 The Near Detector Fit

4.2.1 The Maximum Likelihood Fit Method

The near detector fit, also called the BANFF (**B**eam **A**nd **N**D280 **F**lux extrapolation task **F**orce) fit, uses the maximum likelihood method to determine the optimal set of flux, cross section, and detector parameters given the ND280 data. By fitting all the parameters simultaneously, correlations between the fitted flux and cross section parameters can be determined.

As mentioned in Section 4.1.1, the BANFF fit uses a binned likelihood. By binning the data in

$p - \cos\theta$, the fit is able to constrain the overall event rate as well as the neutrino energy distribution at SK. The $p - \cos\theta$ bins were chosen in such a way as to provide sufficient statistics for a χ^2 fit, while also having finer binning in regions with higher event rates to gain more information about the shape of the distribution. For a given bin, the data and Monte Carlo observed event rates are expected to follow a Poisson distribution. Therefore, the probability to observe N_i^{obs} events in bin i, given a predicted event rate, N_i^{pred}, which depends on the flux ($\vec{b}$), cross section ($\vec{x}$), and detector parameters ($\vec{d}$) described in Section 4.3, is:

$$P(N_i^{obs}|N_i^{pred}) = \frac{(N_i^{pred}(\vec{b},\vec{x},\vec{d}))^{N_i^{obs}} \times e^{-N_i^{pred}(\vec{b},\vec{x},\vec{d})}}{N_i^{obs}!}. \tag{4.5}$$

The full Poisson likelihood term is a product of the individual bin probabilities.

The remaining terms in the likelihood are related to the constraint terms for the beam, cross section, and detector parameters. These are each modeled as independent multivariate Gaussian distributions and, therefore, treated as separate terms in the likelihood. For a vector of parameter values $\vec{y}$ (which can be one of $\{\vec{b},\vec{x},\vec{d}\}$) with n parameters, an associated covariance matrix generated from prior inputs, $(V_y)_{i,j}$, and the difference between the current parameter value and its nominal value, $\Delta\vec{y}$, the probability can be calculated as:

$$\pi(\vec{y}) = (2\pi)^{n/2}|(V_y)_{i,j}|^{1/2} e^{\frac{-\Delta\vec{y}((V_y)^{-1}_{i,j})\Delta\vec{y}^T}{2}}. \tag{4.6}$$

The equation maximized by the fit is the likelihood ratio, where the numerator is defined using Equations 4.5 and 4.6 and the denominator is the likelihood function evaluated at $N_i^{pred} = N_i^{obs}$, which is the maximum value for the numerator,

$$\mathcal{L}_{ND280} = \frac{\pi(\vec{b})\pi(\vec{x})\pi(\vec{d})\prod_i (N_i^{pred}(\vec{b},\vec{x},\vec{d}))^{N_i^{obs}} e^{-N_i^{pred}(\vec{b},\vec{x},\vec{d})}/N_i^{obs}!}{\pi(\vec{b}_{nom})\pi(\vec{x}_{nom})\pi(\vec{d}_{nom})\prod_i (N_i^{obs})^{N_i^{obs}} e^{-N_i^{obs}}/N_i^{obs}!}. \tag{4.7}$$

By using the ratio, comparisons can be made between the likelihood of the predicted values and the maximum possible value. Furthermore, several terms cancel out, such as the determinants of the covariance matrices in Equation 4.6.

The minimized quantity is $\Delta\chi^2_{ND280} \equiv -2\ln\mathcal{L}_{ND280}$, which contains two independent parts, a Poisson contribution from the fitted observables and a Gaussian contribution from the fitted parameters and their covariance. The quantity $\Delta\chi^2_{ND280}$ is defined as

$$\begin{aligned}\Delta\chi^2_{ND280} = \; & 2\sum_{i}^{Nbins} N_i^{pred}(\vec{b},\vec{x},\vec{d}) \; - \; N_i^{obs} \; + \; N_i^{obs}\ln[N_i^{obs}/N_i^{pred}(\vec{b},\vec{x},\vec{d})] \; + \\ & \sum_{\alpha}^{B}\sum_{\beta}^{B}\Delta b_\alpha (V_b^{-1})_{\alpha,\beta}\Delta b_\beta \; + \\ & \sum_{\gamma}^{X}\sum_{\delta}^{X}\Delta x_\gamma (V_x^{-1})_{\gamma,\delta}\Delta x_\delta \; + \\ & \sum_{\rho}^{D}\sum_{\tau}^{D}\Delta d_\rho (V_d^{-1})_{\rho,\tau}\Delta d_\tau,\end{aligned} \tag{4.8}$$

where B, X, and D are the number of flux, cross section, and detector parameters. The number of predicted events in a given bin is calculated using detector weights, cross section response functions, and flux weights (described in Section 4.3), which depend on the sample $p - \cos\theta$ bin, the neutrino interaction mode, and the true neutrino energy.

The basic fitting routine relies on the Minuit minimization package [90] as implemented in the ROOT [91] framework. The MIGRAD algorithm, which is a gradient descent method, is used in the near detector fit to minimize the $\Delta\chi^2$ shown in Equation 4.8. The post-fit uncertainties are then estimated using the HESSE algorithm, which calculates the second derivatives of the parameters around the minimized values to produce the Hessian matrix, the inverse of which gives the covariance matrix of the fitted parameters.

4.3 Fit Parameters in the Near Detector Fit

The nuisance parameters of the near detector fit come from three sources, the T2K neutrino beam flux, the neutrino interaction cross section model, and the detector systematic uncertainty parameters. This section describes the parameters that are used for this analysis.

4.3.1 Flux Parameters

Many of the elements related to the neutrino beam production have an effect on the neutrino flux. These include properties of the proton beam, such as the energy, intensity, and direction of the beam, and the cross section for proton interactions on the target and the interactions of outgoing particles within the target or in the decay volume, such as the pions that later decay into neutrinos. T2K has produced a complex flux model that uses technical design specifications and standard particle physics simulation packages, which are tuned with data taken from monitoring the T2K beam and external experiments [17].

Two of the primary sources of uncertainty on the beam model come from hadron production in the target, which affects the prediction on the number of neutrinos produced, and the interactions of hadrons outside the target, which contributes a significant fraction of the background component of the neutrino beam. With regards to hadron production in the target, the cross section for producing pions, the number of pions produced in the target, and any outgoing nucleons from the interactions provide the dominant source of error at low energies. At higher energies, the uncertainty in kaon production is the dominant source. Interactions which occur outside the target are less likely to be focused (or defocused) by the magnet horns, increasing the background component of the neutrino flux. These, along with the rest of the systematic uncertainties, are included in the flux model through a covariance matrix generated through a series of simulation studies.

Using the model, a flux prediction is produced for ν_μ, $\bar{\nu}_\mu$, ν_e, and $\bar{\nu}_e$ at ND280 and Super-Kamiokande, and is binned in neutrino energy. By incorporating data from the NA61/SHINE experiment [85], the nominal flux prediction can be tuned, reducing the uncertainty due to hadron production in the target. In order to account for different beam conditions in each run period, the flux prediction is done separately for each run. Figure 4.3 shows the tuned flux prediction and the ratio of the tuned flux prediction to the nominal prediction for the dataset used in this analysis. The combined uncertainty on the ND280 prediction can be seen in Figure 4.4. The total uncertainty as a function of energy at SK is very similar to ND280, and can be found in [21].

Within the BANFF fit, the flux prediction is tuned by minimizing Equation 4.8 using a set of

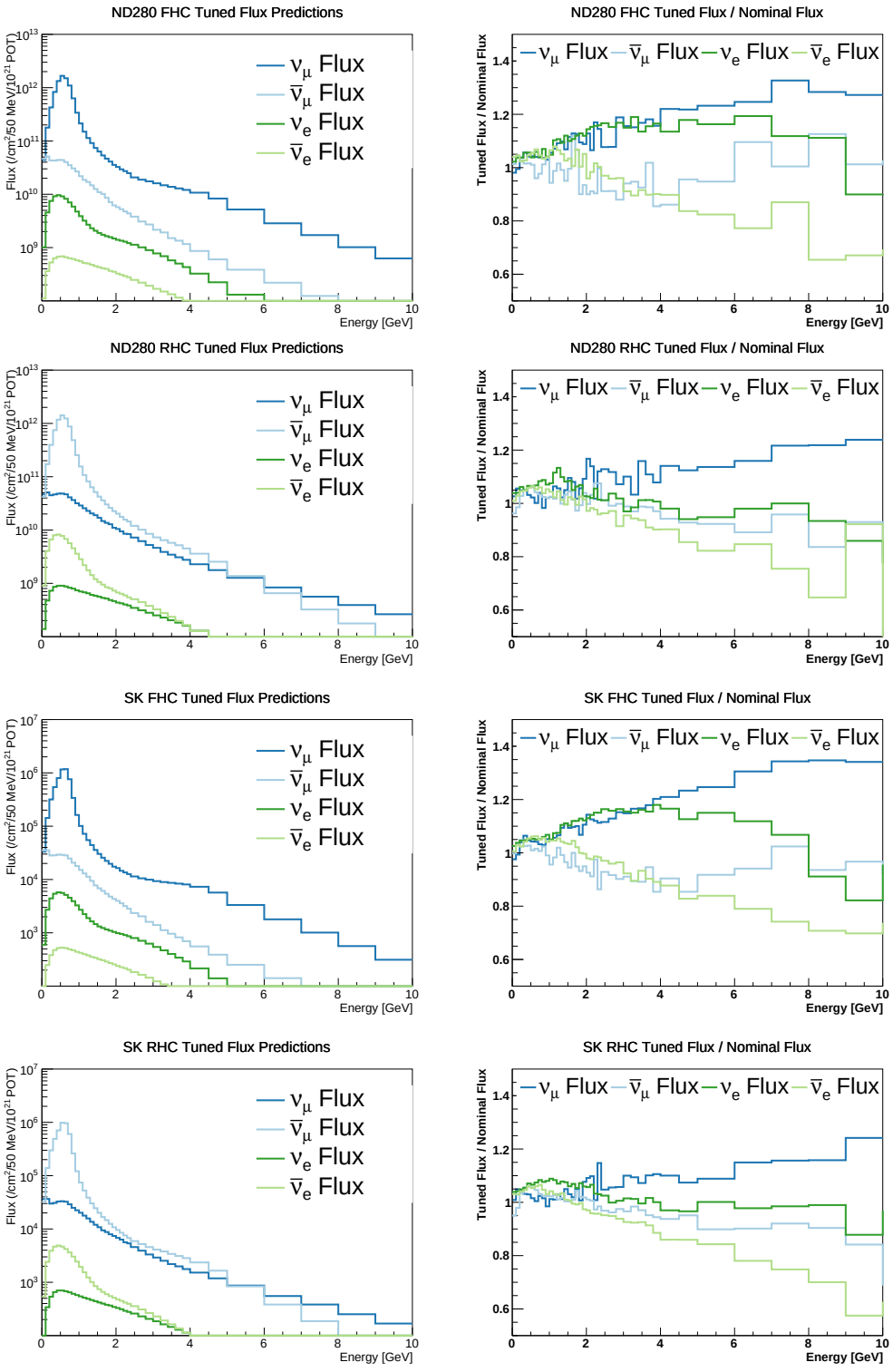

Figure 4.3: T2K tuned flux prediction (left) and ratio of the T2K tuned flux prediction to the nominal prediction (right) for ND280 and SK in both neutrino mode (FHC) and antineutrino mode (RHC).

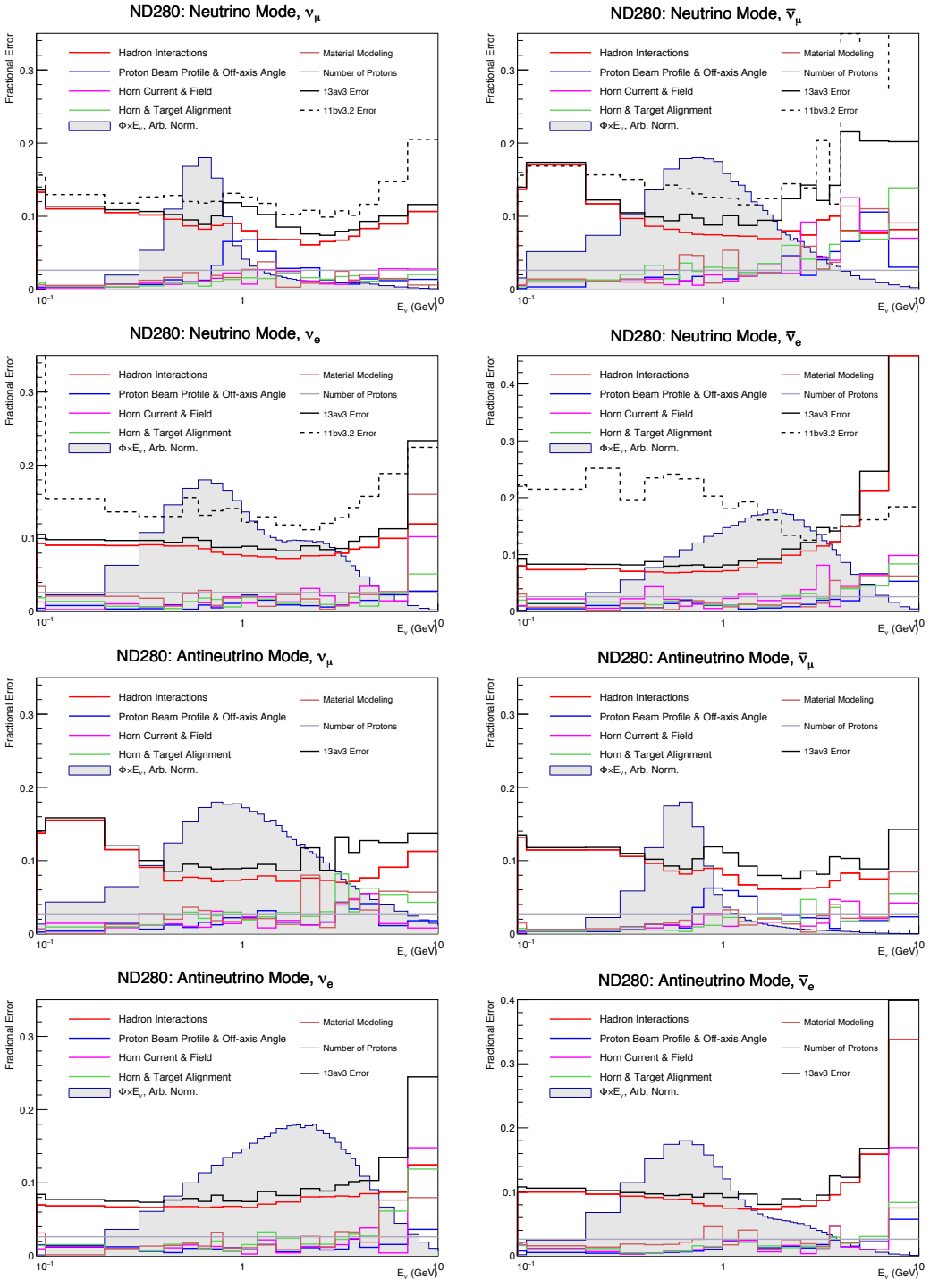

Figure 4.4: The total uncertainties on the ND280 flux prediction. The 13av3 uncertainty (solid black line) is the current version. The 11bv3.2 uncertainty (dashed black line) is an earlier version. Figure from [21].

nuisance parameters. These parameters correspond to bins of neutrino energy (in GeV) and depend on the beam mode, neutrino flavor, and detector. The bins are:

- ν_μ (ν-mode) / $\bar{\nu}_\mu$ ($\bar{\nu}$-mode): 0.0, 0.4, 0.5, 0.6, 0.7, 1.0, 1.5, 2.5, 3.5, 5.0, 7.0, 30.0
- $\bar{\nu}_\mu$ (ν-mode) / ν_μ ($\bar{\nu}$-mode): 0.0, 0.7, 1.0, 1.5, 2.5, 30.0
- ν_e (ν-mode) / $\bar{\nu}_e$ ($\bar{\nu}$-mode): 0.0, 0.5, 0.7, 0.8, 1.5, 2.5, 4.0, 30.0
- $\bar{\nu}_e$ (ν-mode) / ν_e ($\bar{\nu}$-mode): 0.0, 2.5, 30.0

This binning corresponds to 25 parameters in each beam mode, ranging from 0 – 30 GeV for the four relevant neutrino flavors. Using both beam modes for both ND280 and SK, a total of 100 parameters are included in the analysis. Each parameter is defined relative to the tuned flux prediction, so the nominal value is set at 1. The flux parameters have high correlations between the two detectors, the different energy bins, neutrino flavors, and beam modes. The correlation matrix for these parameters can be seen in Figure 4.5, with Table 4.3 describing how the parameters correspond to bin numbers.

4.3.2 Cross Section Parameters

The next set of nuisance parameters is related to how neutrino interactions are modeled. The determination of the oscillation parameters relies on correctly determining the neutrino energy spectrum. Because neutrinos are neutral, the energy of a neutrino must be calculated using the kinematic information of the outgoing particles and the conservation of energy. Theoretical models have been developed to aid in predicting the kinematics of the outgoing particles in various types of interactions. While these models are able to predict exactly what a detector should expect to see for a given interaction type, in reality, the effects of detector thresholds and final state interactions can alter what is observed.

Practically, neutrino interactions in the T2K detectors are simulated using the NEUT neutrino event generator [92], which uses neutrino cross section models to simulate different types of

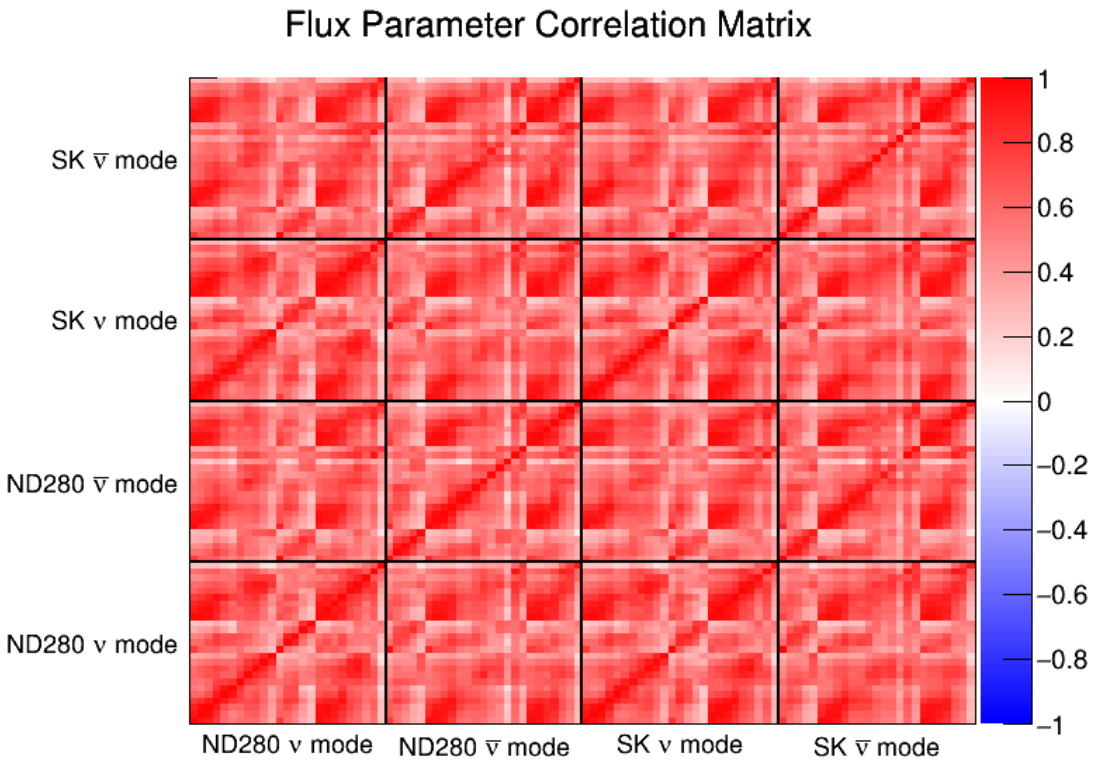

Figure 4.5: Correlation matrix for flux parameters used in the BANFF fit. The labels denote which detector and beam mode that region covers. Each bin in the matrix corresponds to an energy range given in the text.

interactions and their outgoing particles. The kinematic information from the outgoing particles in these simulated interactions can then be used to build a prediction for how many events of each interaction type should be seen in the near and far detectors for a given neutrino beam flux.

In the near detector fit, two methods are used to tune the NEUT cross section model prediction. First, a multiplicative factor can be applied to any events in a given interaction channel, such as all CCQE events or all neutrino events. This serves to increase or decrease the rate at which a given channel occurs, and is applied uniformly across neutrino energies and interaction channel observables. These multiplicative factors are referred to as *normalization parameters*. The neutral current parameters and charged current parameters not associated with CC0π or CC1π interactions are normalization parameters.

Second, parameters associated with how neutrino cross section are modeled are applied as

Detector	Beam Mode	Flavor	Bin Numbers
ND280	Neutrino	ν_μ	0 – 10
ND280	Neutrino	$\bar{\nu}_\mu$	11 – 15
ND280	Neutrino	ν_e	16 – 22
ND280	Neutrino	$\bar{\nu}_e$	23 – 24
ND280	Antineutrino	ν_μ	25 – 29
ND280	Antineutrino	$\bar{\nu}_\mu$	30 – 40
ND280	Antineutrino	ν_e	41 – 42
ND280	Antineutrino	$\bar{\nu}_e$	43 – 49
SK	Neutrino	ν_μ	50 – 60
SK	Neutrino	$\bar{\nu}_\mu$	61 – 65
SK	Neutrino	ν_e	66 – 72
SK	Neutrino	$\bar{\nu}_e$	73 – 74
SK	Antineutrino	ν_μ	75 – 79
SK	Antineutrino	$\bar{\nu}_\mu$	80 – 90
SK	Antineutrino	ν_e	91 – 92
SK	Antineutrino	$\bar{\nu}_e$	93 – 99

Table 4.3: Relation between the flux parameters and their bin number in the flux correlation matrix.

response parameters. Because these parameters are related to the underlying theoretical calculation of the neutrino cross section, they are more complicated than the normalization parameters. When changing these parameters, it is possible to significantly alter the kinematics of the event, and, in turn, how the events are distributed in the samples described in Chapter 5. The most accurate way to determine the effects of altering these parameters would be to rerun the entire analysis from event simulation in NEUT, to event reconstruction and selection, for each event at each step of the fit minimization. For obvious reasons, this is computationally unfeasible. Therefore, weights for each parameter are calculated for every event prior to the fit being run. By saving the precalculated weights as splines, the most computationally intensive part can be run prior to the fit and relevant weights can be interpolated during the minimization process. Many of the CC0π parameters, the CC1π parameters, the BeRPA parameters, and the FSI parameters are response parameters.

4.3.2.1 CC0πParameters

The CC0π parameterization, which describes events where only a muon is observed in the detector, can be organized into two groups of parameters. One group is related to the model of the nuclear medium, while the other describes interactions relevant to CC0π events. The nuclear medium in the CC0π parameterization is based on the relativistic Fermi gas (RFG) nuclear model, where the initial nucleons are considered to have a flat momentum distribution up to a maximum momentum, the so-called "Fermi momentum," p_F. Within the near detector fit, the Fermi momentum is treated as a variable parameter and, because it is dependent on the size of the nucleus, a separate parameter has been included in the fit for interactions occurring on carbon and oxygen.

The Local Fermi Gas (LFG) model is an alternative to the RFG nuclear model. Rather than treating the momentum distribution of the initial nucleon as flat, in a LFG model, effects due to the finite size of the nucleus are included. In this model, the momentum of the initial nucleon depends on its radial position. An additional uncertainty is included in the near detector fit due to differences in lepton kinematics between the NEUT event generator, which uses the RFG model, and the Nieves generator, which uses the LFG model [93]. Studies comparing the Nieves 1p1h model against the model used by T2K have shown that the choice of model can have a significant impact on the fitted parameter values at ND280 and in the oscillation analysis [94]. Unlike the other cross section uncertainties, this uncertainty is treated as an additional covariance in the observable normalization covariance matrix, described in Section 4.3.3.

The random phase approximation (RPA) is a non-perturbative method for describing the interactions and correlations of nucleons within the nucleus. Because of these interactions, the overall neutrino-nucleus cross section is modified and can be parameterized as a function of the transfer four-momentum, Q^2, which is constrained by pion-nucleus scattering data [24]. One method of parameterizing this modification uses the Bernstein polynomials of degree n [95], which form a basis for the power polynomials of order n, and are given by

$$B_{i,n}(x) = \binom{n}{i} x^i (1-x)^{n-i}, \tag{4.9}$$

where x runs from 0 to 1 and $\binom{n}{i}$ is a binomial coefficient.

Using these Bernstein polynomials, a response parameterization, called the BeRPA parameterization, is given by:

$$f(x) = \begin{cases} A(1-x')^3 + 3B(1-x')^2x' + 3p_1(1-x')x'^2 + Dx'^3, & x < 1.2 \\ 1 + p_2\exp(-E(x-U)), & x > 1.2 \end{cases} \tag{4.10}$$

where $x = Q^2$ and $x' = Q^2/1.2$ and p_1 and p_2 are defined as

$$p_1 = D + \frac{UE(D-1)}{3} \tag{4.11}$$

$$p_2 = D - 1. \tag{4.12}$$

CCQE events are the dominant type of interactions in the CC0π model, as well as being the primary interaction type for T2K. The cross section for these events can be parameterized using three nucleon form factors: the electric, magnetic, and axial form factors. The electric and magnetic form factors have been strongly constrained through electron-nucleon scattering [24], but the axial form factor, which is only found in neutrino-nucleon interactions, has not been as tightly constrained. The axial form factor is generally parameterized using the dipole form of:

$$F_A(Q^2) = \frac{g_A}{[1 + Q^2/(M_A^{QE})^2]^2}. \tag{4.13}$$

Here, g_A is the normalization for $Q^2 = 0$ and has been determined to be 1.2670 ± 0.0035 from neutron beta-decay.Within the near detector fit, M_A^{QE} is treated as an effective parameter to describe the nuclear effects of CCQE interactions[1].

In addition to CCQE interactions, the CC0π model includes multi-nucleon, or 2 particle – 2 hole (2p2h), interactions. Within 2p2h interactions, there are two main modes of interactions, plus an interference between the two. Meson exchange current interactions (MEC) events are those which Feynman diagrams include a Δ propagator and Δ pion-less decay, as seen in the lower portion

[1]It should be noted that, in the case of an antineutrino interaction with a hydrogen nucleus ($\bar{\nu} + p \rightarrow X$), M_A^{QE} is fixed at 1.03 GeV, which is based on results from bubble chamber data [24]. In all other cases, M_A^{QE} is free to move.

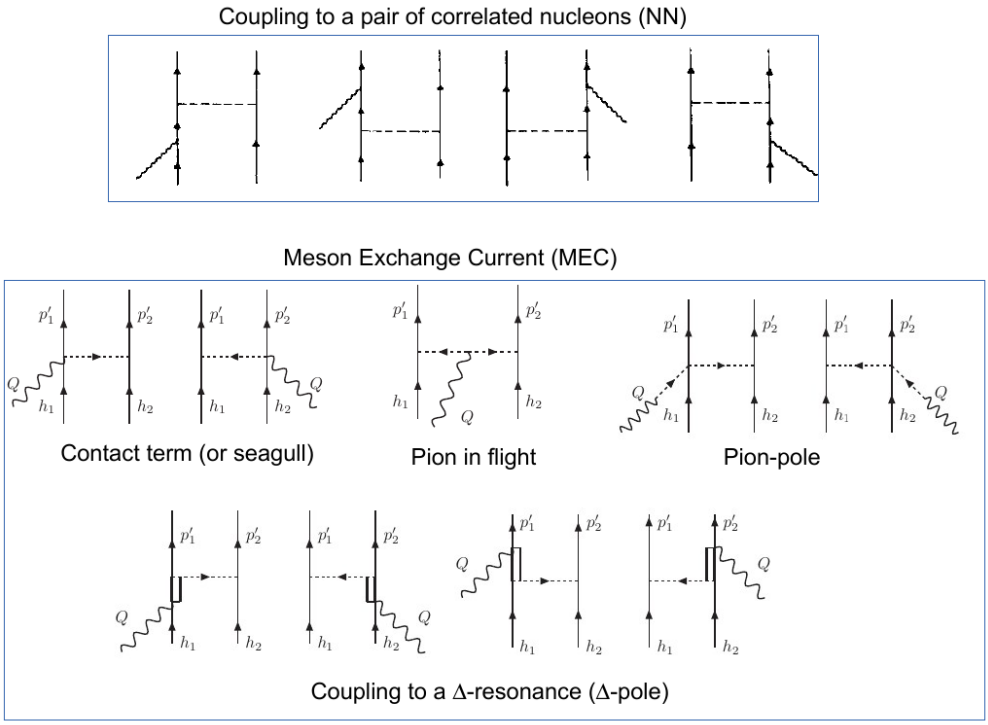

Figure 4.6: 2p2h diagrams. Single lines represent nucleons, double lines represent the Δ, dashed lines represent pions, and curly lines represent the W boson. Adapted from [22, 23].

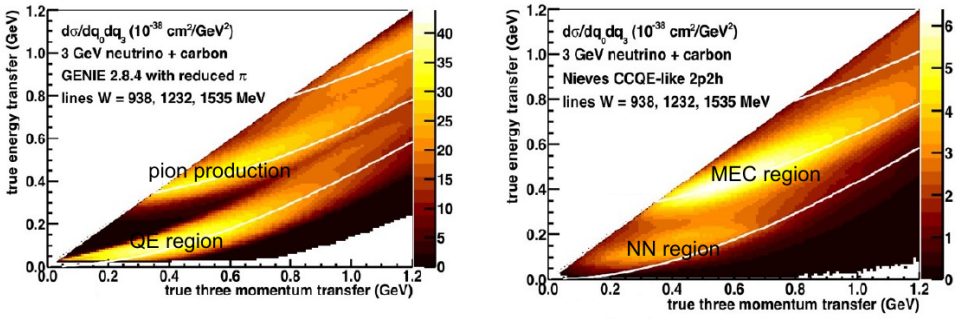

Figure 4.7: The total cross section (left) compared with the 2p2h cross section (right). Figure from [24].

of Figure 4.6. On the other hand, the other primary mode comes from nucleon-nucleon (NN) correlations, like those seen in the upper portion of Figure 4.6. When comparing the distributions of these two modes, a distinct shape difference is seen in the transfer momentum and energy cross section, as shown in Figure 4.7.

In NEUT, the Nieves model for np-nh interaction [93, 96] is included to model 2p2h interactions in the CC0π model. The model employed by the near detector fit uses five parameters to describe these interactions. Two normalization parameters are included to scale the 2p2h cross section for neutrinos and antineutrinos separately. Large uncertainties are applied to these parameters in order to cover differences in alternate models [25]. Because of the shape difference seen in the cross section, a shape parameter is included to shift events between the two extremes for interactions occurring on carbon and oxygen, separately. Finally, as the 2p2h model has been developed for isoscalar nuclei (like carbon and oxygen), a parameter is included to estimate the uncertainty in extrapolating the model from carbon to oxygen. This uncertainty is based on electron scattering measurements of neutron–neutron and neutron–proton pairs [97].

A summary of the CC0πparameters can be found in Table 4.4. Note, the BeRPA U parameter is fixed in the BANFF fit because it introduces complicated correlations between the parameters; therefore, it does not have an error listed.

Parameter	Prior Value	Prior Error	Type	Passed to SK
pF C (MeV)	217	31	Response	NO
pF O (MeV)	225	31	Response	YES
BeRPA A	0.59	0.118	Response	YES
BeRPA B	1.05	0.21	Response	YES
BeRPA D	1.13	0.1695	Response	YES
BeRPA E	0.88	0.352	Response	YES
BeRPA U	1.20	—	Response	YES
M_A^{QE} (GeV)	1.20	0.025	Response	YES
2p2h Norm ν	1.00	1.00	Norm	YES
2p2h Norm $\bar{\nu}$	1.00	1.00	Norm	YES
2p2h Norm C to O	1.00	0.20	Norm	YES
2p2h Shape C	0.00	1.00	Response	NO
2p2h Shape O	0.00	1.00	Response	YES

Table 4.4: CC0π parameters in the BANFF fit. Included in the table are the prior value and error, the type of parameter it is, and whether or not the final value is passed to SK or not.

4.3.2.2 CC Resonant Parameters

In the past, CC resonant interactions served as one of the primary backgrounds in the oscillation analysis. However, with the recent inclusion of the $1R_e$ CC1π sample, CC resonant interactions are now a signal interaction. In NEUT, the Rein-Sehgal model [98] is used to model CC resonant interactions. This model is parameterized by three parameters. The axial mass, M_A^{RES}, is the axial mass of CC resonant interactions, while the axial form factor, $C_A^5(Q^2 = 0)$, is the dominant axial form factor for resonant pion production. The isopin=$1/2$ background scales the non-resonant background for single pion processes, which is assumed to be made up entirely of $I = 1/2$ events in NEUT. A summary of the CC resonant parameters can be seen in Table 4.5.

Parameter	Prior Value	Prior Error	Type	Passed to SK
M_A^{RES}	1.07	0.15	Response	YES
Isoscalar Background	0.96	0.40	Response	YES
CA5	0.96	0.15	Response	YES

Table 4.5: CC resonant parameters in the BANFF fit. Included in the table are the prior value and error, the type of parameter it is, and whether or not the final value is passed to SK or not.

4.3.2.3 Other Charged Current Parameters

While CC0π and CC resonant interactions serve as the signal for T2K, interactions producing multiple pions (Nπ interactions), deep inelastic scattering (DIS), and CC coherent interactions serve as two of the background interactions. While the CC coherent cross section is much smaller than the CC resonant cross section, its signal in the detector can be confused for a CC resonant interaction. In order to account for this interaction, two parameters are included in the fit to cover CC coherent interactions on carbon and oxygen nuclei. The prior uncertainties for these parameters were determined using MINERνA data [99]. For DIS and Nπ interactions, only one parameter, called CC DIS, is currently used in the analysis. This parameter is based on results from MINOS [24] and is dependent on the energy of the interaction.

Two normalization parameters are included in the fit to account for potential differences in the ν_e/ν_μ and the $\bar{\nu}_e/\bar{\nu}_\mu$ cross section ratios [100]. These are included due to a number of differences arising in electron (anti)neutrino and muon (anti)neutrino interactions. Two of these differences include effects due to the mass of the outgoing lepton and radiative corrections. With regards to the former, effects of the nucleon form factors can become convoluted with the difference in the mass of the outgoing muon and electron. For the latter, radiative corrections are applied to both electrons and muons; however, because of the lighter mass of the electron, these corrections have a larger effect on electron neutrino and antineutrino interactions.

Additionally, a correction is applied due to the Coulomb field inside the nucleus. The so-called "Coulomb correction" decreases (increases) the momentum of the outgoing negatively (positively) charged lepton due to the electrostatic attraction (repulsion) of the remnant nucleus and depends on the charge distribution of the nucleus and the position of the interaction inside the nucleus [101]. This correction is not a parameter in and of itself, but it does shift the reconstructed momentum by a few MeV, which allows events to move bins, but they cannot move between samples. Related to the Coulomb corrections, a normalization parameter is applied to charged current neutrino and antineutrino events, separately. These parameters allow for scaling of the total cross section due to the effects of the Coulomb interaction.

A summary of these charged current parameters can be seen in Table 4.6.

Parameter	Prior Value	Prior Error	Type	Passed to SK
CC norm ν	1.00	0.020	Norm	YES
CC norm $\bar{\nu}$	1.00	0.010	Norm	YES
ν_e/ν_μ	1.00	0.028	Norm	YES
$\bar{\nu_e}/\bar{\nu_\mu}$	1.00	0.028	Norm	YES
CC DIS	0.00	0.40	Response	YES
CC Coherent C	1.00	0.30	Norm	NO
CC Coherent O	1.00	0.30	Norm	YES

Table 4.6: Other charged current parameters in the BANFF fit. Included in the table are the prior value and error, the type of parameter it is, and whether or not the final value is passed to SK or not.

4.3.2.4 Neutral Current Parameters

Neutral current events are a source of background contamination in the near and far detector samples. In the case of neutral current pion production event, low momentum pions can be incorrectly identified as muon candidates, which will contaminate the samples for CC0π events (described in Chapter 5). To account for these background events, four normalization parameters are included in the near detector fit. The NC coherent parameter applies a normalization to all neutral current coherent events. Similarly, the NC 1γ parameter applies a normalization factor to NC 1γ interactions, which are a background at SK. Finally, the NC other near and far parameters catch the rest of the neutral current interactions for ND280 and SK, respectively. A summary of the neutral current parameters can be seen in Table 4.7. It should be noted that the NC 1γ and the NC other far parameters are fixed in the near detector fit, as the near detector does not have sensitivity to these parameters. They are included in the near detector fit because the cross section parameterization for the far detector consists of those parameters which are passed to SK from the near detector fit.

Parameter	Prior Value	Prior Error	Type	Passed to SK
NC Coherent	1.00	0.30	Norm	YES
NC 1γ	2.00	2.00	Norm	YES
NC Other near	1.00	0.30	Norm	NO
NC Other far	1.00	0.30	Norm	YES

Table 4.7: Neutral current parameters in the BANFF fit. Included in the table are the prior value and error, the type of parameter it is, and whether or not the final value is passed to SK or not.

4.3.2.5 Final State Interactions

The final state interaction parameters control the transport of pions within the nucleus after a neutrino interaction occurs. These interactions are simulated as a cascade, where the pion is propagated through the nucleus step-wise, allowing for multiple interactions to occur before the particle exits the nuclear medium. FSI allow events to move between different topologies and for

the event kinematics to change. For example, if only one pion is observed from an event that produces multiple pions, then this event would be classified as a CC1π event topology, rather than a CCOther event topology.

Previously, six parameters were used to parameterize FSI. However, recent work [102], which used an improved fitting method to DUET data [103], has reduced the number of parameters to five. Furthermore, the final results of these parameters are now passed on to SK.

The FSI parameters are:

- **FSI inelastic scattering** has a final state pion of the same charge as the initial pion. Low and high energy events are treated as two separate parameters. In both cases, the parameters are applied to inelastic and elastic scattering processes, because the model on T2K does not differentiate between these [104].

- **FSI pion production** acts on high energy interactions which have two or more pions in the final state.

- **FSI pion absorption** applies to low energy events with no pions in the final state.

- **FSI charge exchange** acts on low energy events which have a single pion of the opposite charge from the initial pion ($\pi^+ \rightarrow \pi^-$ or $\pi^- \rightarrow \pi^+$) or a π^0. Previously, there was a high energy version of this parameter. However, the recent fits showed little response to this parameter, so it is not included in the parameterization.

A summary of the FSI parameters can be found in Table 4.8. The correlation matrix for the

Parameter	Input Value	Input Error	Type	Passed to SK
Quasi-Elastic Low Energy	1.069	0.313	Response	YES
Quasi-Elastic High Energy	1.824	0.859	Response	YES
Pion Production	1.002	1.101	Response	YES
Pion Absorption	1.404	0.432	Response	YES
Charge Exchange Low Energy	0.697	0.305	Response	YES

Table 4.8: FSI parameters in the BANFF fit. Included in the table are the prior value and error, the type of parameter it is, and whether or not the final value is passed to SK or not.

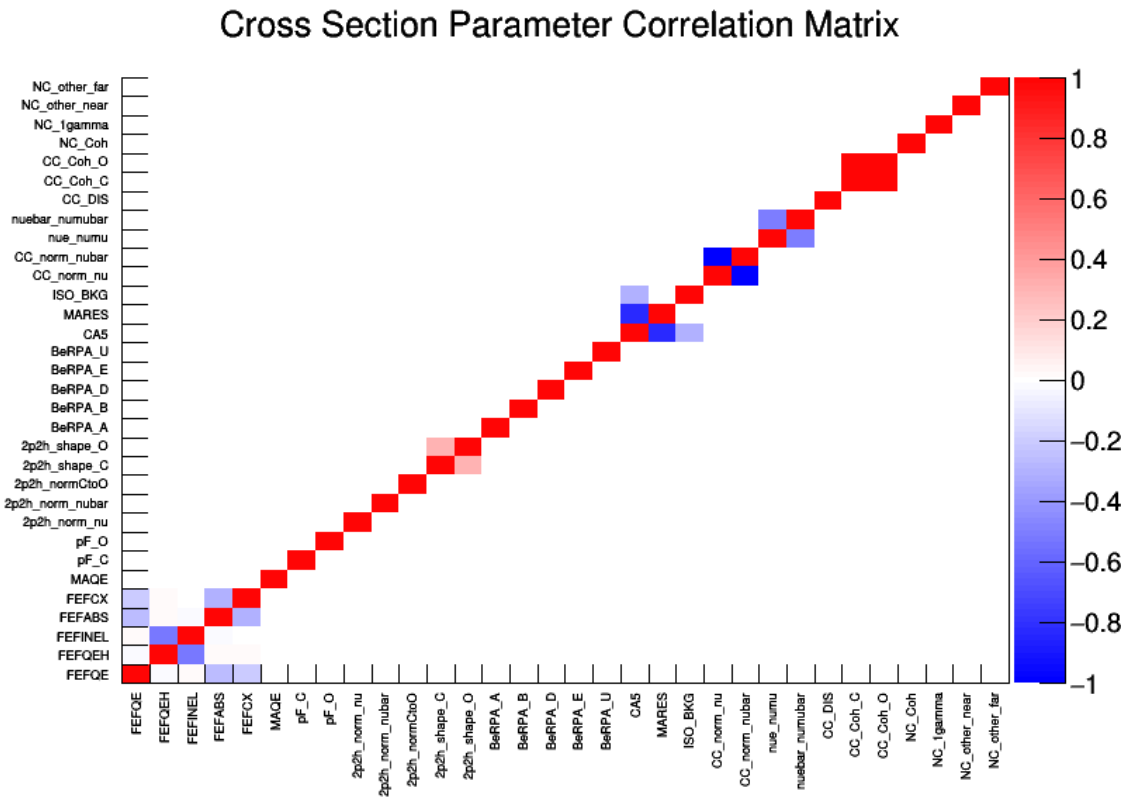

Figure 4.8: Correlations between the cross section parameters.

parameters described in the Sections 4.3.2.1 – 4.3.2.5 can be seen in Figure 4.8.

4.3.3 The Observable Normalization Parameters

The complex structure of ND280 requires a complicated set of detector systematic parameters, discussed in detail in Chapter 6, to be included in the near detector fit. However, including these parameters in the fit is computationally expensive, as they have to be recalculated for every event at each step in the minimization process. In order to reduce the computational expense, the effect of the detector systematic uncertainties are encapsulated in a set of normalization parameters, described in more detail in Section 6.4, in the near detector fit. These parameters are called the observable normalization parameters and they describe the effects of the detector systematic uncertainties of the event rates for a $p - \cos\theta$ bin in each sample. In addition to the parameters, a covariance matrix describing the uncertainties and correlations of the parameters are included in the fit.

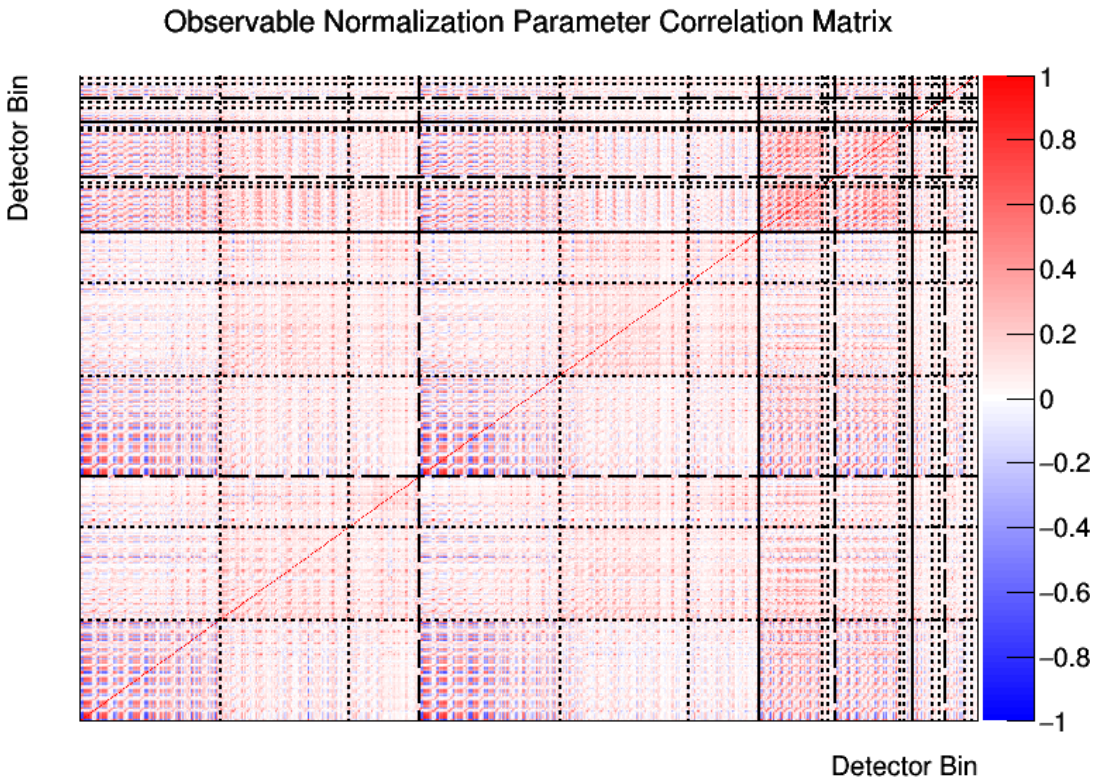

Figure 4.9: The correlation matrix for the observable normalization parameters. The short dashed lines differentiate between the CC0π, CC1π, and CCOther samples, while the long dashed lines separate FGD1 and FGD2 samples. The solid black lines separate the FHC MultiPi, RHC $\bar{\nu}$ MultiPi, and RHC ν MultiPi samples. Within each sample, the parameters are ordered from backward going to forward going angular bins. Each complete set of angular bins share a common momentum bin, which are ordered in from lowest to highest momentum.

As with the flux and cross section parameters, the observable normalization parameters and their covariance (Figure 4.9) are assumed to behave in a Gaussian manner and are included in the likelihood given in Equation 4.8. Within the fit, these parameters are allowed to correlate with the flux and cross section parameters. As the observable normalization parameters provide constraints on the near detector event rates, they are not used in the oscillation fits at SK, where a set of detector systematic parameters for the far detector are used instead.

CHAPTER 5

THE NEAR DETECTOR SELECTIONS

The interactions that are most relevant to the near detector fit are charged current quasi-elastic (CCQE), charged current (CC) resonant pion production, and deep inelastic scattering and multiple pion production (DIS+Nπ).

The ability to select these types of events at ND280 is, therefore, of utmost importance. Event selection at ND280 relies on three time projection chambers (TPCs) and two fine grain detectors (FGDs). The FGDs serve as the target volume for the near detector, with FGD2 providing an oxygen target similar to Super-Kamiokande (SK). In addition, the TPCs allow for particle identification and momentum. This chapter will focus on how events are selected using the FGDs and TPCs to create samples relating the three interactions mentioned previously to what is seen in the detector.

5.1 Selection Considerations

Because the selections exist to help constrain the flux and cross section uncertainties, the samples must be sensitive to the neutrino beam flux and the neutrino cross section. Therefore, when designing the sample selections, there are a number of considerations that must be taken into account.

With regard to the neutrino beam flux, the flavor composition of neutrinos in neutrino and antineutrino beam modes are highly correlated (see Section 4.3.1) as well as between the various neutrino flavors and energies. Because of this large amount of correlation, any large sample of neutrino or antineutrino interactions with a high purity is enough to constrain the uncertainties on the neutrino flux parameters.

The primary goal of the near detector fit is to constrain the uncertainty on CC0π events, which encompasses events with no observed pions, and CC resonant interactions, as these are the signal processes. Secondary to that, it must also decrease uncertainties on the primary backgrounds, CC coherent and DIS+Nπ interactions. While neutral current (NC) interactions also occur in ND280,

they do not provide the same level of constraint provided by charged current events. Therefore, by focusing on CC interactions, it becomes much easier to constrain signal and background events in the near detector.

Additionally, the samples must take into account whether the data is collected when the beam is in neutrino or antineutrino beam mode. Because the beam utilizes protons colliding with a target consisting of protons and neutrons, there is a preference for positive pions (π^+) to be created over negative pions (π^-). Because of this preference, there is higher ν_μ flux in neutrino mode than $\bar{\nu}_\mu$ flux in antineutrino mode. This also means there exists a significant amount of higher energy π^+which cannot be bent out of the beam in antineutrino mode. Therefore, the amount of neutrinos is much higher in antineutrino mode than the number of antineutrinos in neutrino mode. Neutrinos also have a larger cross section than antineutrinos for matter interactions, as can be seen in Figure 2.2. Because antineutrinos interact less often in matter, these events are suppressed when compared to neutrino events.

Because of these two effects, the neutrino flux in antineutrino beam mode provides a significant background, whereas the antineutrino flux in neutrino beam mode is negligible. Furthermore, the background neutrino flux in antineutrino mode is an irreducible background at SK because the lepton charge is unable to be determined in charged current interactions. Therefore, it is useful to create a set of samples which separates neutrino and antineutrino events in antineutrino mode, while the samples for neutrino mode only needs to incorporate neutrino events.

5.2 Data and Monte Carlo Inputs to the Selections

The data collected at T2K is divided by run period, which corresponds to about a year of running the detector. These can be further categorized depending on the detector configuration, such as whether the PØD water bags were filled with water or air or based on the magnet current. For this analysis, Runs 2 – 8 were used, which corresponds to data taken between November 2010 and April 2017. The data from Run 1 was not used because of calibration issues in the detector as well as the top tracker missing from the ECal. Because the ECal was originally meant to be used in

the selection, it could pose difficulties in using this data. As Run 1 represents only a small amount of statistics when compared with later runs, it is reasonable to leave it out because it should have little impact on the results. While additional data has been taken since April 2017, it has not been fully processed and, therefore, was not included in this analysis.

The ND280 Monte Carlo is generated using the NEUT neutrino event generator to simulate neutrino interactions, which are propagated through the ND280 geometry using GEANT4 [105]. The simulation is run separately for each run period and configuration of the PØD water bags, as the interaction rate increases when the bags are filled with water. For the Monte Carlo, two types of events are generated: neutrino interactions occurring in the magnet volume and sand muon events. Sand muon events correspond to events occurring in the sand surrounding the detector and represent the outside background events in the data. These are described in more detail in Section 6.1.

Table 5.1 shows whether the run is in neutrino or antineutrino mode and the amount of protons on target (POT) for each run.

Run Period	Beam Mode	Data POT ($\times 10^{20}$)	MC POT ($\times 10^{21}$)
Run 2a, Water Out	Neutrino	0.359	0.924
Run 2w, Water In	Neutrino	0.434	1.203
Run 3b, Water Out	Neutrino	0.217	0.448
Run 3c, Water Out	Neutrino	1.364	2.632
Run 4a, Water Out	Neutrino	1.783	3.500
Run 5c, Water In	Antineutrino	0.435	2.296
Run 6b, Water Out	Antineutrino	1.273	1.417
Run 6c, Water Out	Antineutrino	0.508	0.528
Run 6d, Water Out	Antineutrino	0.775	0.688
Run 6e, Water Out	Antineutrino	0.851	0.859
Run 7c, Water In	Antineutrino	2.437	3.371
Run 8a, Water Out	Neutrino	4.149	3.631
Run 8w, Water In	Neutrino	1.581	2.641

Table 5.1: The data and Monte Carlo POT, as well as the beam mode, for each run period used in the analysis.

5.3 Description of Selections

The first step in the selections in the near detector is to create a sample that includes the full set of neutrino and antineutrino events, called the CC inclusive sample. This cut removes any events identified as non-CC inclusive, such as neutral current events. Then, the remaining events are categorized by final event topology, which is defined as the set of particles leaving the nucleus. Because the detector is only able to reconstruct the particles leaving the nucleus, final event topology is chosen instead of the type of interaction.

Final event topologies correspond to the three main interactions seen at ND280 and SK. For CCQE events, there are only two outgoing charged particles, a proton and a muon. This makes it rather simple to look for this topology. In practice, it also tends to be even more simple because the outgoing proton tends to not be visible due to detector threshold effects. The event topology associated with CCQE events is CC0π, where one charged lepton track and no secondary pions are visible in the detector. The two other interactions, CC resonant and DIS+Nπ, also have their own topologies, CC1π and CCOther, respectively, and will be described in more detail in Section 5.3.1. These topologies are similar to what is seen in the far detector and are comparable to the samples used by SK, as described in Section 4.1.2.

In order to be considered an event, there must be a muon-like track which starts in the fiducial volume of either FGD1 or FGD2 and then passes into a neighboring TPC. Therefore, the quality of the selection relies on correctly reconstructing the direction and vertex position of each event in the near detector. Each selection takes into account the target FGD, the beam mode, and whether the muon is positively or negatively charged. With this in mind, the cuts used for neutrino mode and antineutrino mode may be different. However, each selection uses a similar cut flow for the CC inclusive selection and a similar structure for dividing the CC inclusive sample into topological samples.

Because of the large neutrino background in the antineutrino beam mode, there are two CC inclusive selections in antineutrino mode, one for $\bar{\nu}_\mu$ and one for the ν_μ background. On the other hand, there is only one CC inclusive selection performed for neutrino mode. The neutrino mode

(also known as forward horn current, or FHC) CC inclusive selection is then separated into CC0π, CC1π, and CCOther samples. Previously, the antineutrino mode (also called reverse horn current, or RHC) CC inclusive selections were separated into 1-track and N-tracks samples. This was due to difficulty separating non-CC0π topologies in the reconstruction and will be discussed in Section 5.3.3.2. Table 5.2 shows the breakdown of selections under this paradigm. Recently, the reconstruction has improved such that non-CC0π topologies can be distinguished Therefore, the RHC CC inclusive selection is now subdivided into CC0π, CC1π, and CCOther samples, like the FHC CC inclusive selection. Table 5.3 shows how the events are funneled now. The exact cuts for each selection are described in the following sections. The number of selected and predicted

All Reconstructed Events		
⇙	⇓	⇘
FHC ν_μ CC Inclusive	RHC $\bar{\nu}_\mu$ CC Inclusive	RHC ν_μ CC Inclusive
⇓	⇓	⇓
CC0π	CC 1-track	CC 1-track
CC1π	CC N-tracks	CC N-tracks
CCOther		

Table 5.2: Breakdown of reconstructed events into samples under the previous paradigm.

All Reconstructed Events		
⇙	⇓	⇘
FHC ν_μ CC Inclusive	RHC $\bar{\nu}_\mu$ CC Inclusive	RHC ν_μ CC Inclusive
⇓	⇓	⇓
CC0π	CC0π	CC0π
CC1π	CC1π	CC1π
CCOther	CCOther	CCOther

Table 5.3: Breakdown of reconstructed events into samples under the new paradigm.

events in each sample can be seen in Tables 5.4 and 5.5 for the previous antineutrino beam mode selections and the new selections, respectively.

Sample	Data	ND280 Prediction
FGD1 FHC ν_μ CC Inclusive	42,205	40,874.71
FGD1 FHC ν_μ CC0π	28,671	27,475
FGD1 FHC ν_μ CC1π	6,638	7,106.14
FGD1 FHC ν_μ CCOther	6,896	6,293.57
FGD1 RHC $\bar{\nu}_\mu$ CC Inclusive	7,926	7,875.1
FGD1 RHC $\bar{\nu}_\mu$ 1-Track	6,159	6,135.82
FGD1 RHC $\bar{\nu}_\mu$ N-Tracks	1,767	1,739.28
FGD1 RHC ν_μ CC Inclusive	4,437	4,145.47
FGD1 RHC ν_μ 1-Track	2,239	2,076.37
FGD1 RHC ν_μ N-Tracks	2,198	2,069.1

Sample	Data	ND280 Prediction
FGD2 FHC ν_μ CC Inclusive	40,121	37,867.46
FGD2 FHC ν_μ CC0π	28,444	26,826.1
FGD2 FHC ν_μ CC1π	5,149	5,498.52
FGD2 FHC ν_μ CCOther	6,528	5,542.84
FGD2 RHC $\bar{\nu}_\mu$ CC Inclusive	7,872	7,601.02
FGD2 RHC $\bar{\nu}_\mu$ 1-Track	6,174	5,934.79
FGD2 RHC $\bar{\nu}_\mu$ N-Tracks	1,698	1,666.23
FGD2 RHC ν_μ CC Inclusive	4,160	3,895.55
FGD2 RHC ν_μ 1-Track	2,099	1,970.47
FGD2 RHC ν_μ N-Tracks	2,061	1,925.08

Table 5.4: Observed and predicted event rates for the previous ND280 sample set. The predicted event rates are Monte Carlo events weighted by POT, flux, detector, and cross section weights. The left column shows the rates for FGD1, while the right column shows FGD2.

Sample	Data	ND280 Prediction
FGD1 FHC ν_μ CC Inclusive	42,405	40,821.52
FGD1 FHC ν_μ CC0π	28,671	27,429.5
FGD1 FHC ν_μ CC1π	6,638	7,095.14
FGD1 FHC ν_μ CCOther	6,896	6,296.88
FGD1 RHC $\bar{\nu}_\mu$ CC Inclusive	8,005	7,839.886
FGD1 RHC $\bar{\nu}_\mu$ CC0π	6,368	6,245.19
FGD1 RHC $\bar{\nu}_\mu$ CC1π	535	542.636
FGD1 RHC $\bar{\nu}_\mu$ CCOther	1,102	1,052.06
FGD1 RHC ν_μ CC Inclusive	4,569	4,264.058
FGD1 RHC ν_μ CC0π	2,707	2,547.87
FGD1 RHC ν_μ CC1π	847	875.593
FGD1 RHC ν_μ CCOther	1,015	840.595

Sample	Data	ND280 Prediction
FGD2 FHC ν_μ CC Inclusive	40,121	37,810.02
FGD2 FHC ν_μ CC0π	28,444	26,772
FGD2 FHC ν_μ CC1π	5,149	5,493.58
FGD2 FHC ν_μ CCOther	6,528	5,544.44
FGD2 RHC $\bar{\nu}_\mu$ CC Inclusive	7,948	7,630.104
FGD2 RHC $\bar{\nu}_\mu$ CC0π	6,451	6,211.62
FGD2 RHC $\bar{\nu}_\mu$ CC1π	465	486.26
FGD2 RHC $\bar{\nu}_\mu$ CCOther	1,032	932.224
FGD2 RHC ν_μ CC Inclusive	4,273	4,030.805
FGD2 RHC ν_μ CC0π	2,648	2,565.66
FGD2 RHC ν_μ CC1π	693	675.982
FGD2 RHC ν_μ CCOther	932	789.163

Table 5.5: Observed and predicted event rates for the new ND280 sample set. The predicted event rates are Monte Carlo events weighted by POT, flux, detector, and cross section weights. The left column shows the rates for FGD1, while the right column shows FGD2.

5.3.1 Forward Horn Current MultiPi Selections

5.3.1.1 Charged Current Inclusive Selection

The first two cuts for the CC inclusive selection are:

- **Event Quality:** Events must have the full spill with all ND280 subdetectors in good working order (the process for determining the working condition of each detector is described in [106]). Furthermore, the event must occur within the time window for each proton bunch in

the neutrino beam. In order to avoid event pileup, events which fall in the same spill, but different bunches, are treated as independent events. This cut ensures the beam was on and running properly and the ND280 subdetectors were all working correctly. It should be noted that this cut is for data events, since it is assumed the MC events have good beam and data quality.

- **Total Multiplicity Cut:** This cut requires that an event has at least one reconstructed track that crosses a TPC. This eliminates any triggered events that have little or no reconstructable information.

These first two cuts are the same for all CC inclusive selections. The cut flow for the rest of the cuts, described below, is also the same for each of the CC inclusive selections.

- **Fiducial Cut:** The fiducial cut requires there to be at least one reconstructed track in the fiducial volume of FGD1 or FGD2. Furthermore, it requires that there be at least one track with portions in FGD1 (or FGD2) and a TPC, with the vertex of the track starting inside the FGD's fiducial volume. The fiducial volumes are:
  - $|x| < 874.51$ mm, $-819.51 < y < 929.51$ mm, $136.875 < z < 446.955$ mm for FGD1,
  - $|x| < 874.51$ mm, $-819.51 < y < 929.51$ mm, $1481.45 < z < 1807.05$ mm for FGD2.

  Cuts in the x and y directions remove interactions which have a vertex that is at least 5 bars from the XY module in the FGD. The z cut removes the most upstream XY module, but keeps the remaining XY modules. The final part of this cut removes short tracks, which makes the TPC reconstruction less reliable.

- **Upstream Background Veto:** The upstream veto cut is to eliminate reconstruction failures that lead to a muon track starting in one of the FGD fiducial volumes, even though the real muon interacted further upstream. By way of example, a muon that originated in the PØD that underwent a large scatter in FGD1 may be reconstructed as two tracks, rather than one. These events are excluded by cutting events where the second highest momentum track

starts 150 mm upstream of the muon track. Furthermore, in the case of FGD2, the event can also be vetoed if the secondary track starts in the FGD1 fiducial volume.

- **Broken Track Cut:** The broken track cut was created to eliminate events with incorrectly reconstructed tracks, where the reconstruction procedure breaks the muon candidate track into two components. Typically, the first track is fully contained in the FGD and the second track begins in the last few layers of the FGD and passes into the TPC. In this case, the second track would be considered the muon candidate, rather than the first track. Therefore, to reject these types of events, if the event has at least one FGD-only track, then the start position of the muon candidate track must be less than 425 mm away from the FGD upstream edge.

- **Muon Particle Identification Cut:** Any events that have passed the above cuts, have the highest momentum track identified as a negative particle, originates inside an FGD's fiducial volume, and crosses a TPC is considered the muon candidate. The particle identification (PID) process for this track is based on the dE/dx measurement in the TPC and compares the energy deposited in the TPC to the expected energy deposit assuming a certain particle type, either muon, electron, or proton. From this information, pulls and discrimination functions are calculated.

  First, electrons are rejected by enforcing

$$\frac{L_\mu + L_\pi}{1 - L_P} > 0.8 \tag{5.1}$$

  and is only applied for a momentum less than 500 MeV/c. The next cut removes the remaining protons and pions by constraining

$$L_\mu > 0.5. \tag{5.2}$$

  In Equations 5.1 and 5.2, L is defined as

$$L_i = \frac{e^{-Pull_i^2}}{\sum_l e^{-Pull_l^2}}, \tag{5.3}$$

where $Pull$ is

$$Pull_i = \frac{dE/dx_{measured} - dE/dx_{expected,i}}{\sigma_{(dE/dx_{measured} - dE/dx_{expected,i})}}. \quad (5.4)$$

In order to break the CC inclusive sample into the three subsamples, pion information from the TPCs and FGDs is used. This breakdown will be discussed in the next section.

5.3.1.2 Selections for MultiPi Topologies

Once events have been selected into the CC inclusive sample and are ready to be divided into subsamples, no more events are cut. This is because all events that have made it into the CC inclusive selection should have one of the aforementioned topologies, CC0π, CC1π, or CCOther. In order to break down the selected events into topological samples, information about secondary tracks and the identification of pions in the FGDs and TPCs is used.

The three topological samples are defined as follows:

- **The CC0π Sample** has no observed secondary pions. This sample has no TPC-identified pions, electrons or positrons as defined by the TPC PID, and no Michel electrons or charged pions found in the FGD.

- **The CC1π Sample** has one negative muon track, one positively charged reconstructed pion, and no other pions selected. In order to be selected into this sample, it is required that there be only one reconstructed Michel electron in the FGD and no pions in the TPC or one positive pion in the TPC or FGD and no reconstructed Michel electrons. Furthermore, events which have a reconstructed negative pion or an electron or positron (which signals the decay of a π^0) in the TPC are rejected.

- **The CCOther Sample** contains the rest of the CC inclusive events that did not meet the criteria to fall into one of the other samples. This means that events with a single negative muon and either multiple positive pion tracks or at least one negative or neutral pion. Additionally, any events which include other particles, including kaons or etas, fall into this sample.

The three cuts used to separate these samples are the TPC secondary track PID cut, the FGD-only reconstructed track cut, and the Michel electron cut. Each of these cuts is similar between FGD1 and FGD2, with slight modifications for FGD2, as needed. Within the BANFF fit, the $p - \cos\theta$ binnings for these samples are:

- **CC0π fit bin edges:**

  p [MeV/c]: 0, 200, 300, 400, 450, 500, 550, 600, 650, 700, 750, 800, 850, 900, 950, 1000, 1050, 1100, 1200, 1300, 1400, 1500, 1600, 1700, 1800, 2000, 2500, 3000, 5000, 30000

  $\cos\theta$: -1.0, 0.5, 0.6, 0.7, 0.76, 0.78, 0.8, 0.83, 0.85, 0.88, 0.89, 0.9, 0.91, 0.92, 0.925, 0.93, 0.935, 0.94, 0.945, 0.95, 0.955, 0.96, 0.965, 0.97, 0.975, 0.98, 0.985, 0.99, 0.995, 1.0

- **CC1π fit bin edges:**

  p [MeV/c]: 0, 300, 350, 400, 500, 600, 650, 700, 750, 800, 900, 1000, 1100, 1200, 1500, 2000, 3000, 5000, 30000

  $\cos\theta$: -1.0, 0.6, 0.7, 0.8, 0.85, 0.88, 0.9, 0.92, 0.93, 0.94, 0.95, 0.96, 0.97, 0.98, 0.99, 0.995, 1.0

- **CCOther fit bin edges:**

  p [MeV/c]: 0, 300, 400, 500, 600, 650, 700, 750, 800, 900, 1000, 1100, 1250, 1500, 1750, 2000, 3000, 5000, 30000

  $\cos\theta$: -1.0, 0.6, 0.7, 0.76, 0.8, 0.85, 0.88, 0.89, 0.9, 0.91, 0.92, 0.93, 0.94, 0.95, 0.96, 0.97, 0.98, 0.99, 0.995, 1.0

The binning for FGD1 and FGD2 is the same. These binnings are chosen such that there is at least one data event per bin. Furthermore, the binning is finer around the peak kinematic regions to utilize information about the shape of the distribution within the BANFF fit.

- **The TPC Secondary Track PID Cut:** In order to determine the presence of pions in the TPC, the pulls and likelihoods from the measured dE/dx, given by Equations 5.3 and 5.4, are used. However, instead of using the primary track, the relevant tracks are now the secondary tracks in the event. These secondary tracks must begin in the same FGD fiducial volume as the muon track and have a matching TPC segment. For pion track cuts, the pion, positron, and proton candidates are considered for positive tracks and the pion and electron are considered for negative tracks.

  In order to identify a charged pion, a cut is set such that any secondary FGD-TPC track is considered to be a pion candidate if

  $$\frac{L_\mu + L_\pi}{1 - L_p} > 0.8, \tag{5.5}$$

  if the momentum is less than 500 MeV/c. Otherwise, the track is a pion if

  $$L_\pi > 0.3. \tag{5.6}$$

- **The FGD-only Reconstructed Track Cut:** For tracks that both start and end in the same FGD as the muon candidate originates, a cut is placed to identify these tracks as secondary π^+'s. Instead of using the general FGD fiducial volume, this cut uses a fiducial volume defined by

  - $-887 < x < 888$ mm (FGD1) or $-843 < x < 848$ mm (FGD2),
  - $-834 < y < 942$ mm (FGD1) or $-820 < y < 938$ mm (FGD2),
  - a z-position that falls between the first and last active layers of the corresponding FGD.

  In order to be considered for the FGD-only reconstructed track cut, the entire track under consideration must fall within this volume. Furthermore, the track must occur in the same time bunch as the muon candidate. In order to determine the PID, a pull can be defined using the energy deposited as a function of the track length, which will allow for the selection of the most probable particle for the track. A positive pion is defined as having an FGD-only

track with $|\cos\theta| > 0.3$, which is the region that has sufficient reconstruction efficiency, and having a pion pull between -2 and 2.5.

- **The Michel Electron Cut:** When pions without enough energy to reach the neighboring TPC decay, there is the potential to contaminate the CC0π sample. In order to reduce this contamination, an additional cut using delayed activity from Michel electrons can be used. Michel electrons originate from pion decay and can signal low momentum pions that were not identified by the FGD-only reconstructed track cut.

  Delayed activity is defined as detector activity that occurs more than 100 ns after the initial neutrino interaction and is used to identify Michel electrons. In general, the majority of events do not have any delayed activity, as seen in Figure 5.1. The signal for the Michel electron must occur outside the beam bunch window, because there is not a way to distinguish between activity due to Michel electrons and activity due to the presence of the beam. A Michel electron hit cluster is required to have at least 7 hits in FGD1 and 6 hits in FGD2 to be defined as a Michel electron. Figure 5.1 shows that the majority of events with one reconstructed Michel electron fall in the CC1π sample, which generally are the product of CC resonant interactions.

The momentum and $\cos\theta$ distributions for FGD1 can be seen in Figure 5.2, while the corresponding efficiency and purity plots are found in 5.3 and 5.4. Plots for FGD1 can be found in Figures C.1 – C.3 of Appendix C.

5.3.2 Reverse Horn Current MultiTrack Selections

Previously, the reverse horn current CC inclusive selection was divided into 1-track and N-tracks (the Multiple Track, or MultiTrack) samples because of early difficulties reconstructing secondary tracks in the antineutrino beam mode. However, the current process is to divide the reverse horn current CC inclusive sample into CC0π, CC1π, and CCOther samples (Multiple Pion, or MultiPi).

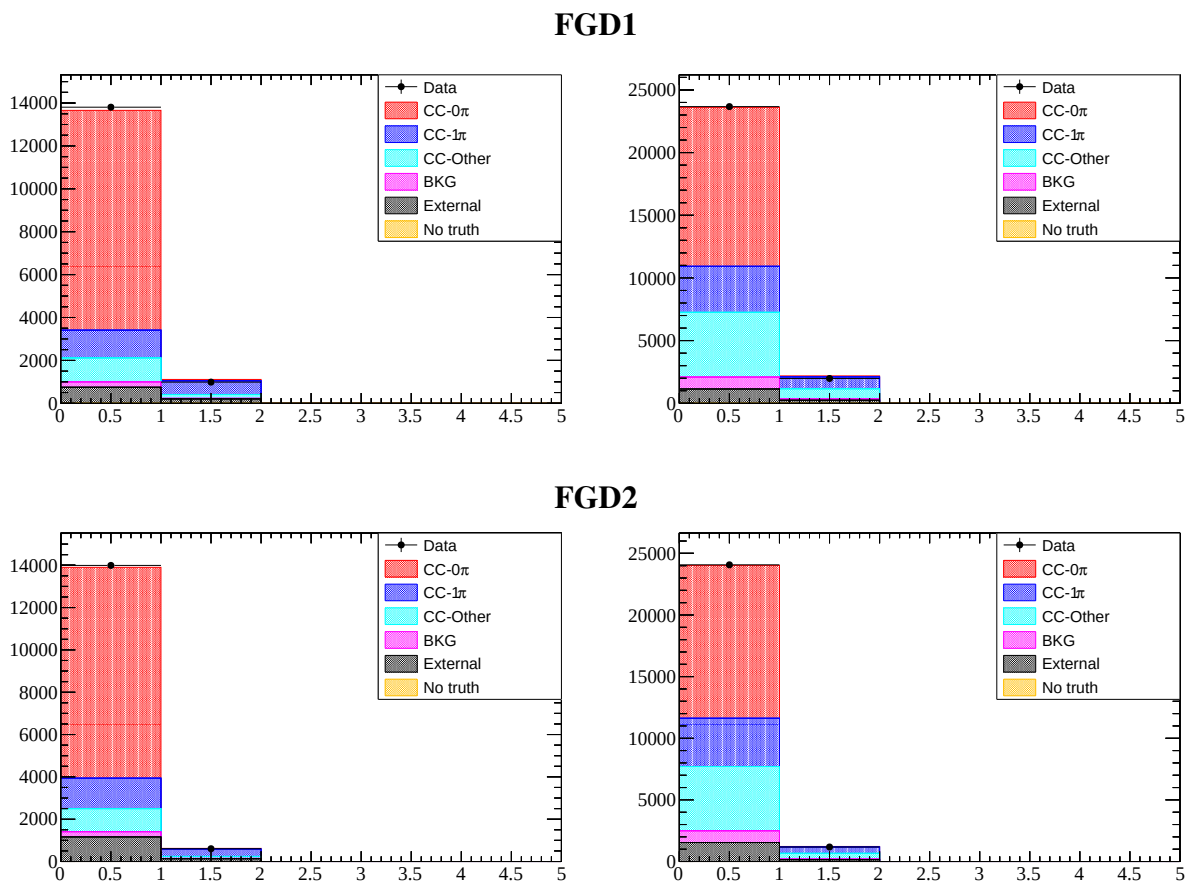

Figure 5.1: Distribution of the number of Michel electrons in FGD1 (top) and FGD2 (bottom) categorized by different interaction topologies. The left plot in each pair shows the distribution when no secondary tracks are seen in the TPC, while the right plot shows the CC inclusive selection with no such constraints. Figure from [7].

This section will provide an overview of the selection process for the previous selections for both $\bar{\nu}_\mu$ and ν_μ, while the new selections will be discussed in Section 5.3.3.

5.3.2.1 Charged Current Inclusive Selection

In general, both the RHC $\bar{\nu}_\mu$ and RHC ν_μ CC inclusive selections use the same initial quality cuts as described in Section 5.3.1.1. The two main differences between the FHC CC inclusive selection and these is the selection of the muon candidate track and the muon PID cut. With regards to the muon candidate track, the RHC $\bar{\nu}_\mu$ selection requires the highest momentum track be positive, because

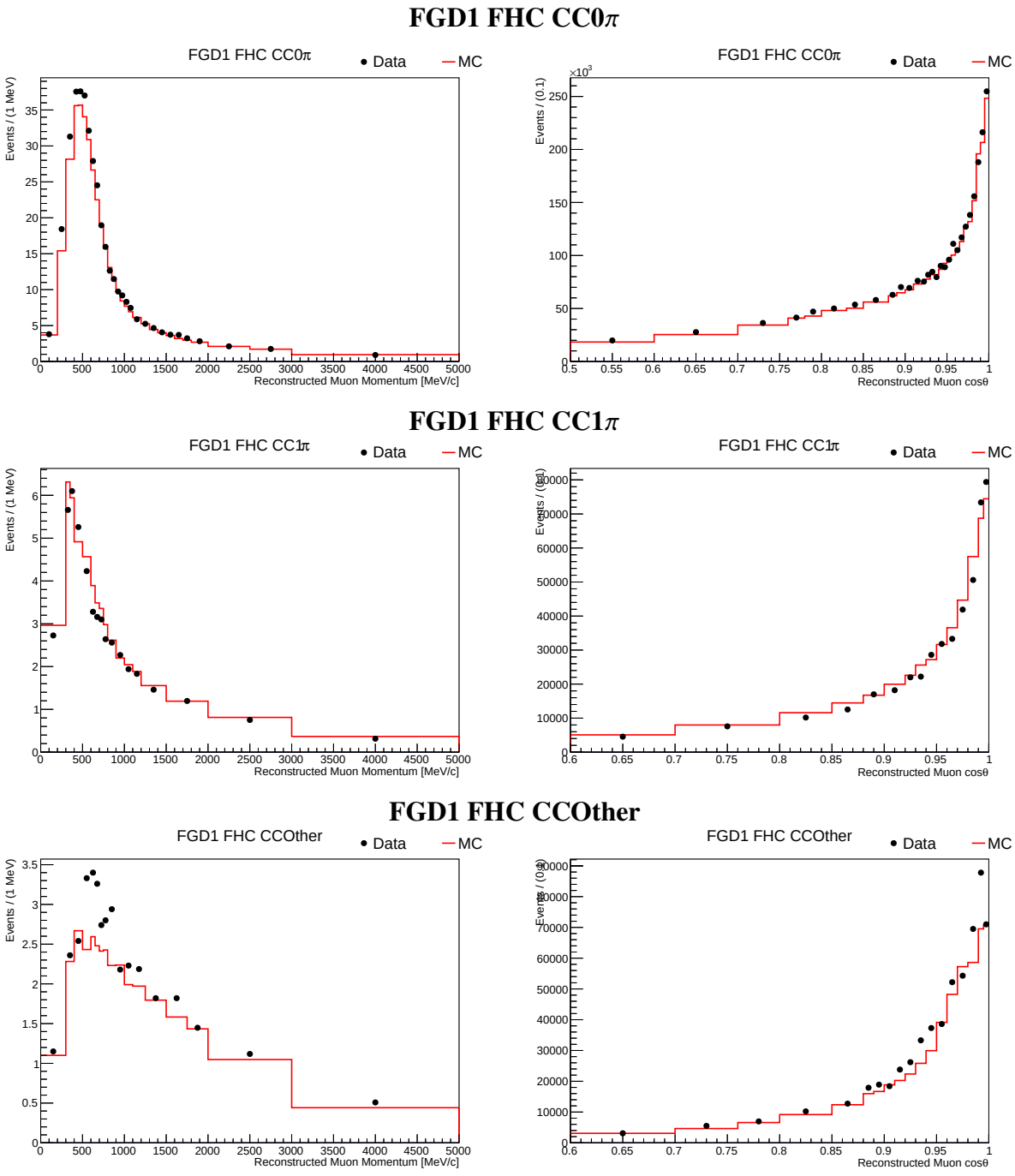

Figure 5.2: Kinematic distributions used as inputs to the BANFF fit for the FGD1 FHC MultiPi selections. The momentum distributions are shown on the left, while the angular distributions are shown on the right.

FGD1 FHC CC0π

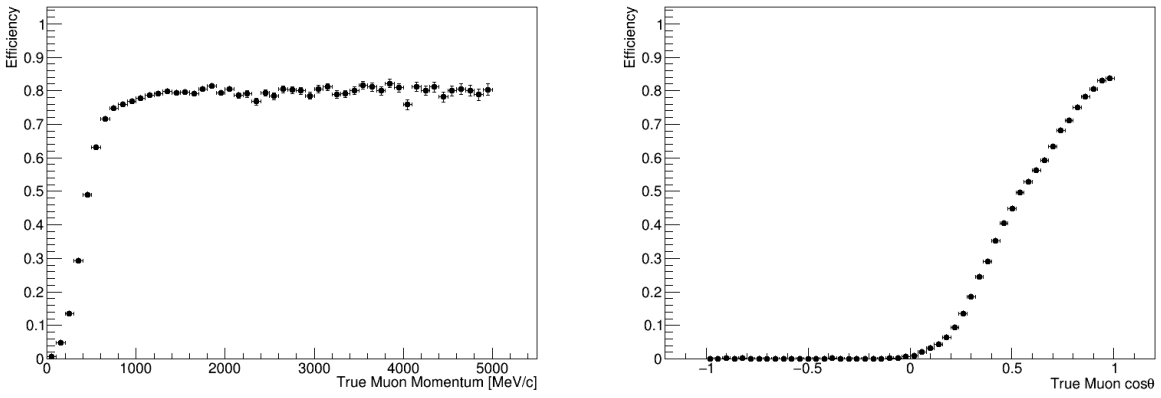

FGD1 FHC CC1π

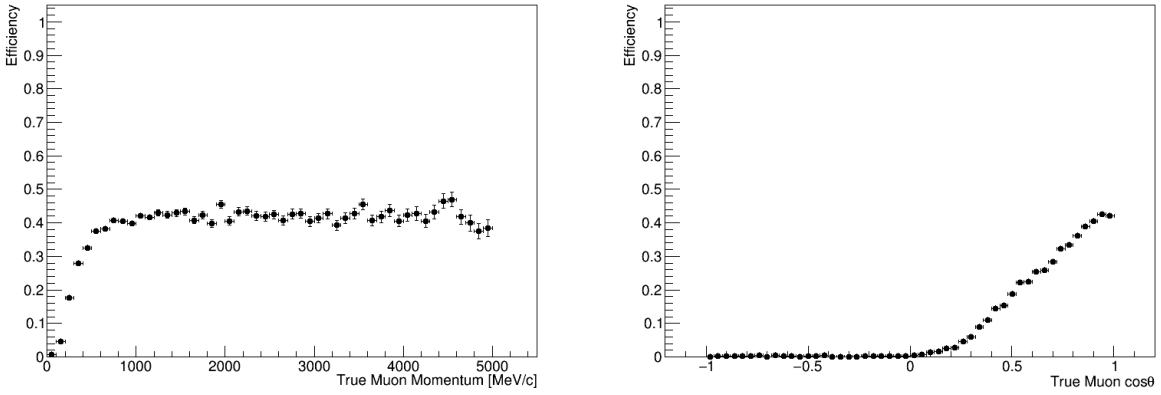

FGD1 FHC CCOther

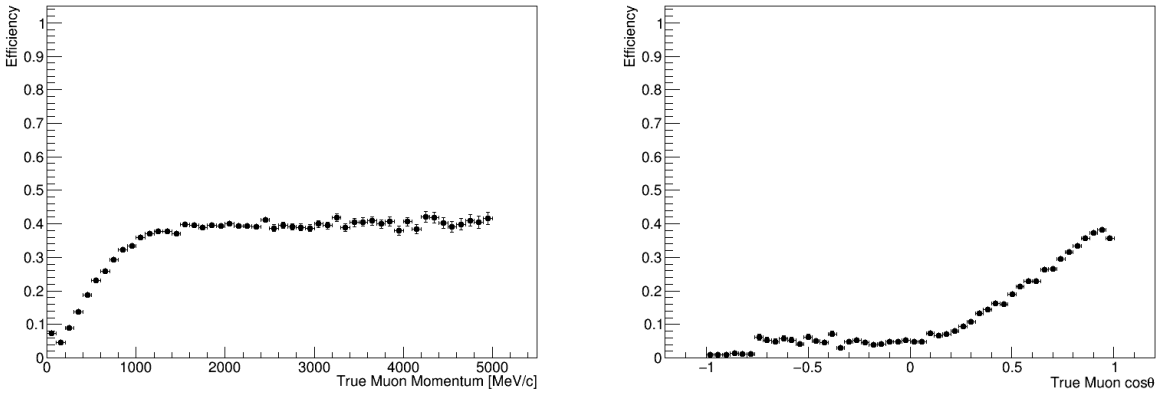

Figure 5.3: Selection efficiency as a function of true muon momentum (left) or true muon cos θ (right) for the FGD1 FHC MultiPi selections.

FGD1 FHC CC0π

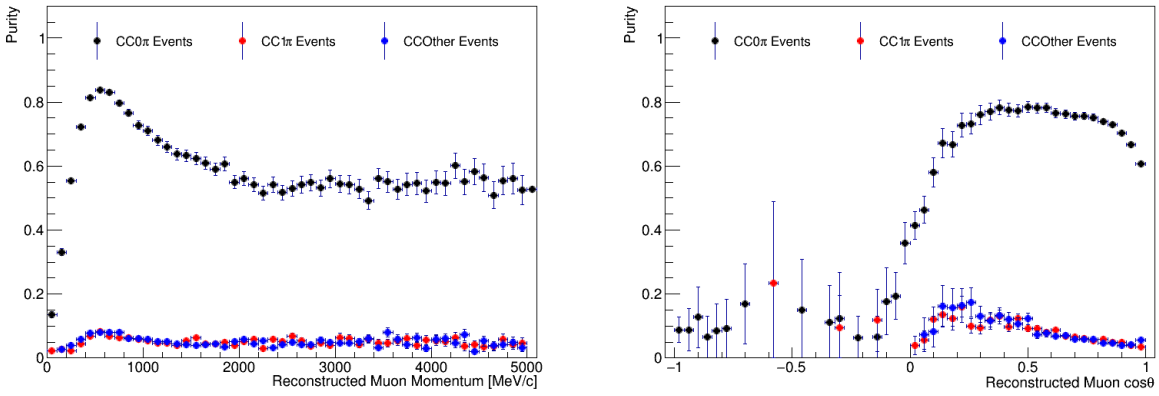

FGD1 FHC CC1π

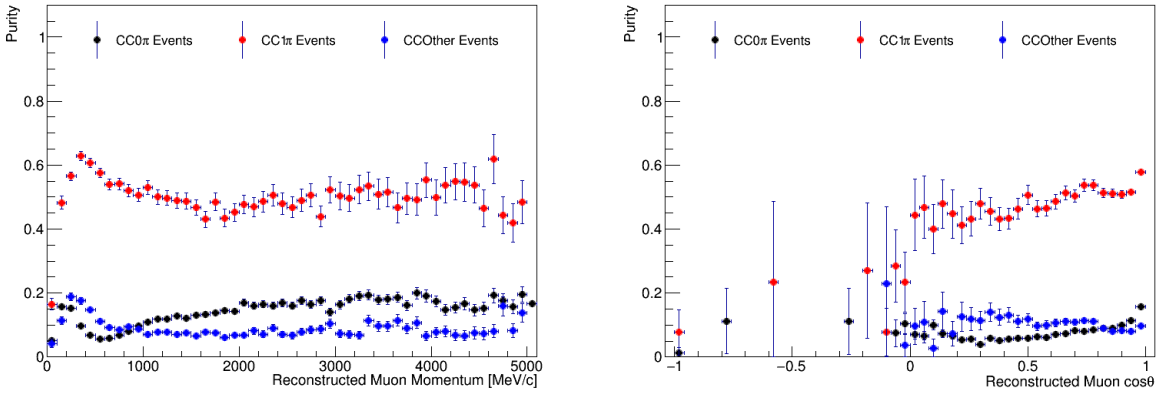

FGD1 FHC CCOther

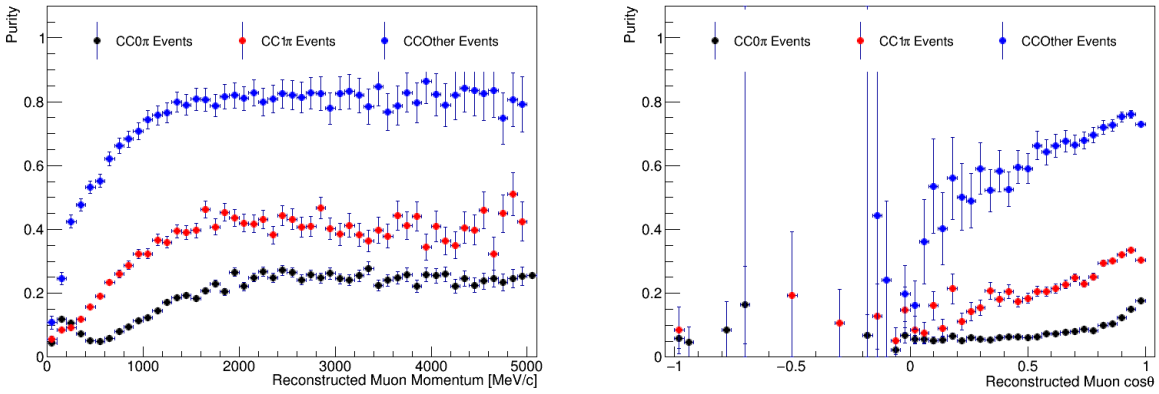

Figure 5.4: Selection purity as a function of reconstructed muon momentum (left) or reconstructed muon cos θ (right) for the FGD1 FHC MultiPi selections.

antineutrino interactions will produce a positively charged muon, compared with the negatively charged muon produced in neutrino interactions. Because the RHC ν_μ selection is looking for the neutrino background in antineutrino beam mode, the highest momentum track is required to be negative.

Similarly, the muon PID cut is slightly different from the FHC CC inclusive selection for both RHC CC inclusive selections. In this case, the pull cuts are more strict for RHC than they were for FHC, which helps eliminate backgrounds for the two selections.

For the RHC $\bar{\nu}_\mu$ selection, the cuts are

$$\frac{L_\mu + L_\pi}{1 - L_p} > 0.9 \tag{5.7}$$

for low momentum (< 500 MeV/c) events and

$$0.1 < L_\mu < 0.7 \tag{5.8}$$

for the rest of the track candidates. The upper bound for L_μ is to eliminate any misidentified low energy μ^- tracks, because these often are reconstructed with the incorrect charge. By including this cut, the ν_μ contamination is reduced.

For the RHC ν_μ selection, the cuts are

$$\frac{L_\mu + L_\pi}{1 - L_p} > 0.7 \tag{5.9}$$

for low momentum (< 500 MeV/c) events and

$$0.1 < L_\mu < 0.8 \tag{5.10}$$

for the rest of the track candidates. The cut in Equation 5.9 is slightly lower than in the FHC selection, in order to avoid cutting signal events. Additionally, this cut is set to reduce the fraction of background electrons in the overall selection. On the other hand, in Equation 5.10, the stricter bound is to aid in rejecting protons and incorrectly reconstructed, low energy μ^+.

5.3.2.2 Selections for MultiTrack Topologies

Unlike the FHC MultiPi selection, the RHC MultiTrack selection uses two simpler topological samples:

- **The CC 1-Track Sample** contains one primary muon candidate track. Only one FGD-TPC matched track is allowed in this sample. However, unlike the CC0π sample, no cut is made on FGD-only track multiplicity. Additionally, delayed Michel electrons would fall into this sample. This is because low energy π^- are quickly absorbed, making it harder to reconstruct these events.

- **The CC N-Tracks Sample** includes any events that have an observed secondary FGD-TPC matched track. Whereas the CC1π and CCOther samples can include FGD-only tracks and no secondary FGD-TPC matched tracks, the CC N-Tracks sample does not contain any FGD-only tracks, unless there is at least one secondary track.

When determining whether an event falls into the CC 1-Track or CC N-Tracks sample, the same process is used for both RHC $\bar{\nu}_\mu$ and RHC ν_μ CC inclusive selections. The BANFF fit binning for the RHC $\bar{\nu}_\mu$ samples are:

- **CC 1-Track fit bin edges:**

  p [MeV/c]: 0, 400, 500, 600, 700, 800, 900, 1100, 1400, 2000, 10000

  $\cos\theta$: -1.0, 0.6, 0.7, 0.8, 0.85, 0.88, 0.91, 0.93, 0.95, 0.96, 0.97, 0.98, 0.99, 1.0

- **CC N-Tracks fit bin edges:**

  p [MeV/c]: 0, 700, 950, 1200, 1500, 2000, 3000, 10000

  $\cos\theta$: -1.0, 0.75, 0.85, 0.88, 0.91, 0.93, 0.95, 0.96, 0.97, 0.98, 0.99, 1.0

The BANFF fit binning for the RHC ν_μ samples are:

- **CC 1-Track fit bin edges:**

p [MeV/c]: 0, 400, 600, 800, 1100, 2000, 10000

$\cos\theta$: -1.0, 0.7, 0.8, 0.85, 0.9, 0.93, 0.95, 0.96, 0.97, 0.98, 0.99, 1.0

- **CC N-Tracks fit bin edges:**

  p [MeV/c]: 0, 500, 700, 1000, 1250, 1500, 2000, 3000, 10000

  $\cos\theta$: -1.0, 0.7, 0.8, 0.85, 0.90, 0.93, 0.95, 0.96, 0.97, 0.98, 0.99, 1.0

Momentum and angular distributions, as well as efficiency and purity plots, for the $\bar{\nu}_\mu$ MultiTrack samples can be found in Figures 5.5 – 5.7 for FGD1. With regards to the ν_μ MultiTrack selections, the momentum and angular distributions and efficiency and purity plots for FGD1 can be found in Figures 5.8 – 5.10. The corresponding FGD2 plots can be found in Figures C.4 – C.6 for the $\bar{\nu}_\mu$ MultiTrack samples and Figures C.7 – C.9 for the ν_μ MultiTrack selections.

5.3.3 Reverse Horn Current MultiPi Selections

One of the key changes to the BANFF fit presented in this work was the transition from using the RHC MultiTrack samples to the RHC MultiPi samples. This change puts the neutrino mode and antineutrino mode samples on the same footing and treats the RHC samples in a way that better mirrors the primary neutrino interactions in ND280 and SK. For a more in-depth discussion on the differences between the two types of selections, see Section 5.3.3.3.

5.3.3.1 Charged Current Inclusive Selection

The same method as the RHC MultiTrack (which itself is a slight modification of the FHC MultiPi CC inclusive selection) is used. The most important part of the the inclusive selection is the determination of a leading muon, a μ^- for the ν_μ background and a μ^+ for $\bar{\nu}_\mu$.

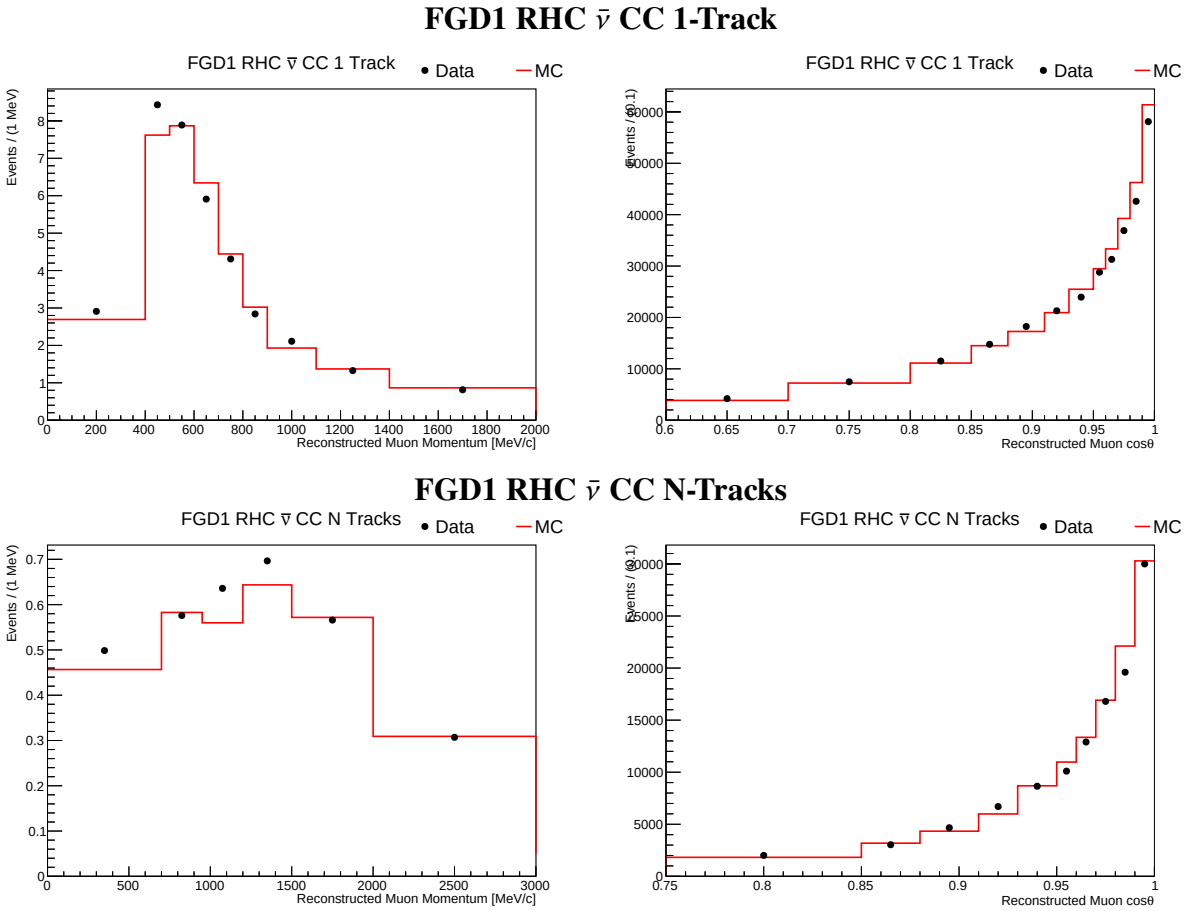

Figure 5.5: Kinematic distributions used as inputs to the BANFF fit for the FGD1 RHC $\bar{\nu}$ MultiTrack selections. The momentum distributions are shown on the left, while the angular distributions are shown on the right.

5.3.3.2 Selections for MultiPi Topologies

As with the FHC MultiPi samples, once the CC inclusive selection has been performed, the sample is divided into three topological samples based on the presence (or lack thereof) of pions.

- **The CC0π Sample** contains no observed pion tracks.
- **The CC1π Sample** has one negative pion (for $\bar{\nu}_\mu$ interactions) or one positive pion (for ν_μ interactions) and no other pion tracks.
- **The CCOther Sample** contains the rest of the events that do not fall into either of the first two samples.

FGD1 RHC $\bar{\nu}$ CC 1-Track

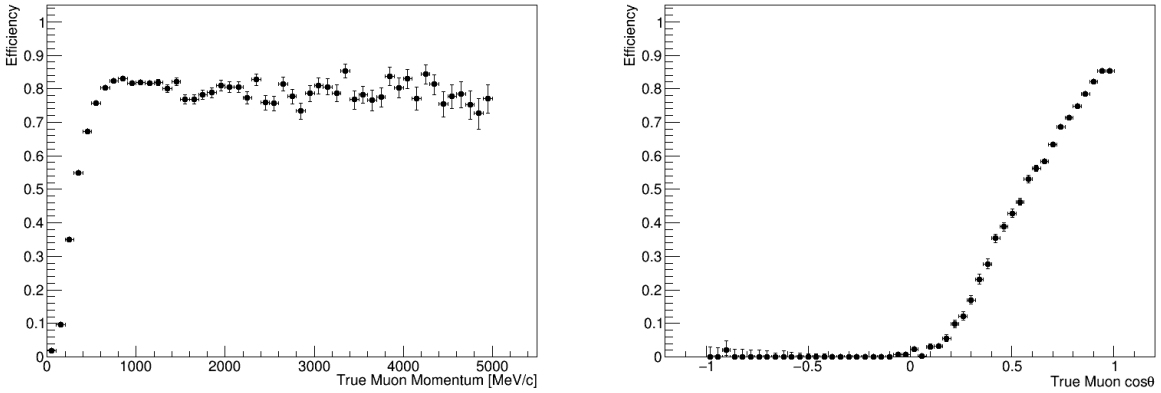

FGD1 RHC $\bar{\nu}$ CC N-Tracks

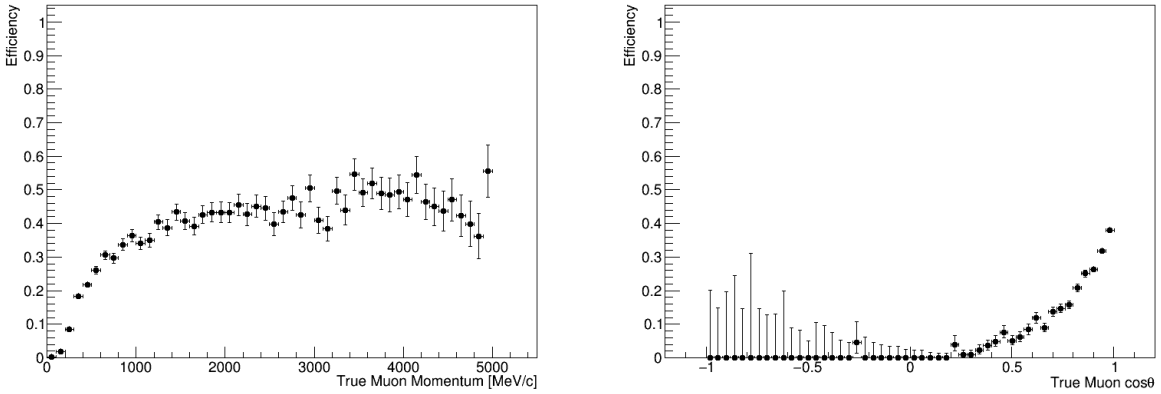

Figure 5.6: Selection efficiency as a function of true muon momentum (left) or true muon $\cos\theta$ (right) for the FGD1 RHC $\bar{\nu}$ MultiTrack selections.

The BANFF fit binning for the RHC $\bar{\nu}_\mu$ samples are:

- **CC0π fit bin edges:**

  p [MeV/c]: 0, 300, 400, 500, 550, 600, 650, 700, 750, 800, 900, 1000, 1100, 1200, 1500, 2000, 4000, 30000

  $\cos\theta$: -1.0, 0.6, 0.7, 0.8, 0.85, 0.9, 0.92, 0.93, 0.94, 0.95, 0.96, 0.965, 0.97, 0.975, 0.98, 0.985, 0.99, 0.995, 1.0

- **CC1π fit bin edges:**

FGD1 RHC $\bar{\nu}$ CC 1-Track

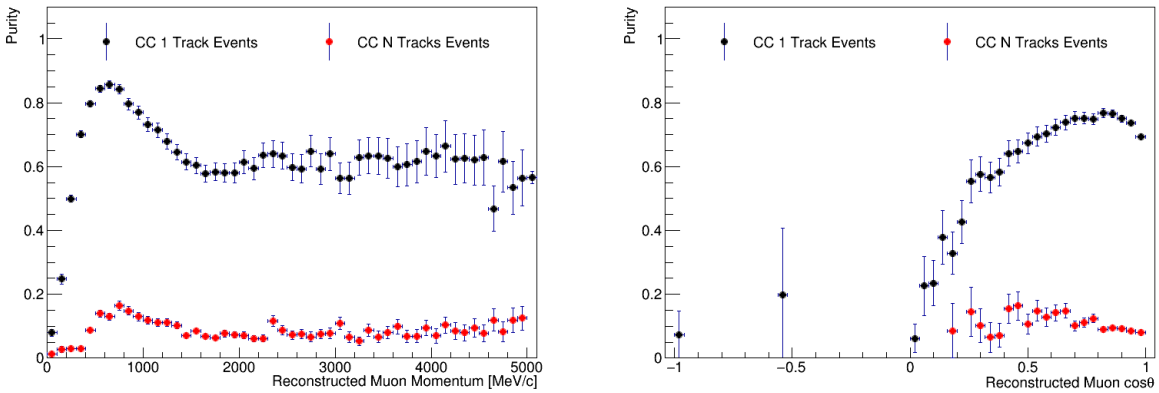

FGD1 RHC $\bar{\nu}$ CC N-Tracks

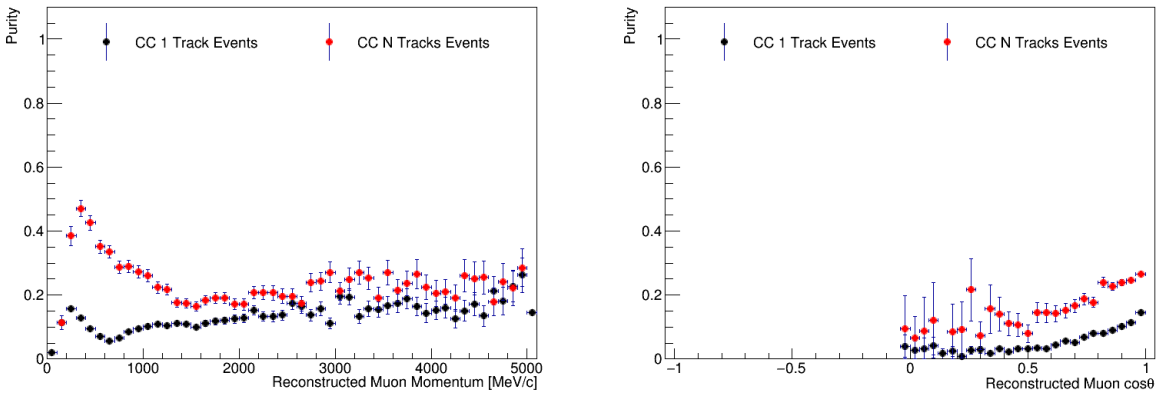

Figure 5.7: Selection purity as a function of reconstructed muon momentum (left) or reconstructed muon $\cos\theta$ (right) for the FGD1 RHC $\bar{\nu}$ MultiTrack selections.

p [MeV/c]: 0, 500, 700, 900, 1300, 2500, 30000

$\cos\theta$: -1.0, 0.7, 0.8, 0.9, 0.94, 0.96, 0.98, 0.99, 1.0

- **CCOther fit bin edges:**

p [MeV/c]: 0, 600, 800, 1000, 1250, 1500, 2000, 4000, 30000

$\cos\theta$: -1.0, 0.7, 0.8, 0.85, 0.9, 0.93, 0.95, 0.97, 0.98, 0.99, 1.0

The BANFF fit binning for the RHC ν_μ samples are:

- **CC0π fit bin edges:**

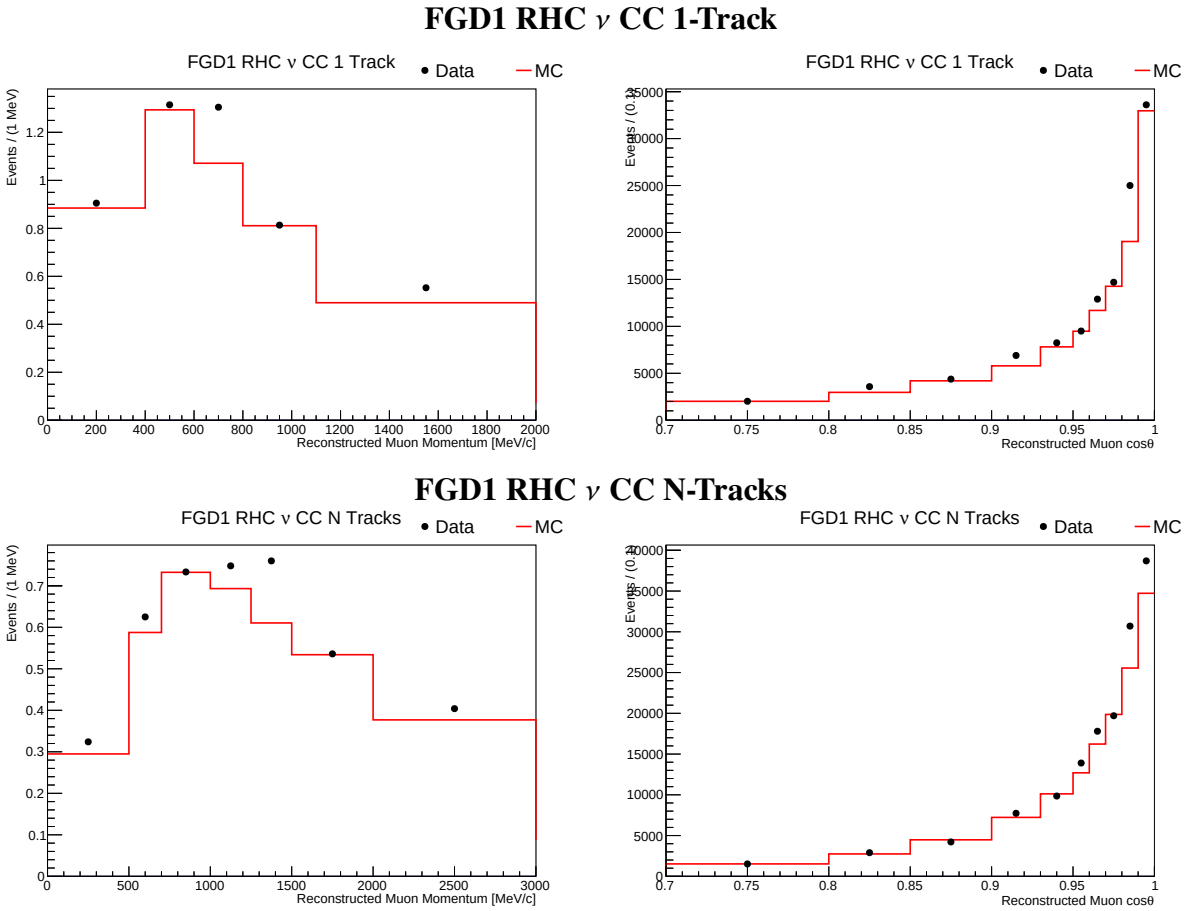

Figure 5.8: Kinematic distributions used as inputs to the BANFF fit for the FGD1 RHC ν MultiTrack selections. The momentum distributions are shown on the left, while the angular distributions are shown on the right.

p [MeV/c]: 0, 300, 500, 700, 800, 900, 1250, 1500, 2000, 4000, 30000

$\cos\theta$: -1.0, 0.7, 0.8, 0.85, 0.88, 0.9, 0.92, 0.94, 0.96, 0.97, 0.98, 0.99, 1.0

- **CC1π fit bin edges:**

  p [MeV/c]: 0, 600, 800, 1500, 30000

  $\cos\theta$: -1.0, 0.7, 0.8, 0.86, 0.9, 0.94, 0.96, 0.97, 0.98, 0.99, 1.0

- **CCOther fit bin edges:**

  p [MeV/c]: 0, 600, 1000, 1250, 2000, 4000, 30000

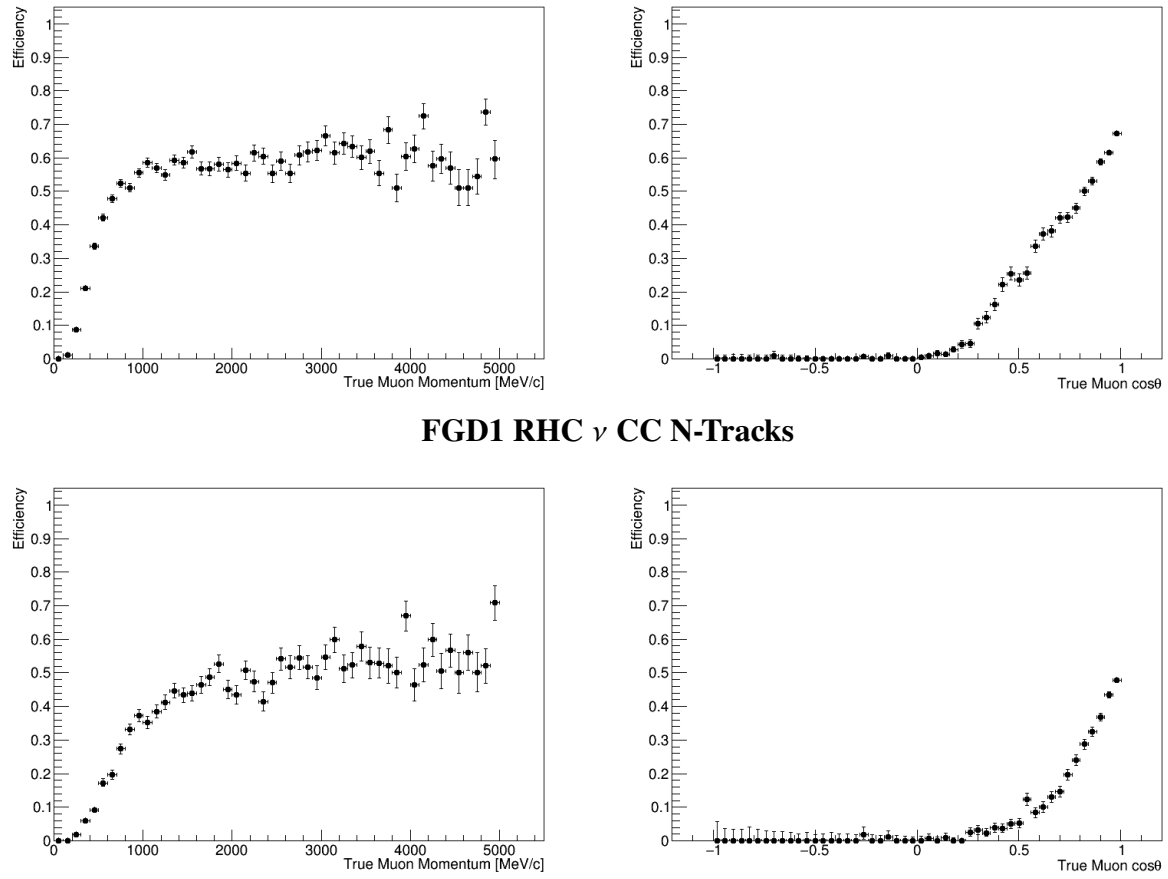

Figure 5.9: Selection efficiency as a function of true muon momentum (left) or true muon $\cos\theta$ (right) for the FGD1 RHC ν MultiTrack selections.

$\cos\theta$: -1.0, 0.7, 0.8, 0.86, 0.9, 0.93, 0.95, 0.97, 0.99, 1.0

Based on this breakdown of samples, it is important to be able to tag pions in events. In the case of a neutral pion, both the RHC $\bar{\nu}_\mu$ and RHC ν_μ selections look for traces of electromagnetic cascades from photons in the TPCs. Additionally, if an electron-like negative track or an electron-like positive track (with momentum greater than 0.9 MeV/c) is present, then at least one neutral pion is assumed to be in the event. When it comes to charged pions, if there is a negatively charged pion-like track or a positively charged pion-like track in the TPC, then it is assumed the event has either a negative or positive pion, respectively.

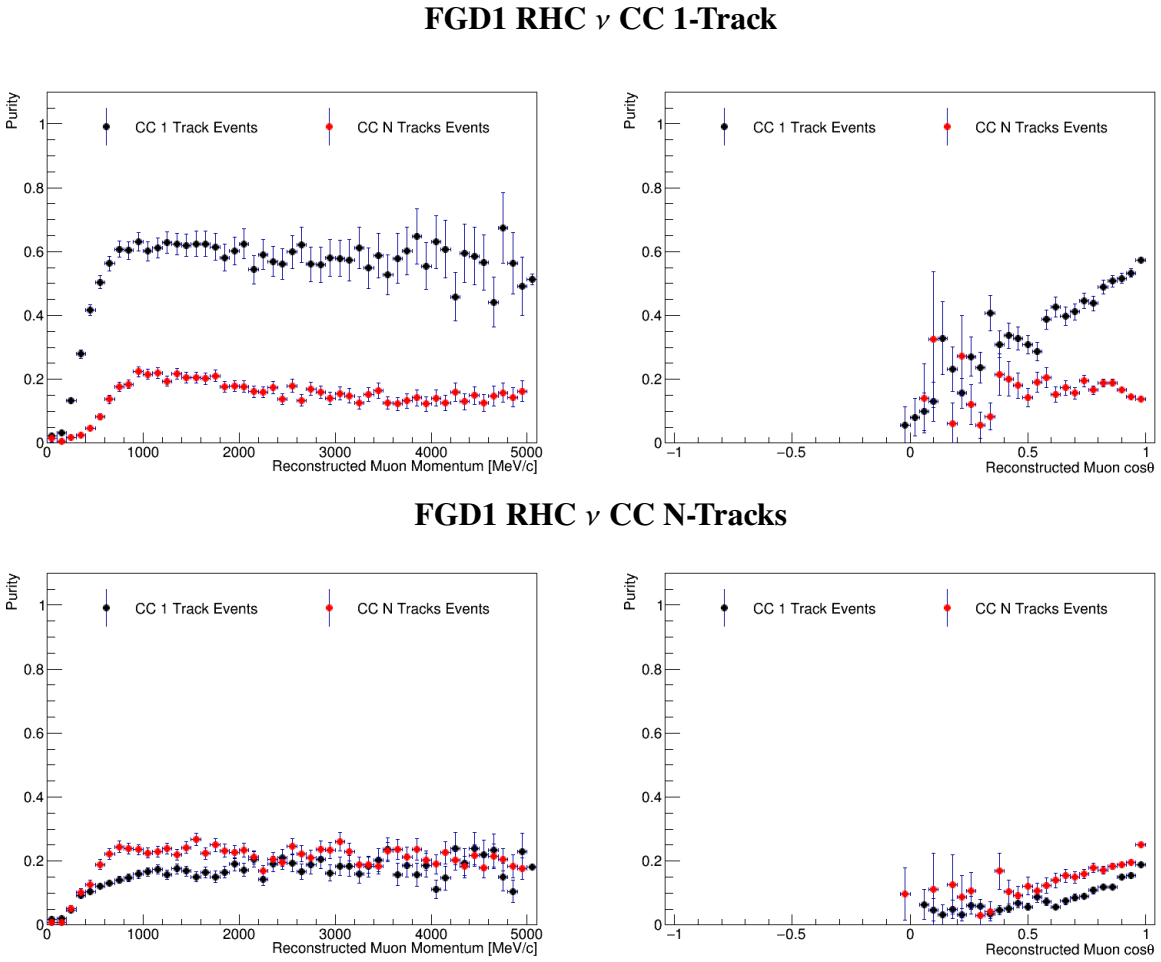

Figure 5.10: Selection purity as a function of reconstructed muon momentum (left) or reconstructed muon $\cos\theta$ (right) for the FGD1 RHC ν MultiTrack selections.

However, pion tagging becomes more difficult when there are Michel electrons or isolated FGD tracks. For the RHC $\bar{\nu}_\mu$ selection, the focus is on negative pions, because they are more abundant in antineutrino interactions. Negative pions are especially problematic because they tend to be captured in the detector medium prior to decaying, which makes tagging negative pions via Michel electrons difficult. Therefore, isolated FGD tracks must be relied upon in order to tag negative pions. It should be noted that, even though the charge of the isolated track cannot be determined currently, it is reasonable to assume the charge is that of the more common pion, which is the negative pion in the case of antineutrino interactions. With this in mind, the following statements can be made for determining the presence of negative or positive pions in the RHC $\bar{\nu}_\mu$ sample:

- A Michel electron in the FGD (in most cases) is the result of a positive pion in the event, whereas
- an isolated pion-like track in the FGD is more likely the result of a negative pion.

Table 5.6 shows that the CC1π sample prefers events with one isolated FGD track and no Michel electrons, whereas when a Michel electron is present, the CCOther sample is the preferable choice. This provides confirmation of the previous statements, as positively charged pions would fall in the CCOther sample and a single negatively charged pion would fall in the CC1π sample.

		# iso tracks = 0		**# iso tracks = 1**	
		FGD1	FGD2	FGD1	FGD2
# ME = 0	CC0π	**61.2%**	**59.7%**	4.0%	7.6%
	CC1π^-	12.9%	12.0%	**46.8%**	**37.0%**
	CCOther	9.0%	8.9%	22.6%	21.0%
	Background	10.8%	11.8%	18.0%	26.3%
	OOFV	6.1%	7.7%	8.7%	8.1%
# ME = 1	CC0π	6.5%	4.0%	1.1%	0.0%
	CC1π^-	5.2%	4.3%	13.8%	10.3%
	CCOther	**20.8%**	**19.0%**	**32.3%**	**25.0%**
	Background	33.7%	35.0%	41.0%	47.1%
	OOFV	33.8%	37.6%	11.8%	17.6%

Table 5.6: Percentage of events with a given number of Michel electrons (ME) and isolated FGD tracks (iso tracks). Background represents events falling into any background samples (which are not used in this analysis), while OOFV includes any events occurring outside of the FGD fiducial volume. Table from [6].

On the other hand, the RHC ν_μ selection focuses on positive pion identification, rather than negative pion identification. Even though selecting positive pions is of more benefit for this selection, it is still important to correctly identify negative pions, especially because they can be misidentified as negative muons if they cross the TPC. In the case of positive pions, the signal from Michel electrons occurring outside the beam bunch time window can be used to tag the existence of a positively charged pion.

Momentum and angular distributions, as well as efficiency and purity plots, for the $\bar{\nu}_\mu$ MultiPi samples in FGD1 can be found in Figures 5.11 – 5.13. With regards to the ν_μ MultiPi selections in FGD1, the momentum and angular distributions and efficiency and purity plots, can be found in Figures 5.14 – 5.16. The corresponding FGD2 plots can be found in Figures C.10 – C.12 for the $\bar{\nu}_\mu$ MultiPi samples and Figures C.13 – C.15 for the ν_μ MultiPi samples.

5.3.3.3 Comparison of MultiTrack and MultiPi samples

Using the RHC MultiPi samples serves one primary purpose in the oscillation analysis, in that these samples more accurately match what is seen at Super-Kamiokande (SK). By way of example, a second track in an event in the CC N-tracks sample may be the result of a proton crossing the TPC. However, the far detector is unable to detect protons because they do not decay and tend not to have enough energy to meet the Cherenkov threshold. Whereas the RHC MultiTrack samples have no cuts based on the number of pions in an event, the RHC MultiPi samples are designed to be differentiated based on the number of pions observed in the event. The SK samples are similarly categorized, as the pions can be detected either through their decay or through the pion having enough energy to meet the Cherenkov threshold.

Additionally, the three RHC MultiPi are designed to better reflect how the three primary types of interactions are observed in the detector. While there are detector effects that can cause discrepancies between the true interaction type and the selected sample, generally, CCQE events are observed as a muon with no pions in the detector, CC resonant pion production have a muon and one pion, and DIS+Nπ contains the rest of the observed events. Using these samples, studies have shown good agreement between the true interaction and the selected sample [6].

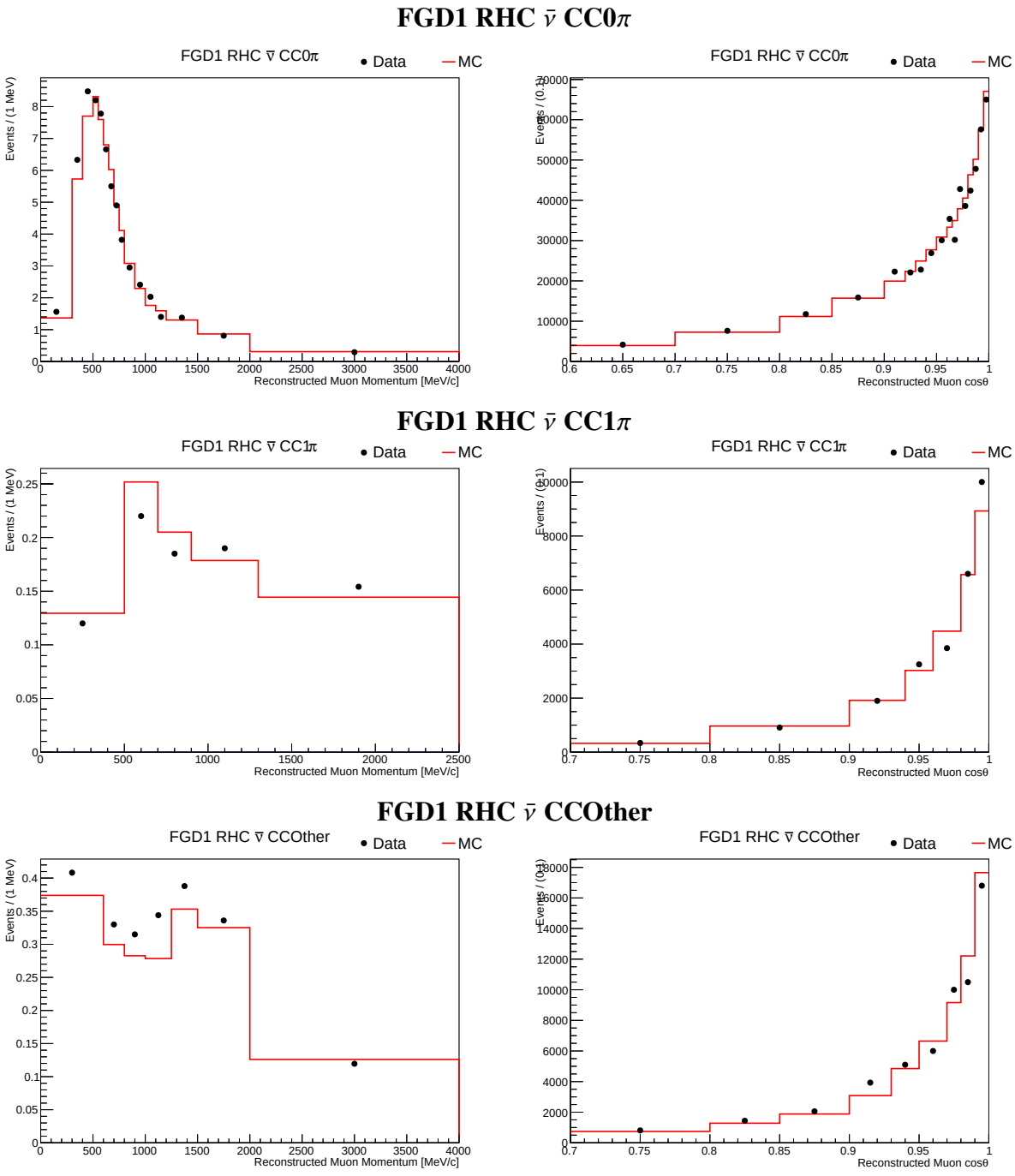

Figure 5.11: Kinematic distributions used as inputs to the BANFF fit for the FGD1 RHC $\bar{\nu}$ MultiPi selections. The momentum distributions are shown on the left, while the angular distributions are shown on the right.

FGD1 RHC $\bar{\nu}$ CC0π

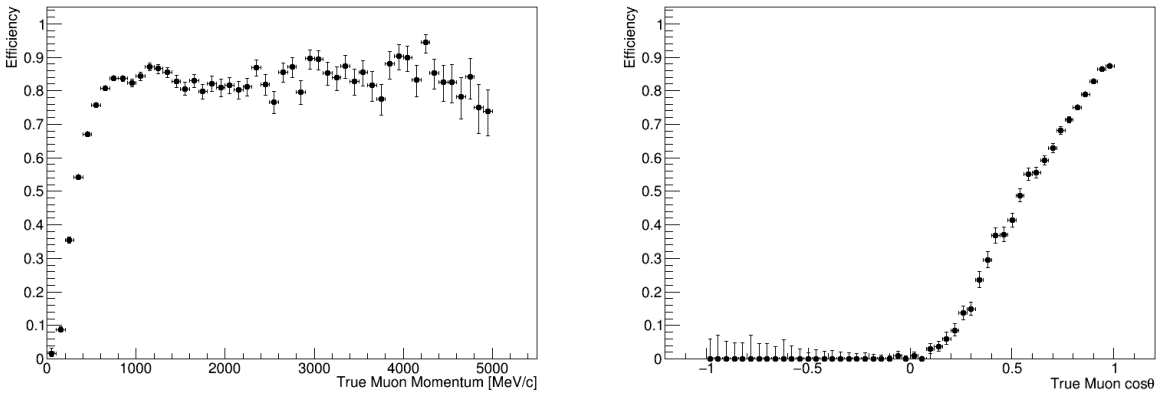

FGD1 RHC $\bar{\nu}$ CC1π

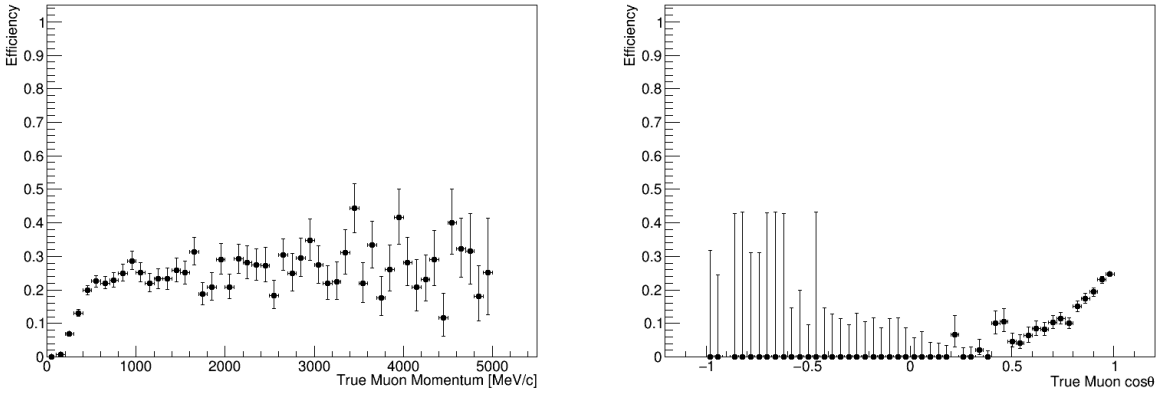

FGD1 RHC $\bar{\nu}$ CCOther

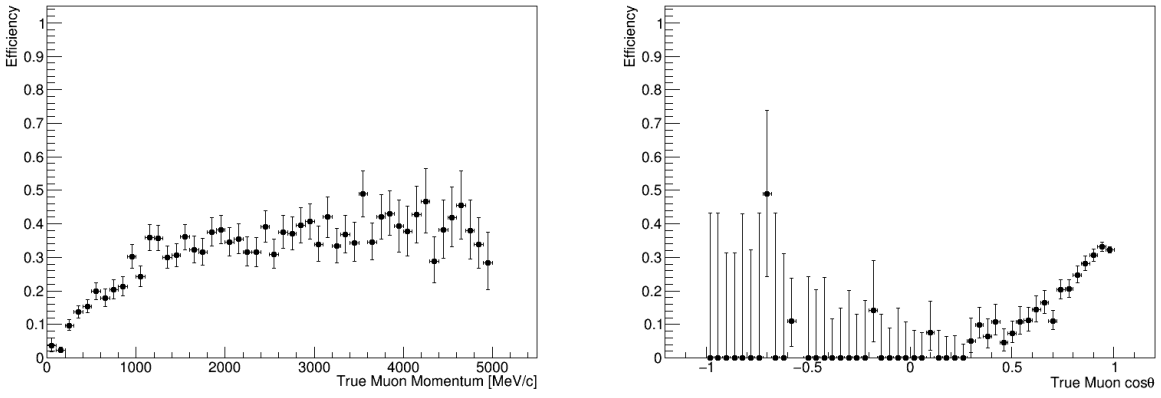

Figure 5.12: Selection efficiency as a function of true muon momentum (left) or true muon cos θ (right) for the FGD1 RHC $\bar{\nu}$ MultiPi selections.

FGD1 RHC $\bar{\nu}$ CC0π

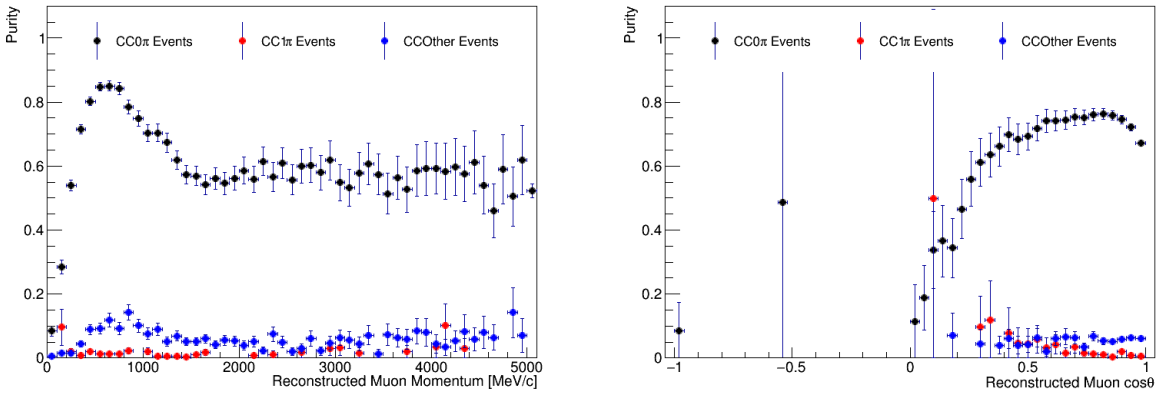

FGD1 RHC $\bar{\nu}$ CC1π

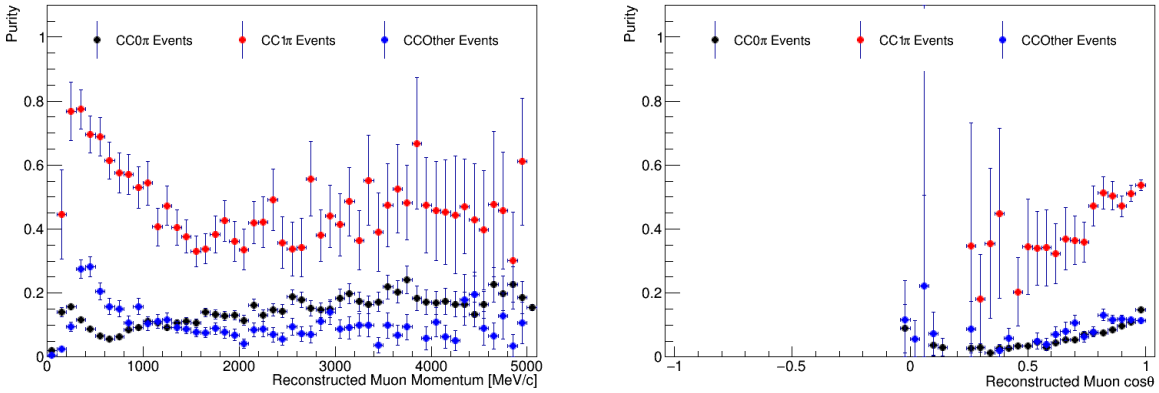

FGD1 RHC $\bar{\nu}$ CCOther

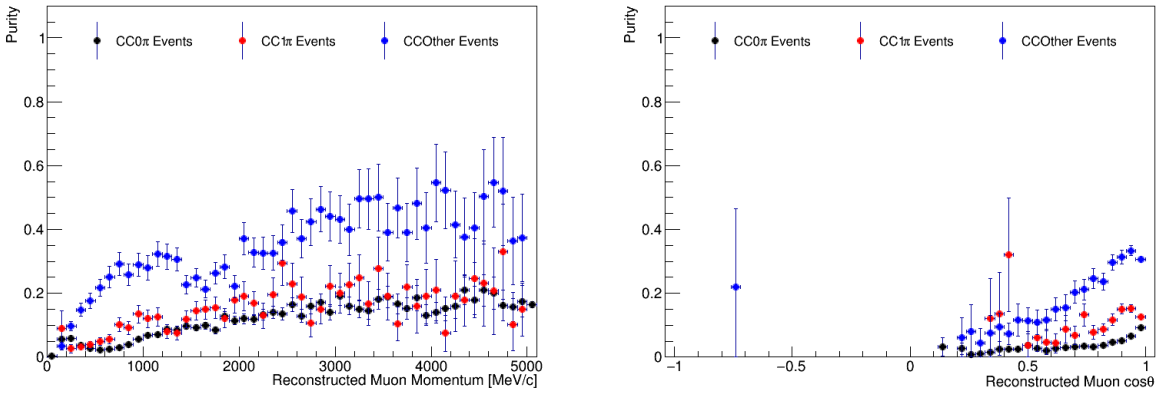

Figure 5.13: Selection purity as a function of reconstructed muon momentum (left) or reconstructed muon cos θ (right) for the FGD1 RHC $\bar{\nu}$ MultiPi selections.

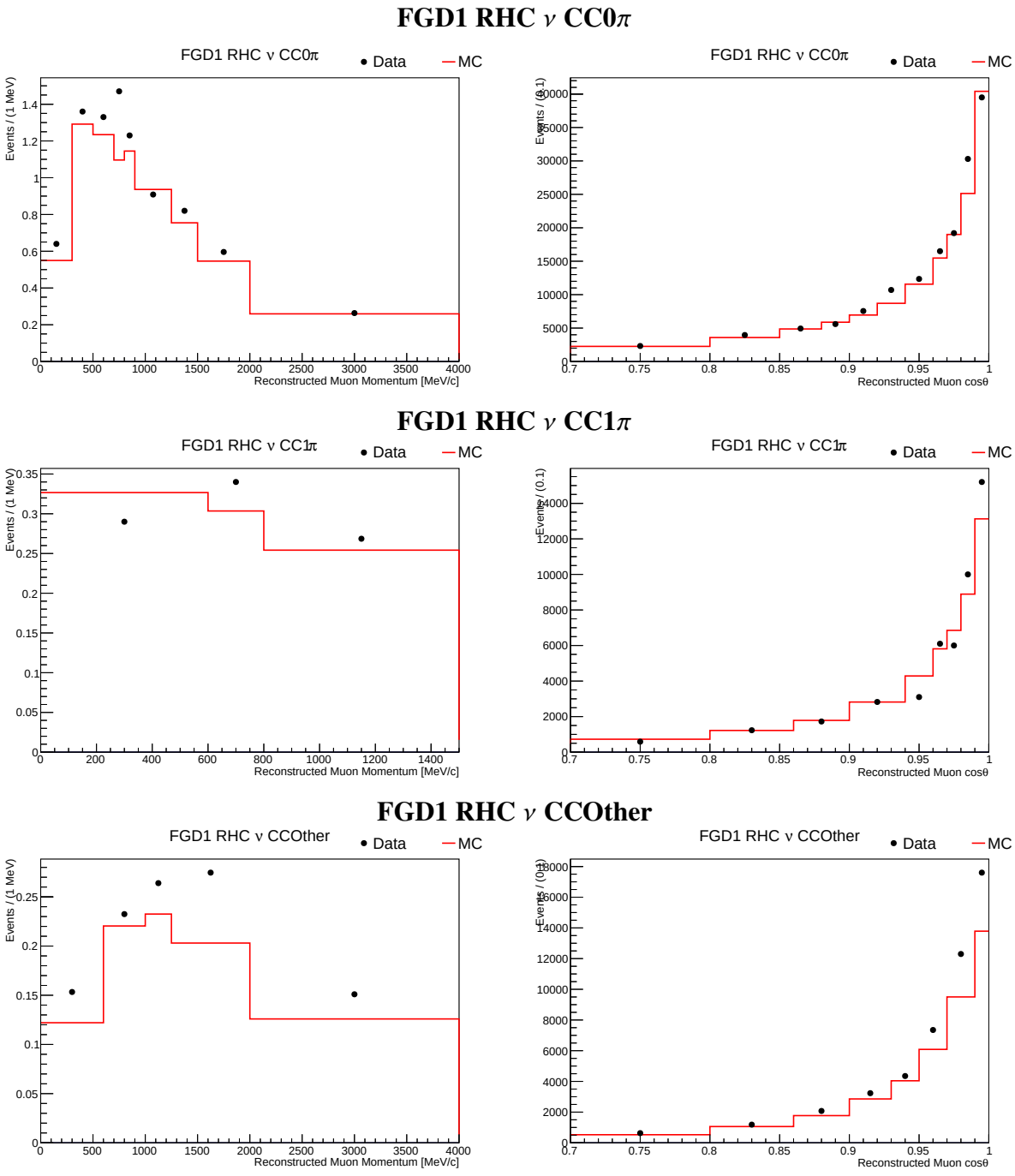

Figure 5.14: Kinematic distributions used as inputs to the BANFF fit for the FGD1 RHC ν MultiPi selections. The momentum distributions are shown on the left, while the angular distributions are shown on the right.

FGD1 RHC ν CC0π

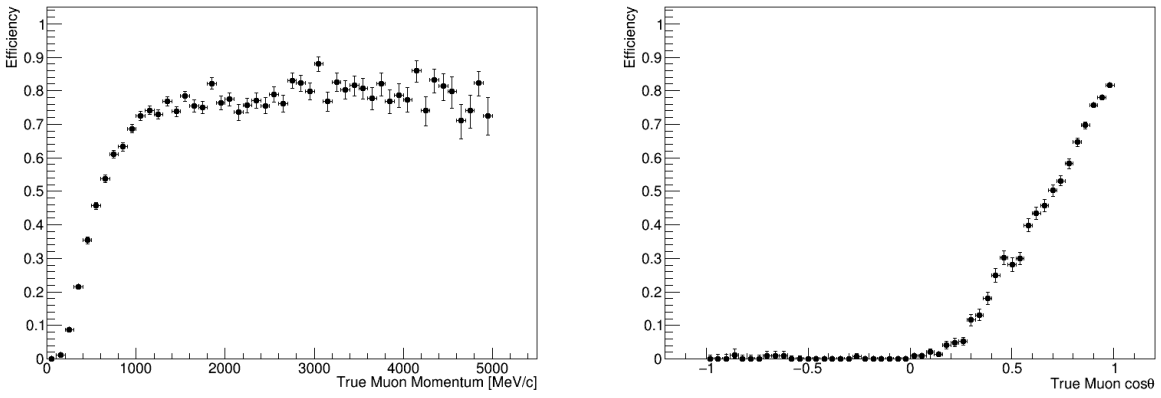

FGD1 RHC ν CC1π

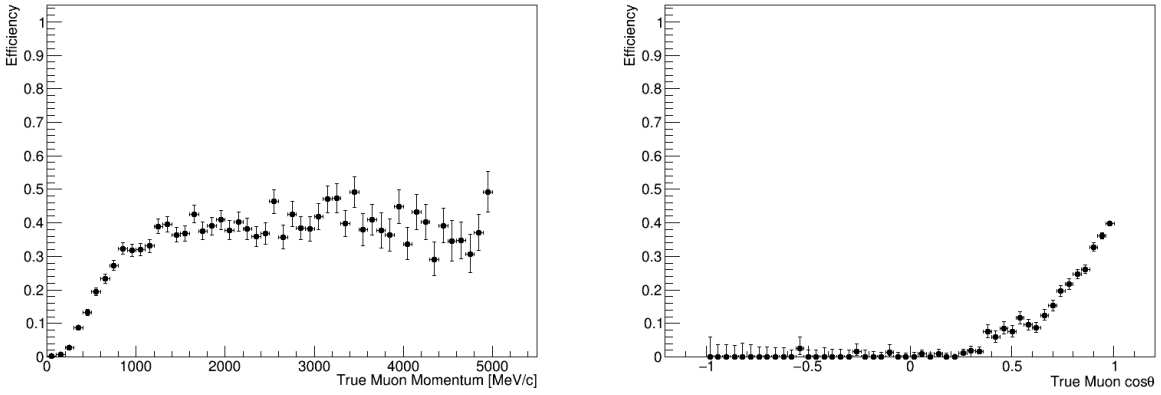

FGD1 RHC ν CCOther

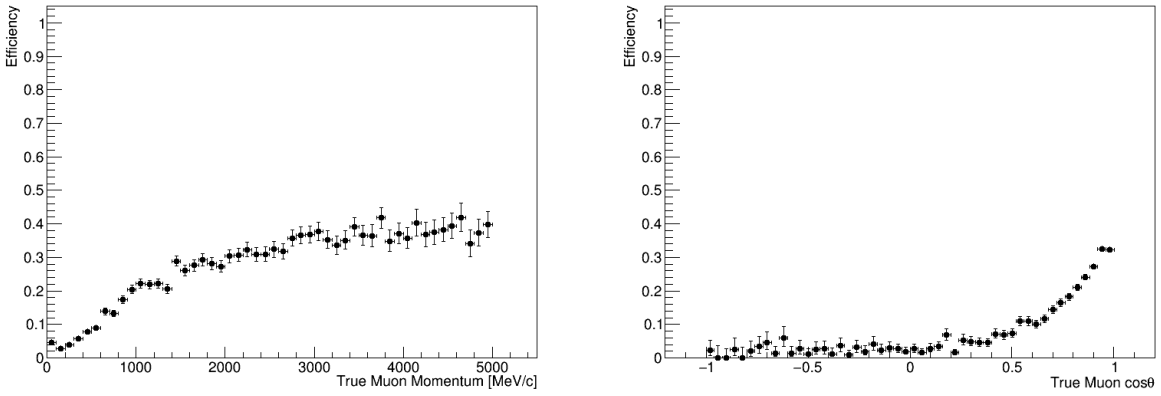

Figure 5.15: Selection efficiency as a function of true muon momentum (left) or true muon cos θ (right) for the FGD1 RHC ν MultiPi selections.

FGD1 RHC ν CC0π

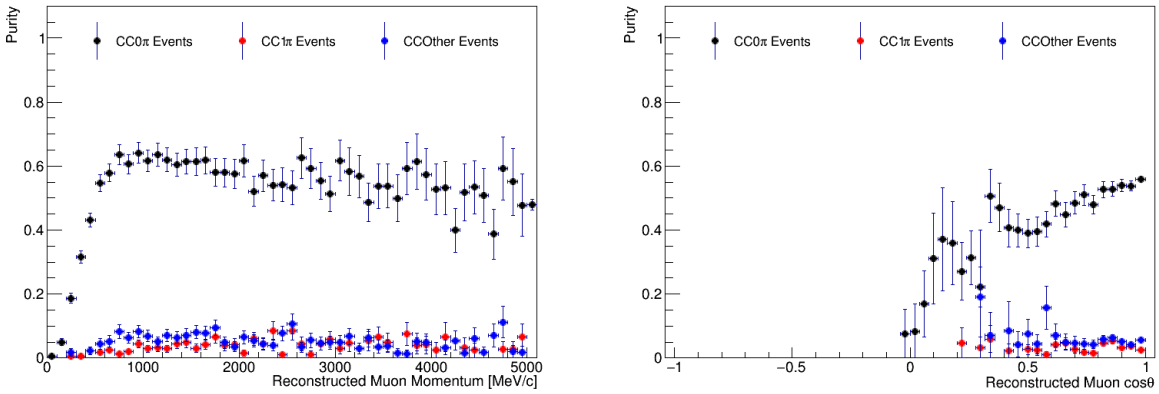

FGD1 RHC ν CC1π

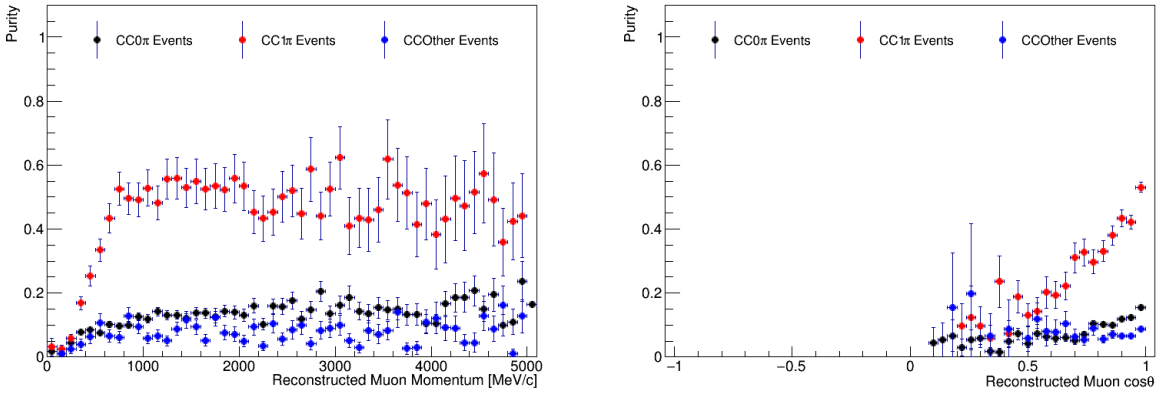

FGD1 RHC ν CCOther

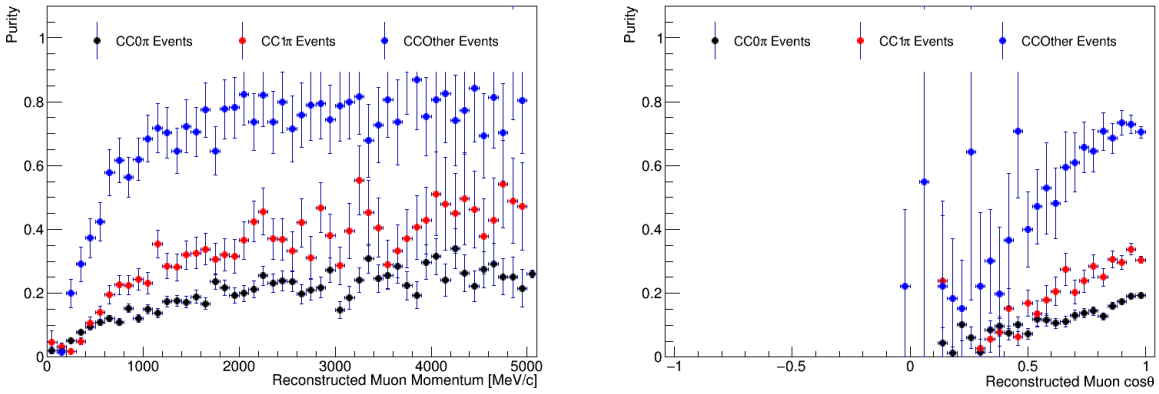

Figure 5.16: Selection purity as a function of reconstructed muon momentum (left) or reconstructed muon cos θ (right) for the FGD1 RHC ν MultiPi selections.

CHAPTER 6

ND280 SYSTEMATIC UNCERTAINTIES IN THE NEAR DETECTOR FIT

As the event selections described in Chapter 5 are dependent on the identification of particles and their kinematics, it is important to understand the uncertainty in making these measurements in the detector. If, for example, a particle is misidentified in the time projection chamber (TPC) or its momentum is incorrectly determined, the predicted event rate at the near detector could be impacted, which would then be propagated to the oscillation analysis through the BANFF fit results. The systematic uncertainties on ND280 will be described in detail in this chapter.

6.1 Detector Systematic Uncertainty Details

Even though many potential sources of uncertainty exist at the near detector, the detector systematic uncertainties associated with the event selections described in Chapter 5 are the most relevant. The majority of the systematic effects described over the course of this chapter are applied to both FHC and RHC samples. However, a select number are not applied to the RHC MultiTrack samples, as these samples have fewer cuts related to the fine-grained detectors (FGDs). A summary of the individual uncertainties can be found in Section 6.3, as well as their impact on the overall detector systematic uncertainty in the near detector fit. The specific details of each uncertainty are described below.

TPC Field Distortions: Because the magnetic field applied in ND280 is not completely uniform, field distortions can arise in the TPCs. Mapping data, taken using Hall probes in the near detector, are used to set the magnetic field used in the ND280 reconstruction [107]. By including this mapping, the magnetic field distortions can be accounted for during the reconstruction process by applying the field map to the TPC hit positions found in the reconstruction and evaluating the change in the y and z positions [108].

Furthermore, the validity of the map is tested by comparing the results to those found using

a laser calibration system in the TPC. This system uses the expected and measured positions of photoelectrons from aluminum dots illuminated by a laser. This testing is done both when the magnet is turned off and when it is turned on. Based on these measurements, a second correction is applied to the hit positions as a function of the drift distance of the photoelectrons.

Both corrections were cross checked using TPC2 and TPC3, as TPC3 is expected to have large distortions due to its position in the yoke. The cross checks showed that including the initial magnetic field correction reduced the relative momentum bias between TPCs, whereas the second correction increased the bias [108]. The first correction is applied during the reconstruction process, while the second correction is used as a systematic uncertainty on the magnetic field distortions in order to mitigate the observed bias.

TPC Momentum Scale: In addition to the systematic uncertainty for the magnetic field distortions, the TPC momentum scale relies upon the magnetic field at ND280. By changing the magnitude of the magnetic field, changes can arise in the TPC track momenta, potentially resulting in migration between $p - \cos\theta$ bins in the selections. Four Hall probes installed at ND280 provide scaling factors for the field strength in the Monte Carlo. These scaling factors are necessary because the nominal MC magnetic field is significantly different from the measured mapping [107]. The uncertainty on the scaling factors come from several sources including the intrinsic resolution of the probes, potential relative misalignment between the probes, and the nonlinear nature of the relationship between the magnet current and the field magnitude.

TPC Momentum Resolution: Due to a number of factors, including differences in the electric and magnetic field distortions at the near detector, there is some uncertainty in the momentum resolution for tracks in the TPC reconstruction. While there is an uncertainty already included for the magnetic field distortions, the reasons behind the data – Monte Carlo discrepancy in momentum resolution are not well understood. For this reason, a conservative

approach is taken and both uncertainties are included [7].

In order to better understand the momentum resolution for the data and Monte Carlo, a study was performed with a control sample of events that had tracks which crossed multiple TPCs [109]. By using events with tracks in multiple TPCs, the track momenta in each TPC can be directly compared without using truth information. The momentum uncertainty is then calculated for a single TPC segment. Good agreement is seen between single TPC segments and tracks that cross multiple TPCs; therefore, the same fractional differences are used for tracks crossing multiple TPCs.

Because the Monte Carlo shows better momentum resolution than the data [7], the inverse momentum in the Monte Carlo is smeared to match that seen in the data. This is done using the fractional difference in the momentum resolution between the data and Monte Carlo, binned in x-position along the TPC [7, 109], as this is the direction of the magnetic field in the TPC. An uncertainty of 0.1 was used for all scaling factors, regardless of x-position.

TPC Particle Identification: In order to determine the particle ID using the TPCs, a truncated average of the charge collected in the TPC is used to perform particle hypothesis test. Two issues are involved in the data – Monte Carlo differences seen in the TPC PID. The first is due to the difference between the mean pull values, while the second is due to the ratio between pull widths. The uncertainties on these ratios are calculated for each type of particle and each TPC and then are binned in particle momentum. An estimation of the systematic bias is achieved through the difference in the pull means, while an estimate of the smearing needing to be applied to the Monte Carlo comes from the ratio of the pull means.

In order to measure the systematic uncertainties, event samples with a high purity of muon, electron, and proton tracks are chosen. The results from the muon studies can also be used for pions, due to muons and pions having similar energy loss in the TPCs. Between particle types, no correlation is needed, while uncertainties between the momentum bins and TPCs are 100% correlated for each particle. Furthermore, uncertainties on the pull mean are 100%

correlated with the uncertainty on the pull width for each type of particle.

FGD Particle Identification: Because non-interacting particles that stop in the FGDs lose all their kinetic energy through ionization, a mass for the particle can be determined by using the energy deposited along the FGD segment. A pull for the particle hypothesis can be generated by calculating the difference between the measured and predicted energy deposit at a given range, normalized by the predicted energy spread for this range. The uncertainty on the measured particle pull comes from correctly choosing the particle based on its pull. Furthermore, measuring the deposited energy depends on the uncertainty from the thickness of the scintillator coating and the charge reconstruction. As the data to Monte Carlo charge reconstruction and differences in the scintillator coating thickness are the same for FGD1 and FGD2, this systematic uncertainty is correlated between the FGD1 and FGD2 selections.

Studies for the FGD PID systematic uncertainty used control samples with events containing a single muon and proton tracks which stopped in either FGD1 or FGD2 [110]. The control samples were created using the TPC PID and then compared with the FGD PID to calculate the efficiency for correctly identifying a muon or proton. The systematic uncertainty for charged pion identification uses the same values as those measured for muons, because the FGD PID does not strongly distinguish between the two.

FGD Time of Flight: In order to determine the track direction and select which FGD volume the neutrino interacted in, the average hit time between FGD1 and FGD2 is compared. A track which crosses both FGDs is reconstructed as backwards going when the average hit time in FGD1 is at least three nanoseconds greater than the average hit time in FGD2 [7]. The systematic uncertainty on the time of flight, therefore, directly affects whether an event is reconstructed as having occurred in FGD1 or FGD2.

This systematic uncertainty directly uses the analysis neutrino sample, instead of a control sample. Events with tracks passing through FGDs are then selected from this sample. The final uncertainty for the time of flight is $\delta\Delta t_{12} = 0.78$ ns and is added directly to the

reconstructed time of flight as $\alpha \times \delta\Delta t_{12}$, where α is a random variable associated with the systematic variations. Because this uncertainty comes from timings calculated in FGD1 and FGD2, it is considered to be 100% correlated between selections for FGD1 and FGD2.

TPC Cluster Efficiency: The uncertainty on correctly reconstructing a cluster, or series of hits, in the TPCs arises from differences in the reconstruction efficiency in the data and Monte Carlo. If not enough clusters are reconstructed in an event, then that event will fail to pass the fiducial volume cut described in Chapter 5. When this happens, the data and Monte Carlo can give different fractions of events passing the initial selection cuts. The efficiency and its uncertainty are calculated for reconstructed clusters in both the horizontal and vertical direction. Because the uncertainty for both horizontal and vertical clusters comes primarily from the underlying hit efficiency, the uncertainty is correlated between the horizontal and vertical clusters.

To determine the cluster reconstruction efficiency difference, two studies using control samples were run. For the horizontal cluster efficiency, control samples of cosmic trigger events with vertical tracks crossing TPC2 were used. On the other hand, for the vertical cluster efficiency, a control sample of CC inclusive events originating in FGD1 was used. This was to ensure mostly horizontal tracks were reconstructed with vertical clusters. The final cluster efficiencies are listed in Table 6.1.

Cluster Type	$(\epsilon^{MC} - \epsilon^{data})/\epsilon^{MC}$	$\epsilon^{data}/\epsilon^{MC}$
Vertical	0.0011 ± 0.0002	0.9989 ± 0.0002
Horizontal	0.0007 ± 0.0001	0.9993 ± 0.0001

Table 6.1: Results for the difference in the TPC cluster efficiency between data (ϵ^{data}) and MC (ϵ^{MC}). Table from [7].

TPC Track Reconstruction Efficiency: This systematic uncertainty describes the efficiency of the TPC reconstruction algorithm successfully reconstructing the tracks from particles

crossing the TPCs. Failing to properly do this can lead to choosing the incorrect event topology for an event, resulting in a miscounting of the total number of events in the CC inclusive sample and migration of events between the subsamples. The TPC track reconstruction efficiency is fully correlated between the three TPCs.

The efficiency is calculated from studies using control samples of through-going muons from beam and cosmic events. These are used to measure the reconstruction efficiency when no other tracks are in the TPC. In order to study the effect of track length on the reconstruction efficiency, the efficiency from cosmic muons with barrel electromagnetic calorimeter tracks are used [7]. The efficiency is then calculated separately for each TPC and are shown in Table 6.2. The studies of the reconstruction efficiency reveal a high overall efficiency with no momentum or angular dependence.

	TPC1	TPC2	TPC3
Data Efficiency	$99.9^{+0.1}_{-0.1}$ %	$99.7^{+0.2}_{-0.7}$ %	$99.3^{+0.5}_{-0.2}$ %
MC Efficiency	$99.6^{+0.2}_{-0.3}$ %	$99.5^{+0.3}_{-0.4}$ %	$99.8^{+0.1}_{-0.2}$ %

Table 6.2: TPC track reconstruction efficiencies for data and Monte Carlo. Table from [8].

Track Charge Identification: In order to determine the charge of the tracks in the TPC, the reconstruction uses information about the track from the full detector, while charge identification in the TPC and additional information from the overall track reconstruction is used to determine the sign of the charge [111]. Two different sources contribute to the uncertainty on the TPC charge identification: the probability of getting the TPC charge incorrect and the probability of incorrectly switching the TPC charge sign in the overall charge identification. The efficiency is calculated as the probability that the overall charge is different from the TPC reconstructed charge.

Studies of this systematic uncertainty were done using a control sample of tracks starting in the PØD and having at least one TPC segment [111]. These studies showed the uncertainty

on the charge identification depends on the reconstructed momentum error. Due to this dependence, the uncertainty is 100% correlated between the different cases as well as being 100% correlated between the FGD1 and FGD2 selections.

FGD-TPC Matching Efficiency: This systematic uncertainty characterizes how well FGD tracks are matched to TPC tracks during reconstruction. If tracks are incorrectly matched, it is possible to localize the track vertex at the wrong position, leading to a miscount in the number of CC inclusive interactions occurring in the FGDs. The efficiency depends on the ability to match a TPC track to a single hit in an adjacent FGD as well as the ability to correctly match a FGD-TPC matched track with an upstream TPC track. Uncertainty due to incomplete matching from out of fiducial volume (OOFV) event migration is not included, but receives its own systematic uncertainty and is discussed below.

The efficiency for this uncertainty was calculated using a control sample of cosmic events with large angles with respect to the neutrino beam that had only one FGD1 – TPC2 – FGD2 track. The studies showed the efficiency for FGD-TPC matched tracks to be 100% for tracks that had more than two hits in the FGD and had an upstream TPC track. This was consistent between the two FGDs. For tracks with two or less matched hits in the FGDs, the efficiencies and uncertainties are shown in Table 6.3. This systematic uncertainty is 100% correlated between FGD1 and FGD2, because the efficiency only pertains to the final two layers in each FGD, which share the same uncertainties in the scintillator bar properties.

	FGD1	FGD2
Data Efficiency	96.9 ± 0.8 %	96.5 ± 0.85 %
MC Efficiency	97.6 ± 0.45 %	97.6 ± 0.50 %

Table 6.3: Efficiencies for FGD-TPC matched tracks with two or less reconstructed hits in the corresponding FGD for data and Monte Carlo. Table from [9].

FGD Hybrid Track Efficiency: The FGD hybrid track efficiency systematic uncertainty characterizes the efficiency of correctly reconstructing a true FGD-only track in the presence

of a FGD-TPC matched track (any pertinent FGD-only tracks in the selections have an FGD-TPC matched track, by definition). FGD-only tracks without an accompanying FGD-TPC matched track are not considered in this efficiency. Because FGD-only tracks are assumed to be either protons or pions, the studies for this uncertainty were performed separately for each particle type.

In order to study the efficiency, a control sample with either one reconstructed track entering the TPC or two tracks which both enter the TPC was used. The "hybrid" portion of the name comes from the use of a particle gun in GEANT4 to generate stopping proton and pion tracks for the FGD-only tracks [110]. These particles were generated with a uniform energy distribution and scattered isotropically throughout the detector. A lower bound of 400 MeV/c was set for the proton momentum due to difficulties reconstructing events below that momentum. The hits from these tracks were then added to the control sample events for both data and Monte Carlo and the FGD-only track reconstruction. After the reconstruction had been run, the efficiency was defined as the number of selected events having at least one reconstructed FGD-only track divided by the total number of selected events in the control sample. Because the FGD-only track reconstruction has a strong dependence on the angle of the track, the efficiency is binned in $\cos\theta$, where θ is the true angle between the muon candidate and the FGD-only track. The overall systematic uncertainty for the pion and proton studies was less than 8% for the track efficiency [110].

Michel Electron Efficiency and Purity: The systematic uncertainty on the Michel electron selection comes from the efficiency of detecting the Michel electron and the purity of the cut. The efficiency to detect a Michel electron is dependent on the probability the electron produces enough hits in the FGD to pass the cut. Cosmic muons stopping in either FGD1 or FGD2 were used as a control sample to study this efficiency. Because muons with large angles do not always pass through a TPC, a PID cut based on the length of the track and its momentum was used to identify the muons [10].

In these studies, the efficiency was calculated separately for T2K runs 2 – 4 using data with cosmic triggers. The efficiency is then defined as the probability to detect an expected Michel electron due to there being a stopped muon in the FGD. Whereas the Michel purity relies on the beam power of each run, the efficiency does not; therefore, the average efficiency of the samples is used for data at all beam powers. Final efficiency values are shown in Table 6.4.

	FGD1	FGD2
Data	56.4 ± 1.6 %	42.8 ± 1.1 %
MC	56.5 ± 1.9 %	41.4 ± 1.4 %

Table 6.4: Efficiencies for the detection of Michel electrons for data and Monte Carlo (MC). Table from [10].

The purity of the Michel electron samples is largely dependent on background from out-of-FGD beam interactions in the detector and magnet volumes, sand muon interactions, and cosmic muons being identified as Michel electrons. Because the Michel electron cut is used to separate CC0π events from non-CC0π events, misidentifying a Michel electron can cause a CC0π event to be labeled as a CC1π or CCOther event. In order to study the external background rate, empty beam spills were selected to remove any products from interaction decays in the FGDs. Furthermore, the measurement was done separately for each run, because the rate is dependent on the average beam power, which can differ between runs. This results in a clean selection of true external background events, which will give a false Michel electron rate proportional to that which is in the physics selections. The same selections were used for both data and Monte Carlo, because no truth information is needed.

As the average beam power changes from run to run, the overall external background rate in both data and Monte Carlo also changes. Between runs 3 and 4 in the data, the beam power increased for data, whereas it remained fairly consistent for the Monte Carlo leading to the difference in the background event rate shown in Table 6.5. It should be noted the production of Monte Carlo occurs infrequently, so an average beam power is chosen during production.

In general, the background rates for data are higher than in Monte Carlo for both FGDs. This is due to through-going cosmic muons leaving many hits in time bins between bunches. In the beam and sand Monte Carlo, cosmic muons are not simulated, leading to a discrepancy in the hit distribution between the data and Monte Carlo and results in consistently lower overall rates in simulation than in data.

	FGD1		FGD2	
	MC ($\times 10^{-3}$)	Data ($\times 10^{-3}$)	MC ($\times 10^{-3}$)	Data ($\times 10^{-3}$)
Run 2	0.603 ± 0.008	1.61 ± 0.05	0.314 ± 0.006	1.21 ± 0.05
Run 3	0.714 ± 0.009	1.80 ± 0.04	0.397 ± 0.006	1.31 ± 0.03
Run 4	0.729 ± 0.009	2.00 ± 0.07	0.387 ± 0.006	1.50 ± 0.06

Table 6.5: Data and Monte Carlo (MC) rates for false Michel electron identification. The rate is defined as the number of expected false Michel electrons per spill. Table from [7].

FGD Masses: The systematic uncertainty of the FGD masses is caused by differences in the simulated and real detector volumes of the scintillator and water module areal densities [11]. Because the water modules are only in FGD2, the uncertainty on the water volume density only applies to FGD2, while the uncertainty in the scintillator XY modules is applicable to both FGDs. The FGD mass uncertainty is implemented as an uncertainty on the densities of the modules, including the coating of the scintillator modules and the polycarbonate vessels for the water modules.

The total uncertainty for the XY modules is a combination of the data – MC difference in mass and direct mass measurements of the XY modules, which can be seen in Table 6.6. On the other hand, the total uncertainty in the water module mass is a combination of the data – MC difference and an uncertainty of each water module, which is dominated by the masses of the plastic and glue, and can also be seen in Table 6.6. The water and scintillator mass uncertainties are treated as separate, because the uncertainty is assigned based on the true vertex location [7]. The correlations between the different components can be seen in Table 6.7.

Module	Difference	Uncertainty	Total
XY	0.41 %	0.38 %	0.6 %
Water	0.26 %	0.46 %	0.55 %

Table 6.6: Data – Monte Carlo (MC) difference, the uncertainty due to direct measurements, and the total uncertainty for the XY and water modules in the FGDs. Table from [11].

	FGD1 total	FGD2 total	FGD2 water-like	FGD2 XY-like
FGD1 total	1	0.70	0	0.84
FGD2 total	0.70	1	0.50	0.91
FGD2 water-like	0	0.50	1	0.26
FGD2 XY-like	0.84	0.91	0.26	1

Table 6.7: Correlations in uncertainties between mass components. "FGD2 water-like" and "FGD2 XY-like" refer to the water module and XY module portions of FGD2, respectively. Table from [7].

Pion Secondary Interactions: Whenever pions are produced in interactions at ND280, there is a chance they interact within the detector producing detection inefficiencies for pions in the FGDs. This process can occur through absorption, decay, quasi-elastic scattering, and other methods. These processes are collectively know as "secondary interactions" (SI). Because pions are the distinguishing feature when defining which topology an event falls under during the selection process described in Chapter 5, it is vital secondary interactions are properly modeled in the Monte Carlo. It has been shown that the model used by GEANT4 for pion interactions does not match well with existing data of pion interactions on nuclei [112]. Therefore, a correction weight is applied to these events. The uncertainty is calculated using studies that compare ND280 data and Monte Carlo as well as uncertainties from external data of pion interactions. The calculated event weight is based on the probabilities of each true pion trajectory in an event interacting for different cross section models. The probabilities are energy dependent and calculated in steps of 0.1 mm along the trajectory. This is done separately for each target nucleus, where the uncertainty is treated as independent for each target, but 100% correlated between FGD1 and FGD2 for each target.

Proton Secondary Interactions: Similar to pions, an outgoing proton from an interaction in ND280 has the ability to go through secondary interactions in the detector. Studies using a control sample of all true protons originating from the neutrino interaction and having undergone an interaction in the volume of interest were performed. The uncertainty in the cross section for the proton secondary interactions is taken into account by applying a weight dependent on how far the the proton traveled before interacting and the density of the scattering medium. The effect of this systematic uncertainty is small [113], but a conservative approach was taken, so it is included in this analysis.

Sand Muon Background: The primary Monte Carlo for ND280 only includes beam events occurring in the ND280 subdetectors and the surrounding magnet. However, interactions from beam neutrinos can occur in the sand outside the detector pit as well as in the pit walls where ND280 is situated. These interactions can look similar to interactions occurring in the FGDs and provide a background to the analysis. Such events are called sand muons, because the primary source of these events is from interactions in the surrounding sand. A dedicated Monte Carlo sample is produced for sand muon events to estimate the effects on the analysis samples, as these events are not included in the primary Monte Carlo.

The event rate of sand muons is estimated by running the selections described in Chapter 5 over the sand muon Monte Carlo, where the data POT is scaled to get the predicted sand muon event rate. The uncertainty on this background is estimated as the difference between the Monte Carlo and data rates and is done separately for positively and negatively charged tracks. The systematic uncertainty was determined to be 10% for neutrino mode and 30% for antineutrino mode [7]. No correlation is applied between beam modes as well as between FGD1 and FGD2, as the underlying cause for the uncertainty is due to the interactions occurring outside the detector volume.

OOFV Background: The out-of-fiducial volume background systematic uncertainty covers interactions that occur outside of the FGD fiducial volumes, but is reconstructed as being

inside either the FGD1 or FGD2 fiducial volume. This includes interactions in one of the other subdetectors or in the first two layers or FGD1 or the first layer of FGD2. There are two main contributing uncertainties on the background rates, the uncertainty on the interaction rates within the other subdetectors and the uncertainty on specific classes of reconstructed events in the FGDs.

The uncertainty on the rate is divided into four categories based on where the true vertex of the interaction occurred, whether it was in the PØD, the ECal, the SMRD, or other subdetectors. The relative difference in the interaction rate between the data and Monte Carlo was studied using neutrino beam data, instead of control samples. The difference is then used as the uncertainty for each of the interaction rates, which are shown in Table 6.8. As each interaction is unrelated to the others, they are uncorrelated with each other. Due to the interactions occurring outside of the FGDs, the underlying sources of the uncertainties are the same for FGD1 and FGD2, so the systematic uncertainty is fully correlated between the two FGDs.

Background Origin	FHC ν_μ	RHC $\bar{\nu}_\mu$	RHC ν_μ
PØD	5.1 %	8.4 %	5.4 %
ECal	11.6 %	8.8 %	6.7 %
SMRD	4.9 %	6.7 %	4.8 %
Other	13.6 %	13.5 %	24 %

Table 6.8: Uncertainties on the OOFV rates based on their subdetector origin. Table from [12].

There are a number of different categories of the reconstruction uncertainties; however, not all of the categories have a significant uncertainty, even if they contribute to the total background rate. An example of this is a neutral particle (which will not leave a track in the detector) enters the FGD, then interacts and creates charged secondary particles. The categories which have a significant source of uncertainty include events starting in the tracker components downstream of the FGD, high angle events, events with a hard scatter in the FGD, events

where hits are not deposited for two consecutive layers, and "last module failure" events, where events are not matched because most hits were missing in the FGD.

Typically, the reconstruction rate and uncertainty are not dependent on the track momentum, so the systematic uncertainty can be calculated separately for each category [12]. Each category is sufficiently different from the others that no correlation is assumed between them. Within each category, FGD1 and FGD2 are fully correlated, because the categories rely mainly on the hit efficiencies of the FGDs. The uncertainties were calculated using events which were known to have started outside the FGD fiducial volume, such as cosmic events, and comparing the rates for the data and Monte Carlo. The non-zero categories are shown in Table 6.9.

Category	FGD1	FGD2
Downstream Event	5 %	5 %
High Angle Event	33 %	28 %
Last Module Failure	35 %	17 %
Consecutive Skipped Layers	55 %	82 %
Hard Scattering	32 %	21 %

Table 6.9: Reconstruction uncertainties for OOFV based on their reconstruction category. Table from [12].

Event Pile Up: Event pile up is the result of an out-of-fiducial volume event being coincident with an in-fiducial volume CC inclusive event in either FGD. This can lead to CC inclusive events being thrown out from the selection due to the external veto cut described in Section 5.3.1.1. The primary source of pile up comes from sand muons for both FHC and RHC selections [7]. The uncertainty on the event pile up is dependent on the beam intensity and mode. While the source of the uncertainty is consistent for different intensities for neutrino or antineutrino mode, it is not necessarily similar between the two modes. Therefore, the two beam modes are treated as uncorrelated, while the beam intensity is 100% correlated within a given beam mode.

As with the sand muon systematic uncertainty, a correction is applied to the Monte Carlo to account for event pile up. Because of the 10% uncertainty for FHC and 30% uncertainty for RHC from the sand muon background uncertainty, as well as other potential differences between the sand muon Monte Carlo and data, a systematic uncertainty is applied on the correction. This uncertainty is based on the difference between data and simulation, which is calculated by comparing the number of TPC1 or TPC2 events per bunch in the data and simulation.

6.2 Propagation of the Detector Systematic Uncertainties

In order to perform the selections described in Chapter 5, evaluate detector systematic uncertainties, and store relevant event information, ND280 analyses use a specialized software package called Psyche (Propagation of SYstematics and CHaracterization of Events). The Psyche package was developed specifically for use with ND280 events. It is able to use both the reconstructed and true event information from Monte Carlo as well as the reconstructed information from data events. While the selections only use reconstructed information from the events, the calculation of the systematic uncertainties uses true event information and is only used with Monte Carlo events. Psyche does not perform any fits itself, rather it is designed to be used within the ND280 fit software and is optimized for low memory use and speed. This section will discuss how Psyche goes about calculating and propagating the different detector systematic uncertainties.

There are two types of systematic uncertainties, depending on how the uncertainty is propagated to the events passing the selection cuts. Observable variation systematic uncertainties, described in Section 6.2.1, vary the reconstructed quantities in events, allowing events to move in and out of selections. These are propagated by rerunning the selection using the varied quantities in order to determine the effect on the number of selected events.

On the other hand, weight systematic uncertainties, as described in Section 6.2.2, apply a weight to each simulated event, without altering the reconstructed quantities themselves. The weight uncertainties are split into two groups, efficiency-like and normalization weights. Efficiency-like

weights are related to a reconstruction or detector probability, where the weight is computed from the probability after running the selection once. Normalization weights generally are associated with the subsamples of the selection and scale the event rate up and down.

6.2.1 Observable Variation Systematics

As mentioned previously, observable variation, or variation, systematic uncertainties are those which allow events to move into and out of selections and, in rare cases, are able to shift an event out of the inclusive selection. When comparing the data and Monte Carlo, differences between the mean values of these distributions can be seen. The variations alter the reconstructed quantities, such as the track momentum and angle, in order to correct for the observed difference. The uncertainties on the systematics are propagated by smearing the relevant reconstructed variables and then rerunning the selection on the smeared event. Depending on the features of the uncertainties, the smearing can be implemented differently. There are four main classes of uncertainties for the observable variations:

1. When the true observable is known, the difference between the reconstructed variable, x_{rec}^{MC}, and its true value, x_{true}, is rescaled. This smeared value is given by,

$$x'_{rec} = x_{true} + (x_{rec}^{MC} - x_{true})(s + \alpha \times \delta s), \tag{6.1}$$

   where α is a random variable corresponding to the probability distribution function (PDF) of the systematic uncertainty, s is a scale factor defined by $\sigma_x^{data}/\sigma_x^{MC}$, and δs is defined as

$$\delta s = s \times \left| \frac{\delta\sigma_x^{data}}{\sigma_x^{data}} - \frac{\delta\sigma_x^{MC}}{\sigma_x^{MC}} \right|. \tag{6.2}$$

   This is used for the momentum resolution and the resolution of the measured deposited charge.

2. When a correction must be applied to the Monte Carlo observable value to match the mean difference between the data and Monte Carlo values, $\Delta\bar{x}$. The altered value, in this case,

becomes

$$x'_{rec} = x^{MC}_{rec} + \Delta\bar{x} + \alpha \times \delta\Delta\bar{x}. \tag{6.3}$$

α is a random variable associated with the corresponding PDF and $\delta\Delta\bar{x}$ is the systematic uncertainty, defined as

$$\delta\Delta\bar{x} = \sqrt{\Delta\bar{x}^2 + (\delta\bar{x}^{data}_{rec})^2 + (\delta\bar{x}^{MC}_{rec})^2}, \tag{6.4}$$

where $\delta\bar{x}^{data(MC)}_{rec}$ is the mean error in the data or Monte Carlo sample. This approach is used for the mean difference of the deposited charge pull. In the case of the time of flight systematic uncertainty, a similar principle is used. However, the MC is not corrected by $\Delta\bar{x}$. The uncertainty for this systematic is the quadratic sum between $\Delta\bar{x}$ and the error of the timing difference distribution,

$$\delta\Delta\bar{x} = \sqrt{\Delta\bar{x}^2 + (\sigma^{data}_{x} - \sigma^{MC}_{x})^2}. \tag{6.5}$$

3. When the reconstruction is altered, x^{alter}_{rec}, to account for a change in the underlying parameter, the new value is

$$x'_{rec} = x^{MC}_{rec} + \alpha(x^{alter}_{rec} - x^{MC}_{rec}). \tag{6.6}$$

This method is used for the magnetic field distortions. For the magnetic field distortions, α is assumed to be a random value in a uniform distribution between 0 and 1.

4. When the observable depends on a scale, s, the altered value is

$$x'_{rec} = x^{MC}_{rec} + \alpha x^{MC}_{rec}\delta s, \tag{6.7}$$

where $x^{MC}_{rec}\delta s$ is the error of the observable. This primarily deals with the momentum scale systematic uncertainty, which relies on the magnet current as its error.

6.2.2 Weight Systematics

Whereas variation systematics have the ability to move events between selections, weight systematics only affect the weight given to a particular event and does not change any of the reconstructed

event values. In the case of efficiency-like systematics, studies comparing data and MC predictions of well known control samples are used to determine the event weights. For example, tracking and matching efficiencies can be computed using redundancy between detectors, such as using tracks with segments in FGD1 and FGD2 to calculate the TPC2 track efficiency. Rather than using analysis samples, which typically do not meet the special requirements needed to calculate these systematics, control samples are used instead. However, the control samples do not always accurately reflect the complexity of the analysis samples and tend to cover a limited phase space. Therefore, the efficiencies calculated using the control samples do not match exactly those of the analysis samples, so a model must be used to extrapolate the control sample efficiency to the analysis sample. A reasonable assumption to use in this model is that the ratio between the data and MC efficiencies is the same for both types of samples [7].

The predicted efficiency of the data analysis sample is

$$\epsilon = \frac{\epsilon^{CS}_{data}}{\epsilon^{CS}_{MC}} \epsilon_{MC}, \tag{6.8}$$

where the $\epsilon^{CS}_{data(MC)}$ are the efficiencies determined from the control samples and ϵ_{MC} is the efficiency of the MC analysis sample. The MC analysis sample efficiency can be determined using truth information. Because there is a limited precision on the efficiencies of the control samples, their statistical error must be taken into account when propagating these uncertainties. Therefore, the systematic uncertainty represents the statistical error of the samples as well as the difference between data and Monte Carlo. In general, the predicted efficiency can then be given by

$$\epsilon'_{data} = (r^{CS} + \alpha \delta r^{CS}) \epsilon_{MC}, \tag{6.9}$$

where $r^{CS} = \epsilon^{CS}_{data}/\epsilon^{CS}_{MC}$ and $\delta r^{CS} = \sqrt{(1 - r^{CS})^2 + (\delta r^{CS}_{stat})^2}$, where δr^{CS}_{stat} is the statistical error on the efficiency ratio. α is a random variable from a Gaussian distribution of mean, 0, and standard deviation, 1. For determining the event weight, there are two definitions that are used, depending on whether it is appropriate to apply an efficiency or an inefficiency. The efficiency weight, w_{eff}, is

$$w_{eff} = \frac{\epsilon'_{data}}{\epsilon_{MC}}, \tag{6.10}$$

while the inefficiency weight, w_{ineff}, is

$$w_{ineff} = \frac{1 - \epsilon'_{data}}{1 - \epsilon_{MC}}. \tag{6.11}$$

Normalization systematic uncertainties, on the other hand, are related to the total event normalization. Examples of these uncertainties are the event pile up or sand muon background, which correspond to out-of-fiducial volume events coincident with in-fiducial volume events or events occurring in the sand surrounding the detector, respectively. The events are weighted according to variations suggested by systematic error studies and are given by

$$w_e = 1 + \alpha \times \delta e_{cat}, \tag{6.12}$$

where w_e is the event weight for the given systematic uncertainty, α is the random variable given by the PDF of the uncertainty, and δe_{cat} is the systematic error associated with the category of events. If an event is not part of the category of events in question, it is given a weight of 1.0.

6.3 Summary of the Individual Systematic Uncertainties

The near detector fit uses six observable variation and twelve weight systematic uncertainties. These eighteen uncertainties will briefly be described Section 6.1. Table 6.10 lists these uncertainties, their type, the type of PDF used, their propagation model, the type of data used to calculate the uncertainty, and which set of samples the uncertainties are applied to.

In general, many of these uncertainties contribute small amounts to the overall detector systematic uncertainty, as can be seen in Tables 6.11 and 6.12. By far, the largest contributor to the overall uncertainty is the pion secondary interactions uncertainty, due to the large difference seen in the data and Monte Carlo.

6.4 The Observable Normalization Matrix

As discussed in Section 4.3.3, the near detector fit does not use the detector systematic uncertainties directly for computational reasons. Rather, these parameters are fit using observable normalization parameters, which are binned in $p - \cos\theta$ for each sample, and a covariance matrix

Uncertainty	Type	PDF	Propagation Model	Data Used	Samples
TPC Field Distortions	Variation	Uniform	Observable Variation	Calibration	Pi / Track
TPC Momentum Scale	Variation	Gaussian	Observable Variation	Calibration	Pi / Track
TPC Momentum Resolution	Variation	Gaussian	Observable Variation	Control Samples	Pi / Track
TPC PID	Variation	Gaussian	Observable Variation	Control Samples	Pi / Track
FGD PID	Variation	Gaussian	Observable Variation	Control Samples	Pi only
FGD Time of Flight	Variation	Gaussian	Observable Variation	Physics Samples	Pi / Track
TPC Cluster Efficiency	Weight	Gaussian	Efficiency-like	Control Samples	Pi / Track
TPC Track Reconstruction Efficiency	Weight	Gaussian	Efficiency-like	Control Samples	Pi / Track
Track Charge Identification	Weight	Gaussian	Efficiency-like	Control Samples	Pi / Track
FGD-TPC Matching Efficiency	Weight	Gaussian	Efficiency-like	Control Samples	Pi / Track
FGD Hybrid Track Efficiency	Weight	Gaussian	Efficiency-like	Control Samples	Pi only
Michel Electron Efficiency and Purity	Weight	Gaussian	Efficiency-like	Control Samples	Pi only
FGD Masses	Weight	Gaussian	Normalization	External Data	Pi / Track
Pion Secondary Interactions	Weight	Gaussian	Normalization	External Data	Pi / Track
Proton Secondary Interactions	Weight	Gaussian	Normalization	External Data	Pi / Track
Sand Muon Background	Weight	Gaussian	Normalization	Simulation	Pi / Track
OOFV Background	Weight	Gaussian	Normalization	Physics Samples	Pi / Track
Event Pile Up	Weight	Gaussian	Normalization	Simulation	Pi / Track

Table 6.10: The detector systematic uncertainties used within the BANFF fit. The final column shows which sets of samples the uncertainties apply to. The samples listed as "Pi" apply to MultPi samples, while "Track" applies to the MultiTrack samples.

which describes the uncertainties and correlations in these bins. The binning for the observable normalization parameters and covariance is more coarse than the fit binning described in Chapter 5 for computational and time considerations. The selection binning used in the fit is designed to have all non-zero bins for the Monte Carlo prediction, which would give over 800 normalization parameters for the FGD1 FHC CC0π sample alone. If the binning for the observable normalization parameters was the same as the fit binning, there would be over 4000 nuisance parameters just for the detector portion. The time required to fit such a large parameter space quickly becomes prohibitive. Therefore, a coarser binning is used to reduce the number of parameters in the fit.

For the neutrino mode samples, the $p - \cos\theta$ binnings are:

- **CC0π bin edges:**

  p [MeV/c]: 0, 200, 400, 550, 600, 650, 700, 750, 900, 1050, 2500, 5000, 30000

  $\cos\theta$: -1.0, 0.6, 0.83, 0.89, 0.94, 0.975, 0.985, 0.99, 0.995, 1.0

Systematic Uncertainty	Inclusive	CC1π	CC0π	CCOther
DETECTOR VARIATION SYSTEMATICS				
TPC Field Distortions	0.0393	0.0245	0.0630	0.0720
TPC Momentum Scale	0.0877	0.0621	0.0737	0.2295
TPC Momentum Resolution	0.0823	0.0549	0.0945	0.2861
TPC PID	0.3428	0.3160	0.7923	0.6163
FGD PID	0.0002	0.0110	0.0339	0.0149
FGD Time of Flight	0.0381	0.0344	0.0704	0.0178
EFFICIENCY-LIKE SYSTEMATICS				
TPC Cluster Efficiency	0.0006	0.0004	0.0006	0.0019
TPC Track Reconstruction Efficiency	0.4221	0.2592	0.4398	1.7861
Track Charge Identification	0.1276	0.1782	0.2704	0.4732
FGD-TPC Matching Efficiency	0.2298	0.1480	0.2703	0.6046
FGD Hybrid Track Efficiency	0.0385	0.1062	0.0999	0.5327
Michel Electron Efficiency and Purity	0.0011	0.0622	0.2529	0.0076
NORMALIZATION SYSTEMATICS				
FGD Masses	0.5926	0.5945	0.5818	0.5967
Pion Secondary Interactions	2.1245	1.4332	3.1731	6.1183
OOFV Background	0.3975	0.3907	0.5409	0.2858
Event Pile Up	0.1117	0.1117	0.1117	0.1117
ALL				
All Magnet Uncertainties	2.2927	1.6582	3.3276	6.4665
Sand Muon Background	0.0671	0.0692	0.0849	0.0309
TOTAL	2.2937	1.6597	3.3287	6.4666

Table 6.11: Integrated uncertainty for each of the systematic uncertainties in FGD1. The proton secondary interactions systematic uncertainty is not included as it has a small effect on the sample. Table from [7].

- **CC1π bin edges:**

  p [MeV/c]: 0, 400, 500, 600, 650, 700, 800, 900, 1000, 3000, 5000, 30000

  $\cos\theta$: -1.0, 0.6, 0.85, 0.88, 0.9, 0.92, 0.93, 0.97, 0.995, 1.0

- **CCOther bin edges:**

  p [MeV/c]: 0, 500, 600, 650, 700, 900, 1100, 3000, 500, 30000

  $\cos\theta$: -1.0, 0.6, 0.95, 0.98, 0.99, 0.995, 1.0

The binnings for the antineutrino mode samples are:

Systematic Uncertainty	Inclusive	CC1π	CC0π	CCOther
DETECTOR VARIATION SYSTEMATICS				
TPC Field Distortions	0.0971	0.0822	0.1581	0.0989
TPC Momentum Scale	0.0791	0.0478	0.0780	0.2343
TPC Momentum Resolution	0.1082	0.0786	0.1354	0.3404
TPC PID	0.4538	0.4273	1.2179	0.7854
FGD PID	0.0003	0.0088	0.0322	0.0185
FGD Time of Flight	0.0783	0.0735	0.0721	0.1130
EFFICIENCY-LIKE SYSTEMATICS				
TPC Cluster Efficiency	0.0006	0.0004	0.0005	0.0014
TPC Track Reconstruction Efficiency	0.5231	0.4624	0.6984	0.6801
Track Charge Identification	0.0935	0.1220	0.0766	0.0777
FGD-TPC Matching Efficiency	0.2850	0.2213	0.3186	0.6063
FGD Hybrid Track Efficiency	0.0030	0.0084	0.0320	0.0864
Michel Electron Efficiency and Purity	0.0043	0.0916	0.4294	0.0065
NORMALIZATION SYSTEMATICS				
FGD Masses	0.3893	0.3879	0.3888	0.3984
Pion Secondary Interactions	2.0518	1.4350	3.6126	5.5949
OOFV Background	0.4699	0.5255	0.4508	0.2053
Event Pile Up	0.1219	0.1219	0.1218	0.1218
ALL				
All Magnet Uncertainties	2.2734	1.6909	3.8818	5.9080
Sand Muon Background	0.0332	0.0364	0.0211	0.0281
TOTAL	2.2737	1.6913	3.8818	5.9081

Table 6.12: Integrated uncertainty for each of the systematic uncertainties in FGD2. The proton secondary interactions systematic uncertainty is not included as it has a small effect on the sample. Table from [7].

- $\bar{\nu}_\mu$ **CC0π bin edges:**

  p [MeV/c]: 0, 300, 400, 500, 550, 2000, 4000, 30000

  $\cos\theta$: -1.0, 0.6, 0.7, 0.8, 0.85, 0.9, 0.96, 1.0

- $\bar{\nu}_\mu$ **CC1π bin edges:**

  p [MeV/c]: 0, 500, 30000

  $\cos\theta$: -1.0, 0.7, 1.0

- $\bar{\nu}_\mu$ **CCOther bin edges:**

p [MeV/c]: 0, 600, 800, 30000

$\cos\theta$: -1.0, 0.7, 1.0

- ν_μ **CC0**π **bin edges:**

  p [MeV/c]: 0, 300, 500, 700, 800, 30000

  $\cos\theta$: -1.0, 0.7, 0.8, 1.0

- ν_μ **CC1**π **bin edges:**

  p [MeV/c]: 0, 600, 800, 30000

  $\cos\theta$: -1.0, 0.7, 1.0

- ν_μ **CCOther bin edges:**

  p [MeV/c]: 0, 600, 30000

  $\cos\theta$: -1.0, 0.7, 1.0

The same binnings are used for FGD1 and FGD2. In the case where multiple fit bins fall within a single normalization bin, the same observable normalization weight is used for all fit bins, because the choice of bin is dependent on the reconstructed momentum and angle.

In order to calculate the central values for the observable normalization parameters, 2000 variations of the detector systematic uncertainties are created. These uncertainties are then applied to the nominal Monte Carlo $p - \cos\theta$ distribution to create a set of 2000 varied distributions. The central values are then calculated for each $p - \cos\theta$ bin:

$$d_i = \frac{N_i^{mean}}{N_i^{nom}}, \tag{6.13}$$

where N_i^{mean} is the average number of events in bin i and N_i^{nom} is the nominal number of events in that bin. The covariance matrix elements are calculated via

$$(V_d)_{ij} = \frac{1}{1999} \sum \frac{(N_i^k - N_i^{mean})(N_j^k - N_j^{mean})}{N_i^{mean} N_j^{mean}}. \tag{6.14}$$

This gives a correlated set of parameters to use within the near detector fit. These parameters and their covariance are used under the assumption that the overall effect of the variations is Gaussian in all bins, which, to first order, is correct for bins with a large number of events. It should be noted, that bins with fewer than 20 events, on average, tend to have a more non-Gaussian shape.

The covariance matrix also includes uncertainties from other sources that can be binned in $p - \cos\theta$. These include the Monte Carlo statistical error and an uncertainty related to differences in the relativistic Fermi gas and local Fermi gas models, termed one particle – one hole (1p1h) effects, discussed in Section 4.3.2.1. The Monte Carlo statistical error is related to the uncertainty of using a finite amount of Monte Carlo when running the fit and in generating the covariance matrix. Rather than using the covariance binning, the statistical uncertainties are calculated for each fit bin. The largest fit bin uncertainty within a given covariance bin is then used as the statistical uncertainty for that bin. This is done to avoid underestimating the uncertainty due to the Monte Carlo statistics. These errors are included as uncorrelated error terms on the diagonal of the observable normalization covariance matrix. The size of the MC statistical errors can be seen in Figure 6.1.

As mentioned in Section 4.3.2.1, studies have shown that the choice of nuclear model can have a significant impact on the oscillation analysis. Therefore, an additional uncertainty is included to account for this effect. For the near detector fit, this is treated as an additional covariance term added to the observable normalization covariance matrix. This covariance is calculated as the bin-by-bin difference in muon kinematics between the NEUT and Nieves model predictions:

$$V_{ij}^{1p1h} = (N_i^{Nieves} - N_i^{NEUT}) \times (N_j^{Nieves} - N_j^{NEUT}), \tag{6.15}$$

where N_i^{Nieves} is the predicted event rate for the i-th bin of the Nieves 1p1h model, while N_i^{NEUT} is the predicted event rate for the i-th bin of the nominal NEUT model.

The observable normalization covariance, without the MC statistical errors or the uncertainty due to the 1p1h effects, can be seen in Figure 6.2, while the full covariance matrix can be seen in Figure 6.3.

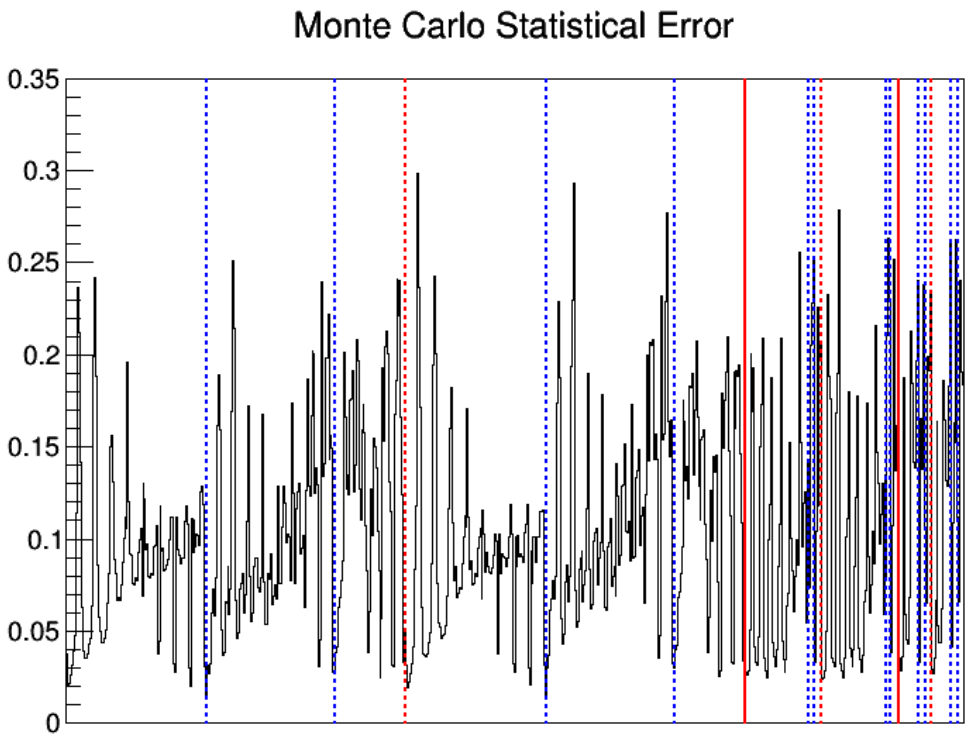

Figure 6.1: The fractional error included in the observable normalization covariance matrix due to the Monte Carlo statistical uncertainty. The blue dashed lines differentiate between the CC0π, the CC1π, and the CCOther samples, while the red dashed lines separate samples in FGD1 and FGD2. The solid red line demarcates the FHC MultiPi, RHC $\bar{\nu}$ MultiPi, and RHC ν MultiPi samples.

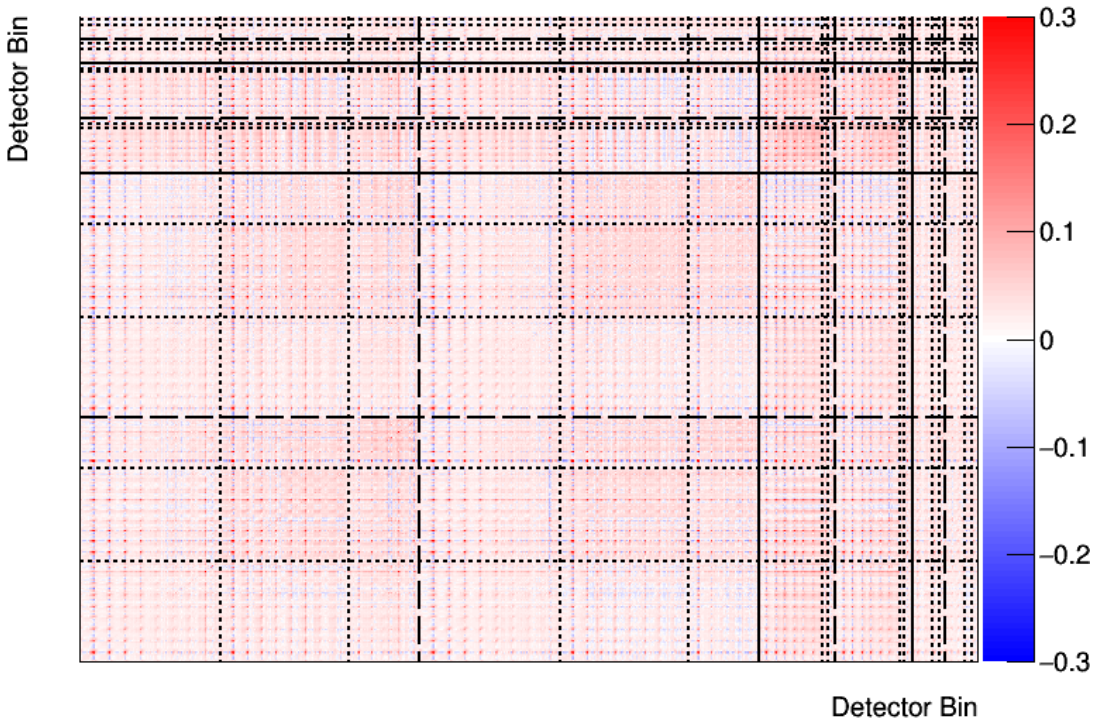

Figure 6.2: The detector covariance matrix without the MC statistical uncertainties or the uncertainties from the 1p1h effects, plotted as $\mathrm{sgn}(V_{ij}) \times \sqrt{|V_{ij}|}$ for easier viewing. The short dashed lines differentiate between the CC0π, CC1π, and CCOther samples, while the long dashed lines separate FGD1 and FGD2 samples. The solid black lines separate the FHC MultiPi, RHC $\bar{\nu}$ MultiPi, and RHC ν MultiPi samples. Within each sample, the parameters are ordered from backward going to forward going angular bins. Each complete set of angular bins share a common momentum bin, which are ordered from lowest to highest momentum.

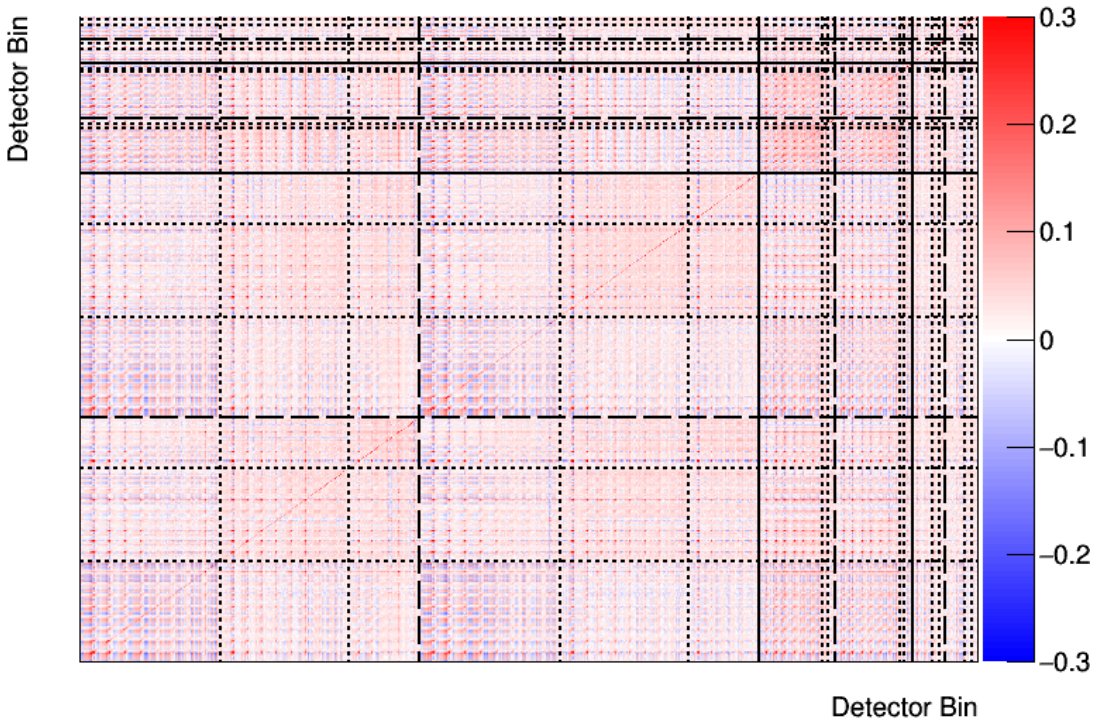

Figure 6.3: The full detector covariance matrix as input to the BANFF fit, plotted as $\mathrm{sgn}(V_{ij}) \times \sqrt{|V_{ij}|}$ for easier viewing. The short dashed lines differentiate between the CC0π, CC1π, and CCOther samples, while the long dashed lines separate FGD1 and FGD2 samples. The solid black lines separate the FHC MultiPi, RHC $\bar{\nu}$ MultiPi, and RHC ν MultiPi samples. Within each sample, the parameters are ordered from backward going to forward going angular bins. Each complete set of angular bins share a common momentum bin, which are ordered from lowest to highest momentum.

CHAPTER 7

RESULTS

In this thesis, one of the biggest changes made was the transition from the RHC MultiTrack to the RHC MultiPi samples in the likelihood fit. In Section 7.1, comparisons between fits run with the RHC MultiTrack samples and the RHC MultiPi samples are provided in order to show the full impact of the new samples. Furthermore, two additional studies, described in Sections 7.2 and 7.3, were performed to test alternate cross section models. At this time, work is being done on T2K to resolve differences seen between data and Monte Carlo for single pion production events, particularly in the outgoing pion spectrum. Each study compared the results of a fit to the nominal Monte Carlo with the results from a fit to Monte Carlo with the alternate cross section model. This comparison provides insight into whether there is freedom in the current cross section model to cover the differences in the underlying model.

7.1 Comparing RHC MultiTrack and RHC MultiPi Samples

As the results from the BANFF fit are included in the T2K oscillation analysis, it is important to understand how moving from the RHC MultiTrack samples to the RHC MultiPi samples affects the fit results. For example, do the CC1π parameters change dramatically when including the RHC MultiPi samples, due to the extra pion information found in these samples? Additionally, it is useful to see how the changes to the BANFF fit affect the Super-Kamiokande (SK) event distribution predictions, as large changes to the event predictions can provide hints at potentially large changes in the final values of the oscillation parameters determined by T2K.

7.1.1 Results

The first step in comparing the two samples sets is to see how their sensitivity to the input parameters differs. In order to test this, each sample set is fit to the nominal Monte Carlo, which shows the sensitivity of the fit to the model parameterization. For example, if there were two degenerate

parameters in the model, the fit would not be able to constrain those parameters as well as a non-degenerate parameter. As can be seen in Figure 7.1, the two sample sets have roughly the same sensitivity to the current parameterization[1]. Because there is virtually no difference in the sensitivity, both sets of samples should provide a similar amount of constraint to the oscillation analysis. However, it is beneficial to use the RHC MultiPi samples over the RHC MultiTrack samples, as they are more consistent with the samples used at SK. Additionally, when compared to the RHC MultiTrack samples, the RHC MultiPi samples have an improved purity with respect to the neutrino interaction types that are being modeled in the cross section model [7].

After observing that the two sample sets have a similar sensitivity to the current model parameterization, a separate fit for each sample set was performed using the T2K data. The results of these two fits can be seen in Figure 7.2. Overall, the fit parameters agree very well, particularly the parameters associated with the flux. Generally, differences between the two fits are expected due to the use of the RHC MultiPi samples, which more closely match the underlying interactions than the RHC MultiTrack samples. In particular, the differences in the FSI parameters can be described by the differences in the event topologies for the two sample sets. The FSI parameters affect the migration of events between samples through the interaction of pions within the nucleus. Because the number of outgoing pions is more important for the RHC MultiPi samples, the data in these samples could prefer different final values for the FSI parameters.

In a similar manner, the differences observed in the 2p2h normalization parameters are reasonable. The shift of the antineutrino normalization parameter to be closer to the neutrino normalization parameter shows evidence that the RHC MultiPi samples, when compared with the RHC MultiTrack samples, are better able to separate 2p2h events from events where the outgoing pion was missed in the reconstruction. Finally, the parameters related to single pion production, like the CC resonant pion production parameters, as well as the parameter for deep inelastic scattering and

[1] A comparison of the observable normalization parameters is not shown in this thesis, as the two sample sets did not have the same binning, making a direct comparison not a straightforward process. However, they were checked in order to verify the parameters were not pulled far from their input value and that no systemic shifts upward or downward occurred as a result of the fit.

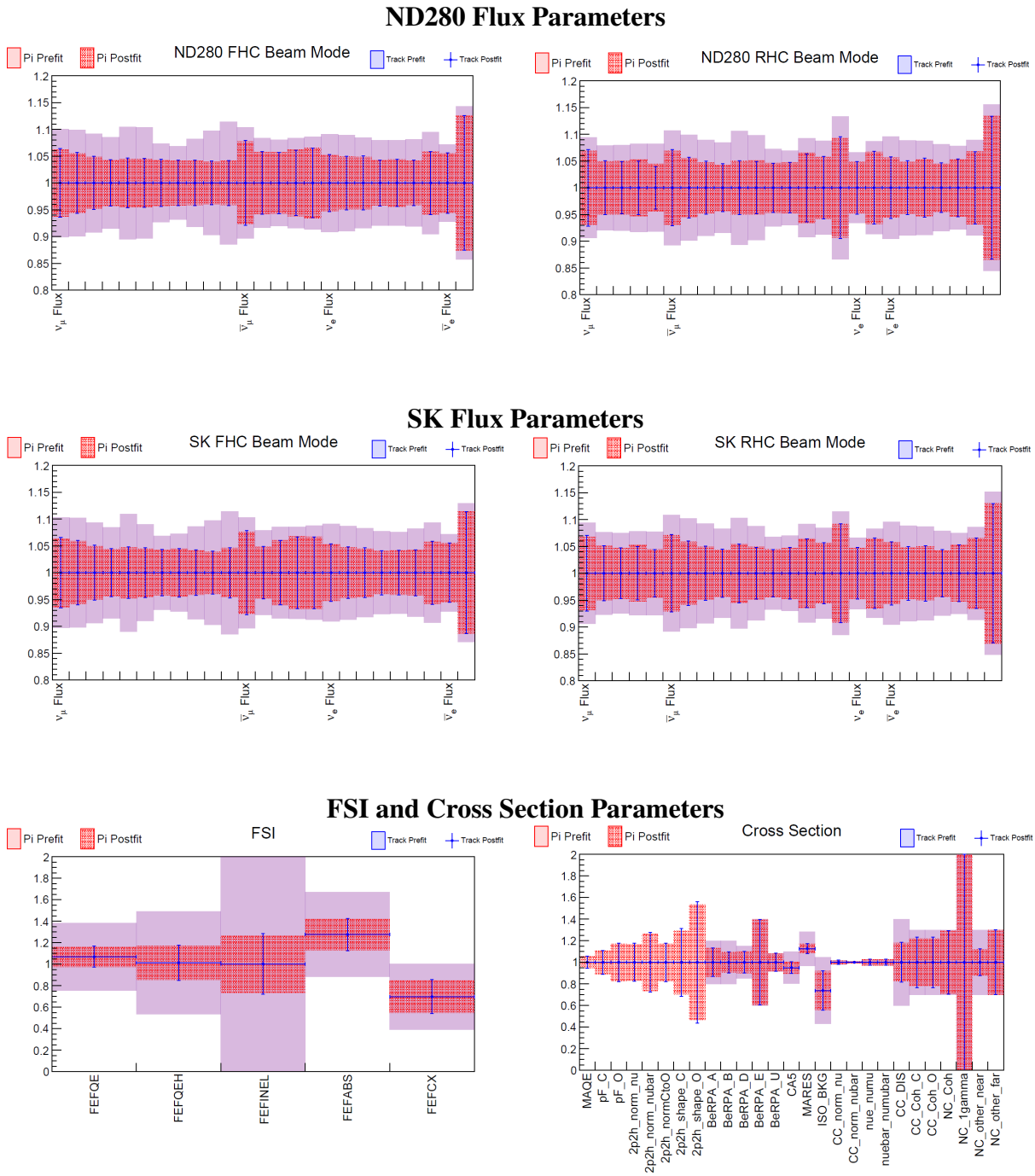

Figure 7.1: Comparison of fits to the nominal Monte Carlo for the RHC MultiTrack samples (blue) and the RHC MultiPi samples (red). The input parameter error bars can be seen in the background. Note, the CCQE cross section parameters do not have any prior constraint applied in the fit, so an input error band is not displayed for these parameters.

multiple pion production (DIS+Nπ) interactions exhibit some differences. However, because the new RHC MultiPi samples are designed in a way to be more consistent with how these interactions would nominally appear in the detector, the fact that these parameters move in the new sample set is understandable.

In addition to comparing the fit parameters, the $p - \cos\theta$ post-fit distributions were compared for the neutrino beam mode samples, as these had the same binning in both fits. These distributions, seen in Figure 7.3, show the neutrino beam mode samples respond in a very similar way for both fits. Further evidence of this can seen in Figure 7.4, where the momentum and $\cos\theta$ distributions are compared separately.

Because the two sample sets had similar sensitivity to the fit parameters and produced similar post-fit distributions, the far detector event distributions, which are used to determine the oscillation parameters values, should be consistent. However, when comparing the unoscillated event distributions, as seen in Figure 7.5, this is not the case, particularly for the $1R_\mu$ sample. Likewise, when examining the oscillated event distributions in Figure 7.6, the distributions are not consistent with one another. While the differences are only about one standard deviation, previous studies on T2K have shown that similar shifts are able to change the oscillation parameter values found in the oscillation analysis [114].

One particular way the final oscillation parameter values could be affected would be a shift in the value of $\sin^2\theta_{23}$. Qualitatively, changes in the value of $\sin^2\theta_{23}$ can be determined by comparing the size of the dip in the oscillated event distributions. Because the SK distribution that uses the RHC MultiPi fit results decreases relative to the distribution using the RHC MultiTrack fit results, this implies the value of $\sin^2\theta_{23}$ will shift closer to maximal mixing ($\sin^2\theta_{23} = 0.5$). When using the RHC MultiTrack samples, the $\Delta\chi^2$ intervals for $\sin^2\theta_{23}$, which can be found in Figure 7.7, are large enough to cover maximal mixing. Due to the RHC MultiPi samples providing a similar level of constraint as the RHC MultiTrack samples, the size of these contours should be similar in the future. Therefore, while $\sin^2\theta_{23}$ likely will shift towards maximal mixing, T2K will not have the constraint to make a statistically significant statement as to the true value of $\sin^2\theta_{23}$.

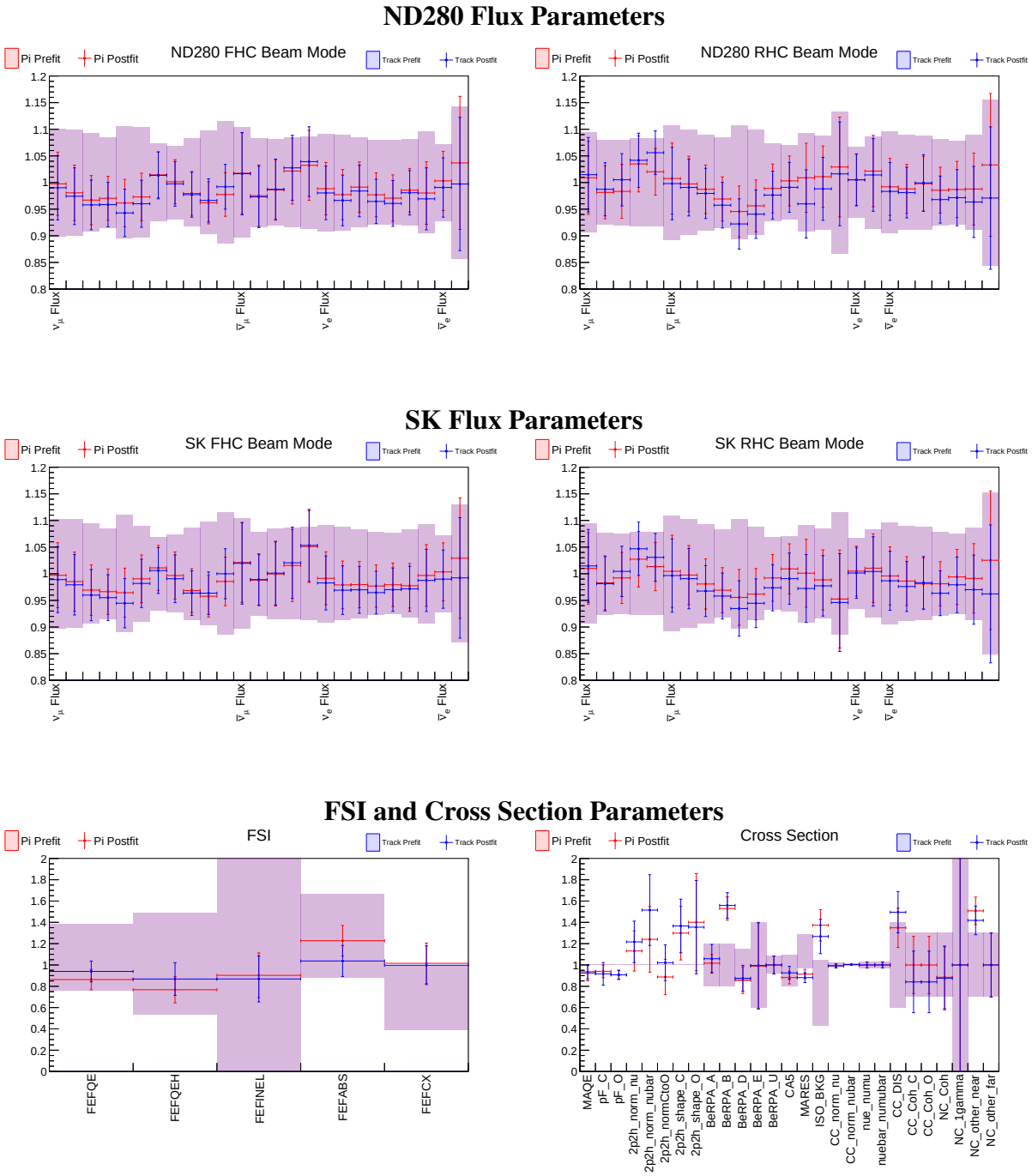

Figure 7.2: Comparison of fits to T2K data for the RHC MultiTrack (blue) and RHC MultiPi samples (red). The input parameter error bars can be seen in the background. Note, the CCQE cross section parameters do not have any prior constraint applied in the fit, so an input error band is not displayed for these parameters.

FGD1 FHC CC0π

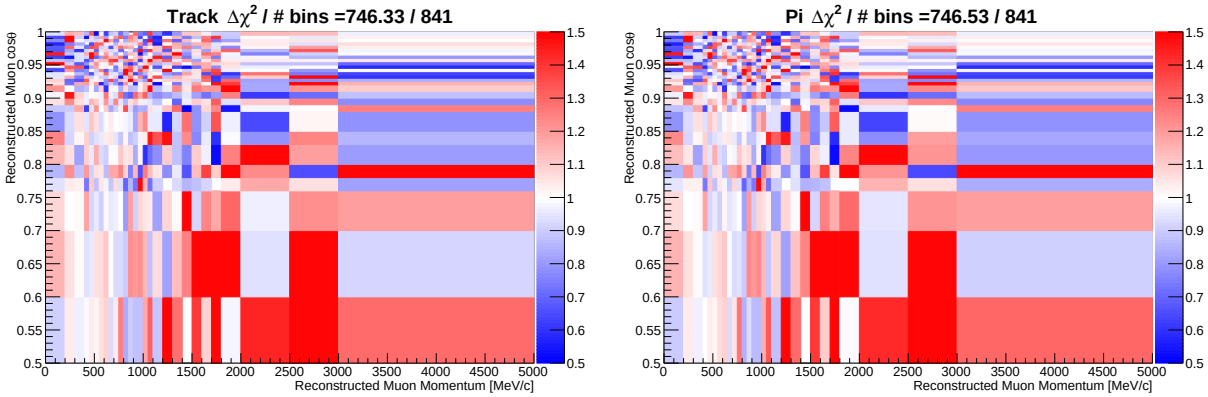

FGD1 FHC CC1π

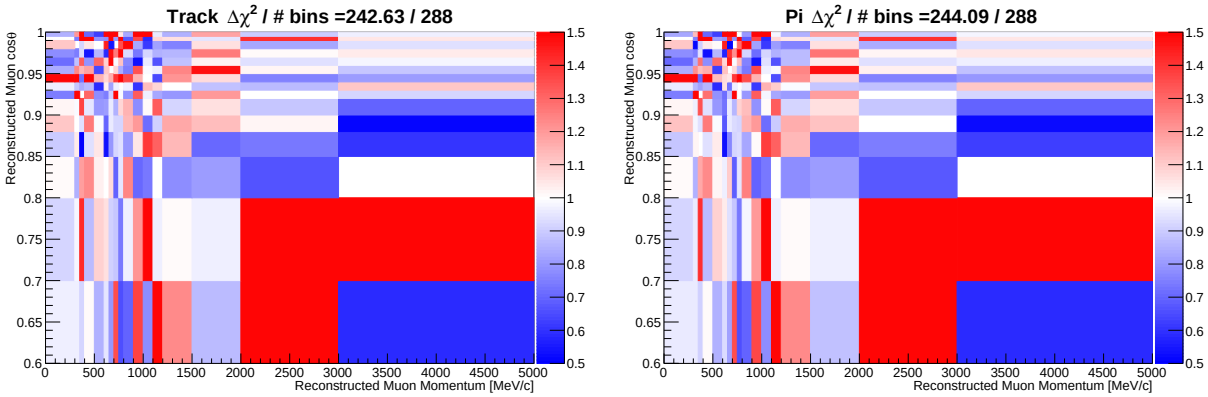

FGD1 FHC CCOther

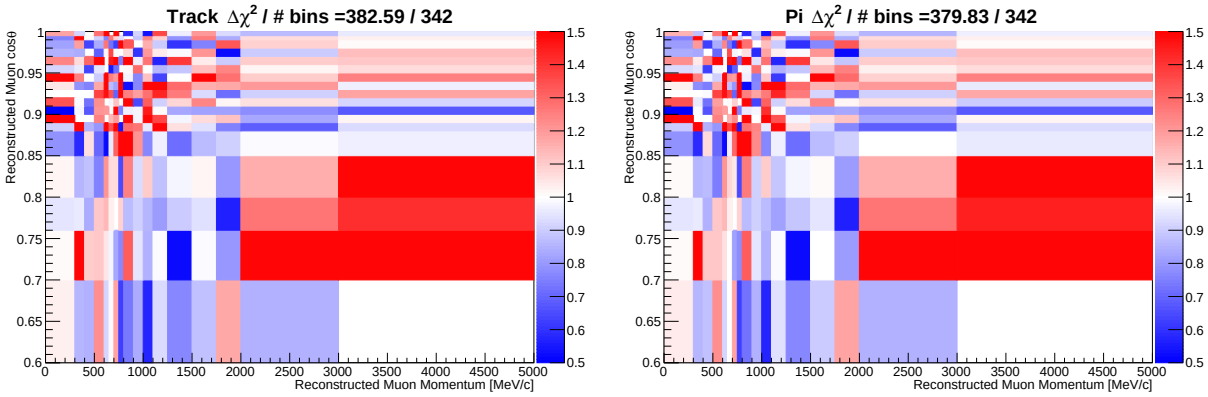

Figure 7.3: Ratios of the data $p - \cos\theta$ distribution to the post-fit distribution for FGD1 for the RHC MultiTrack samples (left) and the RHC MultiPi samples (right). The $\Delta\chi^2$ per number of bins can be seen for each distribution.

FGD1 FHC CC0π

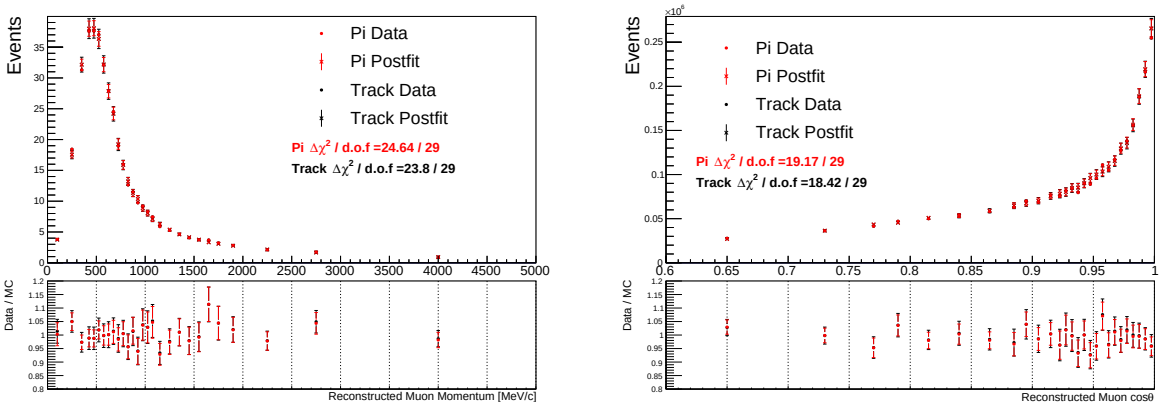

FGD1 FHC CC1π

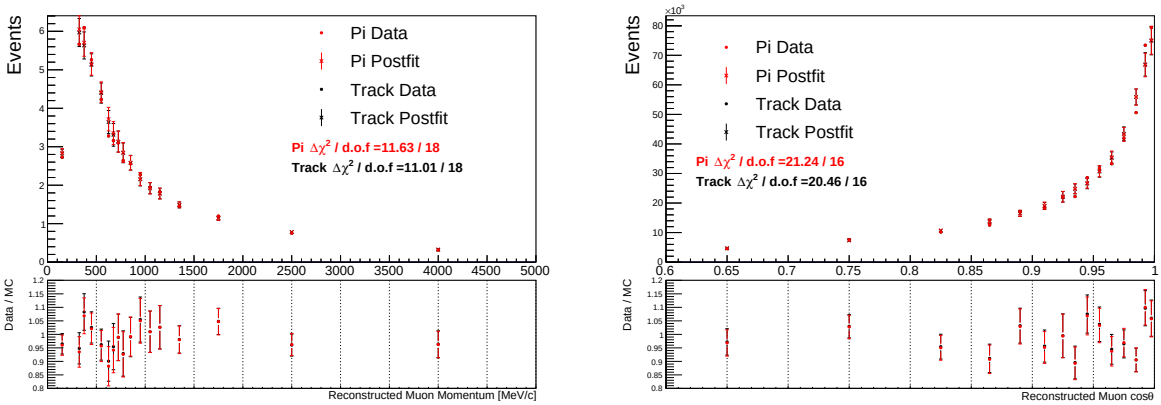

FGD1 FHC CCOther

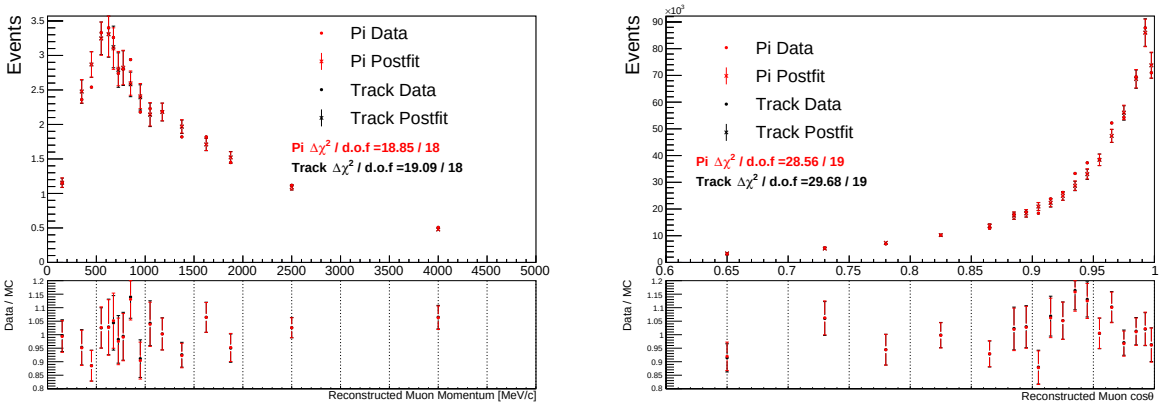

Figure 7.4: The momentum (left) and cos θ (right) distributions for the RHC MultiTrack (black) and the RHC MultiPi (red) samples. The $\Delta\chi^2$ per number of bins is shown for each sample set.

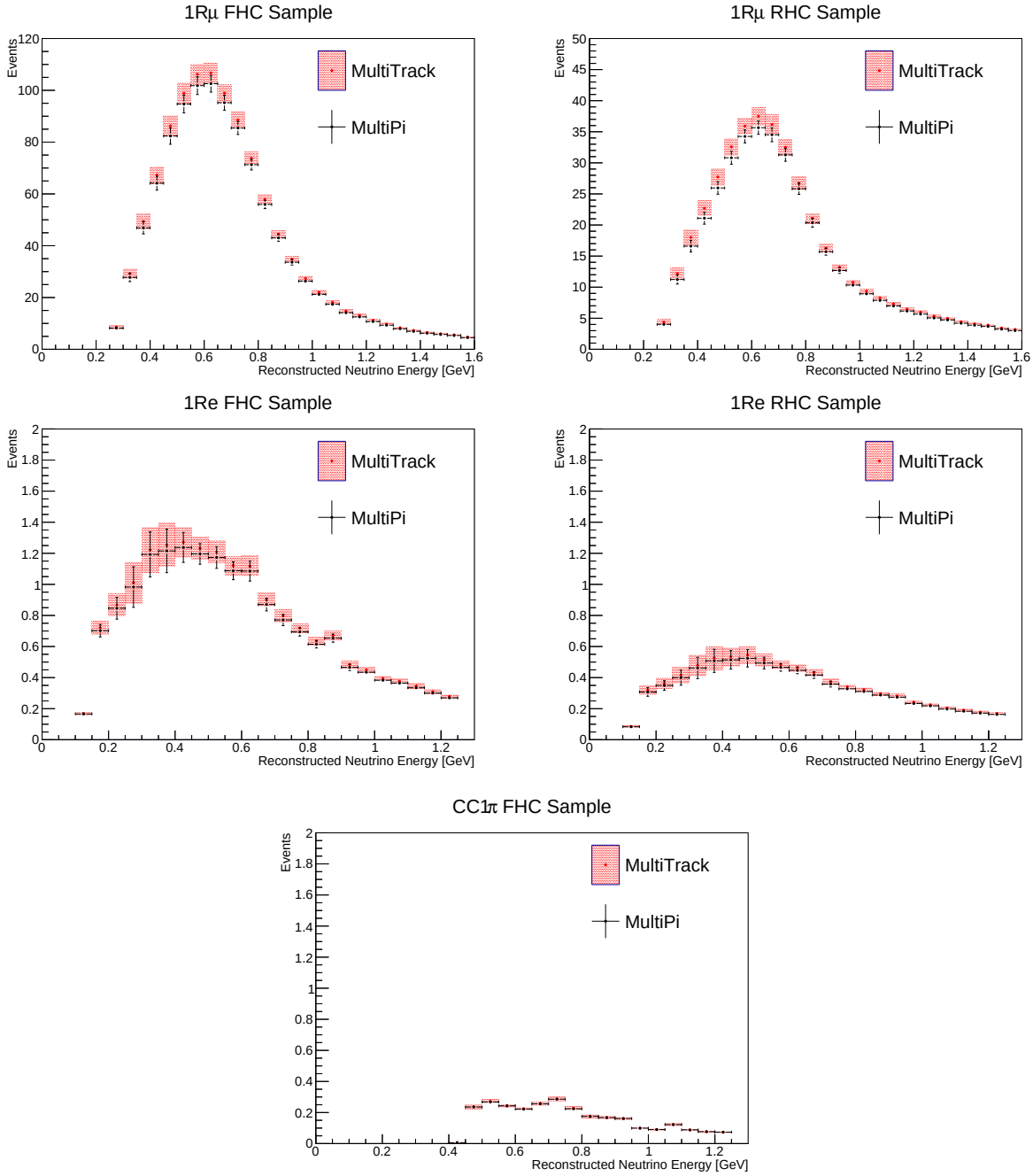

Figure 7.5: Comparison of the SK neutrino energy distributions for the RHC MultiTrack (red) and RHC MultiPi (black) samples. The error bars are the approximate uncertainty from the flux plus cross section systematic uncertainties.

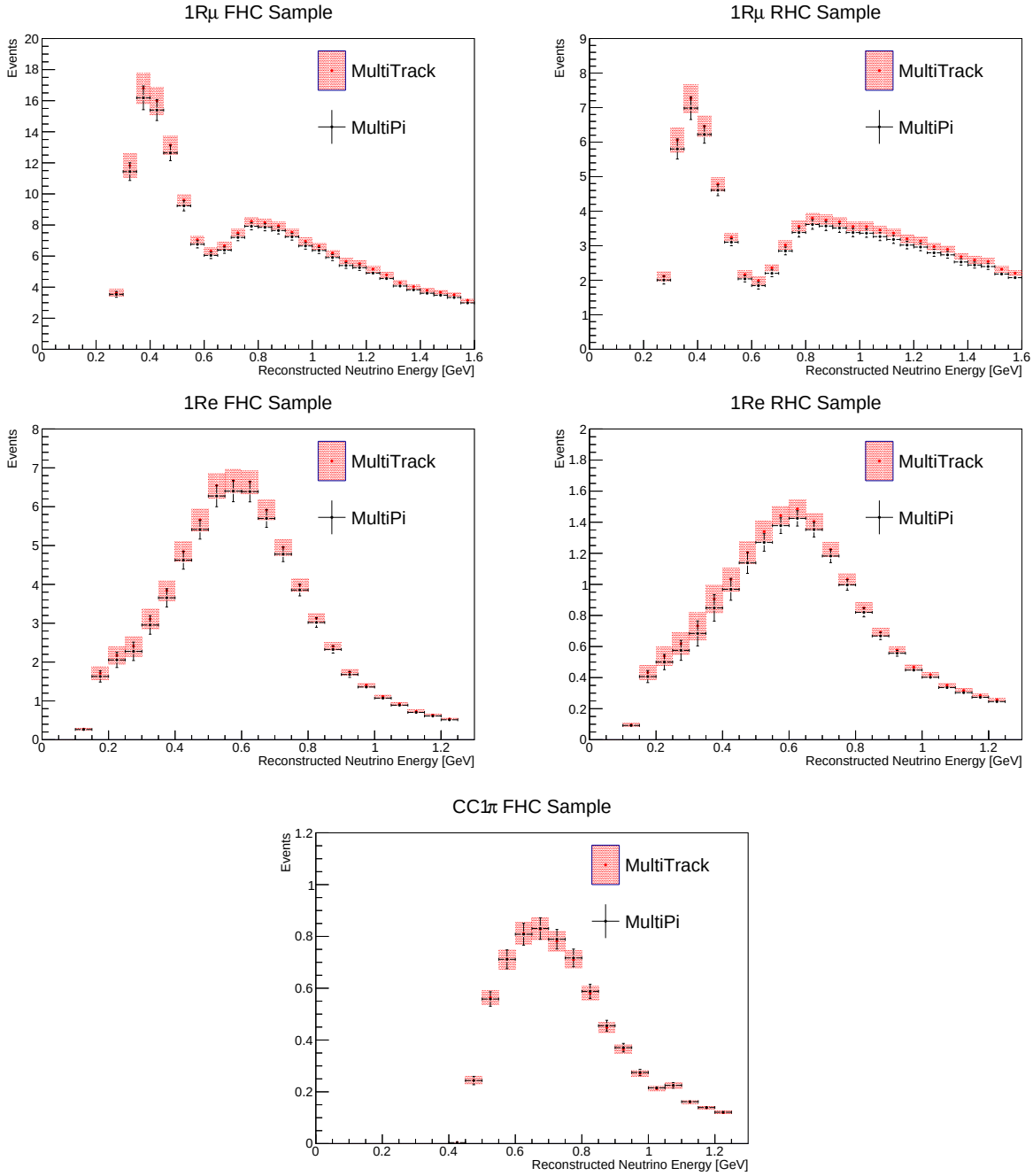

Figure 7.6: Comparison of the SK neutrino energy distributions for the RHC MultiTrack (red) and RHC MultiPi (black) samples. The error bars are the approximate uncertainty from the flux plus cross section systematic uncertainties.

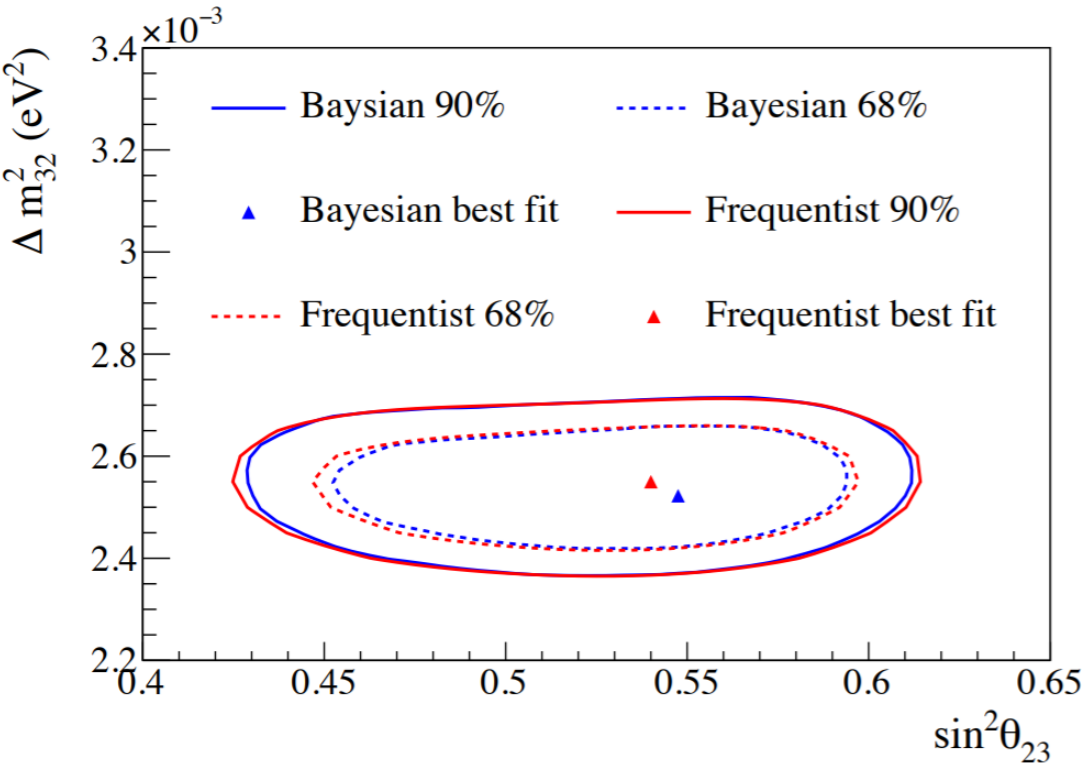

Figure 7.7: Constant $\Delta\chi^2$ 68% and 90% intervals for the hybrid frequentist-Bayesian the fully Bayesian analyses on T2K, assuming the normal mass hierarchy. These intervals are based on a near detector fit using the RHC MultiTrack samples. Figure from [25].

Currently, T2K is in the process of overhauling the cross section model, including the parameters related to CCQE and CC resonant pion production interactions. As such, the final impact on the fundamental oscillation parameters will be a convolution of the new samples with the new cross section model. Until the cross section model is ready, comparisons of the SK event distributions provide insight into whether differences might be expected. However, differences in the distributions may vanish with the inclusion of the new model; therefore, they should be viewed as suggestive of potential change and not as substantial evidence for change. It also provides a necessary step in validating the the final results. Any differences observed here are due to effects from the new samples, as the new cross section model has not been included, and provides a benchmark to compare to when the new model is added.

While the combined effect of the new samples and model cannot be ascertained until the new

cross section model is available, the transition to the RHC MultiPi samples can be done at this time. In doing so, the samples for the near and far detector will be more consistent with one another. Additionally, the new samples provide a better comparison between the underlying interactions and the corresponding topologies seen in the detector.

7.2 Effect of Additional CC Resonant Events with Low Pion Momentum

Currently, the non-resonant pion production model used by the NEUT neutrino event generator is tuned to only neutrino data [24]. It is assumed that this tuning is sufficient for antineutrino events; however, the model developed by Kabirnezhad (the "MK" model) has shown differences in the CC resonant pion production cross section for neutrinos and antineutrinos due to the coupling of resonant and non-resonant background interactions [115]. For this thesis, a simple study was performed to test the effect of additional antineutrino events in the new RHC MultiPi samples that have outgoing charged pions, as the MK model predicts a higher antineutrino cross section than currently assumed. This study was performed to verify that the current cross section model used in the near detector fit is sufficient for handling a change in the number of antineutrino single pion production events in the new samples. Furthermore, because events which have pions that fall below the detection threshold at SK can contaminate the one ring event samples for the oscillation analysis, this study solely looked at simulated events with pion momenta below the detection threshold.

7.2.1 Results

In order to test the effect of the additional antineutrino events, a uniform normalization factor was applied to simulated antineutrino single pion production events with a charged pion escaping the nucleus. In addition to needing a charged pion in the final state, the momentum of the pion had to be less than 200 MeV/c, which is approximately the threshold for a pion to be detected at SK[2]. The effect of this additional factor can be seen in Figure 7.8 for FGD1 (FGD2 can be seen in Appendix

[2]The threshold can be calculated as $E_T = m_\pi c^2/\sqrt{1-1/n^2}$, where n is the index of refraction for water and m_π is the mass of the pion.

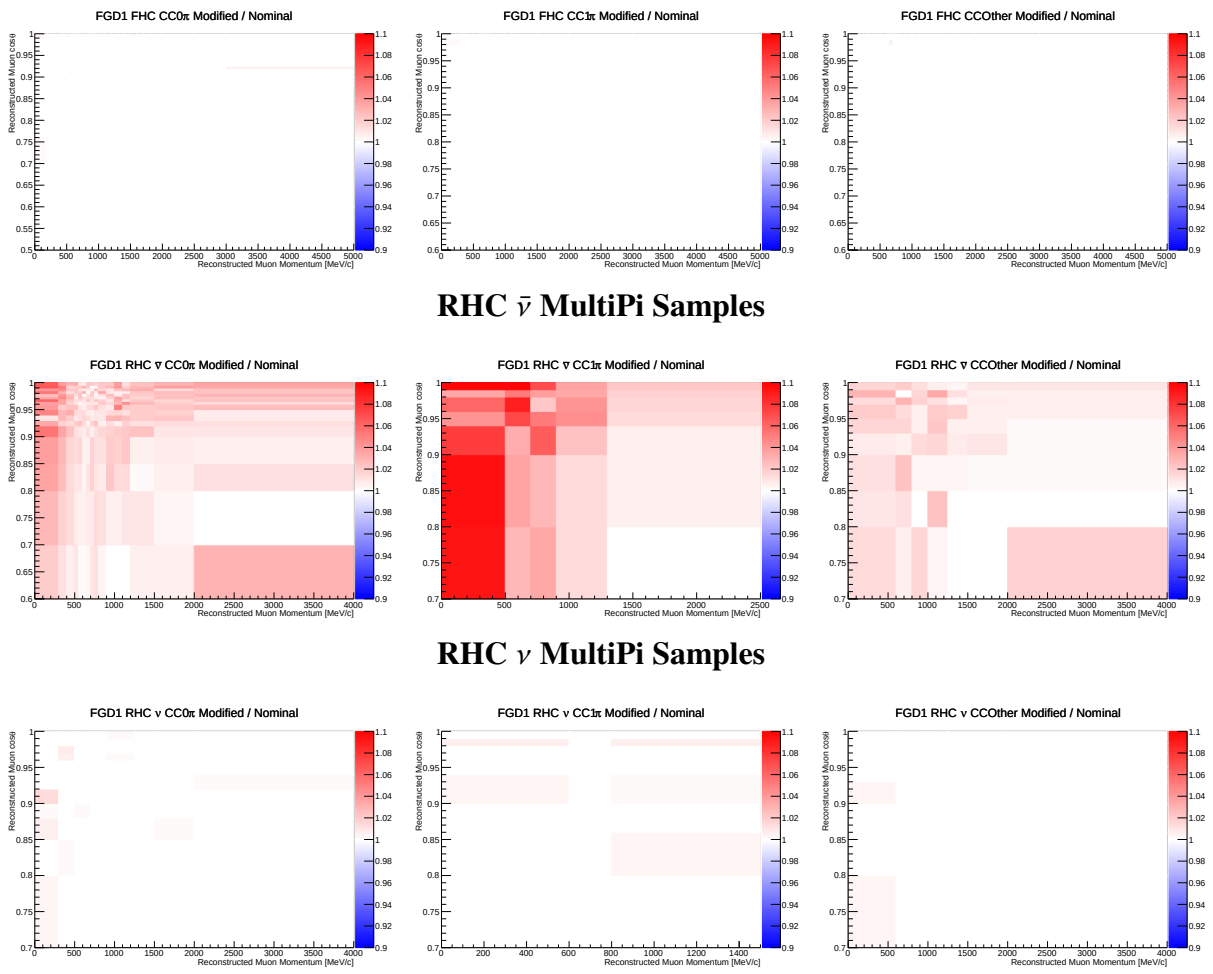

Figure 7.8: Ratios of the modified $p - \cos\theta$ distribution, which includes additional antineutrino single pion production events, to the nominal distribution for FGD1. The CC0π samples (left), CC1π samples (middle), and CCOther samples (right) are shown.

C). As expected the largest effect can be seen in the RHC $\bar{\nu}$ samples, with little change seen in either the FHC MultiPi or RHC ν MultiPi samples.

Overall, there is very little difference in the parameters when fitting the Monte Carlo distribution with additional low energy pions when compared against the fit to the nominal Monte Carlo distribution (see Figure 7.9). In general, the flux parameters, FSI parameters, and the vast majority of the observable normalization parameters, which correspond to the response of the detector, show shifts of less than 1%. Nominally, changes in the CC resonant pion production parameters

(CA5, M_A^{RES}, and the isoscalar background) would have been expected as the affected events are CC resonant events. However, this is not the case. The results indicate the CC resonant pion production model for antineutrino events does not have sufficient freedom in it to compensate for the inclusion of more single pion production events with low momentum pions.

Rather than the CC resonant pion production parameters moving, some of the 2p2h parameters showed small increases. The observed shift in these parameters is reasonable, as the modified events have similar kinematics to the pion production region of the 2p2h cross section (see Figure 4.7). Because of this, the 2p2h shape parameters are compensating with a value where there would be more pion production-like events over QE-like events[3].

Within the new cross section model mentioned in Section 7.1, a new CC resonant pion production model will be implemented, one which includes the effects of coupling between the resonant and non-resonant backgrounds [115]. When the new model becomes available, the results of this study can be compared with a similar study done using the new CC resonant pion production model and uncertainties to see if the new model has the freedom to cover the changes that the current model does not.

7.3 Q^2 Suppression in Single Pion Production Events

Recently, results at MINERνA [116, 117] and MINOS [118] have indicated a disagreement between their data and Monte Carlo for single pion production events with low transfer momentum, Q^2 (below about 0.4 GeV^2). In order to account for this discrepancy, the NOνA[119] collaboration includes a modification to their nominal Monte Carlo [120]. Furthermore, the uncertainty related to this modification has been shown to be a dominant systematic uncertainty in their cross section model [121]. T2K does not include any such modification to their Monte Carlo; however, for this thesis, a study was performed to determine if the current T2K cross section model has the freedom to cover such a modification if it were to be included in the Monte Carlo.

[3] A 2p2h value of 1.0 is an equal mix of both distributions, while 2.0 is only pion production-like events and 0.0 is only QE-like events.

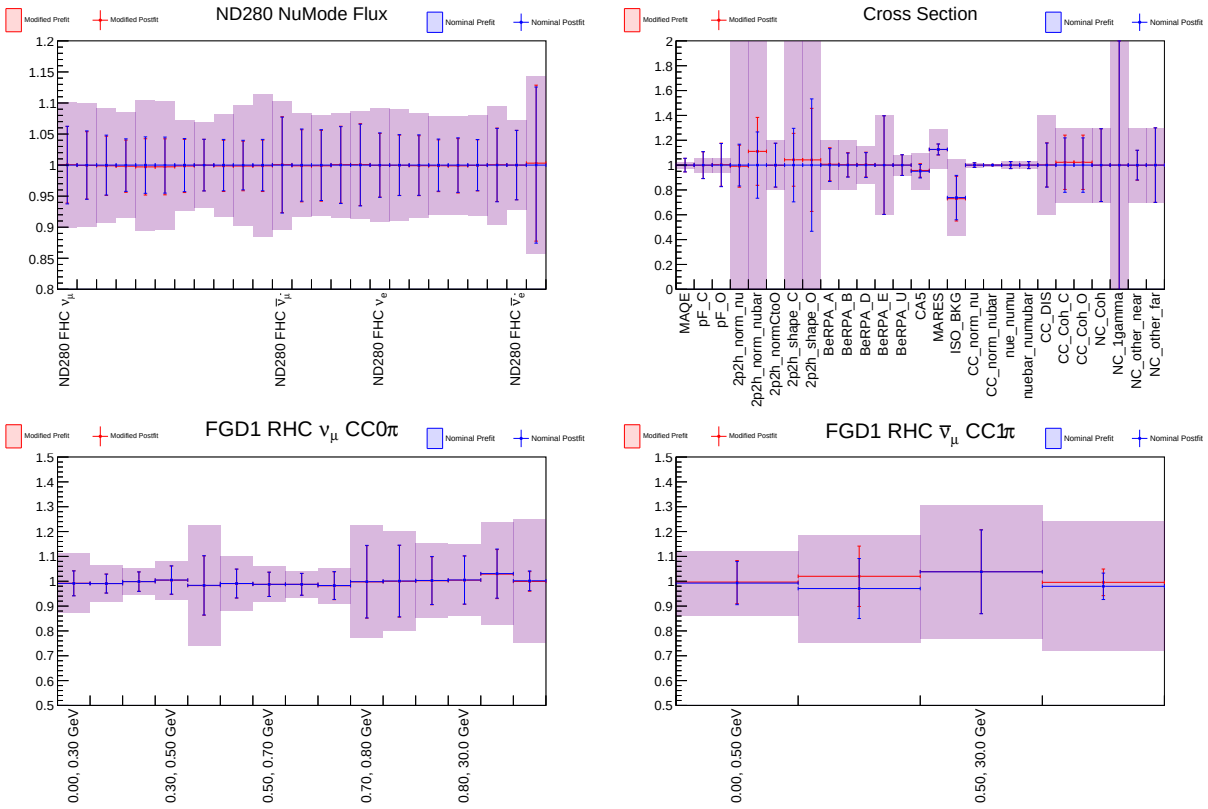

Figure 7.9: Comparison of fits to the nominal Monte Carlo (blue) and the Monte Carlo including additional single pion production events (red). The ND280 neutrino flux parameters (top left) are characteristic of the parameter shifts for the full flux parameter set and the FSI parameters. On the other hand, some shifts are seen in the cross section parameters (top right). Little difference is seen for the majority of the observable normalization parameters (bottom left), while slight changes are seen in the RHC $\bar{\nu}$ CC1π samples (bottom right). The input parameter error bars can be seen in the background.

7.3.1 Results

The modification applied for this study is based on the MINOS discrepancy [118]:

$$\frac{1.01}{1+\exp\left(1-\sqrt{Q^2}/0.156\right)}, \tag{7.1}$$

which is applied to all simulated single pion production events with Q^2 below 0.7 GeV. The modification, as a function of Q^2, can be seen in Figure 7.10. The ratio of the modified Monte Carlo to the nominal Monte Carlo for FGD1 can be seen in Figure 7.11 (FGD2 plots can be found in Appendix C). As expected, the modification targets events with low Q^2, which, in a $p-\cos\theta$

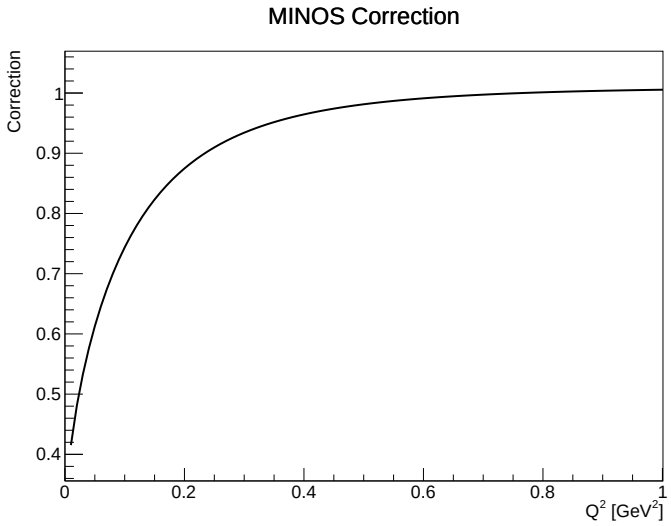

Figure 7.10: The modification applied to the nominal T2K Monte Carlo using the MINOS parameterization.

distribution, is concentrated around the peak energy of T2K and in the higher angle bins. While the reduction is primarily in the CC1π samples, the reduced number of events seen in the CC0π and CCOther samples is due to the migration of true single pion production events into one of these samples.

Figure 7.12 shows the response of the flux and cross section parameters to the suppression of the low Q^2 single pion production events. One feature of these results is the preference for a flux tuning that is approximately 3% below the nominal tuning. As the flux parameters serve to shift the overall number of events up or down in the fit based on the data, this is a reasonable shift to expect. When comparing the number of events in Table 7.1, there is approximately 3% fewer events predicted at ND280 in the modified Monte Carlo than in the nominal Monte Carlo. Therefore, the flux parameters are compensating for the decrease in the predicted event rate.

With regards to the response of the cross section parameters to the modified Monte Carlo, two primary aspects should be highlighted. First, the current CC resonant pion production model shows significant shifts when compared with the nominal fit. This shows that the current model has some freedom to cover the changes applied to the Monte Carlo. For this study, the ideal result

FHC MultiPi Samples

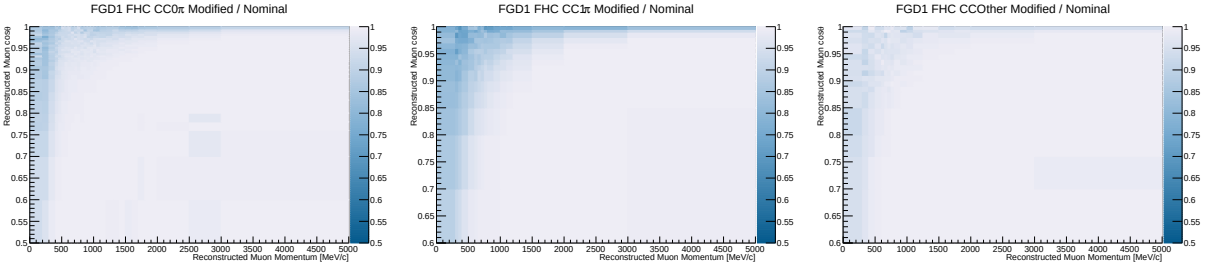

RHC $\bar{\nu}$ MultiPi Samples

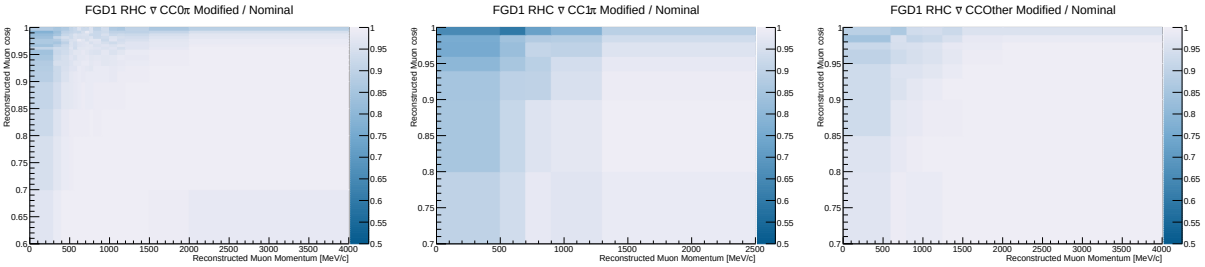

RHC ν MultiPi Samples

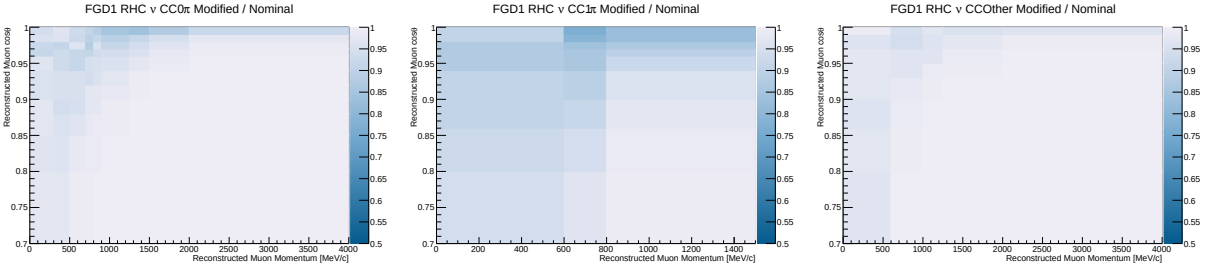

Figure 7.11: Ratios of the modified $p - \cos\theta$ distribution, which includes the low Q^2 suppression weight, to the nominal distribution for FGD1. The CC0π samples (left), CC1π samples (middle), and CCOther samples (right) are shown.

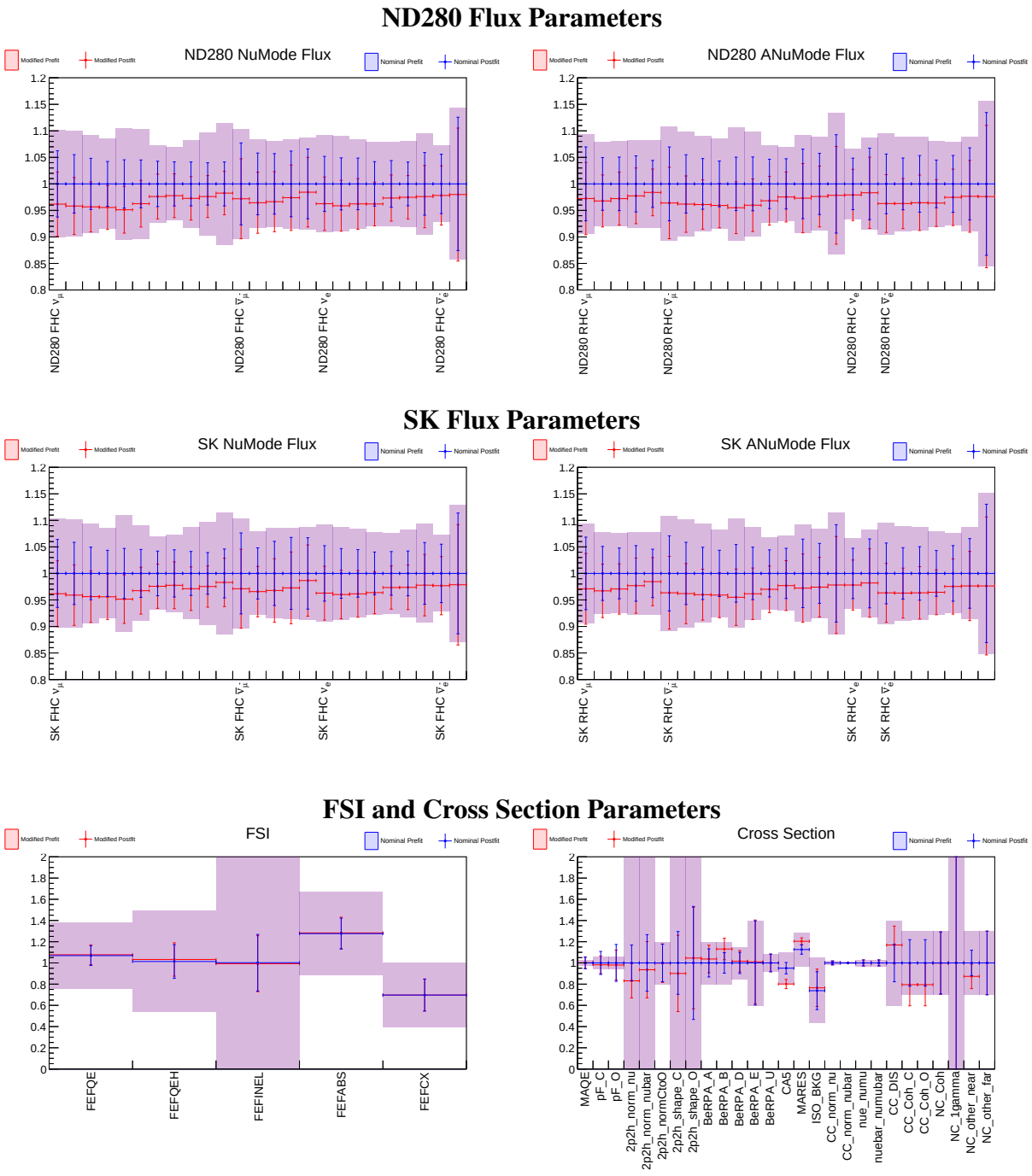

Figure 7.12: Comparison of fits to the nominal Monte Carlo (blue) and the Monte Carlo including the low Q^2 event suppression modification (red).

Sample	Modified	Nominal	Difference
FGD1 FHC ν_μ CC Inclusive	39,529.92	40,821.52	-0.032
FGD1 FHC ν_μ CC0π	26,667.7	27,429.5	-0.028
FGD1 FHC ν_μ CC1π	6,653.39	7,095.14	-0.062
FGD1 FHC ν_μ CCOther	6,208.83	6,296.88	-0.014
FGD1 RHC $\bar{\nu}_\mu$ CC Inclusive	7,602.538	7,839.886	-0.03
FGD1 RHC $\bar{\nu}_\mu$ CC0π	6,065.54	6,245.19	-0.029
FGD1 RHC $\bar{\nu}_\mu$ CC1π	509.598	542.636	-0.061
FGD1 RHC $\bar{\nu}_\mu$ CCOther	1,027.4	1,052.06	-0.023
FGD1 RHC ν_μ CC Inclusive	4,142.413	4,264.058	-0.029
FGD1 RHC ν_μ CC0π	2,478.09	2,547.87	-0.027
FGD1 RHC ν_μ CC1π	833.492	875.593	-0.048
FGD1 RHC ν_μ CCOther	830.831	840.595	-0.012

Sample	Modified	Nominal	Difference
FGD2 FHC ν_μ CC Inclusive	36,583.01	37,810.02	-0.032
FGD2 FHC ν_μ CC0π	25,946.1	26,772	-0.031
FGD2 FHC ν_μ CC1π	5,173.27	5,493.58	-0.058
FGD2 FHC ν_μ CCOther	5,463.64	5,544.44	-0.015
FGD2 RHC $\bar{\nu}_\mu$ CC Inclusive	7,403.615	7,630.104	-0.03
FGD2 RHC $\bar{\nu}_\mu$ CC0π	6,032.98	6,211.62	-0.029
FGD2 RHC $\bar{\nu}_\mu$ CC1π	459.37	486.26	-0.055
FGD2 RHC $\bar{\nu}_\mu$ CCOther	911.265	932.224	-0.022
FGD2 RHC ν_μ CC Inclusive	3,911.185	4,030.805	-0.03
FGD2 RHC ν_μ CC0π	2,490.35	2,565.66	-0.029
FGD2 RHC ν_μ CC1π	641.985	675.982	-0.05
FGD2 RHC ν_μ CCOther	778.85	789.163	-0.013

Table 7.1: Event rates for the modified and nominal Monte Carlo sets. The nominal event rates are Monte Carlo events weighted by POT, flux, detector, and cross section weights. The modified rate includes the same weights as the nominal, plus the additional modification due to the low Q^2 event suppression. The difference is given by $(modified\ -\ nominal)\ /\ nominal$. The left column shows the rates for FGD1, while the right column shows FGD2.

would be for only these parameters to move, as the suppressed events are only CC resonant pion production events. This would show the model has sufficient freedom to fully describe the applied suppression of low Q^2 events. However, there are changes in the other cross section parameters that are consistent with a suppression of low Q^2 single pion production events. When suppressing these events, there will be a reduction in the events populating the pion production-like region of 2p2h events (see Figure 4.7); therefore, the parameters compensate for this by preferring a more quasi-elastic-like value for the 2p2h shape parameters and an overall reduction in the number of events, as is seen in Figure 7.12. Likewise, the BeRPA A and B parameters, which are the dominant BeRPA parameters at low Q^2, show movement to compensate for the reduction of low Q^2 events. Finally, DIS+Nπ events generally have larger Q^2 values, which means these events will not be affected by the modification. Consequently, the upward shift in the CC DIS parameter implies that the fit would expect to see more DIS+Nπ events when the modification is applied, which is consistent with DIS+Nπ events not being suppressed. These compensations show the current CC resonant pion production model does not have the freedom necessary to fully describe the modified distributions.

In addition to observing how the current model does not have the freedom necessary to cover

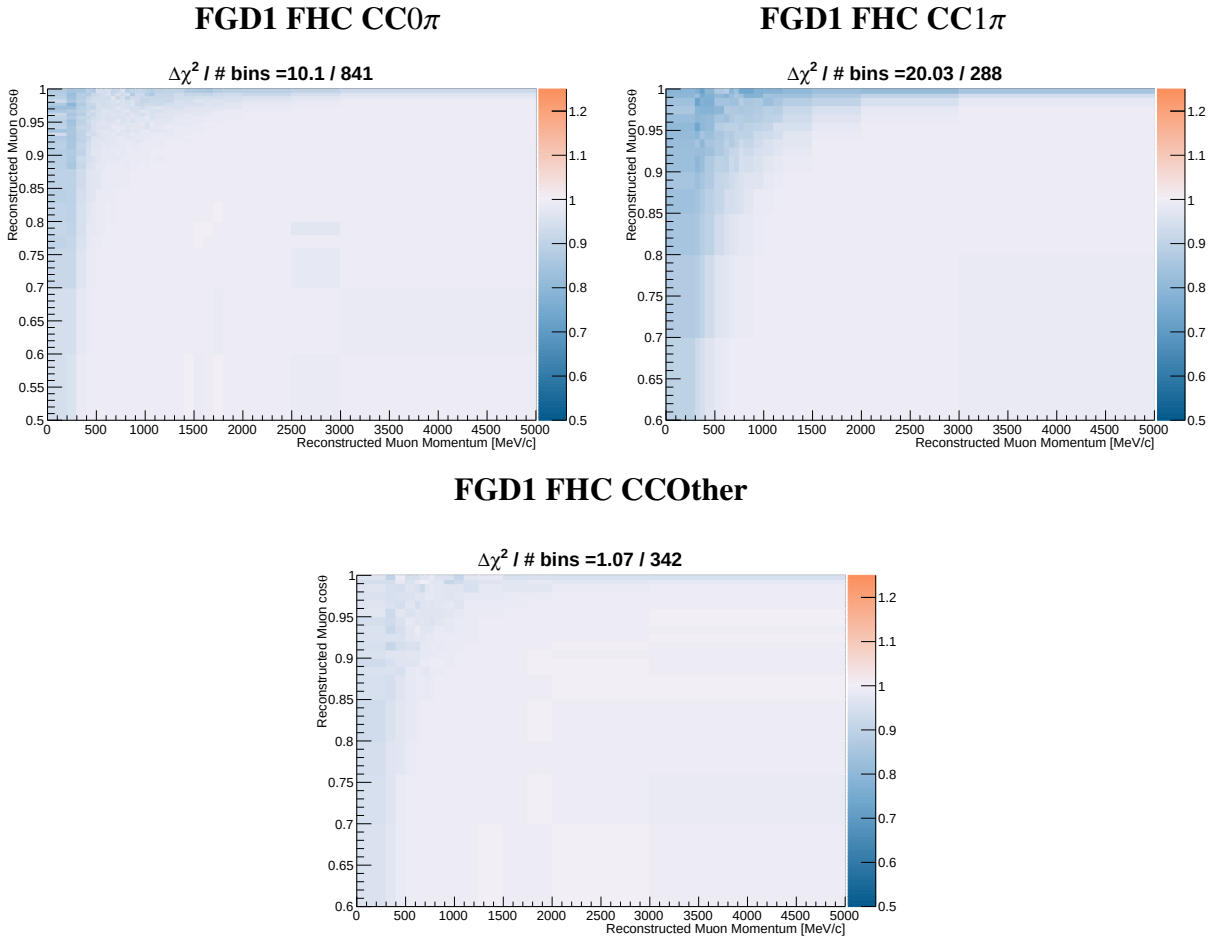

Figure 7.13: Ratios of the modified $p - \cos\theta$ distribution, which includes the low Q^2 suppression weight, to the post-fit distribution for FGD1. The $\Delta\chi^2$ per number of bins can be seen for each distribution.

the applied modification by comparing the post-fit parameter values, the post-fit distributions can also highlight the lack of freedom. Figure 7.13 shows how the modified $p - \cos\theta$ distribution compares to the post-fit distribution. If the current model choice had the freedom to fully cover the modification in the fit, then the $\Delta\chi^2$ values for each distribution should be close to zero, as the only difference between the Monte Carlo sets is the additional weight to suppress low Q^2 events. However, because the $\Delta\chi^2$ value for the CC0π and CC1π samples are not close to zero, this yields further evidence that there currently is not enough freedom to fully cover this modification.

The uncertainty associated with this modification is one of the dominant cross section uncertainties on NOνA. While the T2K CC resonant pion production model appears to have some

freedom to absorb changes due to the suppression of low Q^2 single pion production events, it does not fully cover the changes. Therefore, with the potential for T2K and NOνA to perform a joint oscillation analysis, it would be beneficial for T2K to further study the impact of the differences observed by MINERνA and MINOS. One potential study would be to use the MK model, when it becomes available, to study if more freedom exists in that model parameterization than what is seen in the current model. Another study would be to use MINERνA's parameterization of the event suppression, rather than the MINOS parameterization. In this case, the impact on the near detector fit can be directly compared to verify consistency in how the T2K cross section model responds to each parameterization.

CHAPTER 8

CONCLUSION AND SUMMARY

This thesis showed the effects of using a new set of samples for data collected in the antineutrino beam mode at T2K. Previously, the antineutrino beam mode samples were categorized based on the number of particle tracks seen in the time projection chambers (TPCs), called the RHC MultiTrack samples. One sample collected events with only a muon-like track that crossed the TPC (the CC 1-track sample), while the other selected all events with a muon-like track and any number of other tracks, be they electron, pion, or proton tracks (the CC N-tracks sample). On the other hand, the samples are now separated based on the number of pions visible in the detector, the RHC MultiPi samples, and are able to use information from the TPCs as well as the fine-grained detectors (FGDs). Events that only have a muon-like track fall into the CC0π sample, while events with a muon-like track and an appropriately charged pion-like track (a negatively charged pion for antineutrino interactions and a positively charged pion for neutrino interactions) are placed in the CC1π sample. Finally, any events that do not fall into the first two categories are selected into the CCOther sample.

Using the new samples serves one primary purpose in the overarching oscillation analysis, in that the new samples more accurately match what is seen at Super-Kamiokande (SK). For example, in the RHC MultiTrack samples, a second track in an event in the CC N-tracks sample could be from a proton. However, if a similar event were to occur in the far detector, the proton would be unable to be detected as it does not decay or have enough energy to meet the Cherenkov threshold. On the other hand, the RHC MultiPi samples use pions to distinguish between samples. At the far detector, samples are similarly categorized as the pions can be detected either through their decay or through the pion being energetic enough to meet the Cherenkov threshold.

The study presented in Section 7.1 discusses the effects of using the RHC MultiPi samples, rather than the RHC MultiTrack samples. Using a fit to the nominal Monte Carlo, it was shown that the two sample sets have comparable sensitivity to the fit parameters, which implies that fits

to the T2K data will yield approximately the same level of constraint on the flux and cross section parameters. When comparing the results of fits to the data, differences between the two sample sets were observed. However, these differences can be described either through the prior constraints placed on the parameters or the result of moving to the RHC MultiPi samples, which are more closely related to the cross section models used in the fit. After comparing the effects on the near detector, the near detector fit results were propagated to the far detector event distributions, which showed differences in the predicted event rates for SK. Because the impact of the new samples is coupled to the cross section model, which will be updated soon, the final impact of these differences remains to be seen. Nevertheless, these comparisons are a useful validation for understanding how the new samples affect the SK event distributions, without additionally including the effects of the new cross section model.

Additional studies were performed to study the effect of changes to the single pion production interaction channels at the near detector. One study (covered in Section 7.2) focused on the effect of an increased number of events with an outgoing charged pion that is not energetic enough to meet the Cherenkov threshold. The results showed that, at this time, the CC resonant pion production model for antineutrino events does not have the freedom to respond to these changes. However, with the inclusion of the MK model and uncertainties in the new cross section model, it would be beneficial to revisit this study and determine if the new model has freedom where the old model did not. The other study (described in Section 7.3) focused on the suppression of low Q^2 single pion production events seen by MINERνA and MINOS. The current CC resonant pion production model was shown to have some freedom to cover changes to the Monte Carlo when a modification is applied to suppress low Q^2 single pion production events. However, it was not able to completely cover the modification applied to the Monte Carlo. Due to the potential for T2K and NOνA to perform a joint oscillation analysis, it would benefit both experiments to continue studying the impact of the this uncertainty. Two potential extensions to this study are to study whether the MK model and uncertainties have more freedom than what is seen for the current model and to use the MINERνA parameterization of the event modification, rather than the MINOS parameterization.

APPENDICES

APPENDIX A

COMPARISONS OF DIFFERENT PSYCHE VERSIONS ON THE NEAR DETECTOR FIT

The Psyche software package is used for making selections in ND280 samples and for applying detector variation systematic uncertainties, detector systematic weights, and proton on target (POT) weights in ND280. In 2014, Psyche was updated from version 1 (v1) to version 3 (v3)[1]. In the meantime, the BANFF near detector fit continued to use Psyche v1 as the code for applying detector variations and weights and for loading events at the outset of a BANFF maximum likelihood fit.

Starting in 2017, work began on porting the BANFF software to work with Psyche v3. This appendix will cover the broad differences between Psyche v1 and v3 and their impact on the near detector fit. One of the main differences between the versions is an update to the detector selections and systematic uncertainties. Section A.1 will provide background on the studies presented in this Appendix. Additionally, it will show the validation process that ensured the BANFF code achieved the same distributions and weights as the NuMu group, which is the T2K group tasked with developing the event selections. In Section A.2, a comparison of the fit results between Psyche v1 and Psyche v3 and how those results propagate to the Super-Kamiokande (SK) event rate predictions will be shown.

A.1 Comparison of Detector Weight Application

During the summer of 2018, the BANFF group began looking at how the Psyche v1 and Psyche v3 versions of the BANFF code differed. First, the difference between the event rates for each version were compared. Table A.1 shows the breakdown of events with the various event weights applied. While it was not surprising the rates differed, the BANFF group wanted to delve more into the reasons why the two rates were different.

Initially, it was thought that the differences in the detector systematic weights would be able

[1] Version 2 of Psyche suffered from many issues and was used as a stepping stone to v3.

Sample	V1 Data	V3 Data	V1 Raw MC	V3 Raw MC	V1 POT only	V3 POT only
FHC FGD1 ν_μ CC 0π	17136.00	17135.00	337436.00	302866.00	16090.83	16101.55
FHC FGD1 ν_μ CC 1π	3954.00	3955.00	84982.00	76491.00	4058.36	4075.15
FHC FGD1 ν_μ CC Other	4149.00	4159.00	65286.00	58819.00	3107.04	3123.00
Sample	V1 POT+flux	V3 POT+flux	V1 POT+xsec	V3 POT+xsec	V1 POT+det	V3 POT+det
FHC FGD1 ν_μ CC 0π	17535.92	17543.64	15340.11	15340.70	15905.24	15625.75
FHC FGD1 ν_μ CC 1π	4606.61	4621.26	3819.31	3833.63	4011.58	3911.90
FHC FGD1 ν_μ CC Other	3703.69	3719.39	3078.52	3092.76	3071.21	2993.17
Sample			V1 Prefit	V3 Prefit		
FHC FGD1 ν_μ CC 0π			16723.69	16408.21		
FHC FGD1 ν_μ CC 1π			4381.48	4258.71		
FHC FGD1 ν_μ CC Other			3943.95	3834.01		

Table A.1: Comparison of event rates between Psyche v1 and Psyche v3 during the summer of 2018.

to describe the differences seen. However, when comparing momentum distributions for Psyche v1 and Psyche v3 (see Figure A.1), the detector systematic error bars did not cover the differences seen in the two distributions. Therefore, the BANFF and NuMu groups began comparing results in order to verify they were getting the same results.

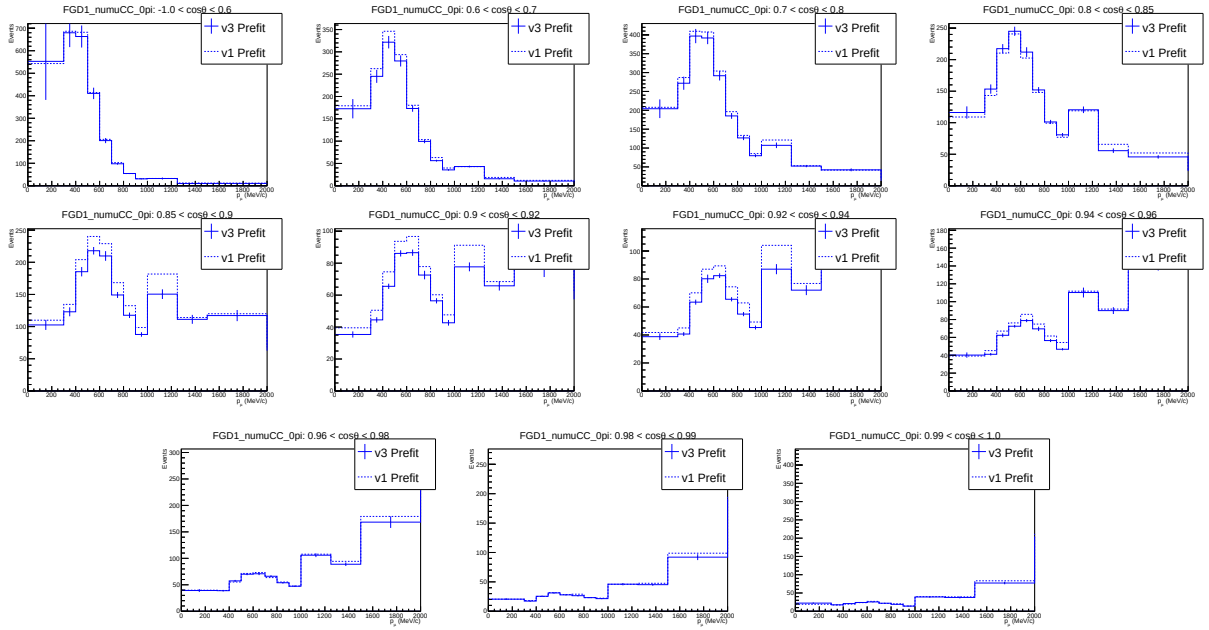

Figure A.1: Momentum distributions comparing Psyche v1 and Psyche v3. The error bars on the v3 distribution are from the Psyche v3 detector uncertainties. More often than not, the difference between Psyche versions is not covered by the error bars.

One of the first tests performed was to compare the number of selected events and that the detector variations and weights were being applied in the same way for Psyche v3. The NuMu group has been using Psyche v3 for a number of years and verifying the BANFF group is getting the same selected events and weights served as a validation process that the BANFF implementation is working properly for Psyche v3. In order to perform these comparisons, the two groups looked at T2K run 4 air (4a).

The BANFF and NuMu groups compared reconstructed muon momentum distributions in Psyche v1 and Psyche v3 (see Figure A.2). While the two have approximately the same shape, it was noticed that the event rates differed quite a bit between BANFF and NuMu. After discussing with the NuMu group, a bug was discovered in how one of the systematic uncertainties was calculated, which resulted in some of the differences seen. Figure A.3 shows the effect of the bug fix on the momentum distributions.

Next, the two groups compared the weights being applied to specific events to verify the weights were applied consistently. Table A.2 shows an abbreviated look at the weights comparison. The results between the two groups match up very well, showing the two groups are calculating the same detector weight for each event.

Run	Subrun	Event	Sample	NuMu Weight	BANFF Weight
4a	0	26	FGD1 FHC CC0π	0.9871199	0.98712
4a	0	883	FGD1 FHC CC0π	0.9894728	0.989473
4a	0	1304	FGD1 FHC CC0π	0.9845622	0.984562
4a	0	2078	FGD1 FHC CC0π	0.9871199	0.98712
4a	0	2107	FGD1 FHC CC0π	0.9871199	0.98712
4a	0	2555	FGD1 FHC CC0π	0.9778962	0.977896
4a	0	3291	FGD1 FHC CC0π	0.9871199	0.98712
4a	0	4539	FGD1 FHC CC0π	0.9885830	0.988583
4a	0	4732	FGD1 FHC CC0π	0.8862785	0.886279
4a	0	4736	FGD1 FHC CC0π	0.9871199	0.98712
4a	0	4781	FGD1 FHC CC0π	0.9894728	0.989473

Table A.2: Comparison of detector weights applied by the BANFF and NuMu groups to specific events.

FGD1 FHC CC0π

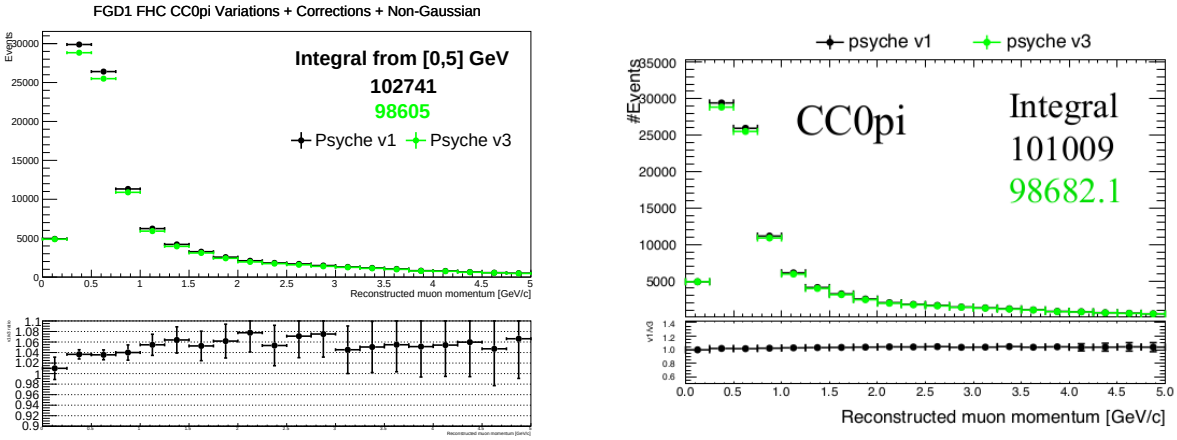

FGD1 FHC CC1π

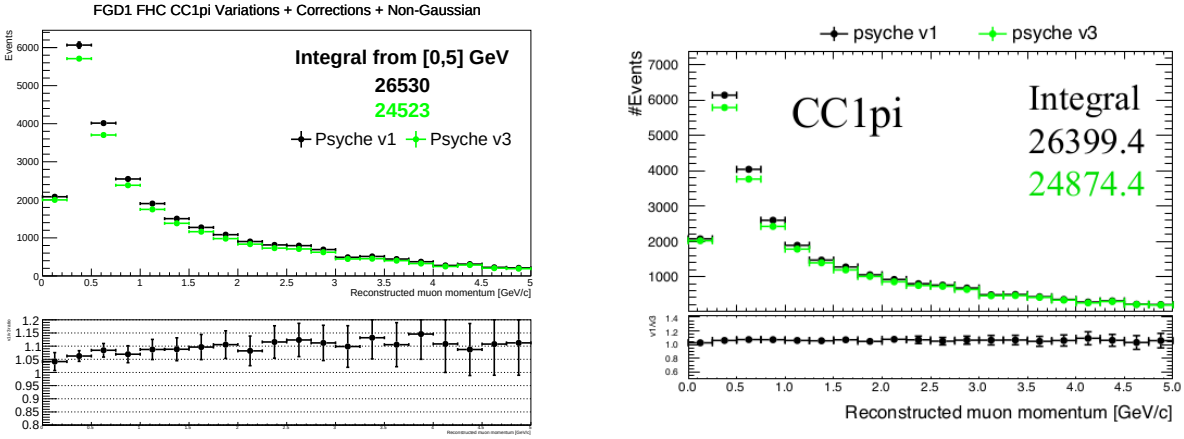

FGD1 FHC CCOther

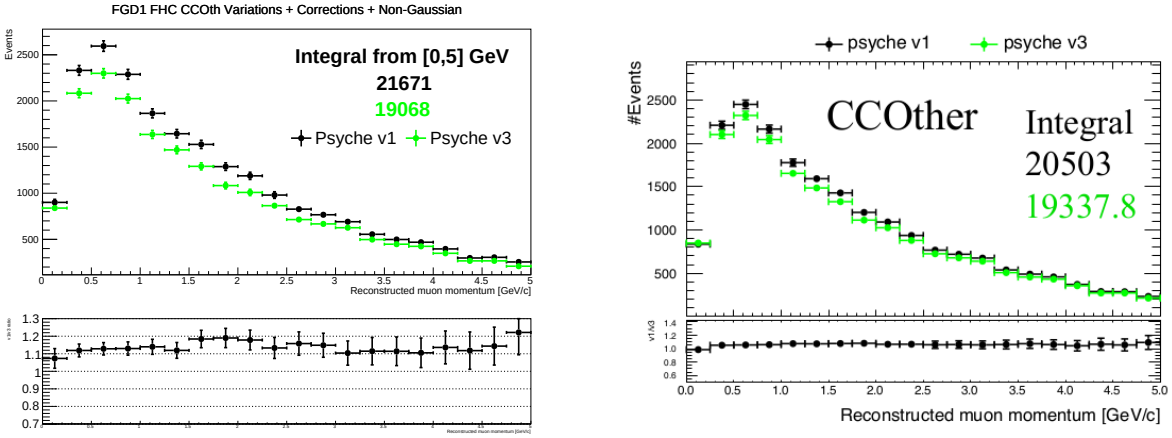

Figure A.2: Comparing BANFF (left) and NuMu (right) reconstructed muon momentum distributions for Psyche v1 and Psyche v3. The BANFF plots include an additional weight related to the non-Gaussianity of some of the detector parameters.

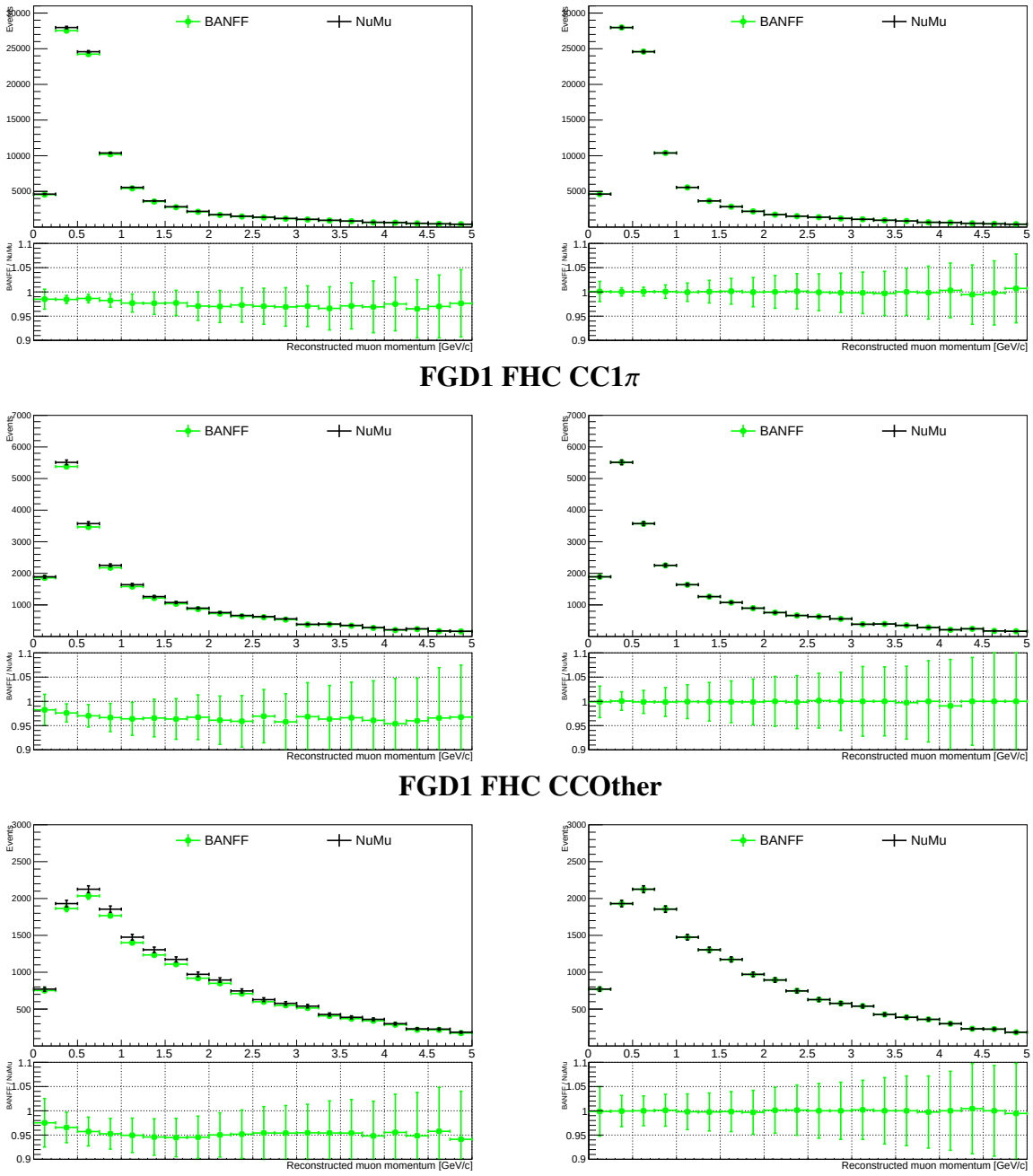

Figure A.3: Effect of detector weight bug in Psyche v3. The left side shows the BANFF using Psyche v3 without the bug fix, while the right side includes the bug fix. In both cases, the NuMu curve includes the bug fix.

One way to double check the event weights are being applied correctly, as well as verifying the same events are being selected, is to plot the weighted distributions. Using Psyche v3, the

two groups compared distributions with only the detector variations applied, the variations and all weights applied, and the variations with each individual weight applied separately. The variations only and variations plus all weights applied plots can be seen in Figures A.4 – A.5. Figure A.6 shows the effect of applying the variations only plus one detector weight (the flux weight, in this case) and is representative of the comparison for each individual weight. Overall, there is excellent agreement between BANFF and NuMu in the number of selected events and weight values being applied to the Run 4a events.

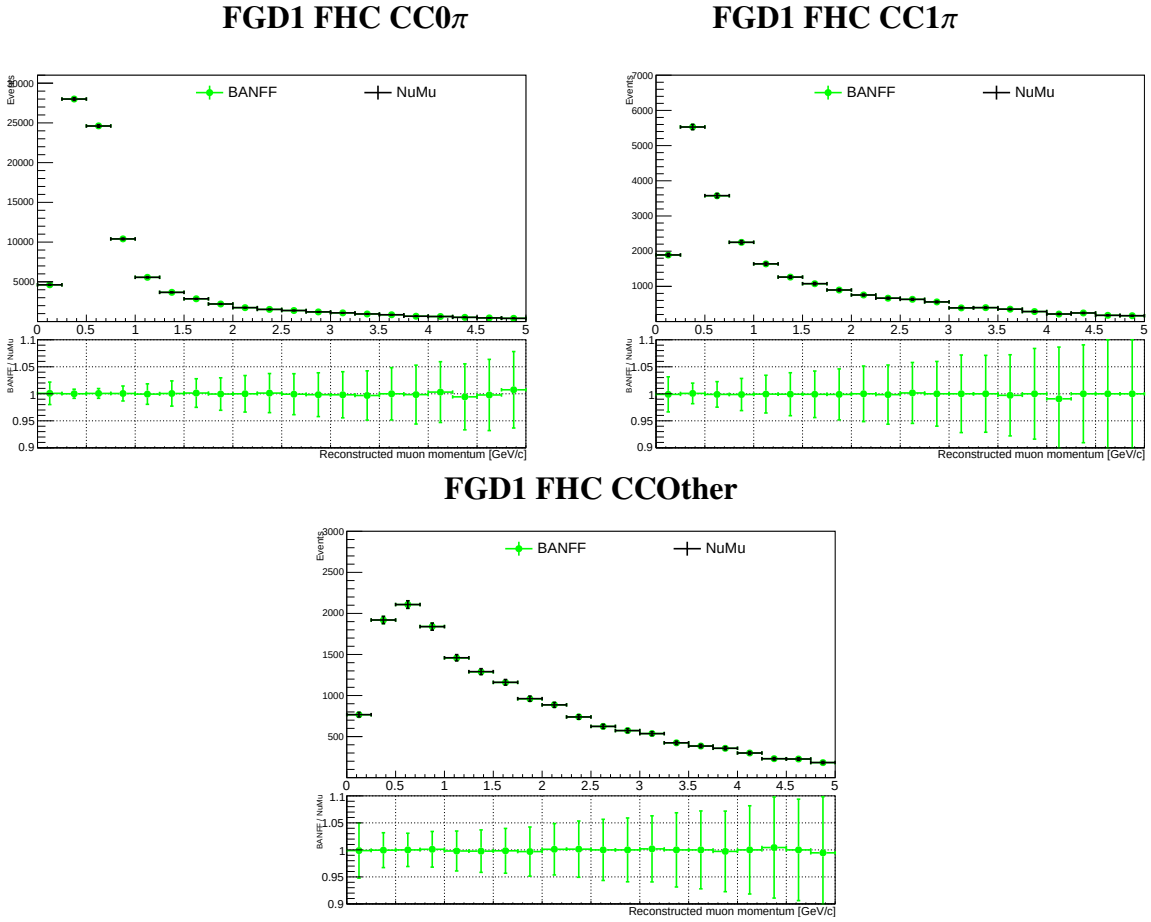

Figure A.4: Comparing selected events in Psyche v3 for BANFF and NuMu with only the detector variations applied.

After looking at both the exact values for weights applied and the plots comparing the BANFF and NuMu selected events, for each individual weight and the combined weight, the BANFF and NuMu groups are confident that Psyche v3 is working as it should for the BANFF group.

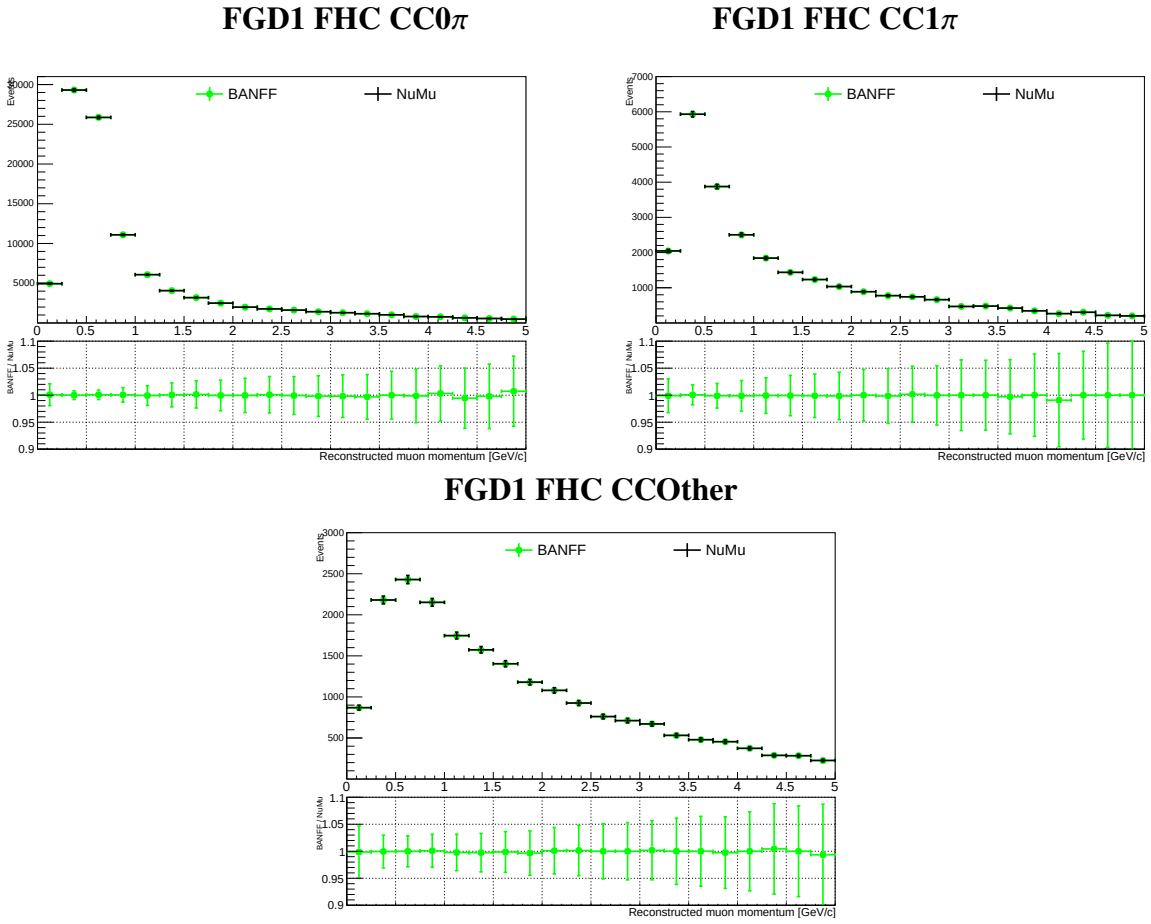

Figure A.5: Comparing selected events in Psyche v3 for BANFF and NuMu with the detector variations, the flux weight, and all detector weights applied.

A.2 Fit Result Comparison

While understanding the differences between Psyche v1 and Psyche v3 are important, ultimately, the goal is to understand how these differences affect the near detector fit results. In order to compare how the differences affect the BANFF results, a systematic approach was taken to use the same inputs and change one thing at a time to see the effects of the change. In addition to the differences in the detector systematic weights and uncertainties between Psyche versions, a bug was discovered in the application of the MC statistical uncertainty and the 1p1h model uncertainty to the observable normalization covariance matrix. These three differences were taken into account by producing observable normalization covariance matrices with different inputs. First, a covariance matrix was

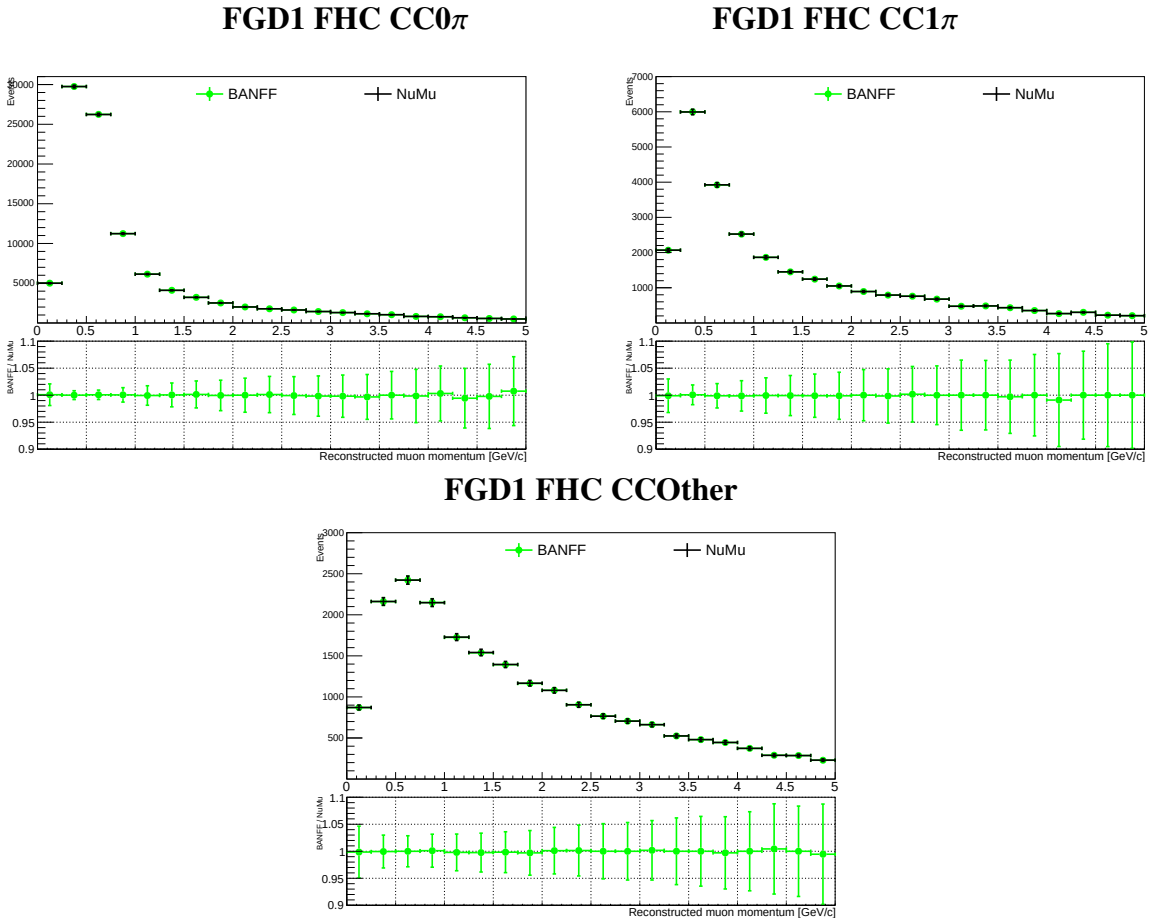

Figure A.6: Comparing selected events in Psyche v3 for BANFF and NuMu with the detector variations and the flux weight applied.

generated using only variations of the detector parameters for both Psyche v1 and Psyche v3. This matrix allows for a comparison of the underlying selections and systematic uncertainty changes between Psyche versions. Second, a covariance matrix was generated using detector parameter variations and adding the MC statistical error to the entries along the diagonal of the covariance matrix. By including the MC statistical error, the impact of the additional uncertainty on the fit can be observed. In a similar manner, a covariance matrix with the 1p1h model uncertainty added to the covariance matrix was generated. This shows the difference in the results given by including the 1p1h correction. Finally, an observable normalization covariance matrix including both the MC statistical error and the 1p1h correction shows the effect of including both uncertainties on the fit.

Initially, studies were performed comparing Psyche v1 results with different detector covariance matrices to one another, and similarly for Psyche v3. From these studies, a number of observations were made [122]:

1. There is little effect on the fit results when the 1p1h model uncertainty is included in the detector covariance matrix.

2. When the MC statistical error is included, both Psyche v1 and Psyche v3 exhibit upward shifts in the flux parameters and downward shifts in the observable normalization parameters.

3. The FSI and cross section parameters have similar results regardless of whether the MC statistical error is included or not.

4. When both the MC statistical error and the 1p1h model error are included, the fit results have very similar results to those seen when only the MC statistical error is included.

Once these studies had been performed, comparisons were made between the Psyche v1 and Psyche v3 results. First, when looking at results due to the detector weights only, significant differences between Psyche v1 and Psyche v3 were seen (Figures A.7 – A.9). Because the only difference in the inputs is due to the version of Psyche used, these differences must arise from the changes in selection and systematic uncertainties between Psyche v1 and Psyche v3. However, when comparing the post-fit distributions between the two versions in Figure A.10, they were found to be largely similar. So, even though the parameter values have larger differences, they are counterbalanced in such a way that the final distributions remain alike.

Because the effect of the 1p1h model error showed little movement in the fit results [122], comparisons of Psyche v1 to Psyche v3 with the 1p1h model error added, both on its own and with the MC statistical error, will not be looked at in this thesis. However, because the MC statistical error had more movement in both Psyche v1 and Psyche v3, it is beneficial to see how these compare to one another. When looking at Figures A.11 and A.13, there is an approximately constant upward shift for the flux parameters and a corresponding downward shift in the detector parameters when

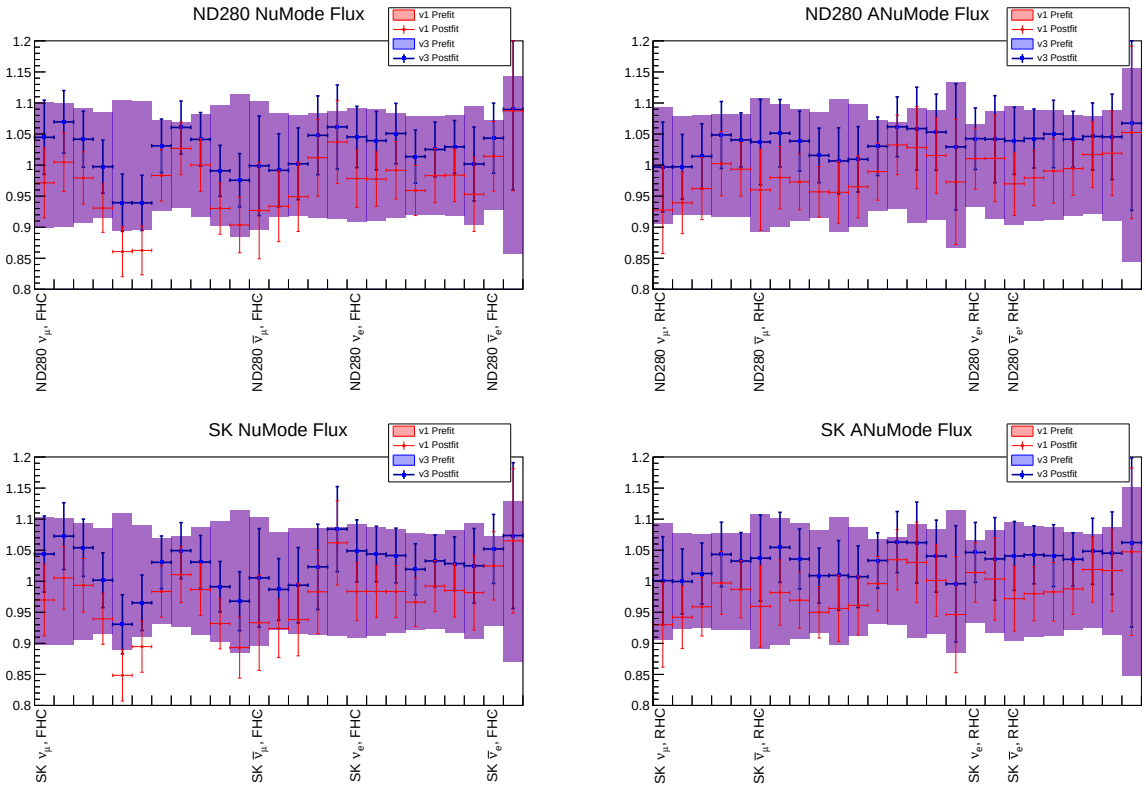

Figure A.7: BANFF fit results for the flux parameters comparing the effect of the detector selections and systematic uncertainties for Psyche v1 (red) and Psyche v3 (blue). The input values value can be seen in the background.

compared to Figures A.7 and A.9, respectively. This shift is approximately the same for both Psyche v1 and Psyche v3. Therefore, it was determined that the effect of the MC statistical error is approximately constant between the two versions of Psyche, which implies that the differences seen between Psyche v1 and Psyche v3 must be coming from the differences in selections and systematic uncertainties. Finally, when looking at the post-fit distributions for Psyche v1 and Psyche v3, little difference is found between the distributions.

In order to test the impact of the changes in the near detector fit results to the oscillation analysis, predictions of the oscillated event distributions at SK were produced using the fit results from the full observable normalization covariance (detector weights plus MC statistical error plus 1p1h model error). Because the 1p1h model uncertainty has very little effect, Figures A.11 – A.13

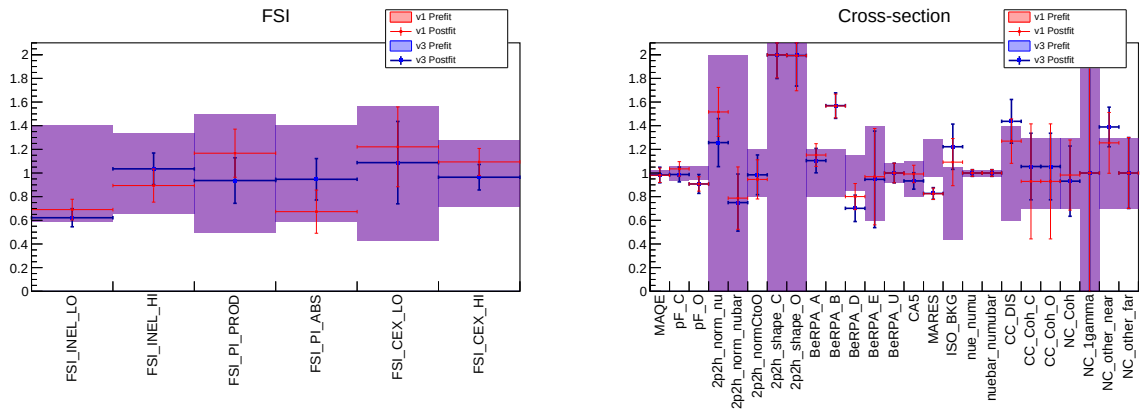

Figure A.8: BANFF fit results for the FSI and cross section parameters comparing the effect of the detector selections and systematic uncertainties for Psyche v1 (red) and Psyche v3 (blue). The input values value can be seen in the background.

provides an idea of the fit results used as inputs to the event prediction. Looking at Figure A.15, the event prediction for each type of neutrino is approximately the same between the two Psyche versions. Because the event predictions are consistent, the final oscillation results should be similar, giving credence that moving from Psyche v1 to Psyche v3 is a viable option.

In summary, the main cause of the differences in the post-fit parameter values between Psyche v1 and Psyche v3 is due to the updates in the sample selections and detector systematic uncertainties. With regards to the differences seen in the MC statistical error and 1p1h model uncertainty, it was found that the MC statistical error results in a shift upward for the flux parameters and and downward for the detector parameters. On the other hand, the 1p1h correction did not result in much change when compared to the shifts from the MC statistical error. Ultimately, it was determined that, even though the parameter values differ, the post-fit distributions between Psyche v1 and Psyche v3 differ little. This is also seen when comparing Psyche v1 to itself or Psyche v3 to itself [122]. When translating these results to the oscillation analysis, the results showed that the SK prediction of the oscillated event distributions each fall within uncertainties, implying the final oscillation results would be consistent, regardless of whether Psyche v1 or Psyche v3 is used.

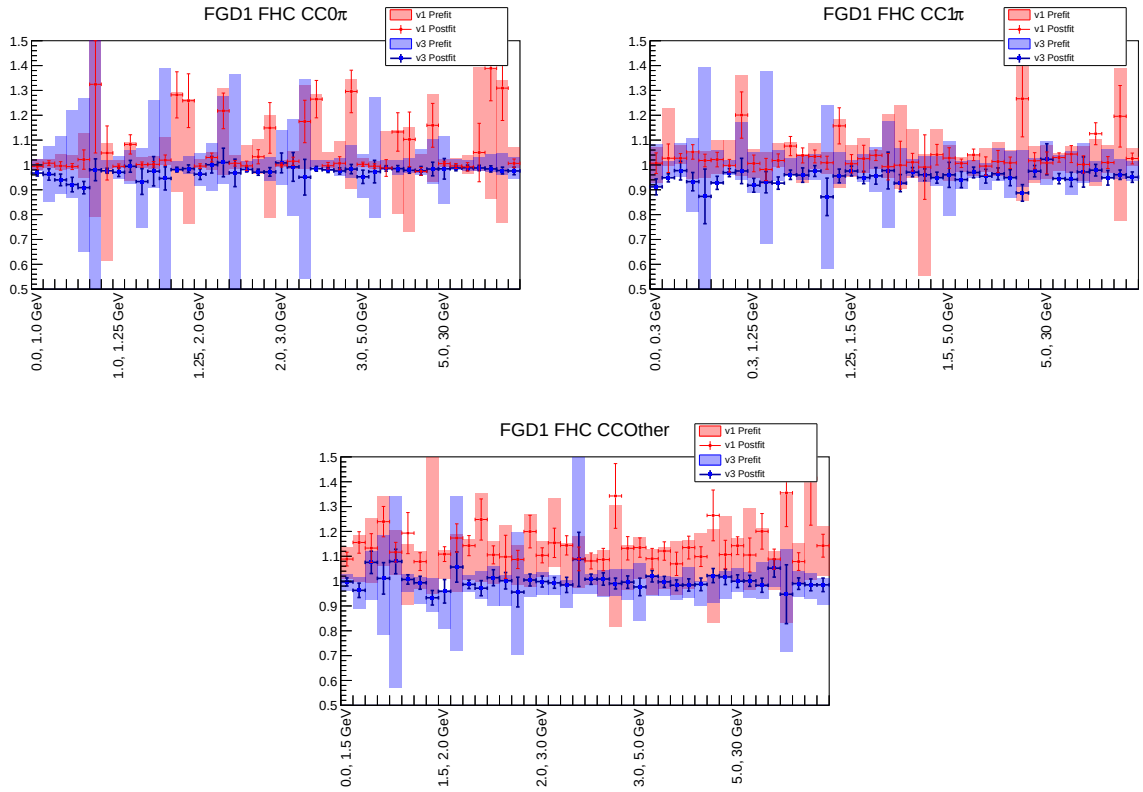

Figure A.9: BANFF fit results for the observable normalization parameters comparing the effect of the detector selections and systematic uncertainties for Psyche v1 (red) and Psyche v3 (blue). The input values value can be seen in the background.

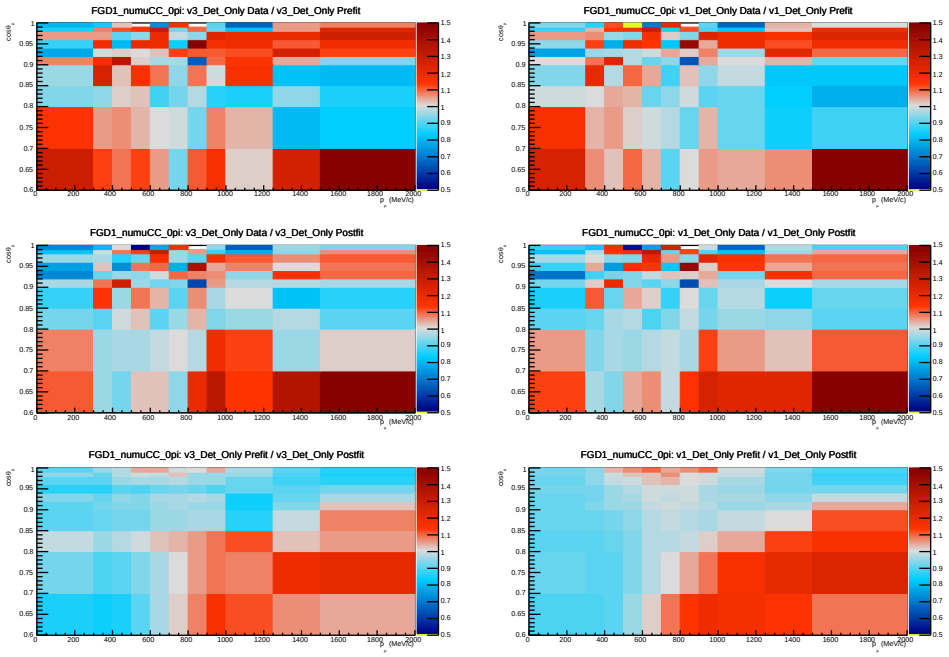

Figure A.10: Comparison of the effect of the detector selections and systematic uncertainties on the BANFF post-fit distributions for Psyche v3 (left) and Psyche v1 (right).

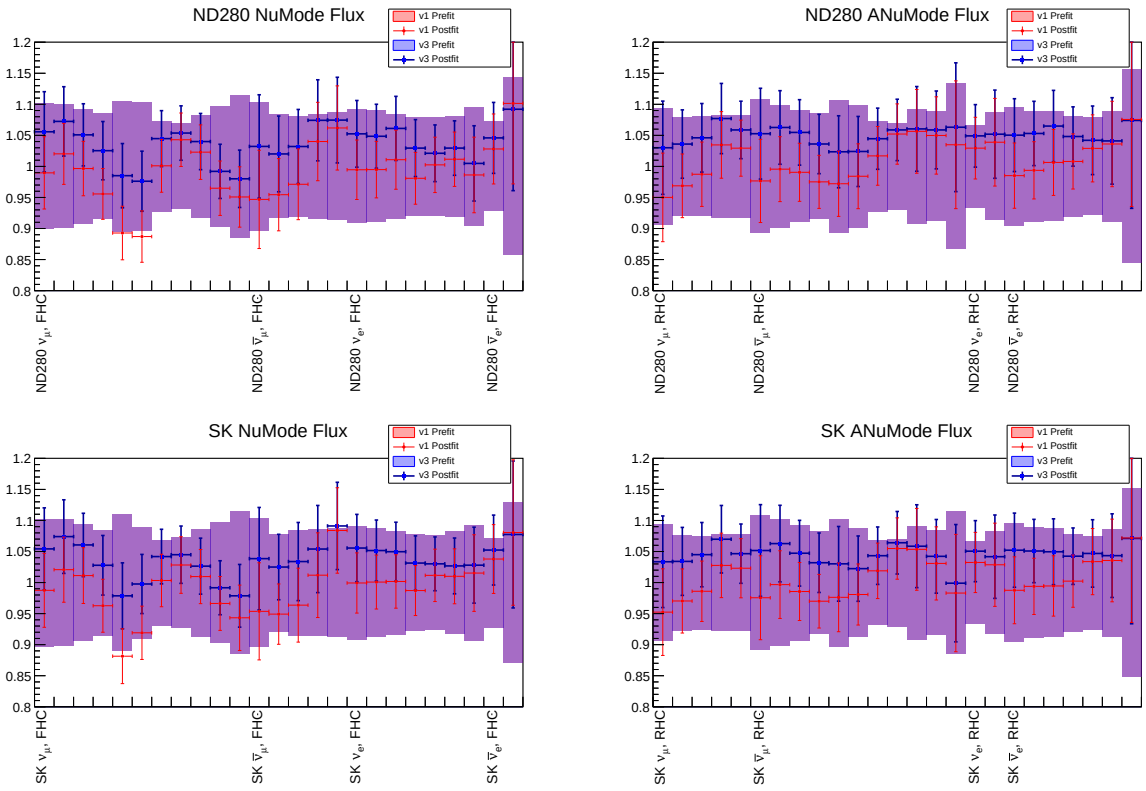

Figure A.11: BANFF fit results for the flux parameters comparing the effect of the detector selections and systematic uncertainties and the MC statistical error for Psyche v1 (red) and Psyche v3 (blue). The input values value can be seen in the background.

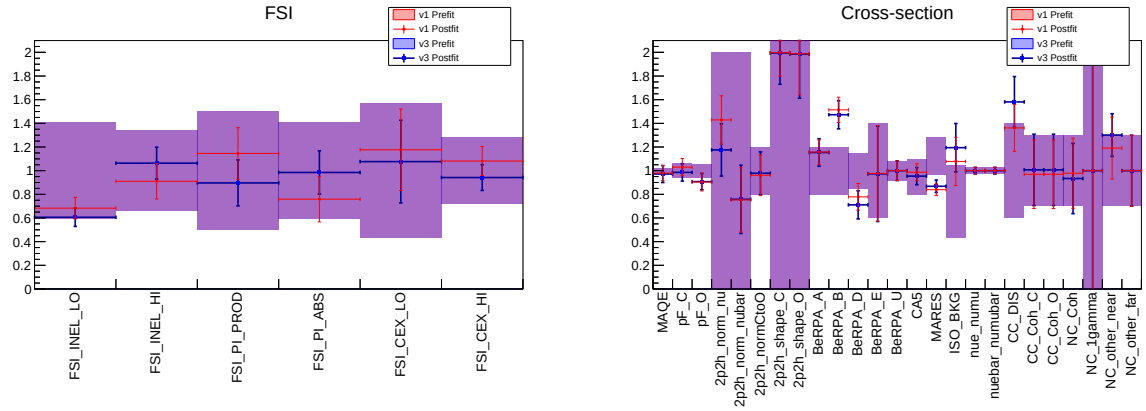

Figure A.12: BANFF fit results for the FSI and cross section parameters comparing the effect of the detector selections and systematic uncertainties and the MC statistical error for Psyche v1 (red) and Psyche v3 (blue). The input values value can be seen in the background.

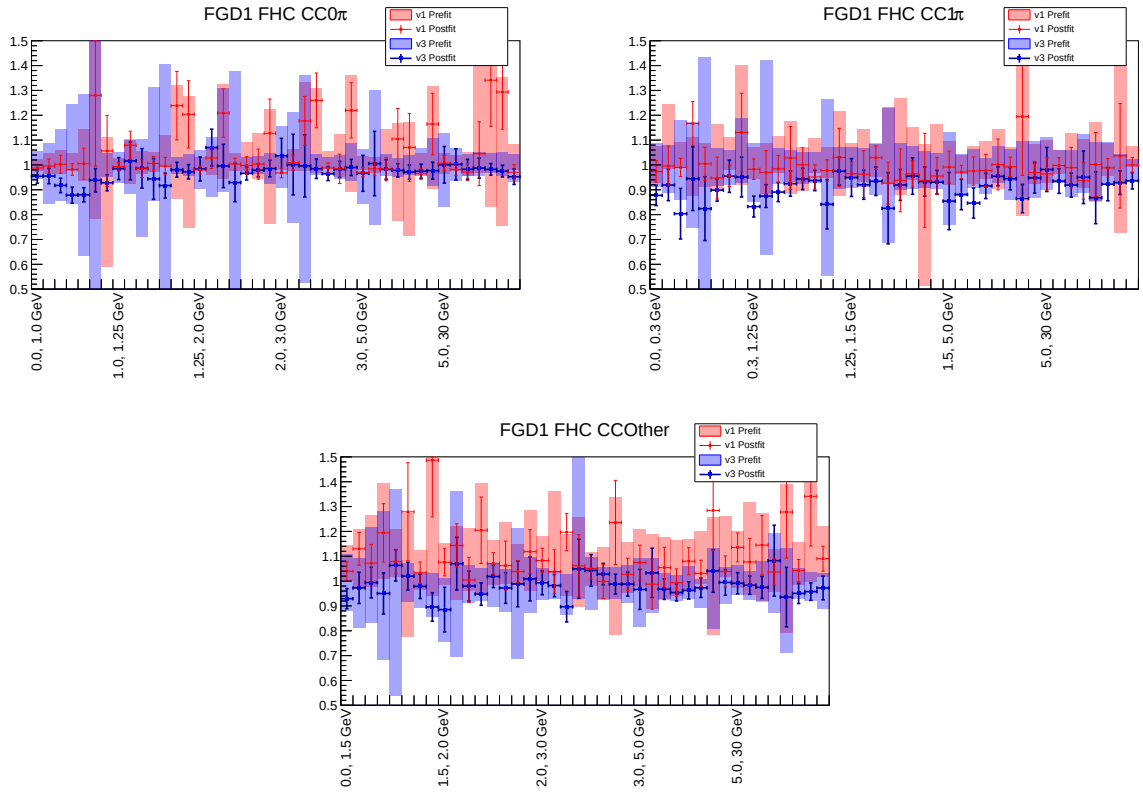

Figure A.13: BANFF fit results for the observable normalization parameters comparing the effect of the detector selections and systematic uncertainties and the MC statistical error for Psyche v1 (red) and Psyche v3 (blue). The input values value can be seen in the background.

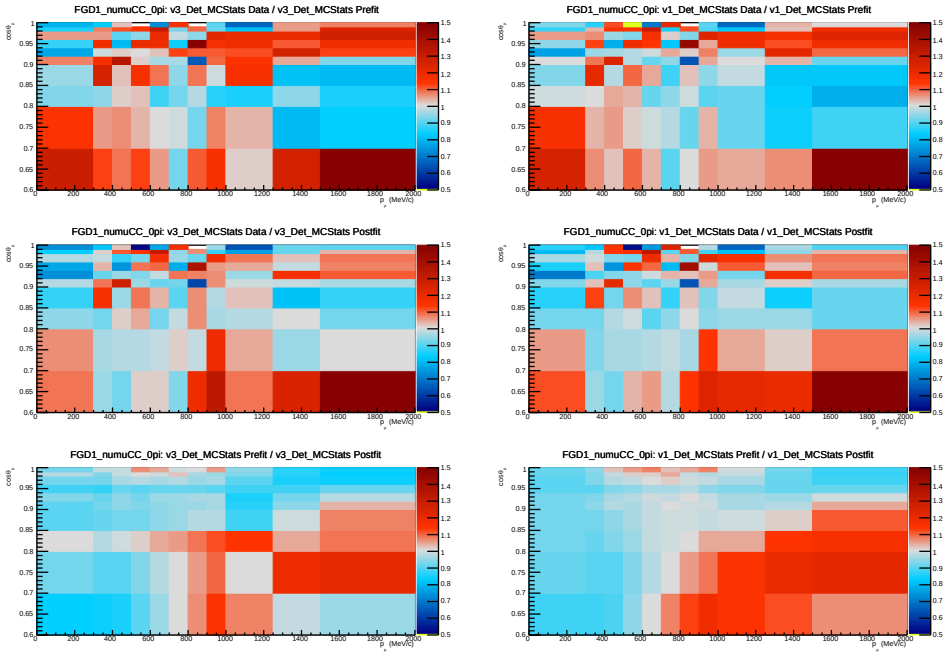

Figure A.14: Comparison of the effect of the detector selections and systematic uncertainties and the MC statistical error on the BANFF post-fit distributions for Psyche v3 (left) and Psyche v1 (right).

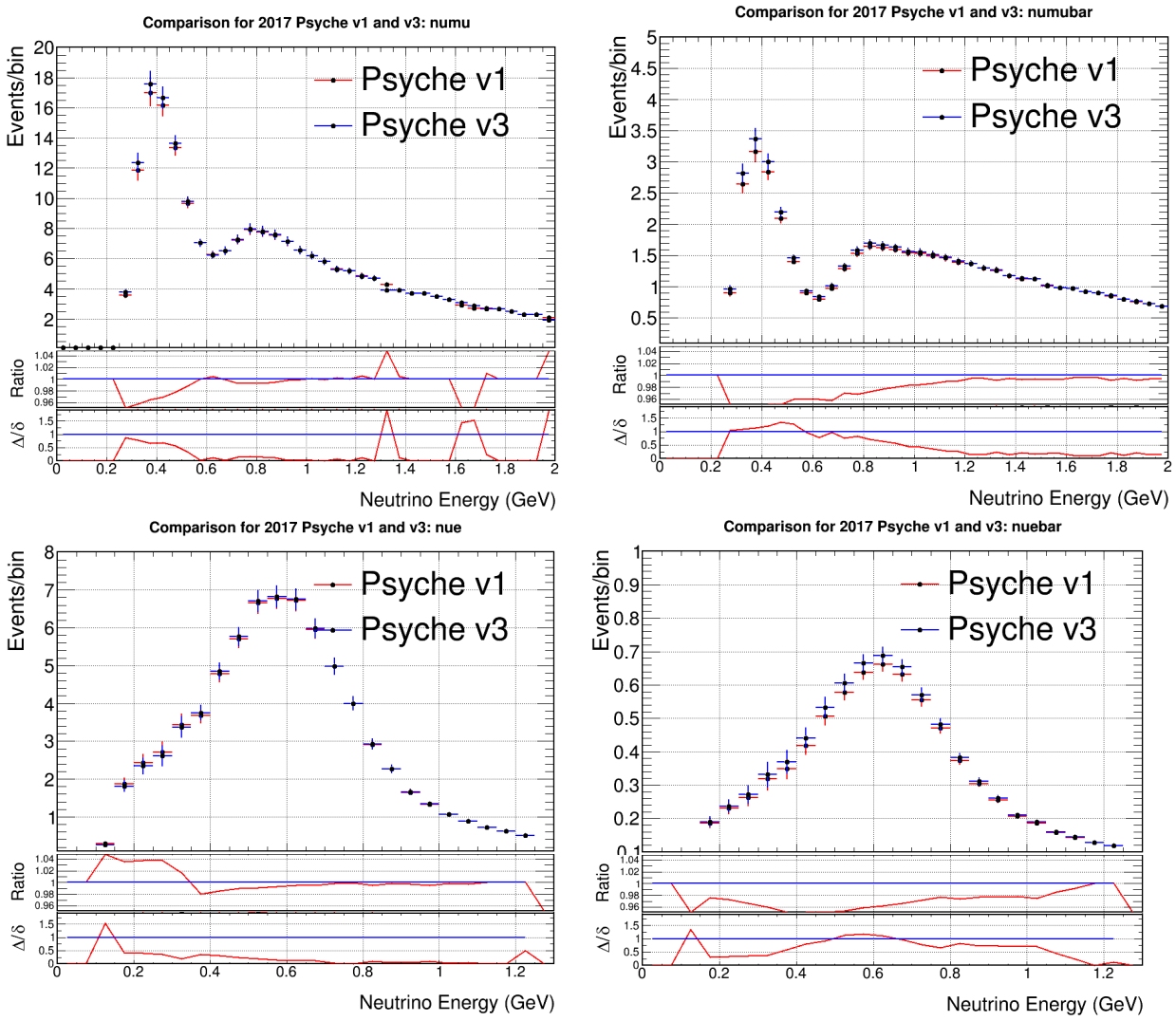

Figure A.15: SK oscillated event predictions for the ν_μ (upper left), $\bar{\nu}_\mu$ (upper right), ν_e (lower left), $\bar{\nu}_e$ (lower right) fluxes. The ratio is of Psyche v1 to Psyche v3 (v1 / v3) and the Δ/δ plot is of (|v1 - v3| / (v1 error)) and measures the difference between the two versions with respect to the v1 error bar.

APPENDIX B

OBSERVABLE NORMALIZATION COVARIANCE MATRIX BINNING STUDIES

Ideally, when generating the observable normalization covariance matrix, each entry along the diagonal should correspond to a single $p - \cos\theta$ fit bin. However, when tallying the number of fit bins, the number quickly reaches an amount that becomes impractical when trying to minimize the likelihood function described in Section 4.2.1 using Minuit. Therefore, a binning is chosen for the detector covariance matrix that combines several fit bins.

B.1 Thoughts Behind Combining Bins

When combining bins, there are a number of considerations to bear in mind. First, the bins should approximately follow the shape of the data. Therefore, it is preferable to not combine bins in the peak kinematic region, which, for T2K, is a reconstructed muon momentum of approximately 600 MeV/c and in the very forward direction, as seen in Figure B.1. Furthermore, as each detector bin corresponds to a $p - \cos\theta$ bin, it is best to look at the covariance (or correlation) matrix where the bins are grouped into blocks with the same angular bins or, conversely, where the bins are grouped into blocks with the same momentum bins, as shown in Figure B.2.

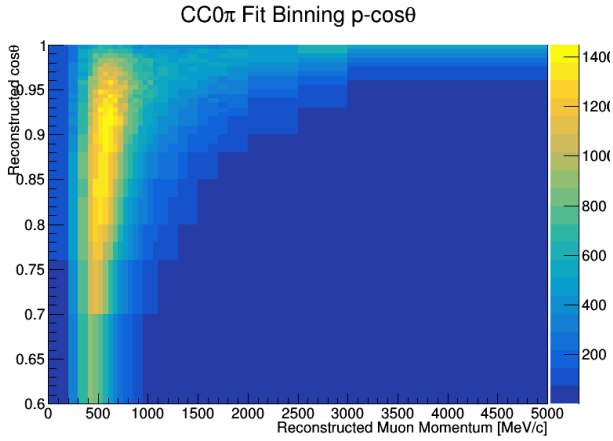

Figure B.1: Monte Carlo event distribution of reconstructed muon momentum and angle.

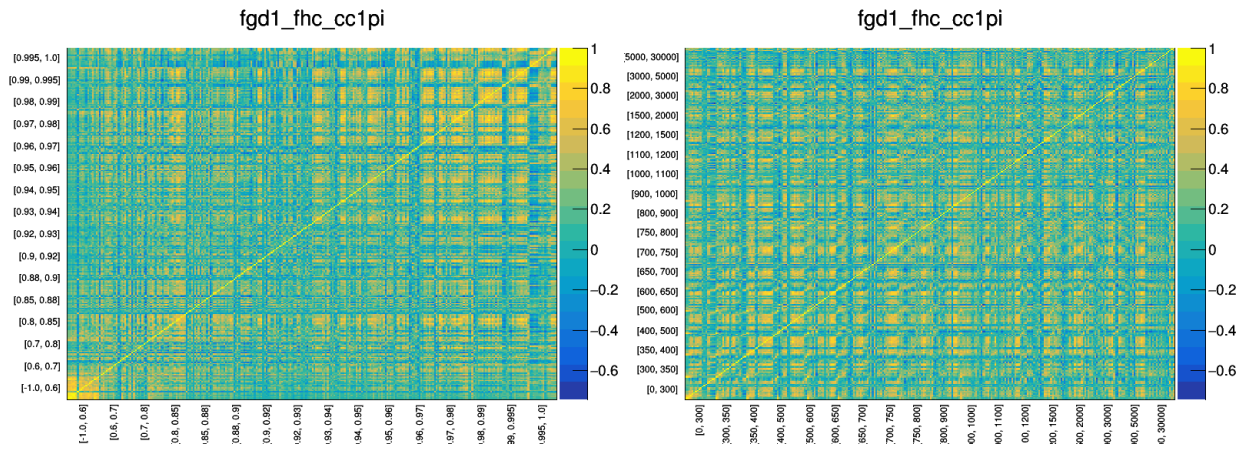

Figure B.2: Correlation matrices where the bins are grouped by angular bins (left) or momentum bins (right).

In this binning study, the detector correlation matrix was used, rather than the covariance matrix, as it is easier to distinguish regions that are highly correlated using a correlation matrix. Here, regions with relatively high correlations were combined, pending they were for bins outside the peak kinematic region. It should be noted the value that defines "high" correlation is fairly arbitrary, as combining bins based purely on the correlation is usually not sufficient to reduce the number of bins to a reasonable number. Therefore, after combining bins based on high correlations, regions of the covariance matrix with correlations of approximately the same amount were combined into single bins, as seen in Figure B.3.

B.2 Results from the Binning Study

In this study, only the forward horn current samples were studied, as the fit binning for these samples changed dramatically compared to previous analyses, while the reverse horn current fit binning has not been changed from previous analyses. Therefore, only results from the FHC samples will be shown.

CC0π Binning and Correlation

For the FGD1 FHC CC0π sample, the process of combining bins can be seen in Figures B.4 and B.5, while the event distributions at each step are shown in Figure B.6. The final correlation

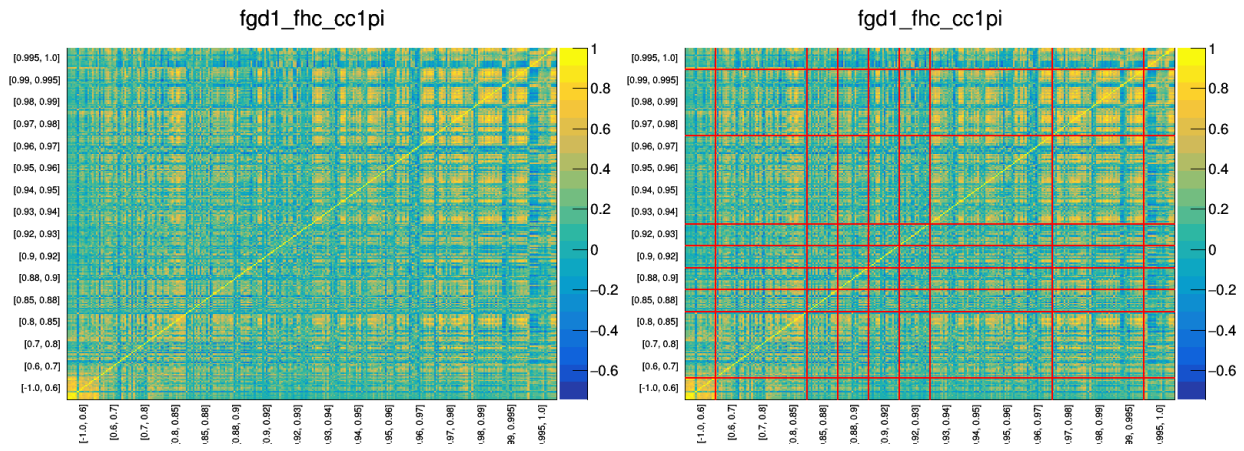

Figure B.3: Correlation matrix before combining bins (left) and with red lines demarcating the regions to be combined (right).

matrix can be seen in Figure B.7. While not shown, the FGD2 FHC CC0π sample shows similar results to those seen here.

CC1π Binning and Correlation

For the FGD1 FHC CC1π sample, the process of combining bins can be seen in Figures B.8 and B.9, while the event distributions at each step are shown in Figure B.10. The final correlation matrix can be seen in Figure B.11. While not shown, the FGD2 FHC CC1π sample shows similar results to those seen here.

CCOther Binning and Correlation

For the FGD1 FHC CCOther sample, the process of combining bins can be seen in Figures B.12 and B.13, while the event distributions at each step are shown in Figure B.14. The final correlation matrix can be seen in Figure B.15. While not shown, the FGD2 FHC CCOther sample shows similar results to those seen here.

B.3 Conclusion and Further Study

In order to reduce the number of observable normalization parameters, a study was performed to combine similarly correlated bins. The total number of bins (along the diagonal) for the reduced observable normalization covariance matrix can be seen in Table B.1.

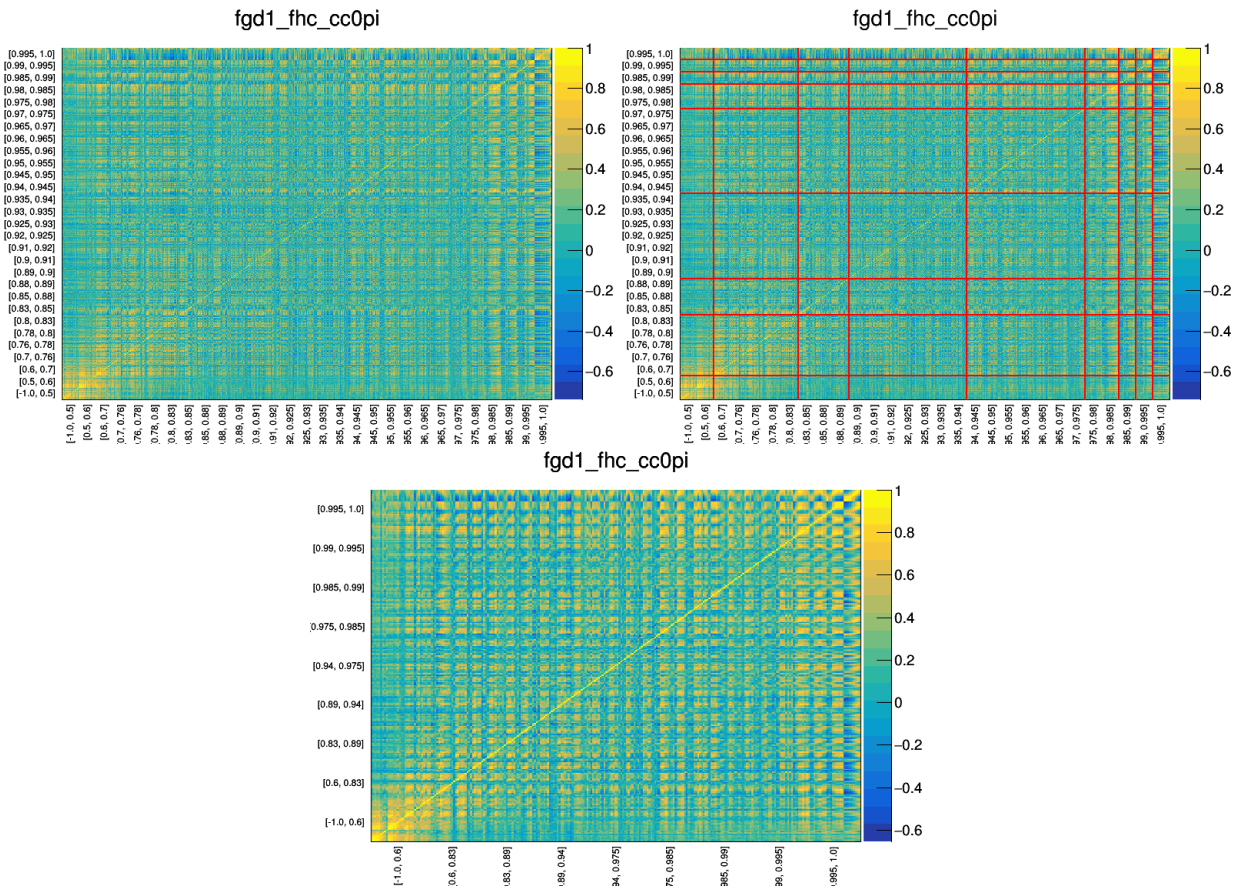

Figure B.4: Combining the CC0π angular bins. Before combining bins can be seen in the top left, the bins to be combined (set off by the red lines) are in the top right, and the resulting matrix after combining bins is on the bottom.

Sample Set	Number of Bins
FHC MultiPi plus RHC MultiTrack	834
FHC MultiPi plus RHC MultiPi	690

Table B.1: The total number of bins along the diagonal of the observable normalization covariance matrix.

While the number of bins shown in Table B.1 was sufficient for this thesis, it is on the upper end of what is reasonable when performing studies from the near detector fit. Additionally, a number of assumptions were made when combining bins, such as only using the correlation matrix

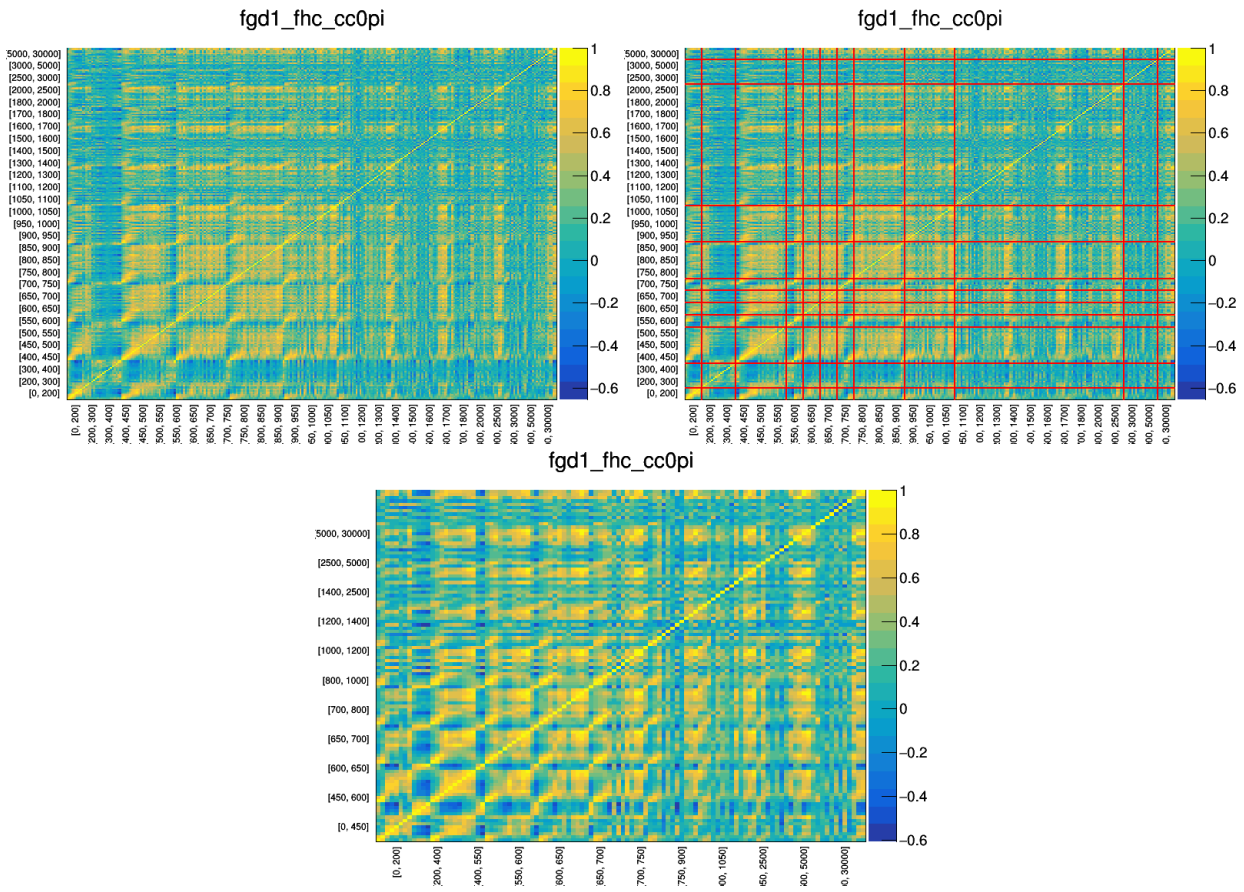

Figure B.5: Combining the CC0π momentum bins. Before combining bins can be seen in the top left, the bins to be combined (set off by the red lines) are in the top right, and the resulting matrix after combining bins is on the bottom.

for combining bins and not using the covariance matrix. Therefore, a more thorough study of combining bins should be done to ensure the BANFF fit is providing a result to the T2K oscillation analysis that is independent of the choice of binning.

In order to perform a more thorough study, two potential routes could be taken. First, the combination process can be done in a way that takes into account differences in the error between adjacent bins and the overall correlation of groups of bins that share the same angular or momentum bin. This process can either be done by eye, or through the use of an algorithm to appropriately combine bins meeting criteria determined either through machine-learning or through human means.

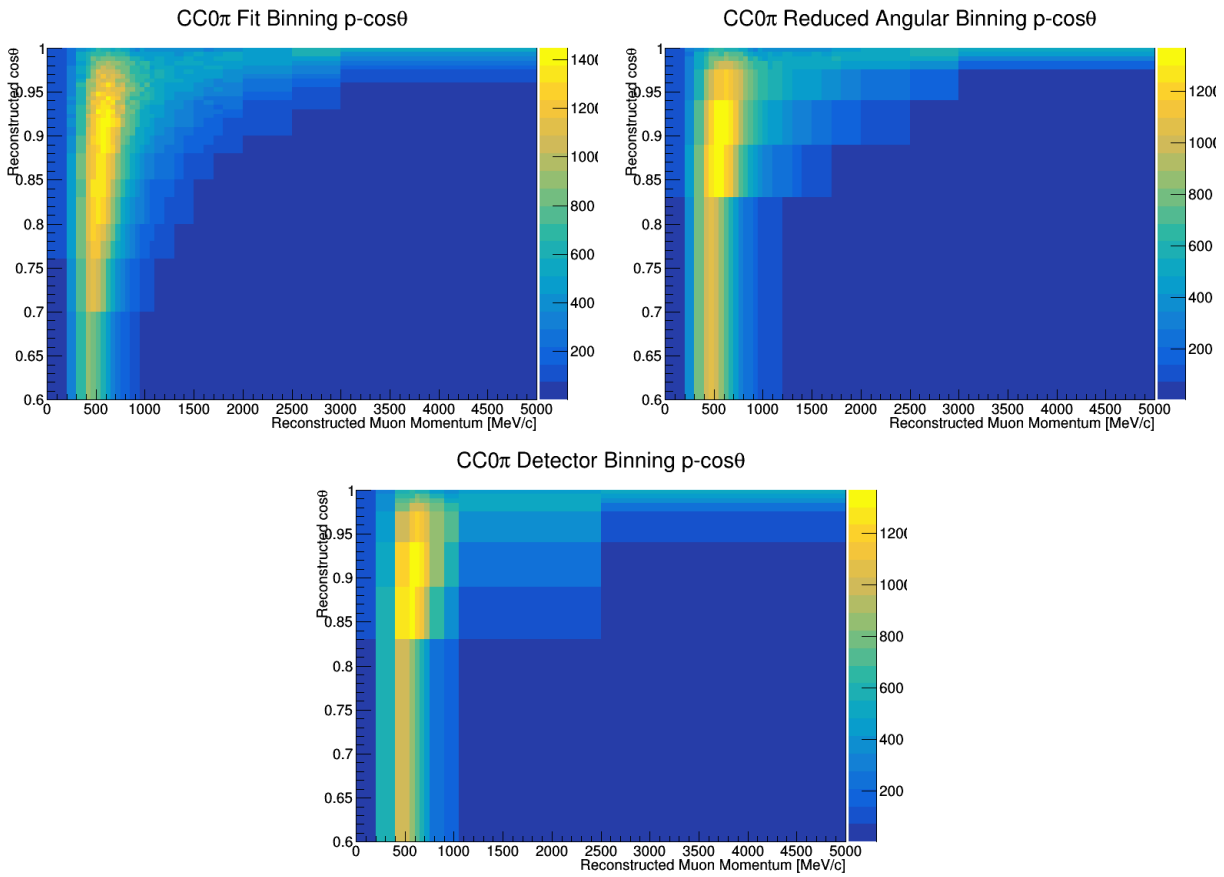

Figure B.6: The FGD1 FHC CC0π $p - \cos\theta$ distributions for the fit binning (top left), the binning with a combined angular binning and the full momentum binning (top right), and the final detector binning (bottom). Each bin is scaled by the bin area.

Another method to reduce the number of bins would be to perform a principal component analysis (PCA) of the observable normalization covariance matrix, which would show the set of parameters that provide the largest freedom to move parameters during the likelihood maximization. Once the PCA has been performed, the number of parameters can be reduced in a number of ways:

1. The largest X values can be chosen, where X is a constant value.

2. Plot the values from largest to smallest, cutting where there is sharp drop off from one value to the next.

3. Integrate over the values, cutting after a set integral has been met.

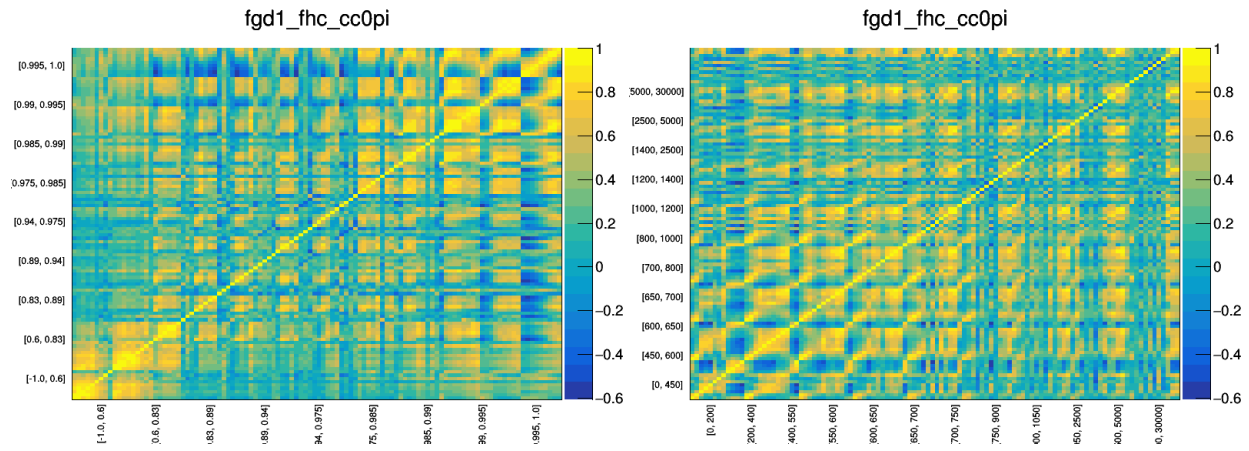

Figure B.7: The final correlation matrices for the FGD1 FHC CC0π sample. The bins are grouped by common angular bins on the left and common momentum bins (which is the order used in the likelihood fit) on the right.

With regards to the first point, one benefit would be that each fit would contain the same number of parameters, regardless of the number of input parameters. However, depending on where this number is set, too much information about the observable normalization covariance matrix can be thrown away, likely reducing the effectiveness of the likelihood fit. As to the second option, this would keep the set of parameters which have a smooth transition between them. However, the definition of "sharp drop" could be hard to determine. Furthermore, there is a potential to keep too many parameters depending on where the drop occurs. Finally, the third option would determine which parameters correspond to some percentage of the information contained in the detector covariance matrix. This choice would ensure that a minimum amount of information is passed into the fit regarding the detector. However, depending on the percentage that is chosen, too many parameters could be passed into the fit, making the fit take an unreasonable amount of time.

Whether the number of bins is reduced through a PCA or through the careful combination of bins, with the increasing number of fit bins, it is essential the number of detector covariance bins be kept at a reasonable level, so that the BANFF fit continues to run in a reasonable amount of time and continue its contributions to the T2K oscillation analysis.

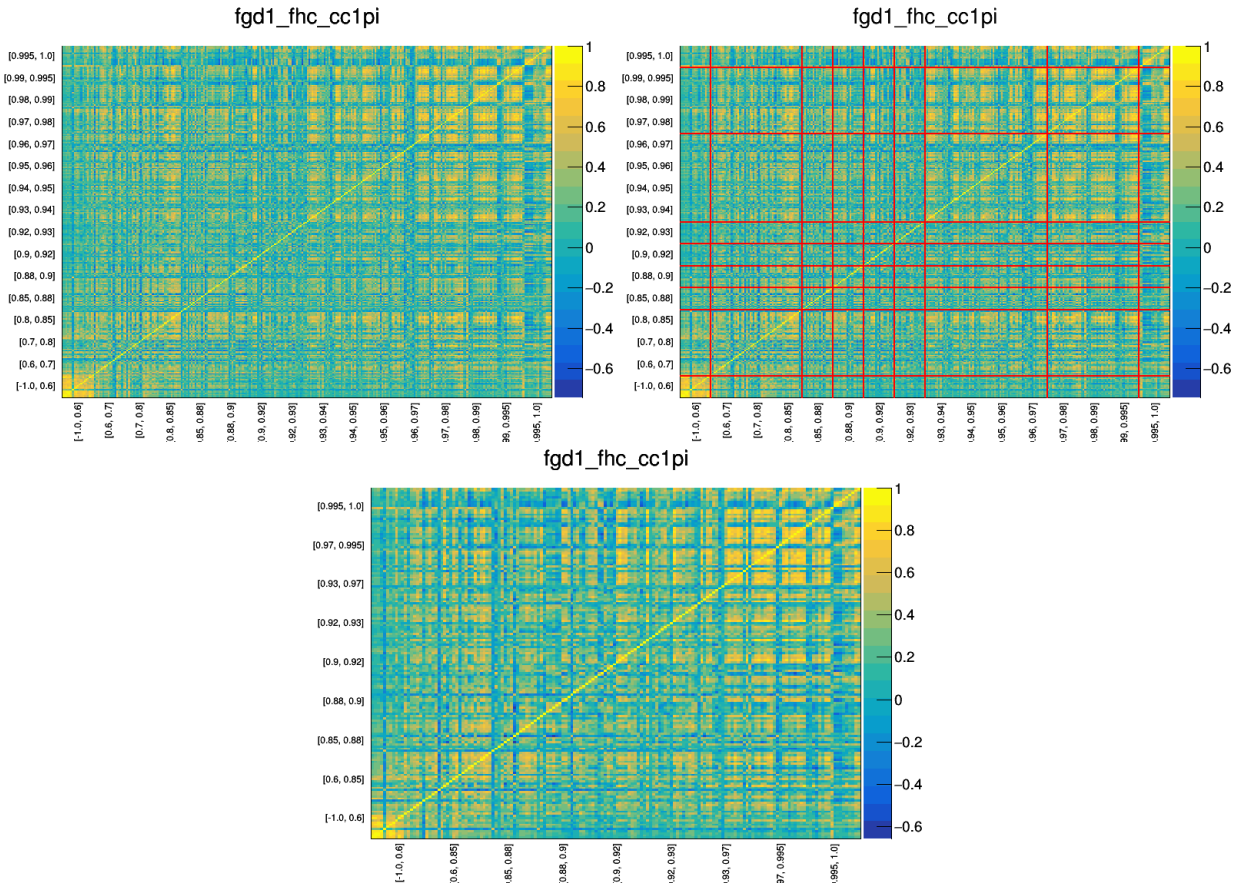

Figure B.8: Combining the CC1π angular bins. Before combining bins can be seen in the top left, the bins to be combined (set off by the red lines) are in the top right, and the resulting matrix after combining bins is on the bottom.

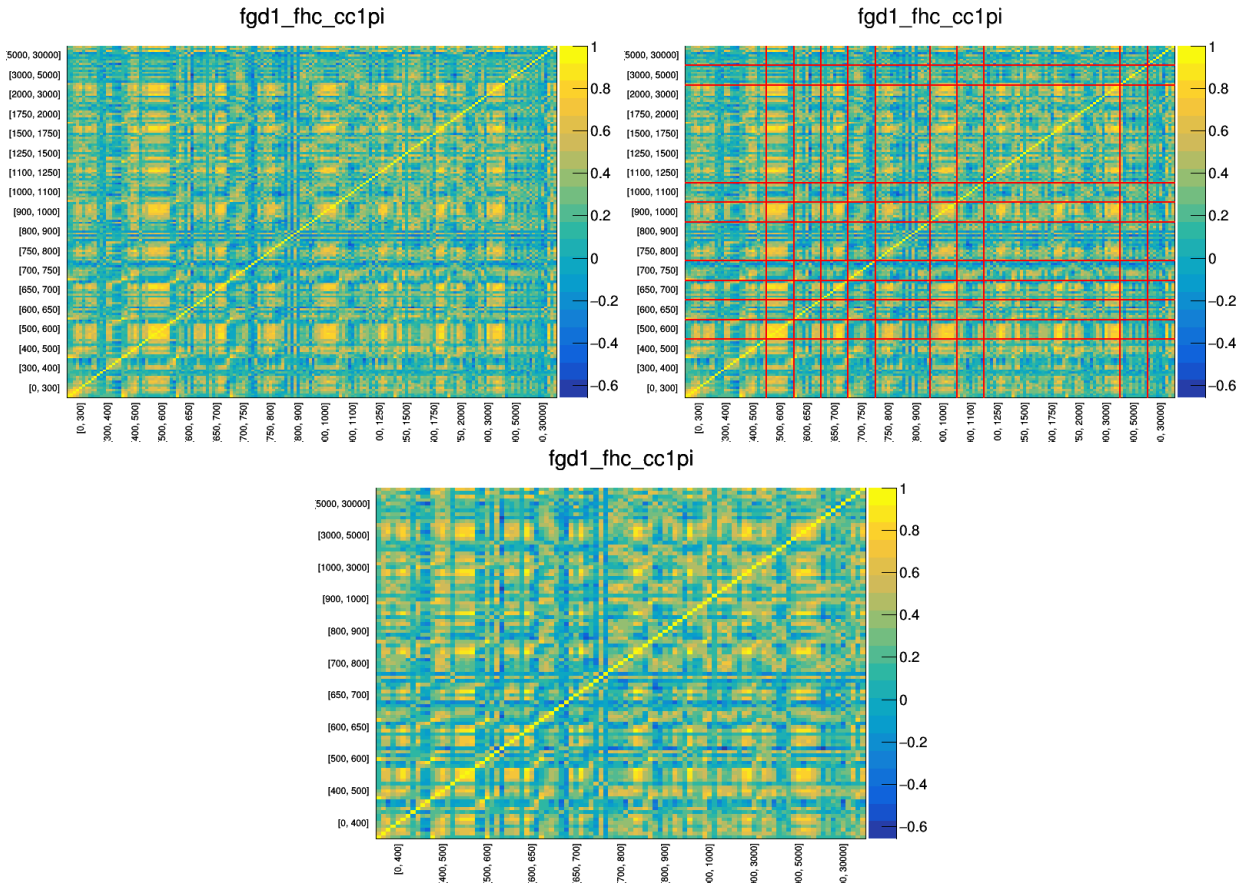

Figure B.9: Combining the CC1π momentum bins. Before combining bins can be seen in the top left, the bins to be combined (set off by the red lines) are in the top right, and the resulting matrix after combining bins is on the bottom.

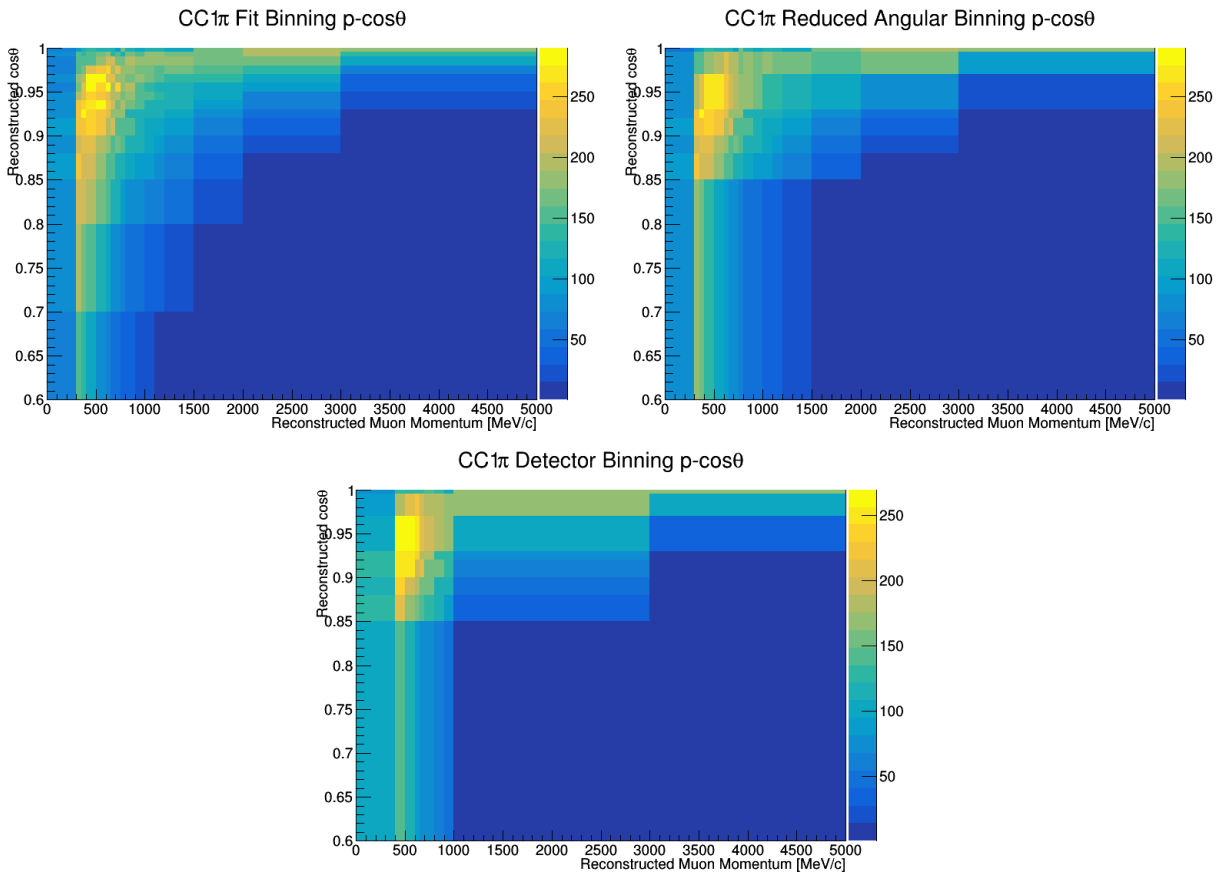

Figure B.10: The FGD1 FHC CC1π $p - \cos\theta$ distributions for the fit binning (top left), the binning with a combined angular binning and the full momentum binning (top right), and the final detector binning (bottom). Each bin is scaled by the bin area.

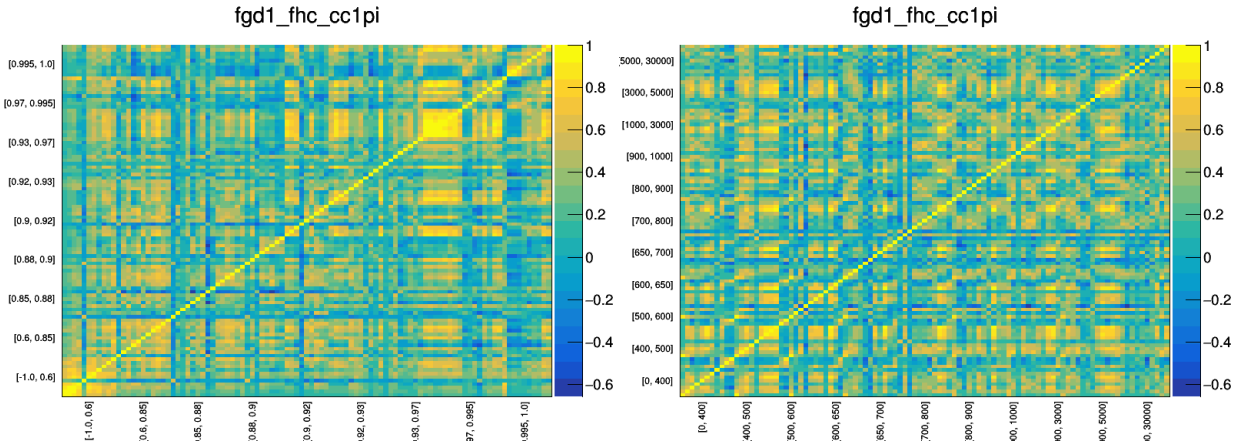

Figure B.11: The final correlation matrices for the FGD1 FHC CC1π sample. The bins are grouped by common angular bins on the left and common momentum bins (which is the order used in the likelihood fit) on the right.

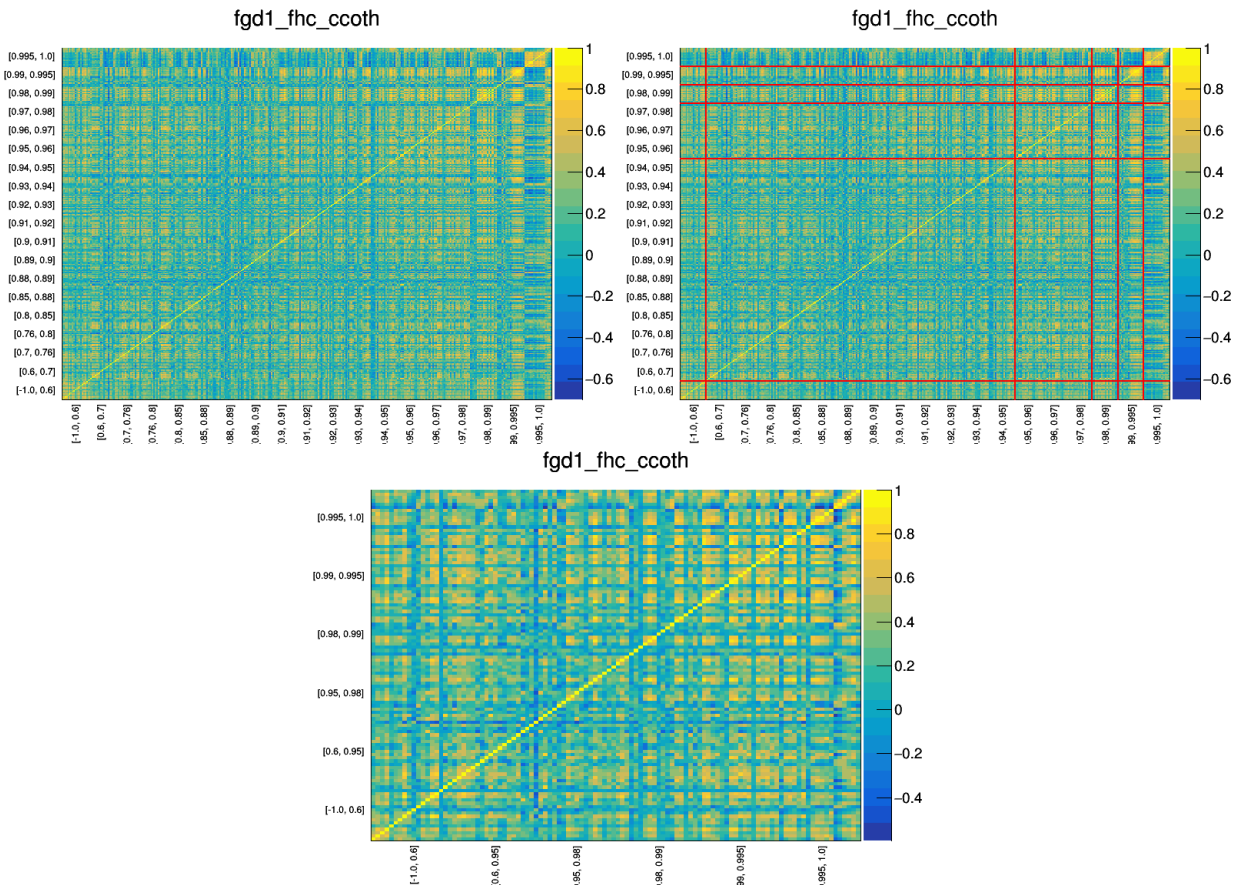

Figure B.12: Combining the CCOther angular bins. Before combining bins can be seen in the top left, the bins to be combined (set off by the red lines) are in the top right, and the resulting matrix after combining bins is on the bottom.

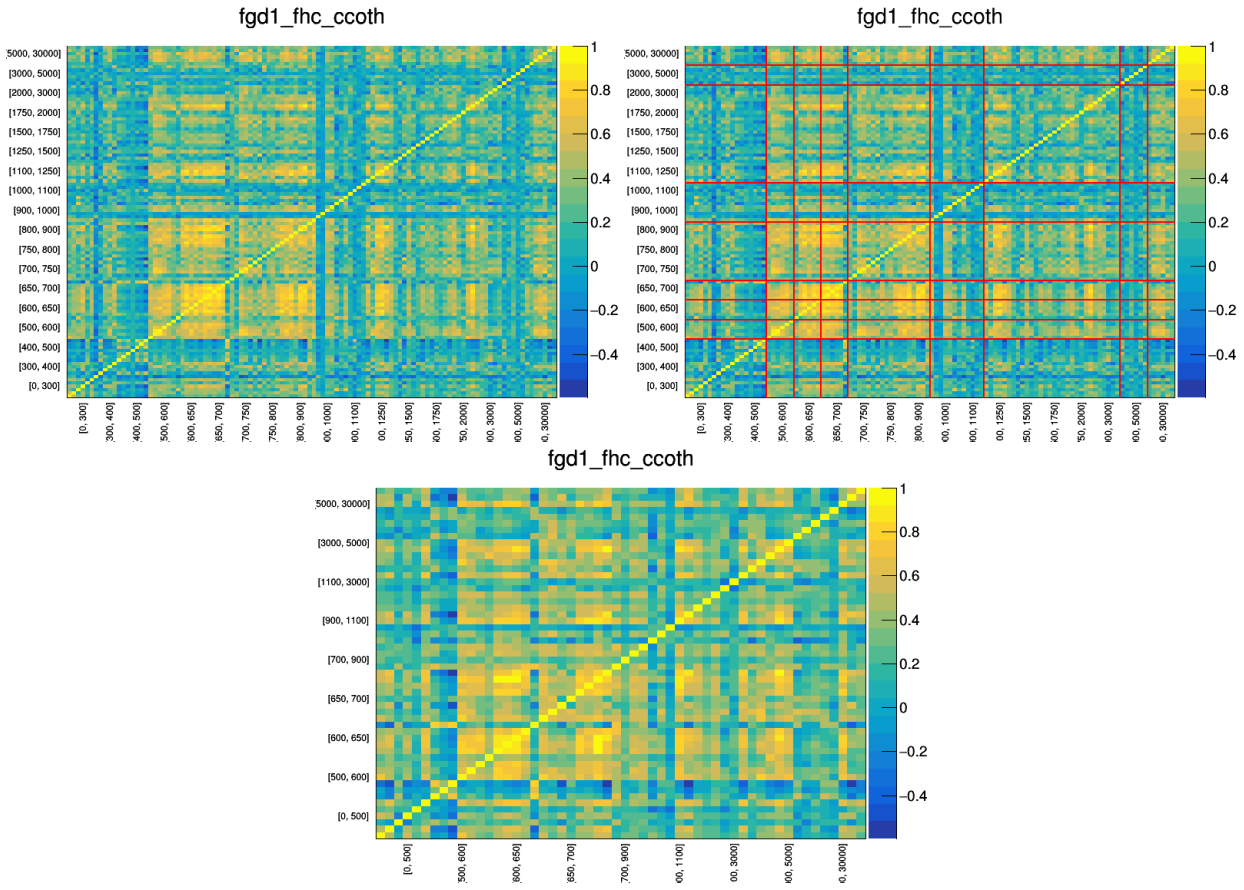

Figure B.13: Combining the CCOther momentum bins. Before combining bins can be seen in the top left, the bins to be combined (set off by the red lines) are in the top right, and the resulting matrix after combining bins is on the bottom.

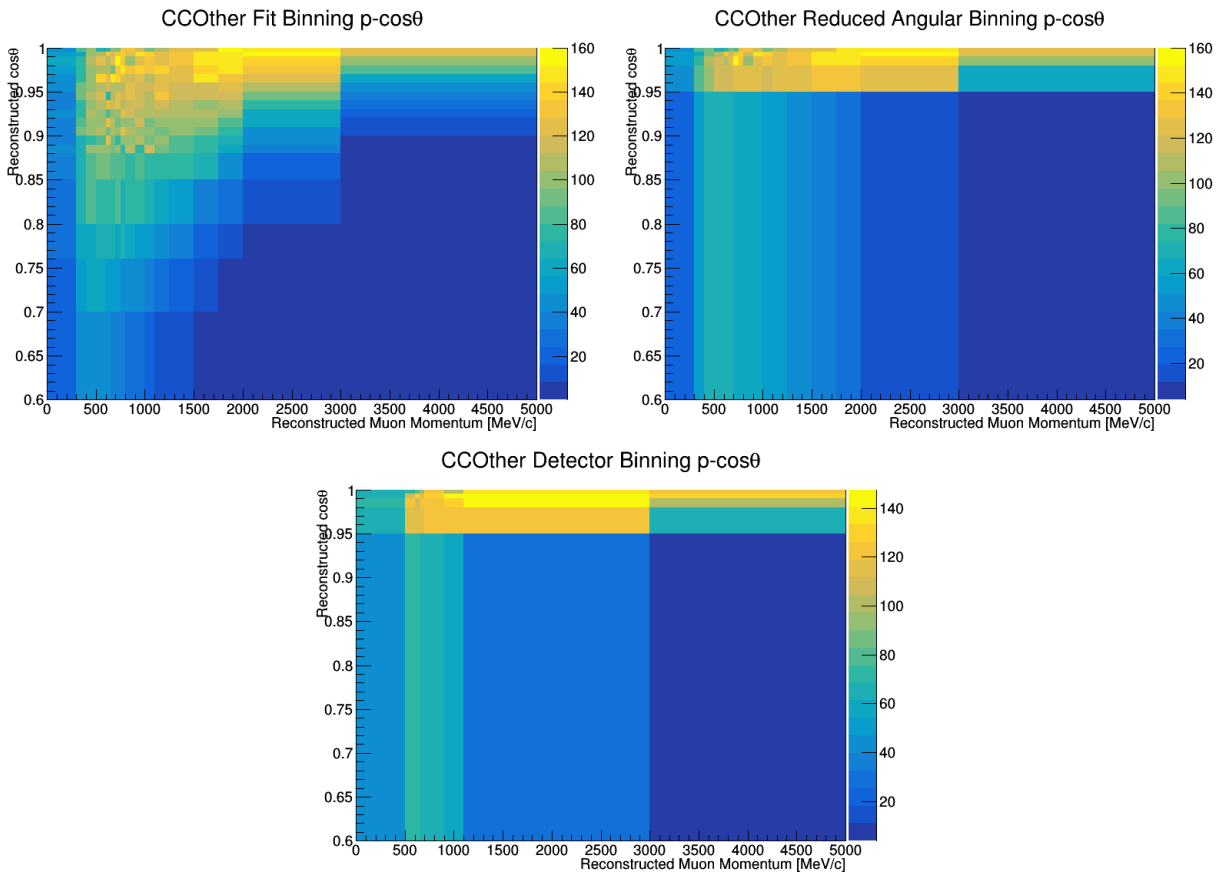

Figure B.14: The FGD1 FHC CCOther $p - \cos\theta$ distributions for the fit binning (top left), the binning with a combined angular binning and the full momentum binning (top right), and the final detector binning (bottom). Each bin is scaled by the bin area.

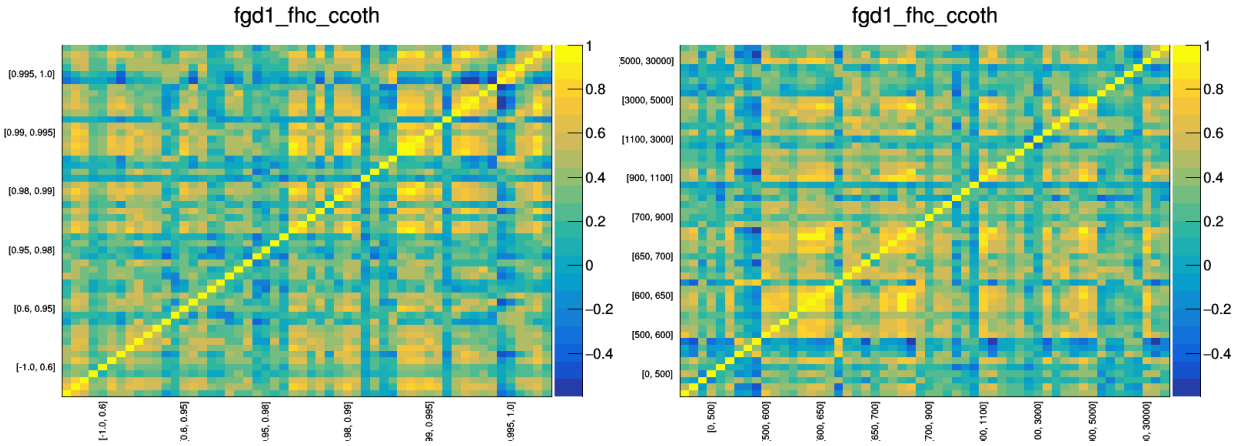

Figure B.15: The final correlation matrices for the FGD1 FHC CCOther sample. The bins are grouped by common angular bins on the left and common momentum bins (which is the order used in the likelihood fit) on the right.

APPENDIX C

FINE-GRAINED DETECTOR 2 RELATED PLOTS

FGD2 FHC CC0π

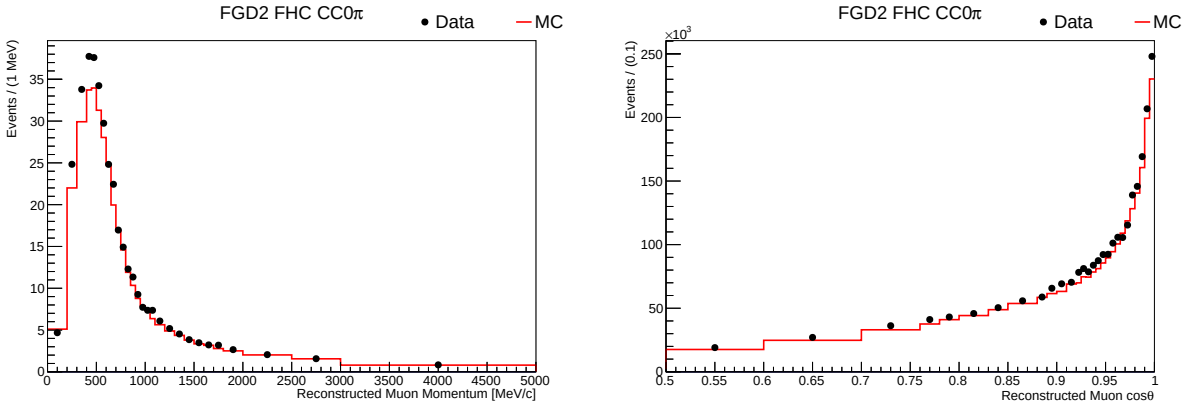

FGD2 FHC CC1π

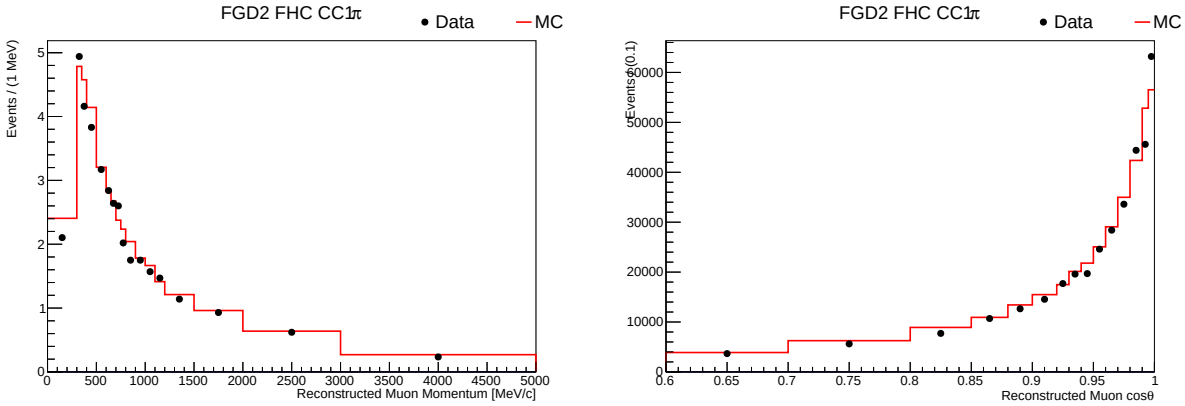

FGD2 FHC CCOther

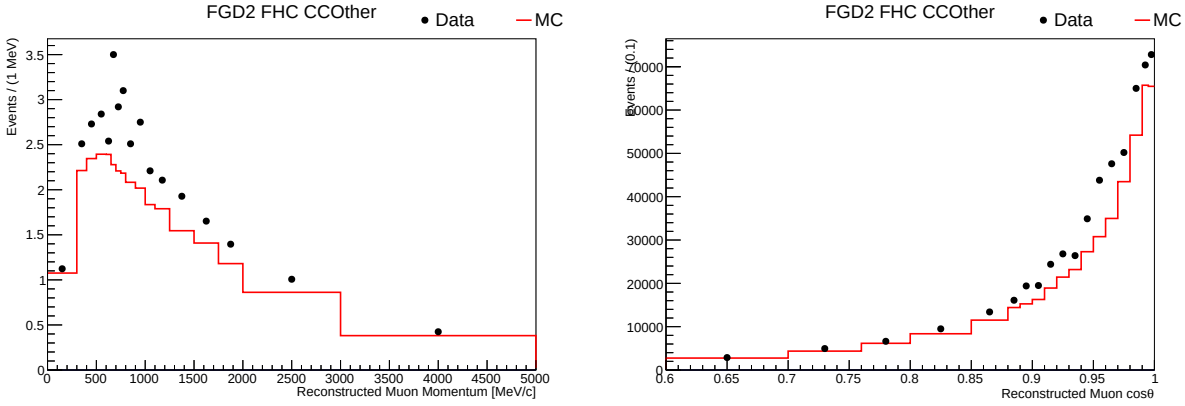

Figure C.1: Kinematic distributions used as inputs to the BANFF fit for the FGD2 FHC MultiPi selections. The momentum distributions are shown on the left, while the angular distributions are shown on the right.

FGD2 FHC CC0π

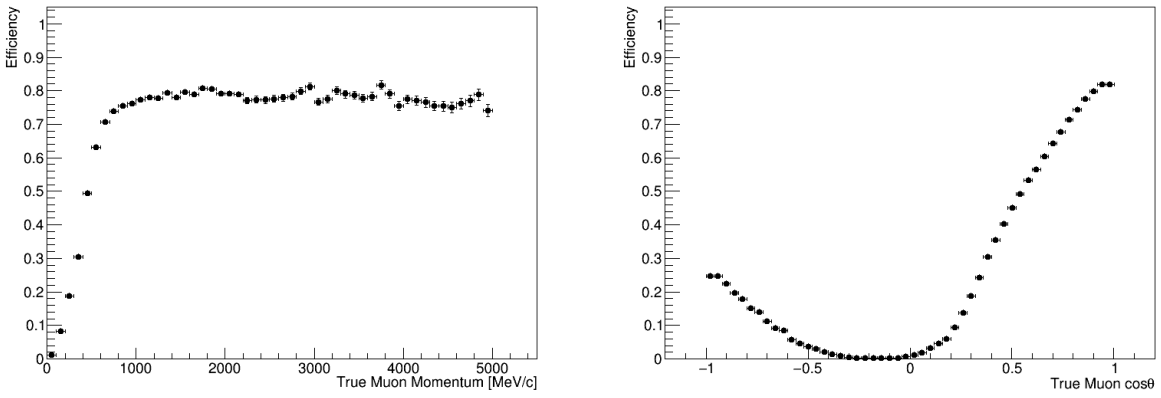

FGD2 FHC CC1π

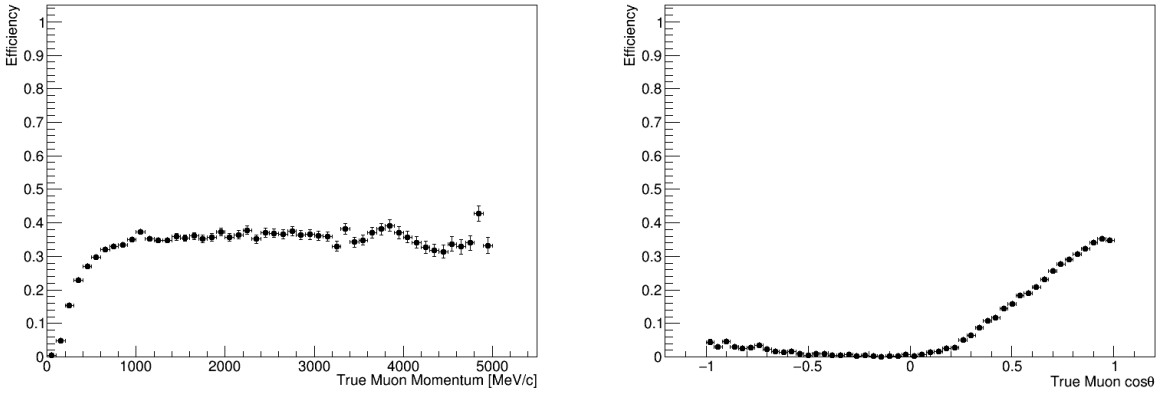

FGD2 FHC CCOther

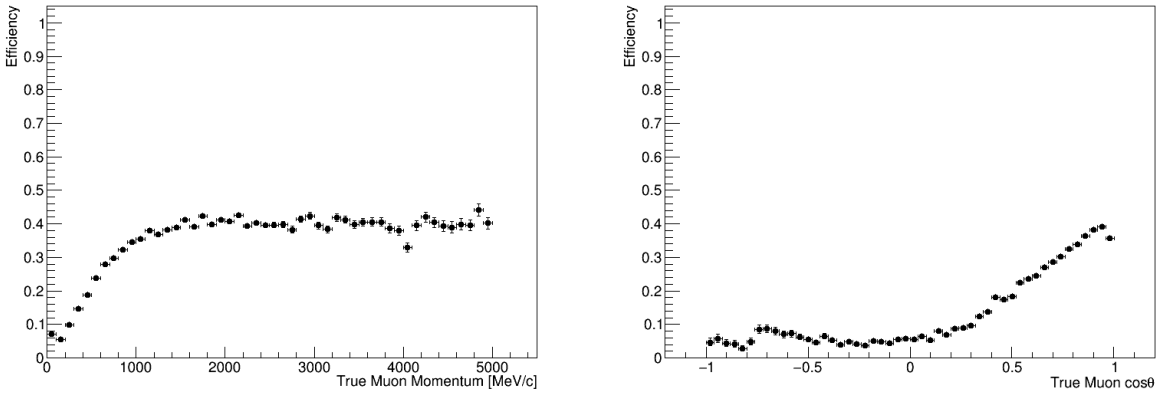

Figure C.2: Selection efficiency as a function of true muon momentum (left) or true muon cos θ (right) for the FGD2 FHC MultiPi selections.

FGD2 FHC CC0π

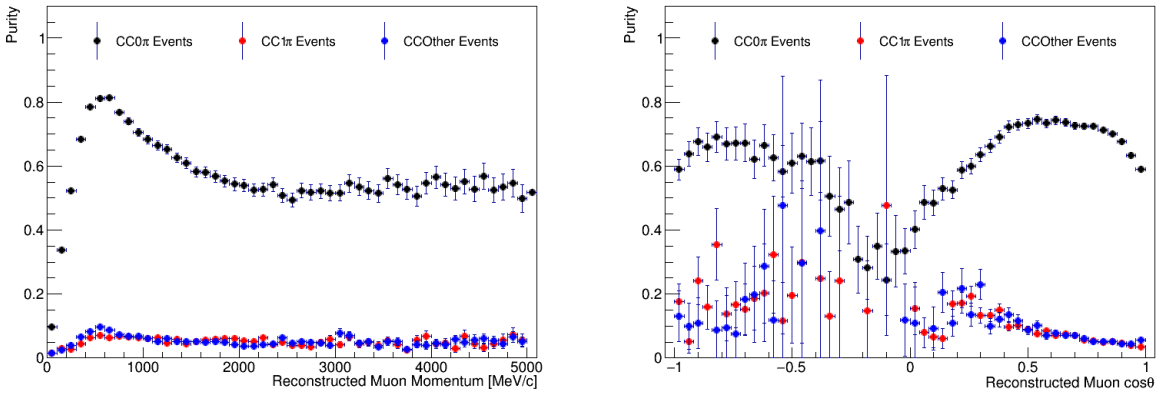

FGD2 FHC CC1π

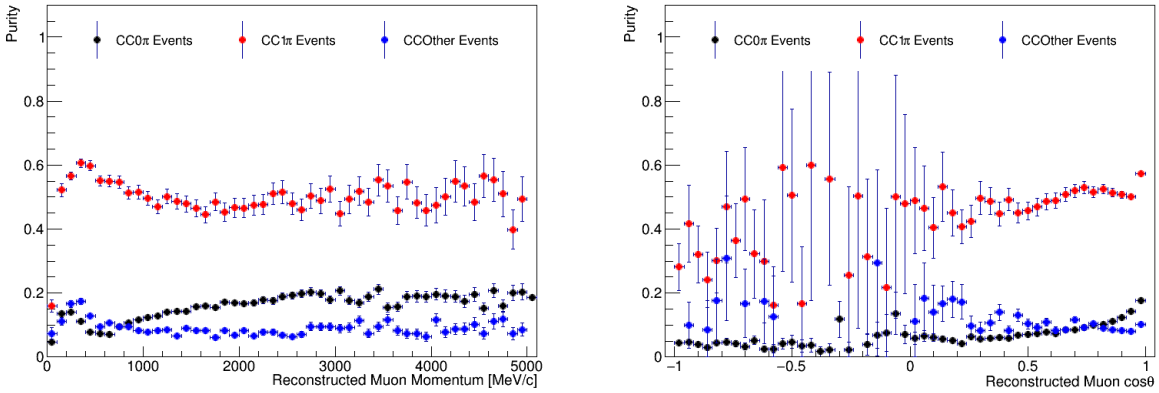

FGD2 FHC CCOther

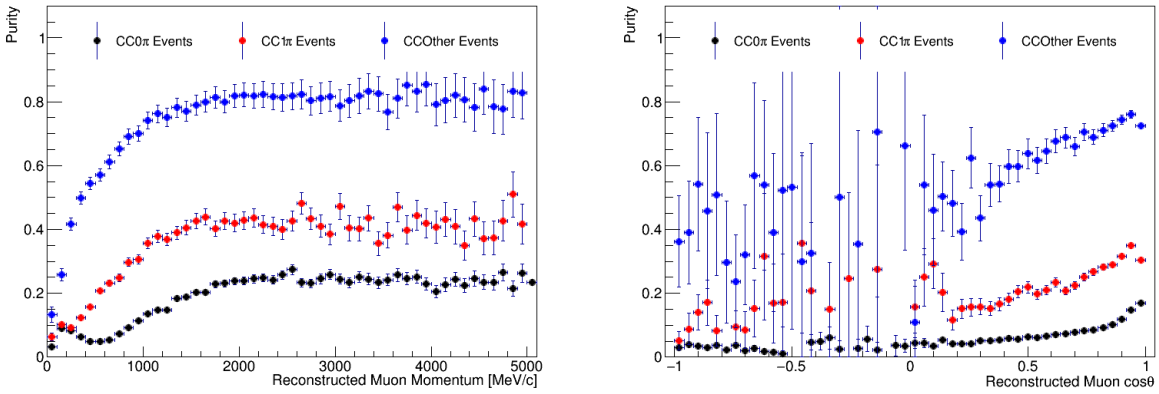

Figure C.3: Selection purity as a function of reconstructed muon momentum (left) or reconstructed muon cos θ (right) for the FGD2 FHC MultiPi selections.

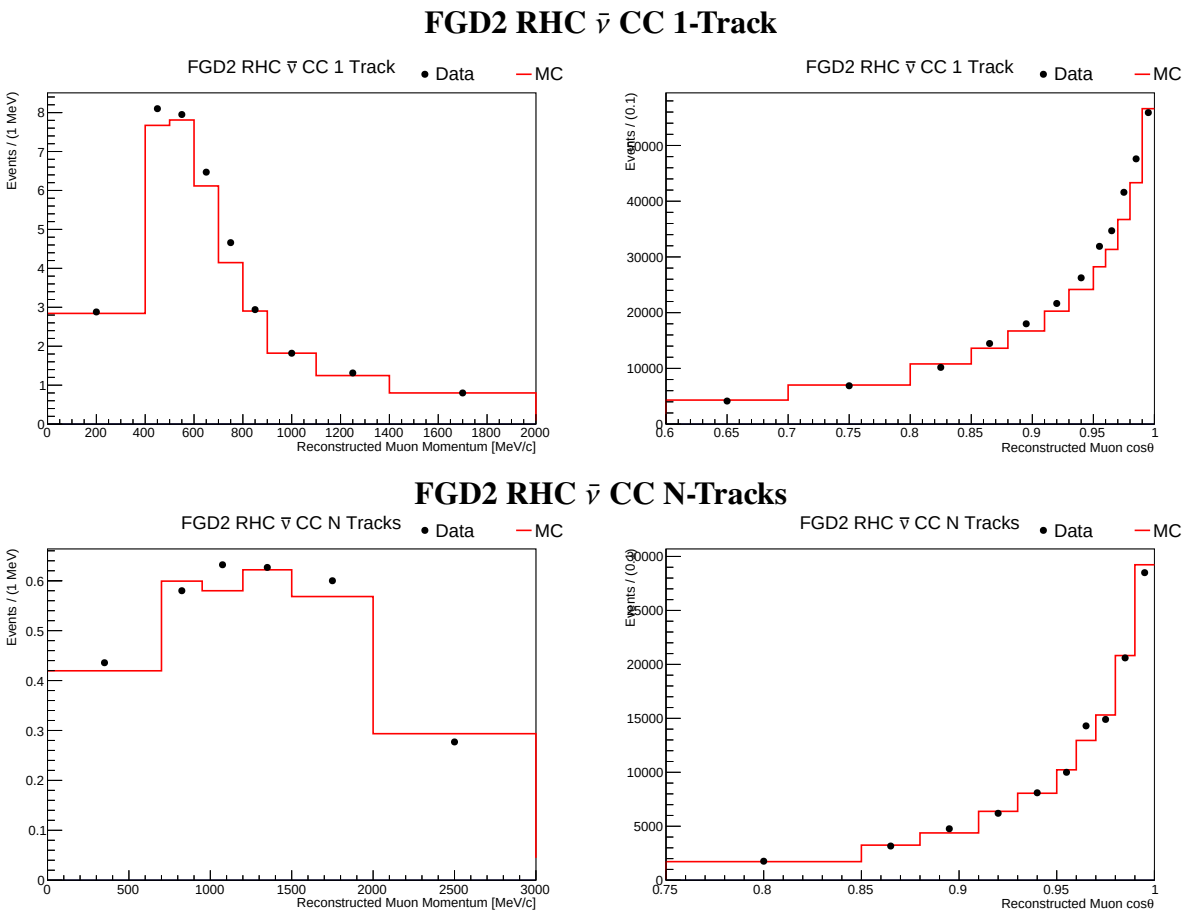

Figure C.4: Kinematic distributions used as inputs to the BANFF fit for the FGD2 RHC $\bar{\nu}$ MultiTrack selections. The momentum distributions are shown on the left, while the angular distributions are shown on the right.

FGD2 RHC $\bar{\nu}$ CC 1-Track

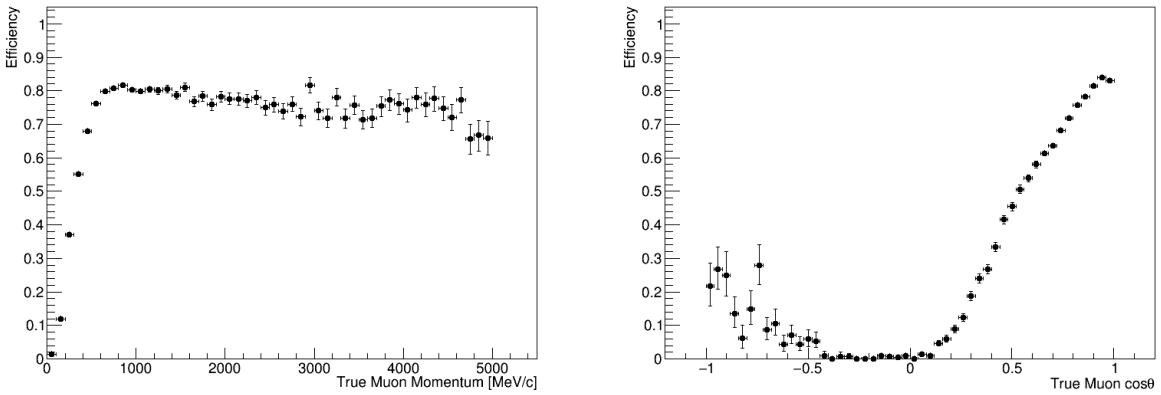

FGD2 RHC $\bar{\nu}$ CC N-Tracks

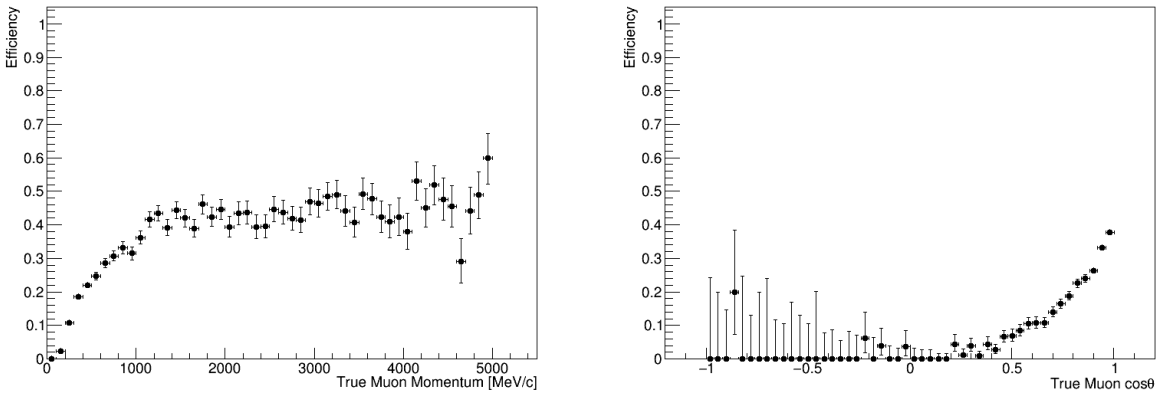

Figure C.5: Selection efficiency as a function of true muon momentum (left) or true muon $\cos\theta$ (right) for the FGD2 RHC $\bar{\nu}$ MultiTrack selections.

FGD2 RHC $\bar{\nu}$ CC 1-Track

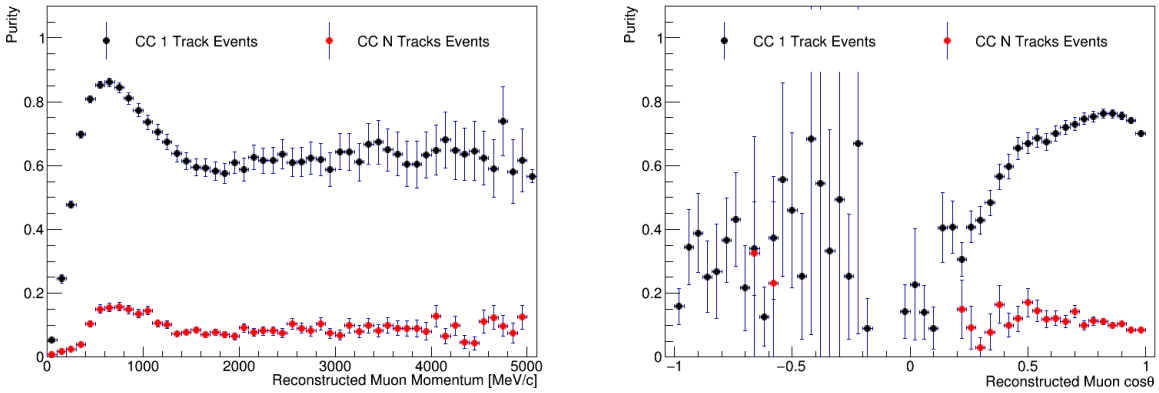

FGD2 RHC $\bar{\nu}$ CC N-Tracks

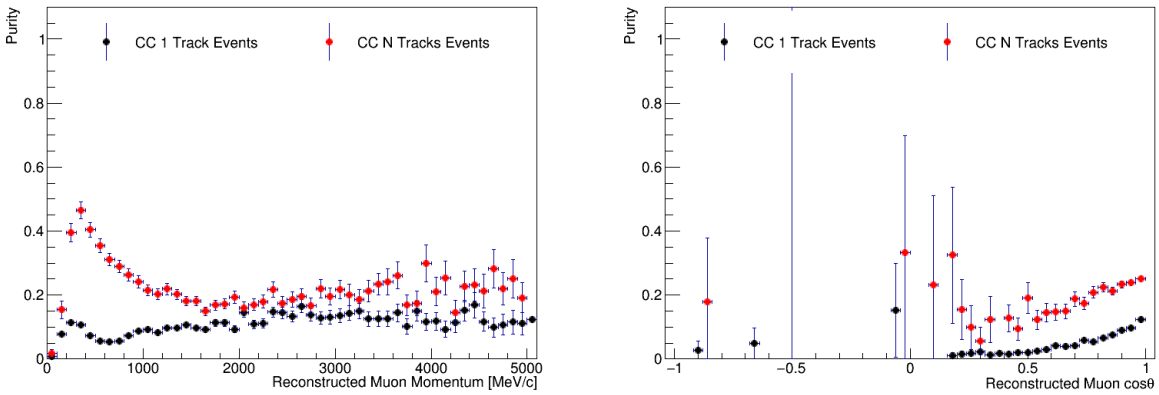

Figure C.6: Selection purity as a function of reconstructed muon momentum (left) or reconstructed muon $\cos\theta$ (right) for the FGD2 RHC $\bar{\nu}$ MultiTrack selections.

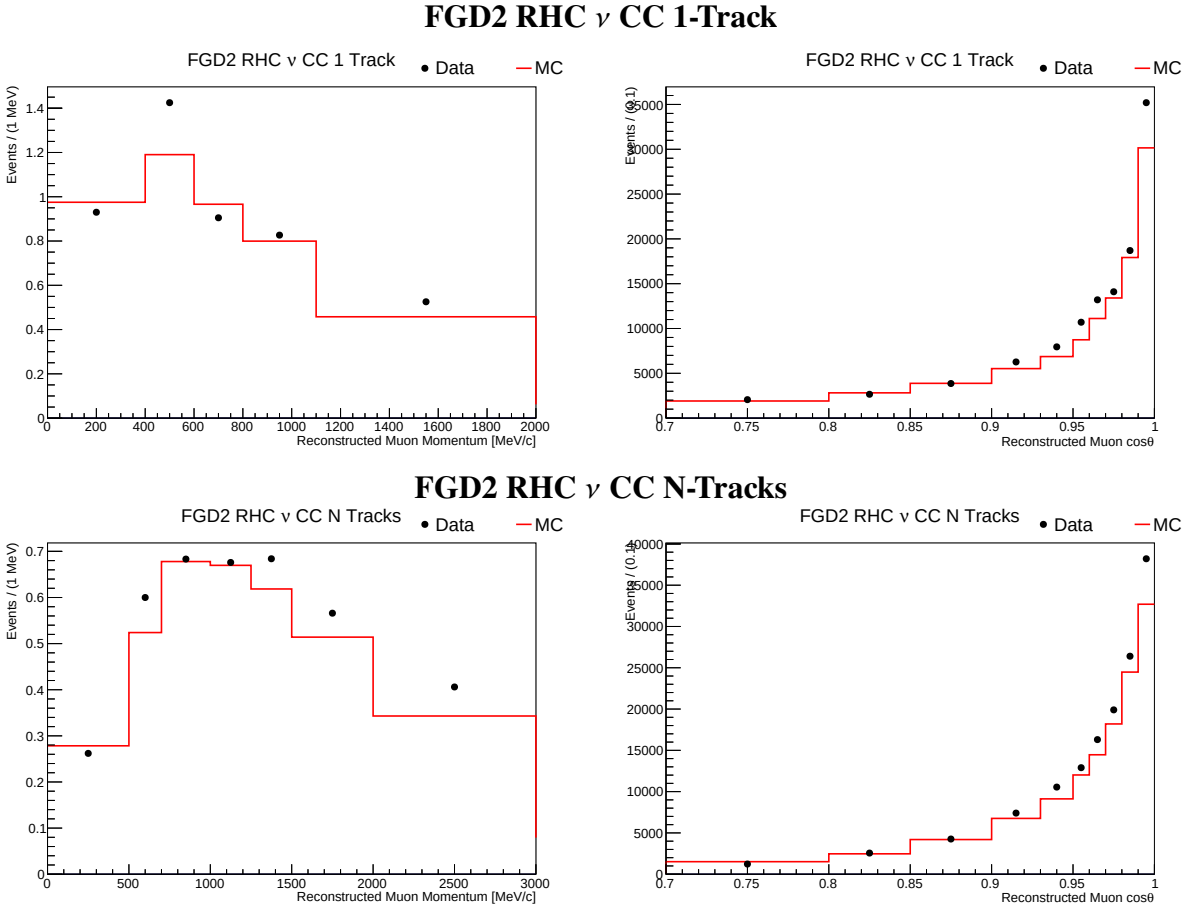

Figure C.7: Kinematic distributions used as inputs to the BANFF fit for the FGD2 RHC ν MultiTrack selections. The momentum distributions are shown on the left, while the angular distributions are shown on the right.

FGD2 RHC ν CC 1-Track

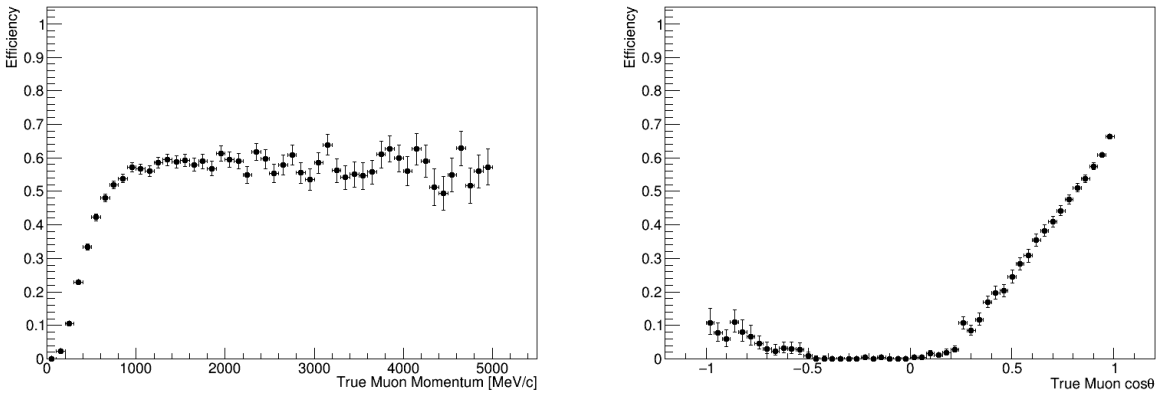

FGD2 RHC ν CC N-Tracks

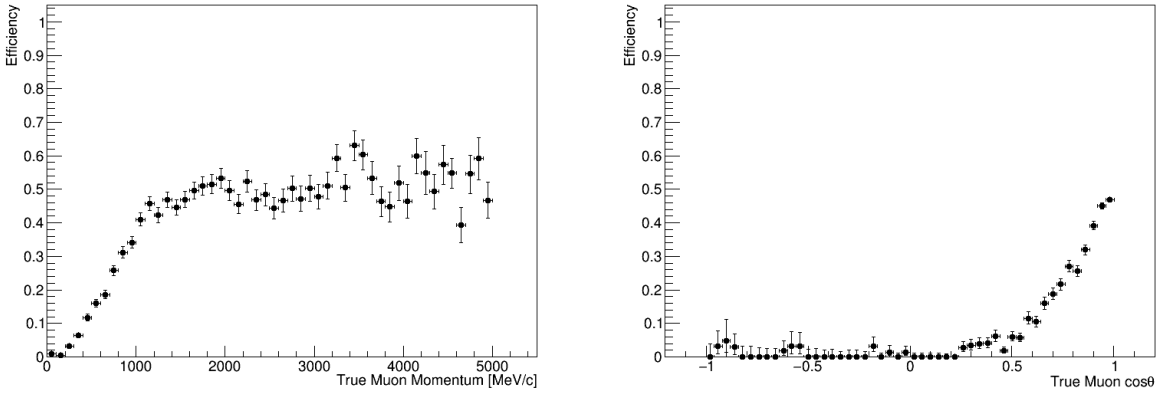

Figure C.8: Selection efficiency as a function of true muon momentum (left) or true muon $\cos\theta$ (right) for the FGD2 RHC ν MultiTrack selections.

FGD2 RHC ν CC 1-Track

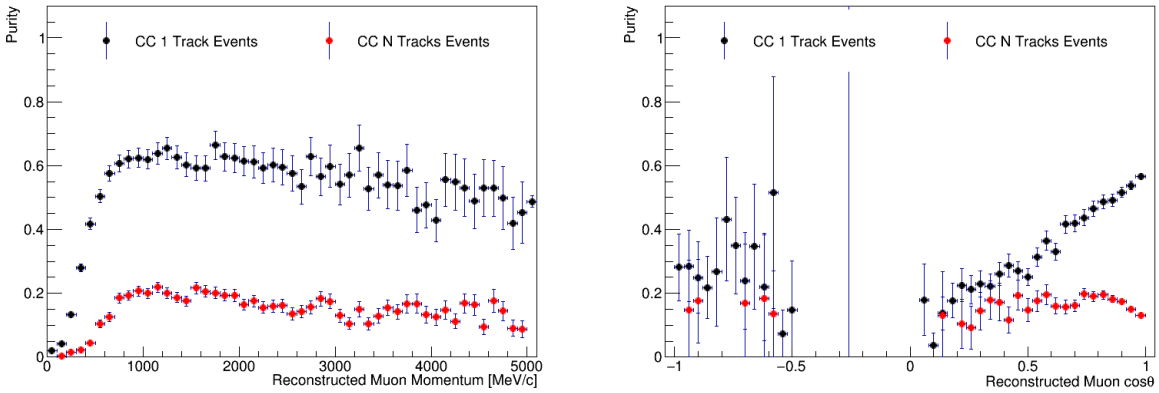

FGD2 RHC ν CC N-Tracks

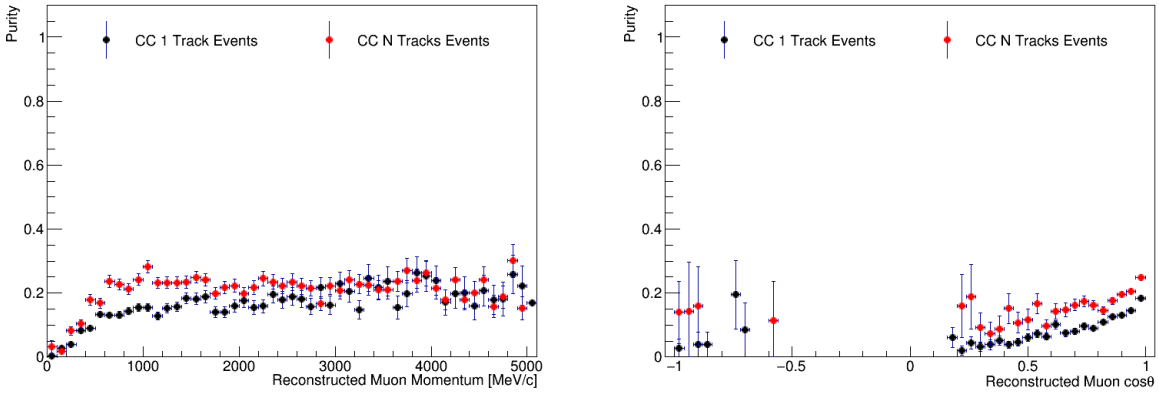

Figure C.9: Selection purity as a function of reconstructed muon momentum (left) or reconstructed muon $\cos\theta$ (right) for the FGD2 RHC ν MultiTrack selections.

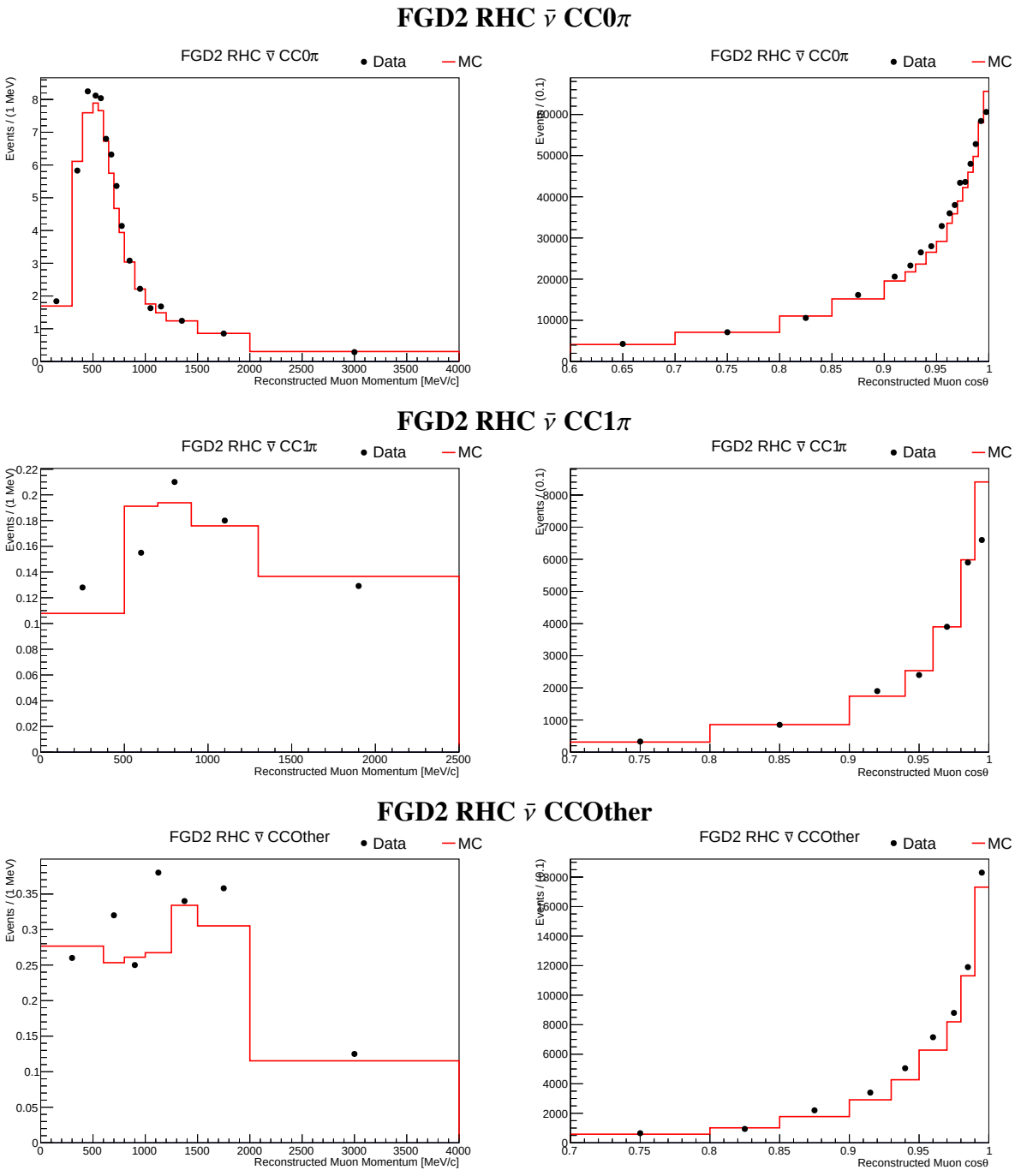

Figure C.10: Kinematic distributions used as inputs to the BANFF fit for the FGD2 RHC $\bar{\nu}$ MultiPi selections. The momentum distributions are shown on the left, while the angular distributions are shown on the right.

FGD2 RHC $\bar{\nu}$ CC0π

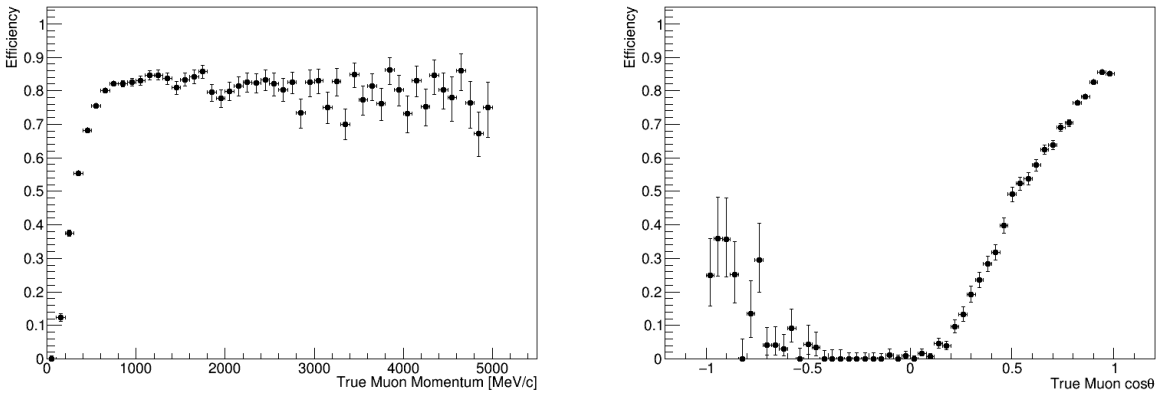

FGD2 RHC $\bar{\nu}$ CC1π

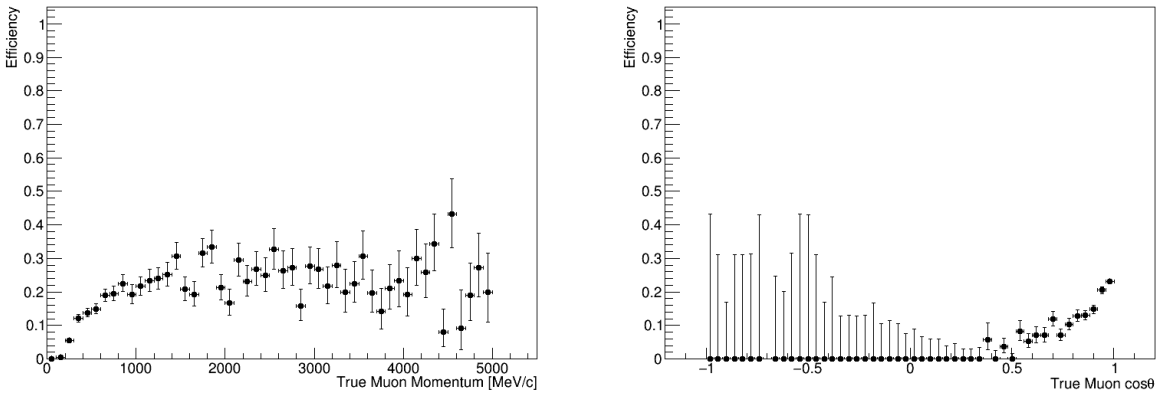

FGD2 RHC $\bar{\nu}$ CCOther

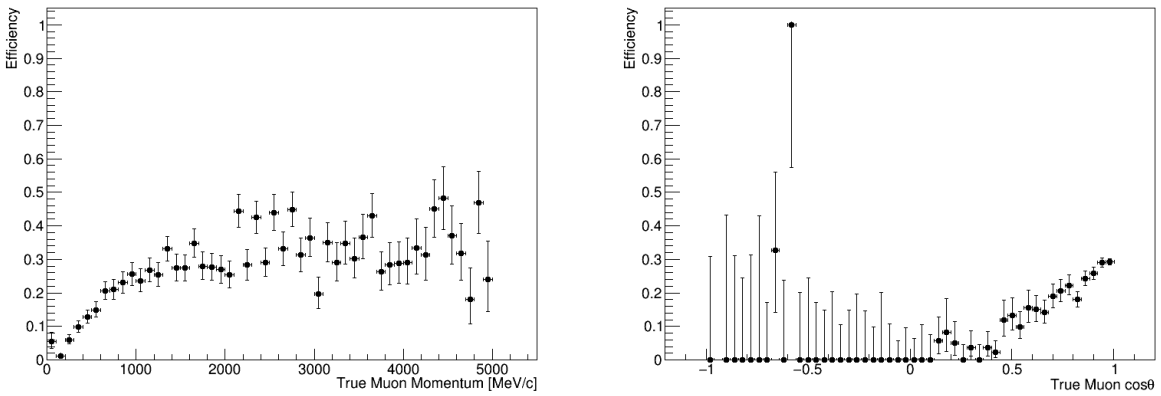

Figure C.11: Selection efficiency as a function of true muon momentum (left) or true muon cos θ (right) for the FGD2 RHC $\bar{\nu}$ MultiPi selections.

FGD2 RHC $\bar{\nu}$ CC0π

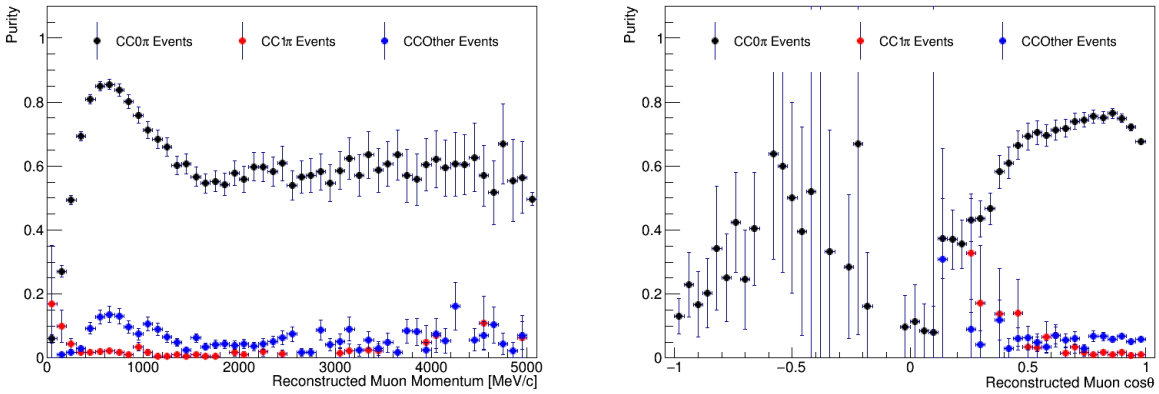

FGD2 RHC $\bar{\nu}$ CC1π

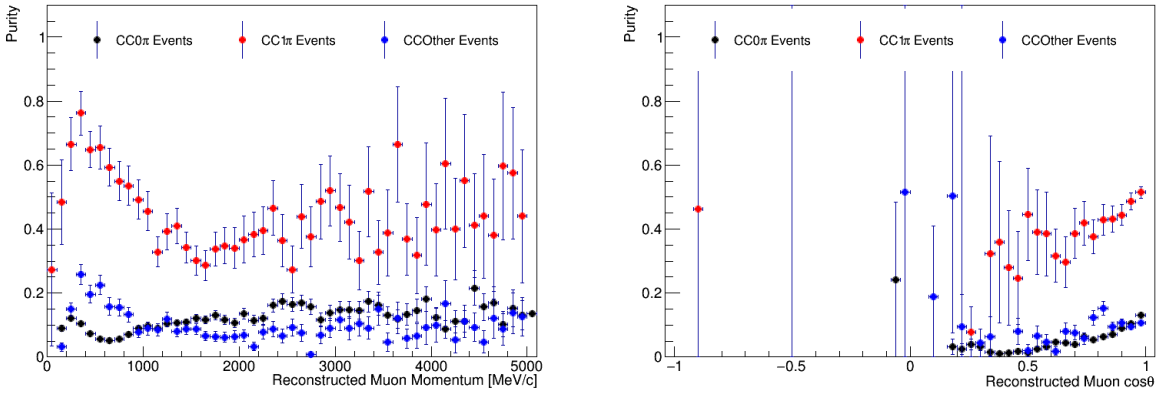

FGD2 RHC $\bar{\nu}$ CCOther

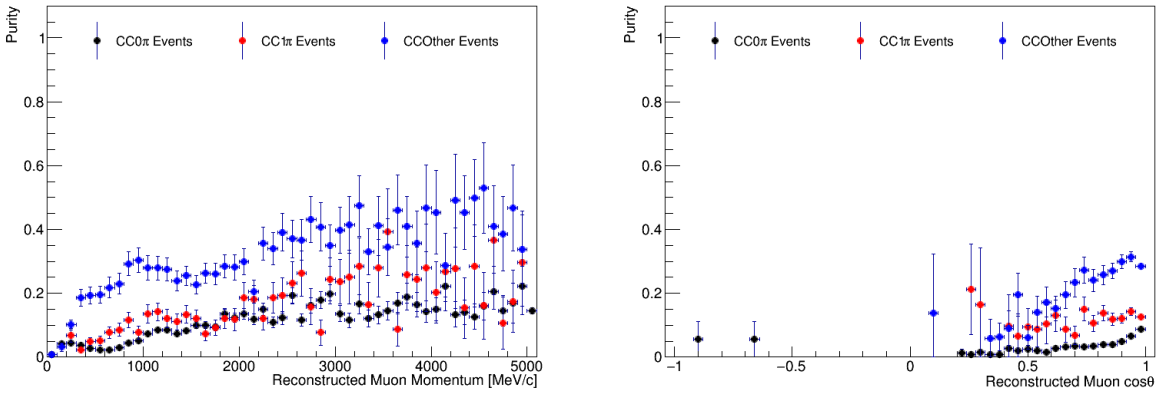

Figure C.12: Selection purity as a function of reconstructed muon momentum (left) or reconstructed muon cos θ (right) for the FGD2 RHC $\bar{\nu}$ MultiPi selections.

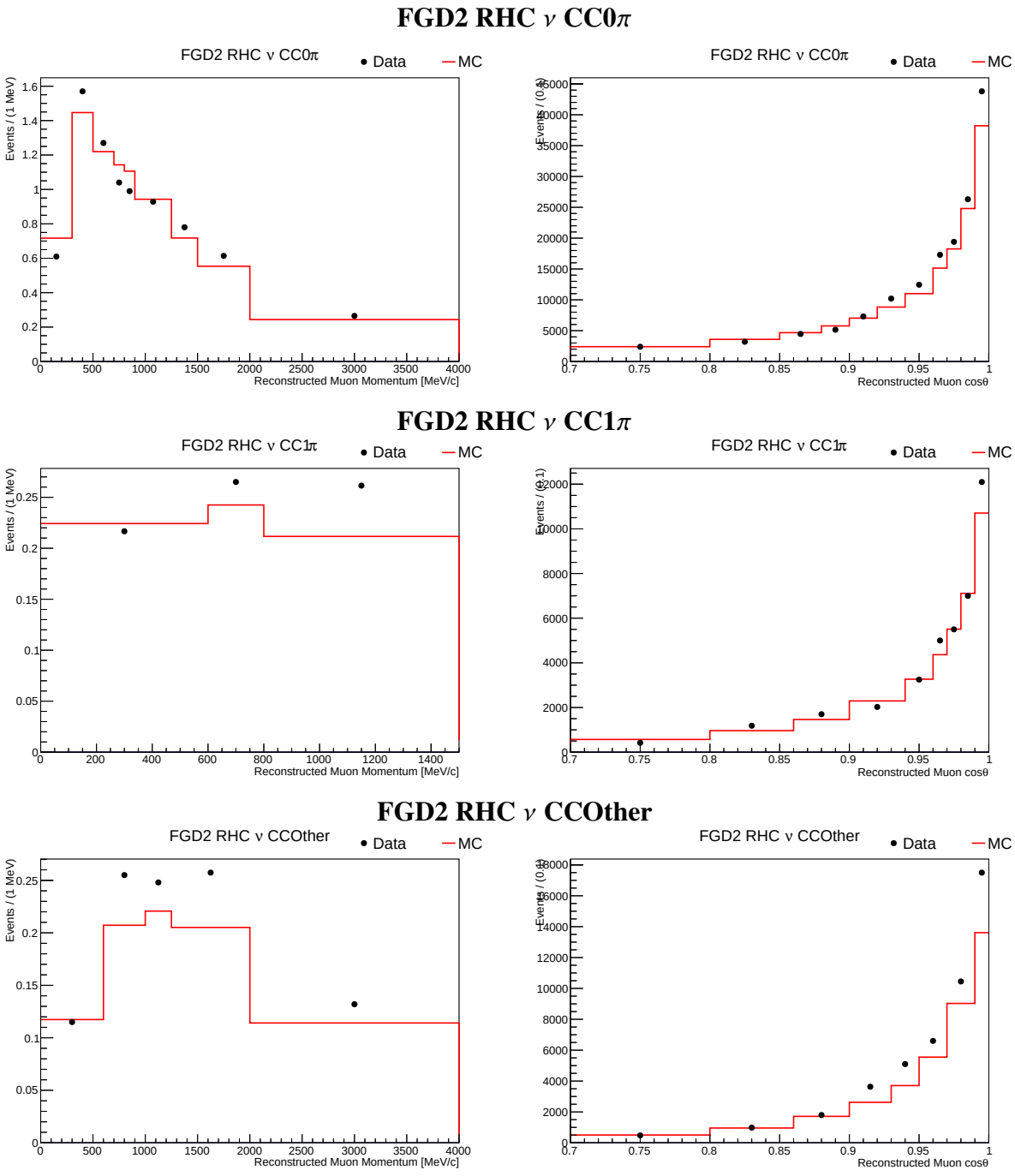

Figure C.13: Kinematic distributions used as inputs to the BANFF fit for the FGD2 RHC ν MultiPi selections. The momentum distributions are shown on the left, while the angular distributions are shown on the right.

FGD2 RHC ν CC0π

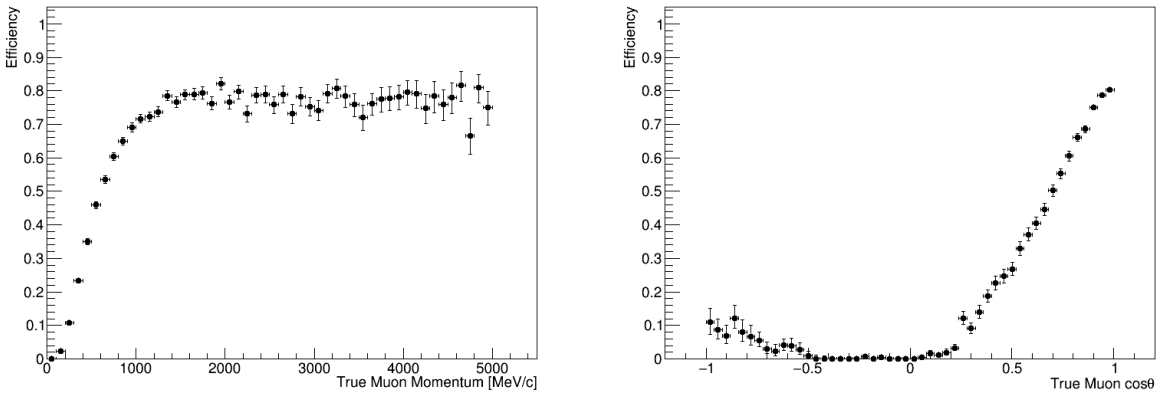

FGD2 RHC ν CC1π

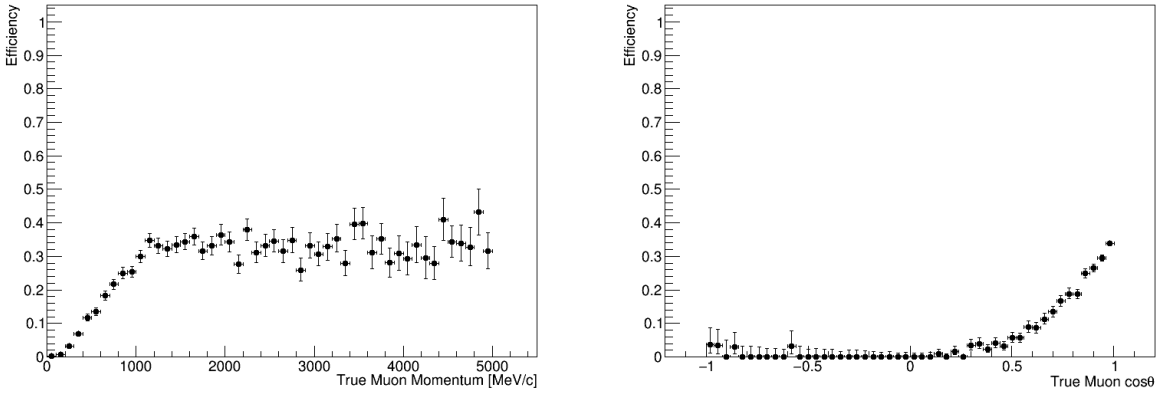

FGD2 RHC ν CCOther

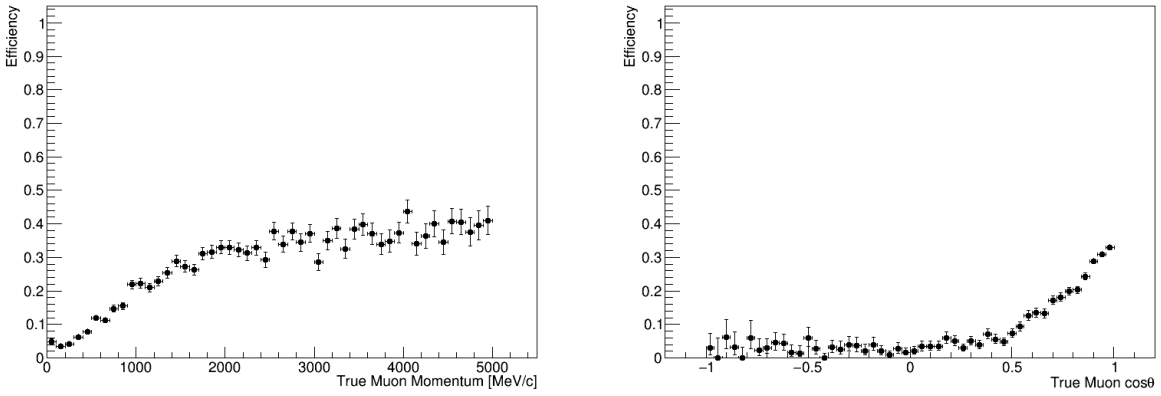

Figure C.14: Selection efficiency as a function of true muon momentum (left) or true muon cos θ (right) for the FGD2 RHC ν MultiPi selections.

FGD2 RHC ν CC0π

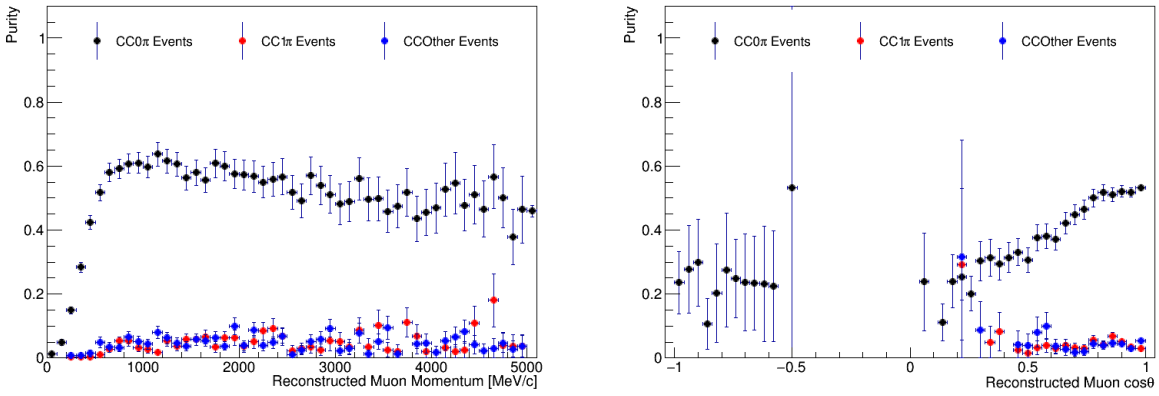

FGD2 RHC ν CC1π

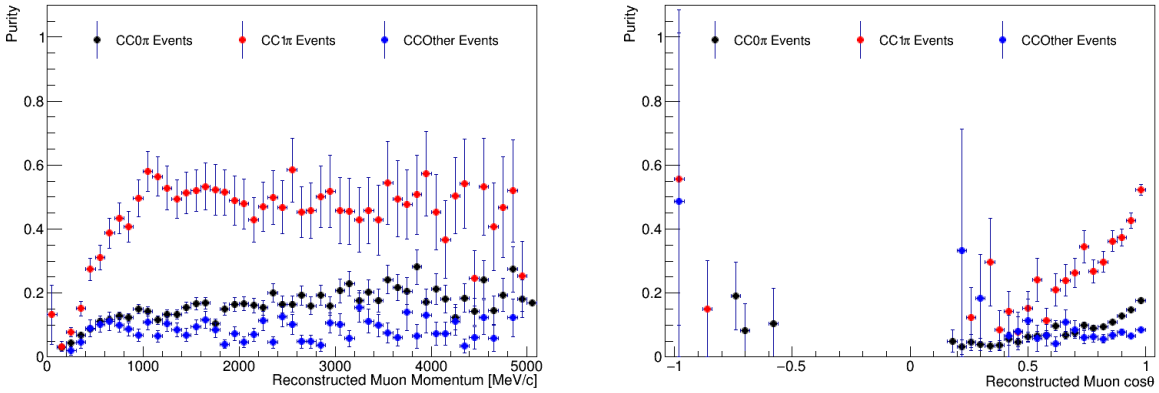

FGD2 RHC ν CCOther

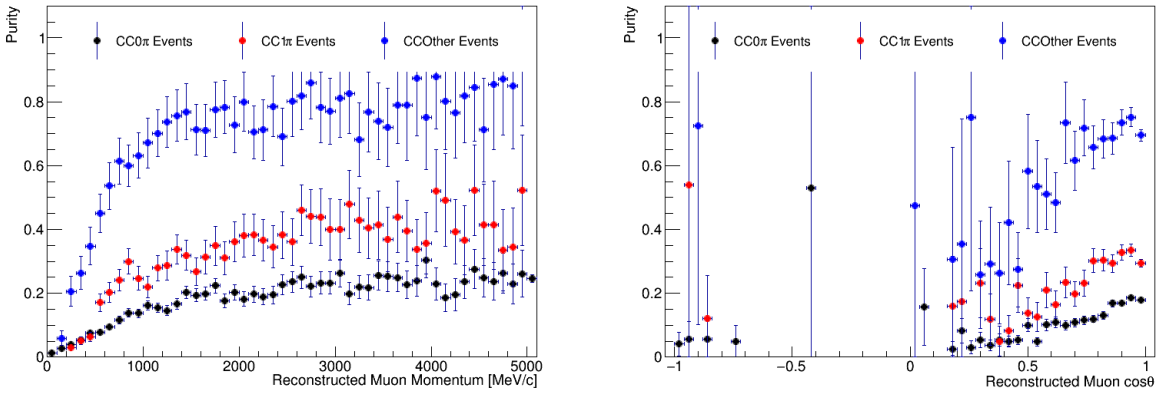

Figure C.15: Selection purity as a function of reconstructed muon momentum (left) or reconstructed muon cos θ (right) for the FGD2 RHC ν MultiPi selections.

FHC MultiPi Samples

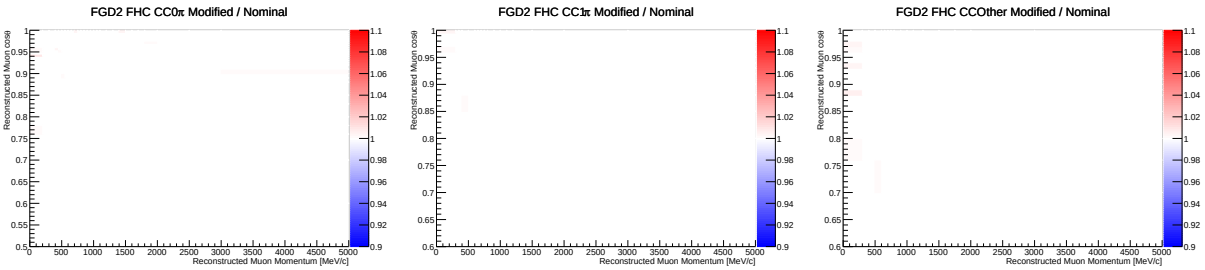

RHC $\bar{\nu}$ MultiPi Samples

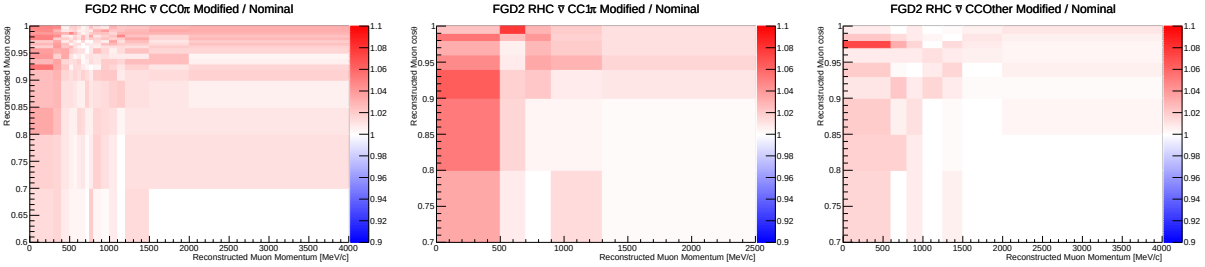

RHC ν MultiPi Samples

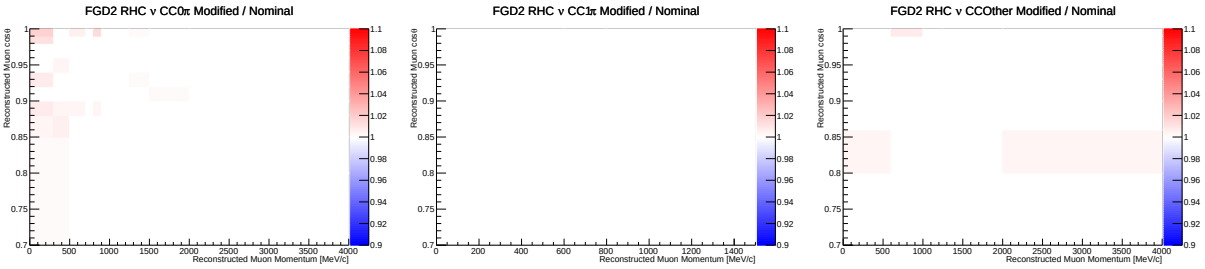

Figure C.16: Ratios of the modified $p - \cos\theta$ distribution, which includes additional antineutrino single pion production events, to the nominal distribution for FGD2. The CC0π samples (left), CC1π samples (middle), and CCOther samples (right) are shown.

FHC MultiPi Samples

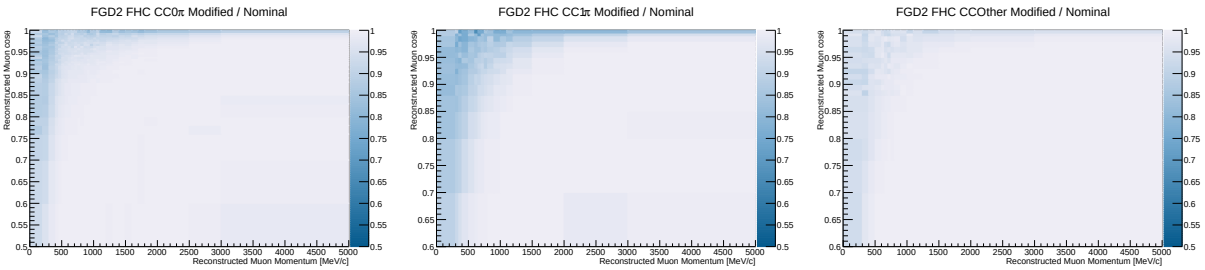

RHC $\bar{\nu}$ MultiPi Samples

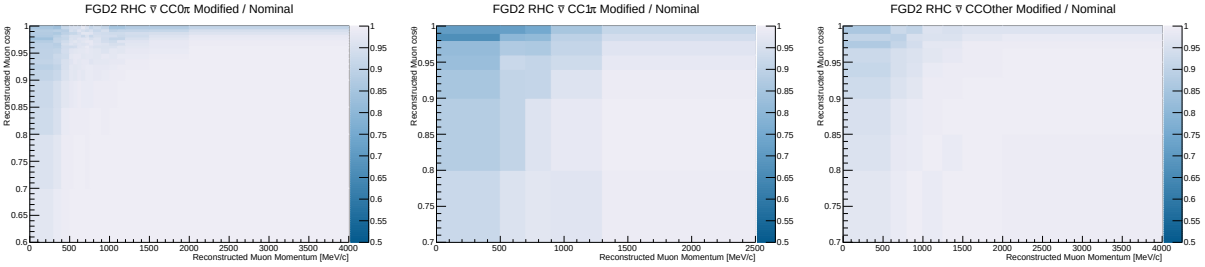

RHC ν MultiPi Samples

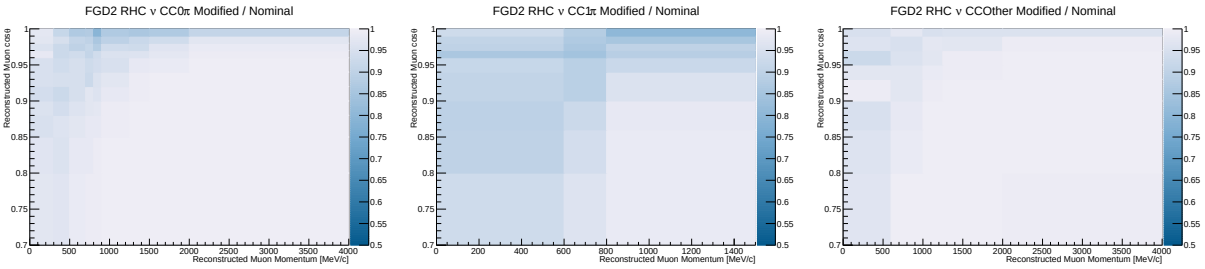

Figure C.17: Ratios of the modified $p - \cos\theta$ distribution, which includes the low Q^2 suppression weight, to the nominal distribution for FGD2. The CC0π samples (left), CC1π samples (middle), and CCOther samples (right) are shown.

BIBLIOGRAPHY

BIBLIOGRAPHY

[1] J. Myslik, Measurement of muon antineutrino disappearance in the T2K Experiment, Ph.D. thesis, University of Victoria (2016), (https://t2k.org/docs/thesis/074)

[2] F. Capozzi et al., "Global constraints on absolute neutrino masses and their ordering", Phys. Rev. D vol. 95 p. 096014 (2017), doi:10.1103/PhysRevD.95.096014, URL https://link.aps.org/doi/10.1103/PhysRevD.95.096014

[3] M. Tanabashi et al. (Particle Data Group), "Review of Particle Physics", Phys. Rev. D vol. 98 p. 030001 (2018), doi:10.1103/PhysRevD.98.030001, URL https://link.aps.org/doi/10.1103/PhysRevD.98.030001

[4] S. Bienstock et al., "Five Sample Joint Oscillation Analysis with T2K Run1-9 Data", Tech. Rep. 367, T2K (2018), Internal T2K Technical Note, https://t2k.org/docs/technotes/367

[5] C. Andreopoulos et al., "T2K Neutrino and Anti-Neutrino 3-Flavour Joint Analysis of Run 1-9 (1.4938×10^{21}-POT ν 1.6346×10^{21}-POT $\bar{\nu}$) data sets", Tech. Rep. 360, T2K (2018), Internal T2K Technical Note, https://t2k.org/docs/technotes/360

[6] M.G. Catanesi et al., "CC multiple pion $\bar{\nu}_\mu$ and ν_μ background event selections in the ND280 tracker using Run 5c to Run 7b data", Tech. Rep. 273, T2K (2018), Internal T2K Technical Note, https://t2k.org/docs/technotes/273

[7] P. Bartet and O. Thers, "ν_μ CC event selections in the ND280 tracker using Run 2+3+4 data", Tech. Rep. 212, T2K (2015), Internal T2K Technical Note, https://www.t2k.org/docs/technotes/212

[8] Y. Petrov and A. Hillairet, "ND280 TPC Track Reconstruction Efficiency", Tech. Rep. 163, T2K (2016), Internal T2K Technical Note, https://www.t2k.org/docs/technotes/163

[9] A. Hillairet, T. Lindner, J. Myslik, and P. Stamoulis, "ND280 tracker tracking efficiency", Tech. Rep. 075, T2K (2012), Internal T2K Technical Note, https://www.t2k.org/docs/technotes/075

[10] J. Kim, C. Nielsen, and M. Wilking, "Michel Electron Tagging in the FGDs", Tech. Rep. 104, T2K (2015), Internal T2K Technical Note, https://www.t2k.org/docs/technotes/104

[11] K. Mahn, S. Oser, and T. Lindner, "FGD mass checks", Tech. Rep. 122, T2K (2012), Internal T2K Technical Note, https://www.t2k.org/docs/technotes/122

[12] F. Dufour, L. Haegel, T. Lindner, and S. Oser, "Systematics on Out-of-Fiducial-Volume Backgrounds in the ND280 Tracker", Tech. Rep. 098, T2K (2015), Internal T2K Technical Note, https://www.t2k.org/docs/technotes/098

[13] J. A. Formaggio and G. P. Zeller, "From eV to EeV: Neutrino cross sections across energy scales", Rev. Mod. Phys. vol. 84 (3) pp. 1307–1341 (2012), doi:10.1103/RevModPhys.84.1307, URL https://link.aps.org/doi/10.1103/RevModPhys.84.1307

[14] S. Gollapinni, "Neutrino Cross Section Future", (2016), https://arxiv.org/pdf/1602.05299.pdf

[15] Y. Fukuda et al. (Super-Kamiokande Collaboration), "Evidence for Oscillation of Atmospheric Neutrinos", Phys. Rev. Lett. vol. 81 pp. 1562–1567 (1998), doi:10.1103/PhysRevLett.81.1562, URL https://link.aps.org/doi/10.1103/PhysRevLett.81.1562

[16] K. Abe et al., "The T2K experiment", Nuclear Instruments and Methods in Physics Research Section A: Accelerators, Spectrometers, Detectors and Associated Equipment vol. 659 (1) pp. 106 – 135 (2011), doi:https://doi.org/10.1016/j.nima.2011.06.067, URL http://www.sciencedirect.com/science/article/pii/S0168900211011910

[17] K. Abe et al. (T2K collaboration), "T2K neutrino flux prediction", Phys. Rev. D vol. 87 (1) p. 012001 (2013), doi:10.1103/PhysRevD.87.012001

[18] T2K Collaboration, "General and frequently updated plots", Private communication (2018)

[19] K. Suzuki et al., "Measurement of the muon beam direction and muon flux for the T2K neutrino experiment", Progress of Theoretical and Experimental Physics vol. 2015 (5) p. 053C01 (2015), doi:10.1093/ptep/ptv054, URL http://dx.doi.org/10.1093/ptep/ptv054

[20] J. Imber, X. Li, and J. Palomino, "Super-Kamiokande event displays for T2K Run5-6 analysis candidates", Tech. Rep. 219, T2K (2015), Internal T2K Technical Note, https://www.t2k.org/docs/technotes/219/tn219supplements/

[21] A. Fiorentini et al., "Flux Prediction and Uncertainty Updates with NA61 2009 Thin Target Data and Negative Focussing Mode Predictions", Tech. Rep. 217, T2K (2018), Internal T2K Technical Note, https://www.t2k.org/docs/technotes/217

[22] W.M. Alberico, M. Ericson, and A. Molinari, "The role of two particle-two hole excitations in the spin-isospin nuclear response", Annals of Physics vol. 154 (2) pp. 356 – 395 (1984), doi:https://doi.org/10.1016/0003-4916(84)90155-6, URL http://www.sciencedirect.com/science/article/pii/0003491684901556

[23] I. Ruiz Simo et al., "Relativistic model of 2p-2h meson exchange currents in (anti)neutrino scattering", Journal of Physics G: Nuclear and Particle Physics vol. 44 (6) p. 065105 (2017), URL http://stacks.iop.org/0954-3899/44/i=6/a=065105

[24] S. Bolognesi et al., "NIWG model and uncertainties for 2017 oscillation analysis", Tech. Rep. 315, T2K (2017), Internal T2K Technical Note, https://www.t2k.org/docs/technotes/315

[25] K. Abe et al. (The T2K Collaboration), "Measurement of neutrino and antineutrino oscillations by the T2K experiment including a new additional sample of ν_e interactions at the far detector", Phys. Rev. D vol. 96 p. 092006 (2017), doi:10.1103/PhysRevD.96.092006, URL https://link.aps.org/doi/10.1103/PhysRevD.96.092006

[26] F. L. Wilson, "Fermi's Theory of Beta Decay", American Journal of Physics vol. 36 (12) pp. 1150–1160 (1968), doi:10.1119/1.1974382, https://doi.org/10.1119/1.1974382, URL https://doi.org/10.1119/1.1974382

[27] D. Griffiths, Introduction to Elementary Particles, Wiley-VCH, second, revised edn. (2008)

[28] C.M.G. Lattes, H. Muirhead, G.P.S. Occhialini, and C.F. Powell, "PROCESSES INVOLVING CHARGED MESONS", Nature vol. 159 pp. 694–697 (1947), doi:10.1038/159694a0, [,42(1947)]

[29] E. J. Konopinski and H. M. Mahmoud, "The Universal Fermi Interaction", Phys. Rev. vol. 92 pp. 1045–1049 (1953), doi:10.1103/PhysRev.92.1045, URL https://link.aps.org/doi/10.1103/PhysRev.92.1045

[30] F. Reines, "The neutrino: from poltergeist to particle", Rev. Mod. Phys. vol. 68 pp. 317–327 (1996), doi:10.1103/RevModPhys.68.317, URL https://link.aps.org/doi/10.1103/RevModPhys.68.317

[31] F. Reines and C.L. Cowan, "The neutrino", Nature vol. 178 pp. 446–449 (1956)

[32] C. L. Cowan et al., "Detection of the Free Neutrino: a Confirmation", Science vol. 124 (3212) pp. 103–104 (1956), doi:10.1126/science.124.3212.103, http://science.sciencemag.org/content/124/3212/103.full.pdf, URL http://science.sciencemag.org/content/124/3212/103

[33] M. Gell-Mann, "The interpretation of the new particles as displaced charge multiplets", Il Nuovo Cimento (1955-1965) vol. 4 (2) pp. 848–866 (1956), doi:10.1007/BF02748000, URL https://doi.org/10.1007/BF02748000

[34] B. Pontecorvo, "Electron and Muon Neutrinos", Sov. Phys. JETP vol. 10 pp. 1236–1240 (1960), [Zh. Eksp. Teor. Fiz.37,1751(1959)]

[35] T. D. Lee, "Intermediate boson hypothesis of weak interactions", in "Proceedings, 10th International Conference on High-Energy Physics (ICHEP 60): Rochester, NY, USA, 25 Aug - 1 Sep 1960", pp. 567–572 (1960)

[36] G. Danby et al., "Observation of High-Energy Neutrino Reactions and the Existence of Two Kinds of Neutrinos", Phys. Rev. Lett. vol. 9 pp. 36–44 (1962), doi:10.1103/PhysRevLett.9.36, URL https://link.aps.org/doi/10.1103/PhysRevLett.9.36

[37] M. L. Perl et al., "Evidence for Anomalous Lepton Production in $e^+ - e^-$ Annihilation", Phys. Rev. Lett. vol. 35 pp. 1489–1492 (1975), doi:10.1103/PhysRevLett.35.1489, URL https://link.aps.org/doi/10.1103/PhysRevLett.35.1489

[38] K. Kodama et al., "Observation of tau neutrino interactions", Physics Letters B vol. 504 (3) pp. 218 – 224 (2001), doi:https://doi.org/10.1016/S0370-2693(01)00307-0, URL http://www.sciencedirect.com/science/article/pii/S0370269301003070

[39] B. T. Cleveland et al., "Measurement of the solar electron neutrino flux with the Homestake chlorine detector", Astrophys. J. vol. 496 pp. 505–526 (1998)

[40] R. Davis, D. S. Harmer, and K. C. Hoffman, "Search for Neutrinos from the Sun", Phys. Rev. Lett. vol. 20 pp. 1205–1209 (1968), doi:10.1103/PhysRevLett.20.1205, URL https://link.aps.org/doi/10.1103/PhysRevLett.20.1205

[41] J. N. Bahcall, N. A. Bahcall, and G. Shaviv, "Present Status of the Theoretical Predictions for the ^{37}Cl Solar-Neutrino Experiment", Phys. Rev. Lett. vol. 20 pp. 1209–1212 (1968), doi:10.1103/PhysRevLett.20.1209, URL https://link.aps.org/doi/10.1103/PhysRevLett.20.1209

[42] P. A. Cherenkov, "Visible emission of clean liquids by action of γ radiation", Doklady Akademii Nauk SSSR vol. 2 pp. 451+ (1934), URL http://ufn.ru/en/articles/2007/4/g/

[43] K. S. Hirata et al., "Results from one thousand days of real-time, directional solar-neutrino data", Phys. Rev. Lett. vol. 65 pp. 1297–1300 (1990), doi:10.1103/PhysRevLett.65.1297, URL https://link.aps.org/doi/10.1103/PhysRevLett.65.1297

[44] J. N. Bahcall and P. I. Krastev, "Do hep neutrinos affect the solar neutrino energy spectrum?", Physics Letters B vol. 436 (3) pp. 243 – 250 (1998), doi:https://doi.org/10.1016/S0370-2693(98)00920-4, URL http://www.sciencedirect.com/science/article/pii/S0370269398009204

[45] N. Jelley, A.B. McDonald, and R.G.H. Robertson, "The Sudbury Neutrino Observatory", Annual Review of Nuclear and Particle Science vol. 59 (1) pp. 431–465 (2009), doi:10.1146/annurev.nucl.55.090704.151550, https://doi.org/10.1146/annurev.nucl.55.090704.151550, URL https://doi.org/10.1146/annurev.nucl.55.090704.151550

[46] Q. R. Ahmad et al. (SNO Collaboration), "Measurement of the Rate of $\nu_e + d \rightarrow p + p + e^-$ Interactions Produced by ^8B Solar Neutrinos at the Sudbury Neutrino Observatory", Phys. Rev. Lett. vol. 87 p. 071301 (2001), doi:10.1103/PhysRevLett.87.071301, URL https://link.aps.org/doi/10.1103/PhysRevLett.87.071301

[47] Q. R. Ahmad et al. (SNO Collaboration), "Direct Evidence for Neutrino Flavor Transformation from Neutral-Current Interactions in the Sudbury Neutrino Observatory", Phys. Rev. Lett. vol. 89 p. 011301 (2002), doi:10.1103/PhysRevLett.89.011301, URL https://link.aps.org/doi/10.1103/PhysRevLett.89.011301

[48] E. Kearns, "Experimental measurements of atmospheric neutrinos", Nuclear Physics B - Proceedings Supplements vol. 70 (1) pp. 315 – 323 (1999), doi:https://doi.org/10.1016/S0920-5632(98)00441-1, proceedings of the Fifth International Workshop on topics in Astroparticle and Underground Physics, URL http://www.sciencedirect.com/science/article/pii/S0920563298004411

[49] K.S. Hirata et al., "Observation of a small atmospheric ν_μ/ν_e ratio in Kamiokande", Physics Letters B vol. 280 (1) pp. 146 – 152 (1992), doi:https://doi.org/10.1016/0370-2693(92)90788-6, URL http://www.sciencedirect.com/science/article/pii/0370269392907886

[50] B. Pontecorvo, "Neutrino Experiments and the Problem of Conservation of Leptonic Charge", Sov. Phys. JETP vol. 26 pp. 984–988 (1968), [Zh. Eksp. Teor. Fiz.53,1717(1967)]

[51] Z. Maki, M. Nakagawa, and S. Sakata, "Remarks on the Unified Model of Elementary Particles", Progress of Theoretical Physics vol. 28 (5) pp. 870–880 (1962), doi:10.1143/PTP.28.870, http://oup.prod.sis.lan/ptp/article-pdf/28/5/870/5258750/28-5-870.pdf, URL https://dx.doi.org/10.1143/PTP.28.870

[52] J. B. Albert et al. (EXO-200 Collaboration), "Search for $2\nu\beta\beta$ decay of ^{136}Xe to the 0^+_1 excited state of ^{136}Ba with the EXO-200 liquid xenon detector", Phys. Rev. C vol. 93 p. 035501 (2016), doi:10.1103/PhysRevC.93.035501, URL https://link.aps.org/doi/10.1103/PhysRevC.93.035501

[53] W. Xu et al., "The Majorana Demonstrator: A Search for Neutrinoless Double-beta Decay of76Ge", Journal of Physics: Conference Series vol. 606 p. 012004 (2015), doi:10.1088/1742-6596/606/1/012004, URL https://doi.org/10.1088%2F1742-6596%2F606%2F1%2F012004

[54] K. Abe et al., "XMASS detector", Nuclear Instruments and Methods in Physics Research Section A: Accelerators, Spectrometers, Detectors and Associated Equipment vol. 716 pp. 78 – 85 (2013), doi:https://doi.org/10.1016/j.nima.2013.03.059, URL http://www.sciencedirect.com/science/article/pii/S0168900213003690

[55] G. C. Branco, R. González Felipe, and F. R. Joaquim, "Leptonic CP violation", Rev. Mod. Phys. vol. 84 pp. 515–565 (2012), doi:10.1103/RevModPhys.84.515, URL https://link.aps.org/doi/10.1103/RevModPhys.84.515

[56] C.R. Das, J. Pulido, J. Maalampi, and S. Vihonen, "Determination of the θ_{23} octant in long baseline neutrino experiments within and beyond the standard model", Phys. Rev. D vol. 97 p. 035023 (2018), doi:10.1103/PhysRevD.97.035023, URL https://link.aps.org/doi/10.1103/PhysRevD.97.035023

[57] G. Altarelli and F. Feruglio, "Discrete flavor symmetries and models of neutrino mixing", Rev. Mod. Phys. vol. 82 pp. 2701–2729 (2010), doi:10.1103/RevModPhys.82.2701, URL https://link.aps.org/doi/10.1103/RevModPhys.82.2701

[58] A. E. Cárcamo Hernández, S. Kovalenko, J.W.F. Valle, and C. A. Vaquera-Araujo, "Predictive Pati-Salam theory of fermion masses and mixing", Journal of High Energy Physics vol. 2017 (7) p. 118 (2017), doi:10.1007/JHEP07(2017)118, URL https://doi.org/10.1007/JHEP07(2017)118

[59] S. P. Mikheyev and A. Yu. Smirnov, "Resonance Amplification of Oscillations in Matter and Spectroscopy of Solar Neutrinos", Sov. J. Nucl. Phys. vol. 42 pp. 913–917 (1985), [,305(1986)]

[60] L. Wolfenstein, "Neutrino oscillations in matter", Phys. Rev. D vol. 17 pp. 2369–2374 (1978), doi:10.1103/PhysRevD.17.2369, URL https://link.aps.org/doi/10.1103/PhysRevD.17.2369

[61] E.K. Akhmedov, "Neutrino physics", in "Proceedings, Summer School in Particle Physics: Trieste, Italy, June 21-July 9, 1999", pp. 103–164 (1999), hep-ph/0001264

[62] M. Freund, "Analytic approximations for three neutrino oscillation parameters and probabilities in matter", Phys. Rev. D vol. 64 p. 053003 (2001), doi:10.1103/PhysRevD.64.053003, URL https://link.aps.org/doi/10.1103/PhysRevD.64.053003

[63] K. Abe et al. (T2K Collaboration), "Measurements of Neutrino Oscillation in Appearance and Disappearance Channels by the T2K Experiment With 6.6×10^{20} Protons on Target", Phys. Rev. D vol. 91 (7) p. 072010 (2015), doi:10.1103/PhysRevD.91.072010

[64] S. P. Mikheyev and A. Yu. Smirnov, "Resonant amplification of ν oscillations in matter and solar-neutrino spectroscopy", Il Nuovo Cimento C vol. 9 (1) pp. 17–26 (1986), doi:10.1007/BF02508049, URL https://doi.org/10.1007/BF02508049

[65] J. N. Abdurashitov et al., "Measurement of the response of a Ga solar neutrino experiment to neutrinos from a ^{37}Ar source", Phys. Rev. C vol. 73 p. 045805 (2006), doi:10.1103/PhysRevC.73.045805, URL https://link.aps.org/doi/10.1103/PhysRevC.73.045805

[66] C. Giunti et al., "Update of short-baseline electron neutrino and antineutrino disappearance", Phys. Rev. D vol. 86 p. 113014 (2012), doi:10.1103/PhysRevD.86.113014, URL https://link.aps.org/doi/10.1103/PhysRevD.86.113014

[67] A. A. Aguilar-Arevalo et al. (MiniBooNE Collaboration), "Significant Excess of Electronlike Events in the MiniBooNE Short-Baseline Neutrino Experiment", Phys. Rev. Lett. vol. 121 p. 221801 (2018), doi:10.1103/PhysRevLett.121.221801, URL https://link.aps.org/doi/10.1103/PhysRevLett.121.221801

[68] Ade, P. A. R. et al. (Planck Collaboration), "Planck 2015 results - XIII. Cosmological parameters", A&A vol. 594 p. A13 (2016), doi:10.1051/0004-6361/201525830, URL https://doi.org/10.1051/0004-6361/201525830

[69] M. G. Aartsen et al. (IceCube Collaboration), "Search for sterile neutrino mixing using three years of IceCube DeepCore data", Phys. Rev. D vol. 95 p. 112002 (2017), doi:10.1103/PhysRevD.95.112002, URL https://link.aps.org/doi/10.1103/PhysRevD.95.112002

[70] K. Abe et al. (T2K Collaboration), "Search for short baseline ν_e disappearance with the T2K near detector", Phys. Rev. D vol. 91 p. 051102 (2015), doi:10.1103/PhysRevD.91.051102, URL https://link.aps.org/doi/10.1103/PhysRevD.91.051102

[71] K.M. Tsui, Sterile neutrino oscillation studies with the T2K far detector Super-Kamiokande, Ph.D. thesis, The University of Tokyo (2019), (https://t2k.org/docs/thesis/095)

[72] T. Sekiguchi et al., "Development and operational experience of magnetic horn system for T2K experiment", Nuclear Instruments and Methods in Physics Research Section A: Accelerators, Spectrometers, Detectors and Associated Equipment vol. 789

pp. 57 – 80 (2015), doi:https://doi.org/10.1016/j.nima.2015.04.008, URL http://www.sciencedirect.com/science/article/pii/S0168900215004672

[73] K. Suzuki et al., "Measurement of the muon beam direction and muon flux for the T2K neutrino experiment", Progress of Theoretical and Experimental Physics vol. 2015 (5) p. 053C01 (2015), doi:10.1093/ptep/ptv054

[74] D. Beavis et al., "Long Baseline Neutrino Oscillation Experiment at the AGS", (1995), E889 Physics Design Report, BNL-52459, URL http://puhep1.princeton.edu/~mcdonald/nufact/e889/chapter3a.pdf

[75] K. Abe et al., "Measurements of the T2K neutrino beam properties using the INGRID on-axis near detector", Nuclear Instruments and Methods in Physics Research Section A: Accelerators, Spectrometers, Detectors and Associated Equipment vol. 694 pp. 211 – 223 (2012), doi:https://doi.org/10.1016/j.nima.2012.03.023, URL http://www.sciencedirect.com/science/article/pii/S0168900212002987

[76] M. Yokoyama et al., "Development of Multi-Pixel Photon Counters", eConf vol. C0604032 p. 0126 (2006), arXiv:physics/0605241 [physics.ins-det]

[77] D. Allan et al., "The electromagnetic calorimeter for the T2K near detector ND280", Journal of Instrumentation vol. 8 (10) p. P10019 (2013), URL http://stacks.iop.org/1748-0221/8/i=10/a=P10019

[78] S. Assylbekov et al., "The T2K ND280 off-axis pi-zero detector", Nuclear Instruments and Methods in Physics Research Section A: Accelerators, Spectrometers, Detectors and Associated Equipment vol. 686 pp. 48 – 63 (2012), doi:10.1016/j.nima.2012.05.028

[79] P.-A. Amaudruz et al., "The T2K Fine-Grained Detectors", Nuclear Instruments and Methods in Physics Research Section A: Accelerators, Spectrometers, Detectors and Associated Equipment vol. 696 pp. 1 – 31 (2012), doi:10.1016/j.nima.2012.08.020

[80] N. Abgrall et al., "Time Projection Chambers for the T2K Near Detectors", Nuclear Instruments and Methods in Physics Research Section A: Accelerators, Spectrometers, Detectors and Associated Equipment vol. 637 (1) pp. 25 – 46 (2011), doi:10.1016/j.nima.2011.02.036

[81] G. Charpak, J. Derre, Y. Giomataris, and P. Rebourgeard, "MICROMEGAS, a multipurpose gaseous detector", Nucl. Instrum. Meth. vol. A478 pp. 26–36 (2002), doi:10.1016/S0168-9002(01)01713-2

[82] S. Fukuda et al., "The Super-Kamiokande detector", Nuclear Instruments and Methods in Physics Research Section A: Accelerators, Spectrometers, Detectors and Associated Equipment vol. 501 (2) pp. 418 – 462 (2003), doi:https://doi.org/10.1016/S0168-9002(03)00425-X, URL http://www.sciencedirect.com/science/article/pii/S016890020300425X

[83] J. Kameda, "Updated study of the systematic error in ν_μ disappearance analysis from Super-Kamiokande", Tech. Rep. 159, T2K (2013), Internal T2K Technical Note, https://www.t2k.org/docs/technotes/163

[84] L. Alvarez-Ruso et al., "NuSTEC11Neutrino Scattering Theory Experiment Collaboration http://nustec.fnal.gov. White Paper: Status and challenges of neutrino–nucleus scattering", Progress in Particle and Nuclear Physics vol. 100 pp. 1 – 68 (2018), doi:https://doi.org/10.1016/j.ppnp.2018.01.006, URL http://www.sciencedirect.com/science/article/pii/S0146641018300061

[85] N. Abgrall et al., "NA61/SHINE facility at the CERN SPS: beams and detector system", Journal of Instrumentation vol. 9 (06) p. P06005 (2014), URL http://stacks.iop.org/1748-0221/9/i=06/a=P06005

[86] L. Aliaga et al., "Design, calibration, and performance of the MINERvA detector", Nuclear Instruments and Methods in Physics Research Section A: Accelerators, Spectrometers, Detectors and Associated Equipment vol. 743 pp. 130 – 159 (2014), doi:https://doi.org/10.1016/j.nima.2013.12.053, URL http://www.sciencedirect.com/science/article/pii/S0168900214000035

[87] R. Akutsu et al., "Super-Kamiokande events and data quality studies for T2K Run 8", Tech. Rep. 317, T2K (2017), Internal T2K Technical Note, https://www.t2k.org/docs/technotes/317

[88] X. Li and M. Wilking, "FiTQun Event Selection Optimization", Tech. Rep. 319, T2K (2017), Internal T2K Technical Note, https://www.t2k.org/docs/technotes/319

[89] A. Kaboth, R. Calland, and D. Payne, "A Joint ND280-SK $1R_\mu$-SK $1R_e$ Fit using MCMC", Tech. Rep. 171, T2K (2014), Internal T2K Technical Note, https://www.t2k.org/docs/technotes/171

[90] F. James and M. Roos, "Minuit - a system for function minimization and analysis of the parameter errors and correlations", Computer Physics Communications vol. 10 (6) pp. 343 – 367 (1975), doi:https://doi.org/10.1016/0010-4655(75)90039-9, URL http://www.sciencedirect.com/science/article/pii/0010465575900399

[91] R. Brun and F. Rademakers, "ROOT — An object oriented data analysis framework", Nuclear Instruments and Methods in Physics Research Section A: Accelerators, Spectrometers, Detectors and Associated Equipment vol. 389 (1) pp. 81 – 86 (1997), doi:https://doi.org/10.1016/S0168-9002(97)00048-X, URL http://www.sciencedirect.com/science/article/pii/S016890029700048X

[92] Y. Hayato, "A neutrino interaction simulation program library NEUT", Acta Phys. Polon. vol. B (40) pp. 2477–2489 (2009)

[93] J. Nieves, I. Ruiz Simo, and M. J. Vicente Vacas, "Inclusive charged-current neutrino-nucleus reactions", Phys. Rev. C vol. 83 p. 045501 (2011), doi:10.1103/PhysRevC.83.045501, URL https://link.aps.org/doi/10.1103/PhysRevC.83.045501

[94] S. Bolognesi et al., "Assessing the effect of cross-section model uncertainties on the T2K oscillation analyses with fake data studies using the BANFF, MaCh3 and VALOR fit frameworks", Tech. Rep. 285, T2K (2016), Internal T2K Technical Note, https://t2k.org/docs/technotes/285

[95] S. Dulat et al., "New parton distribution functions from a global analysis of quantum chromodynamics", Phys. Rev. D vol. 93 p. 033006 (2016), doi:10.1103/PhysRevD.93.033006, URL https://link.aps.org/doi/10.1103/PhysRevD.93.033006

[96] R. Gran, J. Nieves, F. Sanchez, and M. J. Vicente Vacas, "Neutrino-nucleus quasi-elastic and 2p2h interactions up to 10 GeV", Phys. Rev. D vol. 88 p. 113007 (2013), doi:10.1103/PhysRevD.88.113007, URL https://link.aps.org/doi/10.1103/PhysRevD.88.113007

[97] C. Colle et al., "Extracting the mass dependence and quantum numbers of short-range correlated pairs from $A(e,e'p)$ and $A(e,e'pp)$ scattering", Phys. Rev. C vol. 92 p. 024604 (2015), doi:10.1103/PhysRevC.92.024604, URL https://link.aps.org/doi/10.1103/PhysRevC.92.024604

[98] D. Rein and L.M. Sehgal, "Neutrino-excitation of baryon resonances and single pion production", Annals of Physics vol. 133 (1) pp. 79 – 153 (1981), doi:https://doi.org/10.1016/0003-4916(81)90242-6, URL http://www.sciencedirect.com/science/article/pii/0003491681902426

[99] L. Fields et al. (MINERvA Collaboration), "Measurement of Muon Antineutrino Quasielastic Scattering on a Hydrocarbon Target at $E_\nu \sim 3.5$ GeV", Phys. Rev. Lett. vol. 111 p. 022501 (2013), doi:10.1103/PhysRevLett.111.022501, URL https://link.aps.org/doi/10.1103/PhysRevLett.111.022501

[100] Melanie Day and Kevin S. McFarland, "Differences in quasielastic cross sections of muon and electron neutrinos", Phys. Rev. D vol. 86 p. 053003 (2012), doi:10.1103/PhysRevD.86.053003, URL https://link.aps.org/doi/10.1103/PhysRevD.86.053003

[101] K. S. Kim and M. K. Cheoun, "Final state interaction and Coulomb effect for neutrino-nucleus scattering in the quasielastic region", AIP Conference Proceedings vol. 1189 (1) pp. 163–168 (2009), doi:10.1063/1.3274148, https://aip.scitation.org/doi/pdf/10.1063/1.3274148, URL https://aip.scitation.org/doi/abs/10.1063/1.3274148

[102] T. Feusels et al., "Tuning of the NEUT Cascade Model using $\pi^{\pm}$-A Scattering External Data to Improve Final State Interaction and Secondary Interaction Systematic Uncertainties", Tech. Rep. 325, T2K (2017), Internal T2K Technical Note, https://www.t2k.org/docs/technotes/325

[103] E. S. Pinzon Guerra et al. (DUET Collaboration), "Measurement of σ_{ABS} and σ_{CX} of π^+ on carbon by the Dual Use Experiment at TRIUMF (DUET)", Phys. Rev. C vol. 95 p. 045203 (2017), doi:10.1103/PhysRevC.95.045203, URL https://link.aps.org/doi/10.1103/PhysRevC.95.045203

[104] P. de Perio, Y. Hayato, and R. Tacik, "NEUT nuclear effects", Tech. Rep. 033, T2K (2012), Internal T2K Technical Note, https://www.t2k.org/docs/technotes/033

[105] S. Agostinelli et al., "Geant4 – a simulation toolkit", Nuclear Instruments and Methods in Physics Research Section A: Accelerators, Spectrometers, Detectors and Associated

Equipment vol. 506 (3) pp. 250–303 (2003), doi:10.1016/S0168-9002(03)01368-8, URL https://www.sciencedirect.com/science/article/pii/S0168900203013688

[106] M. Bass et al., "Quality assessment strategy of the 2010b data set at ND280.", Tech. Rep. 021, T2K (2011), Internal T2K Technical Note, https://www.t2k.org/docs/technotes/021

[107] E. Frank, A. Marchionni, and M. Messina, "B-field calibration and systematic errors", Tech. Rep. 081, T2K (2011), Internal T2K Technical Note, https://www.t2k.org/docs/technotes/081

[108] C. Bojechko et al., "Measurement and Correction of Magnetic Field Distortions in the Time Projection Chambers", Tech. Rep. 061, T2K (2012), Internal T2K Technical Note, https://www.t2k.org/docs/technotes/061

[109] A. Cervera and L. Escudero, "Study of momentum resolution and scale using tracks that cross multiple TPCs", Tech. Rep. 222, T2K (2015), Internal T2K Technical Note, https://www.t2k.org/docs/technotes/222

[110] W. Oryszczak and W. Warzycha, "FGD systematics: PID and IsoRecon hybrid efficiency", Tech. Rep. 223, T2K (2015), Internal T2K Technical Note, https://www.t2k.org/docs/technotes/223

[111] F. Sanchez and J. vo Medina, "ND280 global charge identification systematic error", Tech. Rep. 229, T2K (2016), Internal T2K Technical Note, https://www.t2k.org/docs/technotes/229

[112] J. Myslik, "Determination of pion secondary interaction systematics for the ND280 tracker ν_μ analysis", Tech. Rep. 125, T2K (2013), Internal T2K Technical Note, https://www.t2k.org/docs/technotes/125

[113] A. Cervera et al., "CC-0Pi Multi-Topology Selection and Systematics in FGD1", Tech. Rep. 216, T2K (2015), Internal T2K Technical Note, https://www.t2k.org/docs/technotes/216

[114] S. Bienstock et al., "Assessing the effect of cross-section model uncertainties on the T2K oscillation analyses with simulated data studies using the BANFF, MaCh3, P-Theta and VALOR fit frameworks", Tech. Rep. 331, T2K (2018), Internal T2K Technical Note, https://www.t2k.org/docs/technotes/331

[115] M. Kabirnezhad, "Single pion production in neutrino-nucleon interactions", Phys. Rev. D vol. 97 p. 013002 (2018), doi:10.1103/PhysRevD.97.013002, URL https://link.aps.org/doi/10.1103/PhysRevD.97.013002

[116] C. L. McGivern et al. (MINERvA Collaboration), "Cross sections for ν_μ and $\overline{\nu}_\mu$ induced pion production on hydrocarbon in the few-GeV region using MINERvA", Phys. Rev. D vol. 94 p. 052005 (2016), doi:10.1103/PhysRevD.94.052005, URL https://link.aps.org/doi/10.1103/PhysRevD.94.052005

[117] O. Altinok et al., "Measurement of ν_μ charged-current single π^0 production on hydrocarbon in the few-GeV region using MINERvA", Phys. Rev. D vol. 96 p. 072003 (2017), doi:10.1103/PhysRevD.96.072003, URL https://link.aps.org/doi/10.1103/PhysRevD.96.072003

[118] P. Adamson et al. (MINOS Collaboration), "Study of quasielastic scattering using charged-current ν_μ-iron interactions in the MINOS near detector", Phys. Rev. D vol. 91 p. 012005 (2015), doi:10.1103/PhysRevD.91.012005, URL https://link.aps.org/doi/10.1103/PhysRevD.91.012005

[119] D. S. Ayres et al. (NOvA), "The NOvA Technical Design Report", (2007), doi:10.2172/935497

[120] M. Sanchez, "NOvA Results and Prospects", (2018), doi:10.5281/zenodo.1286758, URL https://doi.org/10.5281/zenodo.1286758

[121] J. Wolcott, "Impact of cross section modelling on NOνA oscillation analyses", (2018), URL https://indico.cern.ch/event/703880/contributions/3159021/

[122] J. Morrison, M. Scott, and J. Walker, "BANFF Psyche v1/v3 Comparisons", T2K Collaboration Meeting Parallel Talk, https://t2k.org/asg/oagroup/meeting/2018/2018-12-03/v1v3banff